Doctoral Dissertation

Silicon Photonic Crystal
Optical Antennas and their Applications

(シリコンフォトニック結晶光アンテナとその応用)

Ryo Tetsuya

(鉄矢 諒)

Yokohama National University

Department of Physics, Electrical and Computer Engineering

September 2022

論文要旨

　本論文では，シリコン（Si）フォトニクスにおけるフォトニック結晶光アンテナについて，特に光レーダ（Light Detection and Ranging：LiDAR）に向けた送受信特性改善と，その他の応用として自由空間光通信への可能性について議論する.

　ここ十数年，Si フォトニクス技術を用いた小型で安価な LiDAR チップ開発が，大学やベンチャー企業，研究機関において盛んである. LiDAR とは周囲の距離情報をイメージ化する 3次元センサの一つであり，特に自動運転実現に向けた運転支援や産業ロボット，地図作成，建設，仮想/拡張現実（VR/AR）など様々な応用先が期待されている. 既存の商用化されている LiDAR 装置は光のビーム走査に機械部品をもつので，大型かつ高価であり車載用途では振動や物理的衝撃に対する信頼性で不安が残る. 一方で Si フォトニクスによる非機械式のビーム走査を実現する素子による LiDAR システム開発が注目されている. Si フォトニクスとは，現代社会を支える電子機器に欠かせない Si 集積回路（IC）チップを製作する Complementary Metal-Oxide-Semiconductor（CMOS）プロセスを基盤として，光導波路や光スイッチ，光変調器，受光器などの光集積素子を，Silicon-On-Insulator（SOI）基板上に製作する技術のことである. 近年 Si フォトニクスファウンダリサービスが充実しており，独自で高価な設備を購入し保守管理する必要がなく，Si フォトニクスチップの設計と評価に集中した研究開発を行うことができる. このような Si フォトニクス技術に基づいた，光フェーズドアレー（OPA）や焦点面アレー（FPA）を光ビーム走査素子として用いた LiDAR チップ開発は，LiDAR 実証の報告例があり特に注目を集めている. OPA はアレー集積した各光アンテナの位相調整によりレンズフリーで任意のビームを形成することができる. しかし 2 次元アレー集積では，アンテナ間のクロストークを避けるためにピッチを狭くすることが難しく，広視野化と大規模集積に限界があり，もう 1 次元方向を回折格子導波路と波長掃引でビーム走査するハイブリッド型が主流になっている. 一方で FPA は放射させる光アンテナの位置切り替えとレンズを組み合わせることでビーム走査を実現する. OPA と比べて簡易な構成であるのは利点であるが，解像点数がアンテナ数に依存するので高解像度化には大規模集積が課題である.

　本研究室でも Si フォトニクスで製作可能なフォトニック結晶導波路（PCW）を送受信光アンテナとして用いる LiDAR チップの研究を進めてきた. PCW は SOI 基板の Si スラブに SiO_2 で満たされた円孔を三角格子状に配列した 2 次元 PC に，円孔を取り除いた線欠陥を導入することで得られる光導波路であり，Si スラブの面内方向には主にフォトニックバンドギャップ，垂直方向には Si と SiO_2 の高屈折率差による全反射を利用して光を強く閉じ込めることができる. PCW を伝搬するスローライトを用いて光バッファや小型光変調器，光パルス制御，光検出器など様々な素子への応用が期待されているが，PCW に円孔直径の変調や回折格子などの二重周期構造を導入することで，伝搬光を放射モードへと変換することができ，光の送受信アンテナとして機能する. また，PCW を伝搬するスローライトは群屈折率が数 10 程度と大きく巨大な角度分散を生み出し，わずかな波長や導波路屈折率変化によって放射されるビームの角度を大きく変化させることができ，また PCW への入力方向を切り替えることで角度範囲を倍増することができる. LiDAR 応用を考えたとき，対象物に当たった光が散乱しその一部が受信器に戻ってくると仮定すると，できる限り開口の長い PCW を用意する必要がある. しかし Si フォトニクスで製作される PCW は一般に数 10 dB/cm の導波路損失があり，単純に導波路を長くしても PCW に結合した光が伝搬しているうちに損失してしまい，長尺化による受信性能のスケーリングが期待できない.

　そこで本研究では，まずサブアレー構成による PCW 光アンテナの送受信特性改善を試みた. サブアレー型 PCW 光アンテナは，短尺な PCW を複数縦列に配置し，損失の小さい Si 導波路と 1×2 多モード干渉型カプラからなるトーナメント状の光分配器で構成し，送信時にはそれぞれの PCW に光を分配して放射し，受信時には逆過程で光を合波させて一つの受信光

を得る．これによりサブアレー構成全体として導波路損失の影響を抑制し受信強度を改善するのが目的である．理論計算では，通常の PCW では 1 mm 程度で受信強度が飽和してこれ以上の開口を活かすことができないが，PCW を分割しながら長尺化していくことでこの強度飽和が緩和され，2，4 分割ではそれぞれ 3.4，5.3 倍まで改善していくことがわかり，サブアレー構成が PCW 光アンテナのスケーリングに有効であることが示された．また，受信だけでなく送信では，各 PCW がある程度長い開口をもつことで細いビーム幅（0.1°程度）を形成するエレメントファクタに加えて，分割することで回折ビームが生じるアレーファクタを効果的に利用することで，2，4 分割では 0.04，0.02°という細いビーム幅を得ることができる．通常の OPA では光アンテナ間のピッチを半波長以下に収めることが難しく，グレーティングローブが生じることで視野角を制限するが，本構成では各 PCW の長さを適切に設計することでグレーティングローブをエレメントファクタで−10 dB 以下まで抑制することができる．

　次に実際に製作したサブアレー型 PCW を用いてビーム形状とビーム走査を評価した．それぞれ全長が約 1，2，4 mm である通常の PCW と 2，4 分割のサブアレー型 PCW を製作した．2，4 分割の素子は製作時の不均一性により各 PCW からのビーム放射角度がわずかに異なり，遠方でビームの分裂やビーム幅が広がる問題があったが，各 PCW に設けた TiN 熱光学ヒータによりそれぞれのビーム角度を調整することで，0.04，0.02°という理論値に近いビーム幅をもつビーム形状を得ることができた．同じビーム幅を OPA で得るためには 1000 個以上の光アンテナを集積する必要があり，わずかな素子数かつ少ないヒータ個数で高品質なビーム形状を生み出すことができる．また 2 分割の素子を用いて波長掃引と熱光学制御を組み合わせた約 30°の角度範囲でのビーム走査も実証し，高解像度な LiDAR ビーム走査素子としての有用性を示した．

　一方で PCW 光アンテナの LiDAR 実証に向けて，周波数変調連続波（Frequency-modulated continuous-wave：FMCW）方式の光学実験系を加えた送受信性能評価についても取り組んだ．LiDAR の測距方式で広く用いられるのは，光パルスの飛行時間から距離を算出する Time-of-Flight（ToF）方式であり，パルスレーザ光源と光検出器を用いた簡易な構成で実現できるのが利点であるが，直接検波方式なので太陽光や他の LiDAR 装置の光など環境光の影響を受けやすく，十分な信号対雑音比（SNR）を得るためには，高強度パルス光源や高感度な検出器が必要となる．また，人の目に対する安全性も考慮すると，高強度化が難しく長距離検出には課題がある．一方で FMCW 方式では，ある周期で周波数変調した連続光を照射し，対象物からの反射光とあらかじめ分けた参照光をミキシングしバランスフォトダイオード（BPD）で受信する．コヒーレント検出で得られる周波数差成分をもったビート信号から距離を算出する．ToF 方式と比べて複雑な構成であるが，コヒーレント検波により，同じ光源から出た光どうしでしか干渉しないので，環境光や他の LiDAR との干渉をほとんど無視することができる．また連続光を照射するが，ToF で一般に用いられる波長 900 nm と比べて 1550 nm は太陽光スペクトルの強いピーク波長からさらに離れており，アイセーフ波長でもある．さらに対象物の速度や振動をドップラ検出することができ，一度に取得できる情報量が増すので，4，5 次元 LiDAR への可能性が期待される．製作したサブアレー型 PCW 光アンテナを用いて FMCW LiDAR の送受信実験により信号強度を比較し，通常の PCW に対して分割しながら全長を倍増していくことで，2，4 分割の素子でそれぞれ SNR が 6，12 dB と改善し，送受信において性能をスケーリングできることが実証された．また，FMCW LiDAR の実験系で距離を算出する際に取得したビート信号スペクトルのピーク値を検出するので，不要なピークがあると誤検出につながるので問題である．そこで，本研究当初に組んでいた LiDAR 測定系を見直し，不要なノイズ信号の除去に取り組んだ．具体的には任意波形生成器（AWG）や LN 変調器，光アンプ，バンドパスフィルタなどの装置がビート信号スペクトルに与える影響を調査し測定系を改善した．

PCW 光アンテナの送受信性能を改善するために，サブアレー構成以外に熱光学制御による
ビーム形状制御に取り組んだ．Si フォトニクスで製作される PCW は，導波路損失による受
信強度への影響だけでなく，製作時の不均一性によりビーム形状を劣化させることがあり，
これを抑制する必要があった．そこで PCW 内に温度勾配を形成することで，屈折率分布を制
御しビームの放射角度を調整することでビーム形状の改善することを考えた．そこで初期的
な実験として青色レーザを PCW 端部に照射し温度勾配を形成した．理論値よりやや広がっ
たビームをもつ素子に対してビーム形状制御することで，理論値に近いビーム形状を得るこ
とができ，また FMCW LiDAR 送受信実験においても SNR の改善が確認でき，熱光学制御が
送受信性能改善に有効であることを実証した．

PCW 光アンテナで強度変調信号を用いたとき，放射された変調信号強度を見積もり，応用
先拡大として，2 地点への自由空間光送信実験を行った．無線通信の負荷を分散させるための
手法の一つとして自由空間光通信が注目されており，光ファイバを敷設せずにできること，
有線を導入するのが困難な場所，電磁波の影響を受けにくい，傍受されにくいといった特徴
をもつ．PCW 光アンテナを送信器として用いるためには，高速なビーム切替や正確なビーム
角度制御が求められる．本研究では初期的な実験として，NRZ-OOK 変調した信号光を PCW
光アンテナから放射させ，約 1.5 m 離れた 2 地点のファイバコリメータに対して 1 kHz の切
り替え速度で送信した．それぞれのファイバコリメータからシングルモードファイバを介し
て，オシロスコープで 20 Gbps までのアイパターンを確認することができた．一方でスロー
ライト効果により，PCW 内を伝搬する変調信号の位相と放射された信号の位相間不整合が生
じることで，変調周波数への制約がある．

前述の実験において高解像度化が期待できるサブアレー構成 PCW 光アンテナとコヒーレ
ント検波するための Ge BPD を集積した LiDAR チップを製作し，ポイントクラウド画像取得
による LiDAR 実証を試みた．PCW 光アンテナには PCW の Si スラブ上に設けた浅堀回折格
子を採用し，熱光学ヒータには PCW の線欠陥部分を p 型 Si で挟んだ p-i-p 型ヒータを採用し
た．SiO₂ クラッド中に形成される TiN ヒータと比べて，直接 PCW を加熱できるので消費電
力が低い．サブアレー型 PCW は並列に 32 本集積しており，マッハツェンダー型のスイッチ
ツリーで入力切替を行う．PCW の導波路方向には波長掃引や熱光学制御によってビーム走査
を行い，PCW の直行方向にはレンズと入力切替を組み合わせる FPA の方式を用いることで 2
次元ビーム走査を実現した．また，ビームの放射角度に対してコリメート条件を維持できる
プリズムレンズを採用した．OPA でも FPA でも高解像度化には大規模集積が欠かせないが，
本構成では FPA の構成と，スローライト効果による広いビーム角度範囲を組み合わせること
で，簡易な構成で高解像度なビーム走査を実現する LiDAR 素子が期待できる．チップへの光
入力には，光ファイバアレーのブロックを紫外線硬化樹脂によりチップ端のスポットサイズ
変換器に接着した．スイッチツリーの制御と Ge BPD からの信号検出のために，プリント基
板にワイヤボンディングした．外部の DAC 制御のオペアンプ回路により，熱光学ヒータを駆
動しビーム形状制御し，波長掃引によるビーム走査を組み合わせて，再帰反射フィルムを貼
り付けた対象物に対して，2 次元ビーム走査を行った．波長ごとに Ge BPD から検出したビー
ト信号スペクトルから距離を算出することでポイントクラウド画像を取得した．これにより，
サブアレー構成の高解像度を活かした LiDAR 動作を実証することができた．

以上の研究より，サブアレー構成と熱光学制御により PCW 光アンテナの送受信性能が改
善できることが示され，また PCW 光アンテナを 2 次元ビーム走査素子として用いる Si フォ
トニクス LiDAR チップの開発，および自由空間光通信への応用の可能性が期待される．

Contents

Chapter 1
Introduction

1.1 Light Detection and Ranging

1.1.1 Expectation for LiDAR application

Light detection and ranging (LiDAR), one of the 3D sensors that visualize the range information of surrounding objects, has been attracting increasing attention and expectation [1-1, 2, 3, 4] because of its wide range of applications, such as driving assistance, industrial robots, mapping, construction, and virtual/augmented reality. In particular, an expected key technology is a car-mounted sensor, enabling long-range and high-resolution detection automatic driving. The development of a compact and inexpensive LiDAR system will play an important role in realizing fully automatic driving, which is equivalent to level 5 as defined by SAE International [1-5], without the need for a driver and with automated operation in all situations.

A wide variety of 3D sensors exist, from those in practical use to those in the development stage, as shown in Fig. 1.1. 3D sensors are classified into two main categories: passive sensors that do not emit any radiation from the device side to the object and only use information obtained from the object for
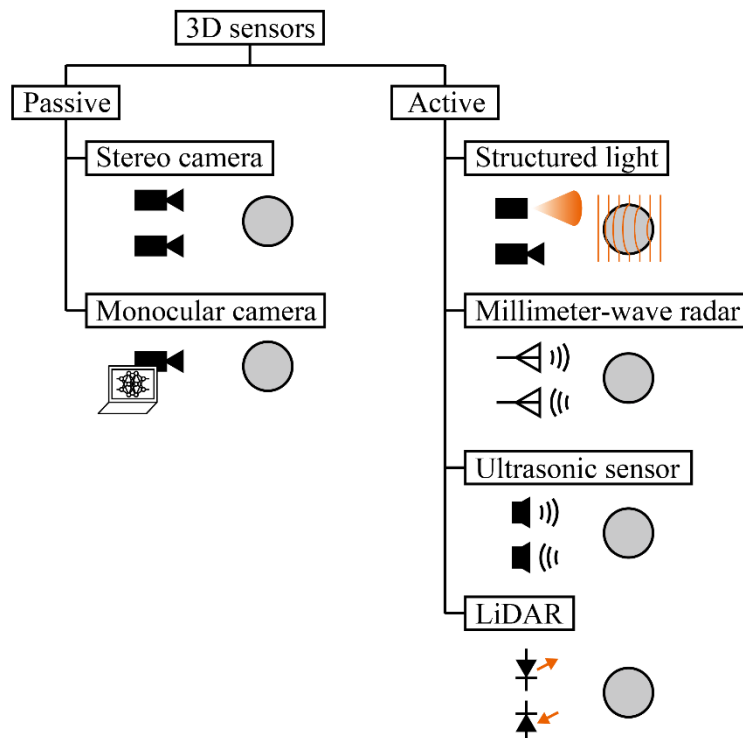

Fig. 1.1 Category of 3D sensors.

imaging, and active sensors that emit radio waves or light from the device to the object and use the information obtained from the reflection from the object for imaging. Passive sensors mainly use only the photodetector of a camera, which is simpler because it does not require a transmission mechanism, and can obtain high-resolution images because of mature camera technology. On the basis of the principle of triangulation, stereo cameras can measure any distance as long as it is captured by a camera, because the distance is calculated from the difference in visibility; these cameras are already in practical use. However, precise positioning of the two cameras is required, and calibration is essential not only for initial adjustment but also for environmental changes such as temperature variation [1-6, 7]. Single image-based 3D sensors are compact and low cost because 3D images are obtained by using machine learning or artificial intelligence to estimate distance information from a single image captured by a monocular camera without requiring a highly accurate configuration the way a stereo camera dose. However, training data need to be collected according to the ranging targets and the location where it will be used. Active sensors require a transmitting mechanism in addition to a receiving mechanism. Structured illumination illuminates a pattern on an object and calculates the distance from the distortion of the pattern observed by the camera. As with stereo cameras, calibration of the pattern is required [1-9]. Millimeter-wave radar and ultrasonic sensors are already in practical use. Compared with cameras, millimeter-wave radar is more resistant to environmental changes such as nighttime and bad weather. However, compared with light, millimeter-wave radar has a longer wavelength, making it difficult to achieve high resolution. Ultrasonic sensors are also used for short-range applications, and long-range detection is difficult [1-10]. Although each sensor has its own advantages and disadvantages, sensor fusion methods, in which multiple sensors are used to compensate for each other's disadvantages and can achieve a performance superior to that of a single sensor, are promising approaches [1-11].

LiDAR, in which radio of radar is replaced with, has been attracting attention especially in recent years; LiDAR itself is a technology with a long history, having appeared soon after the invention of the laser in the 1960s, and its market size is expected to grow to 3.4 billion dollars by 2026 [1-12]. The main factors in the expectations for LiDAR are the increasing instances of LiDAR implementation in unmanned aerial vehicles (UAVs), such as drones that enable photography at low altitudes, terrain mapping, and surveys in areas that are inaccessible to humans, as well as the introduction of LiDAR systems for terrain survey and measurement at construction sites. The possibility of 4D LiDAR is expected to expand its applications by being able to detect not only 3D spatial information but also the speed and vibration of objects, which will increase its superiority to other sensors, making LiDAR more attractive.

LiDAR is classified into ranging and illumination methods. The ranging methods differ in the method used to measure the distance, which is calculated by measuring the round-trip time of the light. The basic principle is to calculate the distance by measuring the round-trip time of the light, which is mainly based on the time of flight (ToF) method [1-13], amplitude-modulated continuous-wave (AMCW) method [1-14], and frequency-modulated continuous-wave (FMCW) method [1-15]. ToF and AMCW are also called direct ToF (d-ToF) and indirect ToF (i-ToF), respectively. The illumination method is the difference in the method of transmitting light to the target object, where the most appropriate light source should be prepared according to the selected ranging method. The field of view in the illumination method is also important because it directly affects the field of view of LiDAR.

An example of the distance measurement principle is shown in Fig. 1.3. If the speed of light is c, the distance to the object is R, and the observed time difference is Δt, then R is defined as

$$R = c\frac{\Delta t}{2} \tag{1.1}$$

The advantage of the ToF method is that it can be realized with a simple configuration using a pulsed laser light source and a photodetector. However, because direct detection is used, it is easily affected by ambient light such as sunlight or light from other LiDAR devices, To ensure a sufficient signal-to-noise ratio, a high-intensity pulsed light source is required for transmission, and a highly sensitive detector such as single photon avalanche photodiode is required for reception. A light source with a wavelength of around 900 nm is used, which avoids the strong peak wavelengths of the sunlight spectrum. The AMCW method emits amplitude-modulated continuous-wave light onto an object and calculates the distance by observing the phase difference of the reflected light. If the modulation frequency is f_{AM} and the observed phase difference is $\Delta\varphi$, then R is represented by the following equation:

$$R = \frac{c}{2}\frac{\Delta\varphi}{2\pi f_{AM}} \tag{1.2}$$

Compared with the ToF method, the AMCW method has the advantages of miniaturization and higher resolution. However, it cannot detect long distances if the phase changes more than 2π in a round trip. In contrast, the FMCW method, which is also used in radar, transmits continuous wave light with a frequency sweep at a period T and bandwidth B, mixes the reflected light with a reference light divided beforehand for coherent detection, and calculates the distance from the beat frequency, which is a frequency difference Δf that corresponds to the round-trip time, as shown in the following equation:

$$R = \frac{c}{2}\frac{T}{B}\Delta f \tag{1.3}$$

The advantage of the FMCW method is that interference with ambient light and other LiDARs is almost negligible because coherent detection allows only light emitted from the same light source to interfere with each other, whereas the configuration is more complicated than that of the two methods described above. In addition, because continuous wave light is emitted into space, it must meet safety standards for human eyes. The wavelength of 1550 nm, which is mainly used in the FMCW method, satisfies the requirements. Furthermore, the information of velocity and vibration of the target object can be obtained by Doppler detection if a sawtooth frequency sweep is changed to a triangular frequency sweep.

As shown in Fig. 1.4, the illumination methods can be classified into a flash type that spreads light widely and a type that scans the light beam. The former type is mainly used in the ToF method and does not require a beam scanning mechanism, making it a simple configuration. However, it is limited to short-distance applications due to significant power attenuation caused by light spreading. The beam scanning type is suitable for long-range detection because the power is concentrated and transmitted to the object with narrow beam divergence, resulting in higher resolution. Therefore, beam scanning devices are important to realize long-range and high-resolution LiDAR.
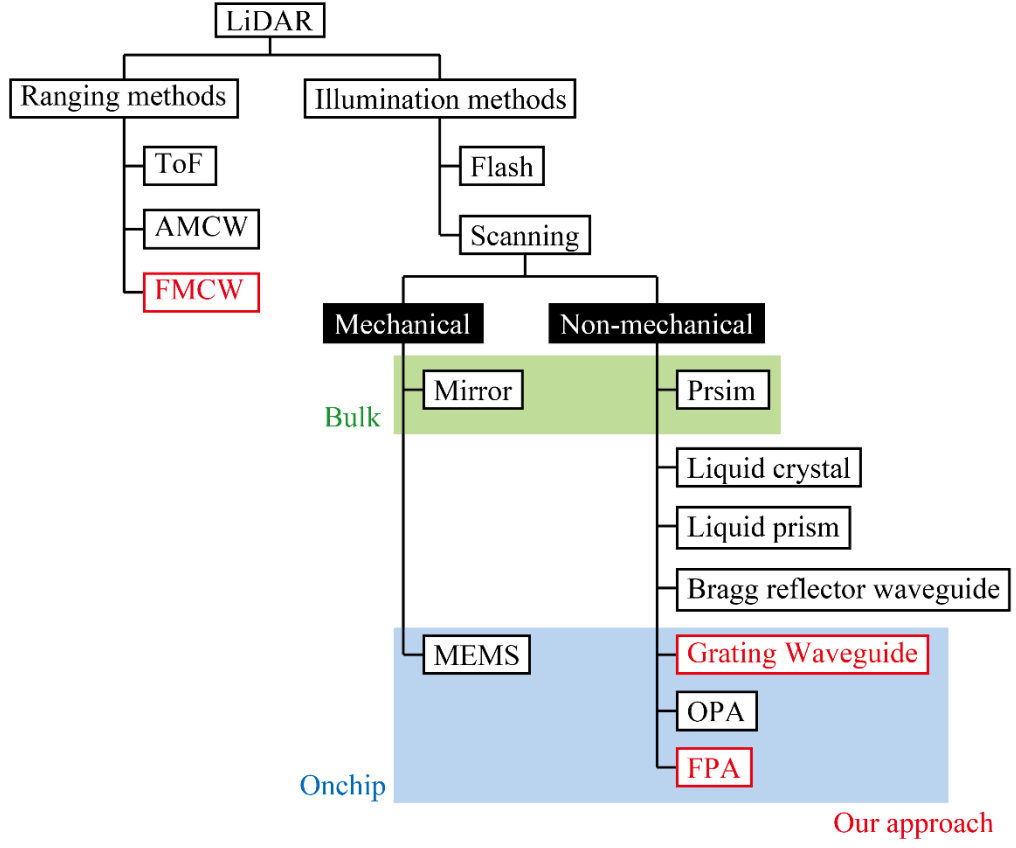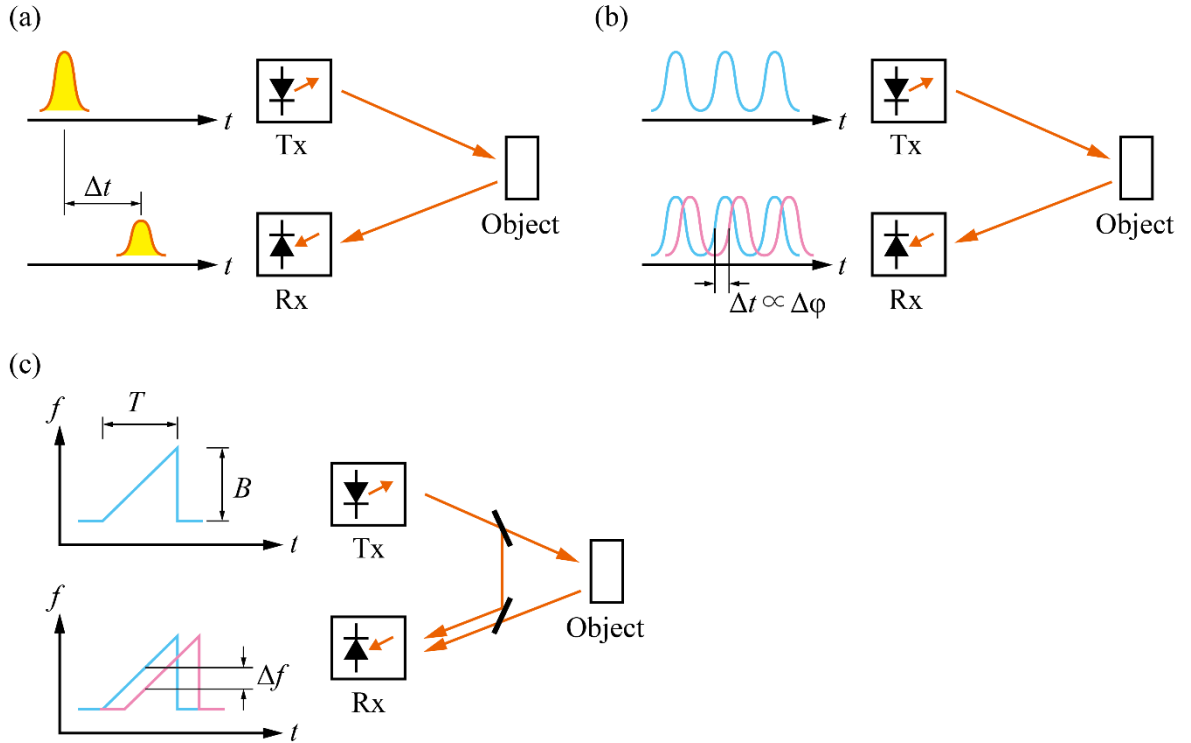
Fig. 1.2 Category of LiDAR.

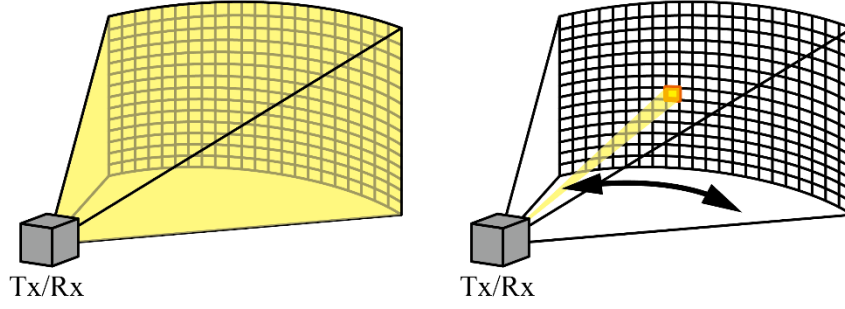Fig. 1.3 Examples of ranging methods. (a) ToF. (b) AMCW. (c) FMCW.

Fig. 1.4 Comparison of flash type and beam steering type.

1.1.2 Beam steering device

Various mechanisms are used to realize beam scanning, as shown in Table 1.1. Although some of these beam scanning devices can realize 2D scanning, the performances of the categorized scanning mechanisms in the 1D direction are compared in this work. Most existing commercial beam scanning mechanisms are based on rotating mirrors or prisms to scan the beam mechanically [1-16]. They have almost no optical loss, high performance, and a wide field of view (FOV) because of their simple configuration. However, the mechanisms for moving mirrors and other components are mechanical, making them large and expensive, and concerns have been raised about their reliability against vibration in automotive applications. Therefore, the development of compact and low-cost beam scanning devices has been actively studied. MEMS, which electrically drives a micro-mirror to scan a reflected light beam, is expected to be a compact and inexpensive system [1-17, 18, 19, 20]. Although the beam angle is smaller than that of a mechanical mirror, the optical loss is small because the beam is simply reflected. However, a trade-off exists between high resolution and high speed because the beam divergence is determined by the area of the mirror. For example, making a mirror small for high-speed operation results in large beam divergence. This problem can be overcome, by using a phased array configuration with small MEMS mirrors to improve the beam quality [1-21, 22, 23]. As described below, the phased array configuration requires complex phase adjustment for each element when integrated on a large scale. The MEMS phased array configuration has the same problem of complicated control of each mirror. In addition, because the mirrors are physically driven, a reliability issue arises with respect to long-term use and vibration, similar to mechanical beam scanning.

The development of non-mechanical beam scanning devices has also attracted great attention. This technology has the advantage of enabling LiDAR to increase the throughput by switching the beam only at an arbitrary point of interest, whereas raster scanning is general in the mechanical scanning where the beam moves continuously because the position is switched by physically rotating a mirror or prism when the beam angle is switched. One of the examples of non-mechanical beam scanning based on a simple principle is a combination of wavelength sweep and prism [1-24]. Beam scanning by wavelength sweep is also possible using a multilayer structured waveguide fabricated by compound semiconductors such as GaAs [1-25], which propagates slow light produced by the effect of large group index of about 10, allowing a large change in beam angle with a small change of wavelength compared with ordinary grating waveguides [1-26]. In addition, because an optical amplifier by current injection is also possible, the output power can be increased, and a high-quality beam with a narrow beam divergence can be generated by taking advantage of the aperture. Conversely, a liquid crystal is used for the method that combines diffraction and refraction by changing the refractive index of the material without changing the wavelength [1-27, 28, 29], where it is classified into transmissive and reflective types. Its advantage is that no burden is imposed on the light source because the system can be realized by simply replacing

the scanning device in existing LiDAR devices. However, the FOV is relatively small. Liquid prisms and liquid lenses are similar methods [1-30, 31, 32, 33], yet they also have a small FOV and require a combination of lenses to expand the FOV, making the configuration complex.

Another non-mechanical beam scanning device that has been extensively studied for nearly a decade is the optical phased array (OPA) [1-34, 35]. Forming arbitrary beams without lenses is possible by integrating optical antennas and adjusting the phase of each antenna. This technique is also used in radar to improve directivity and gain. However, the beam divergence depends on the size of the element integration, and the FOV is limited by the grating lobe, which is determined by the pitch between the antennas. To obtain a narrow beam divergence, large-scale integration is required. However, this process becomes complicated as the numbers of antennas and phase adjustment points increase. Generally, grating lobes do not occur within ±90° if the element spacing is less than half a wavelength. However, if the pitch is increased to suppress crosstalk between antennas, then grating lobes appear as undesired beams, which is a problem because they can lead to false range detection. A report found that OPAs can achieve a FOV of 180° in the 1D direction by using a structure that overcomes crosstalk [1-36]. Realistically, however achieving 2D beam scanning using only an OPA structure is difficult because the pitch is limited in the 1D direction as well.

The focal plane array (FPA) method is also a promising technology as a non-mechanical beam device [1-37]. Unlike OPA, the phases of all transmitting optical antennas do not need to be adjusted; only the switch needs to be adjusted to transmit from one location, thus reducing the number of adjustment points when the system is integrated on a large scale. The FOV and beam divergence depend almost entirely on the lens, and the grating lobe caused by crosstalk between antennas does not need to be considered, as is the case with OPAs, thus enabling the free design of the device. However, because the number of resolution points depends on the number of elements, beam scanning becomes discrete, and capturing objects between beam spots is not possible.

To realize 3D LiDAR, these beam scanning mechanisms need to be combined, and a 2D beam scanning and ranging mechanism must be added. In particular, the development of 3D LiDAR with fully non-mechanical beam scanning using silicon photonics has been actively studied, and LiDAR systems using OPA and FPA configurations have attracted much attention.

1.2 Silicon Photonics LiDAR

1.2.1 Silicon photonics

The development of LiDAR systems based on silicon photonics platforms, which fabricate elements such as optical waveguides, optical switches, optical modulators, and photodetectors using a complementary metal-oxide-semiconductor (CMOS) process on a silicon-on-insulator (SOI) substrate, has been actively studied. The main advantage of silicon photonics is its high compatibility with CMOS technology for fabricating silicon integrated circuits (ICs) [1-39, 40, 41]. IC chips fabricated from silicon wafers, which have high crystalline quality and are inexpensive, are found in many electronic products and home appliances that support our daily lives, and mass production using the mature CMOS process is economical due to the low price per chip. In addition to its manufacturing advantages, silicon is a good material for photonics. Silicon has high transmittance at infrared wavelengths used in optical communications. The high refractive index difference between silicon and silica provides strong light confinement, enabling chip-scale photonic devices. In particular, the development of LiDAR using OPA or FPA has been active, and demonstration reports of 4D LiDAR that combines 2D beam scanning and FMCW methods have been published recently.

Table 1.1 Comparison of beam steering devices.
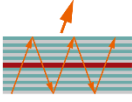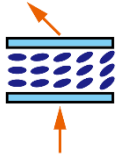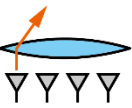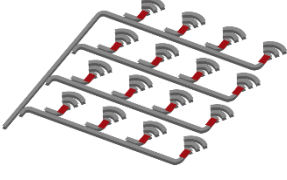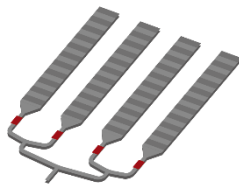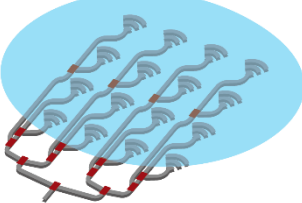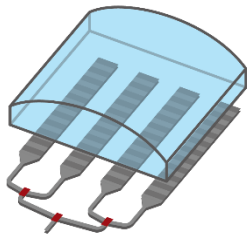
Structure	FOV [°]	Resolution [°]	Group & Year	Ref.
Mirror	360	0.1	Velodyne, 2019	[1-16]
MEMS mirror	16	N/A	SU, 2006	[1-17]
	±31	N/A	UF, 2010	[1-18]
	±28.5	N/A	UM, 2016	[1-19]
Prism	25	0.01	Baraja, 2022	[1-24]
DBE VCSEL	41	0.04	Titech, 2012	[1-25]
Liquid crystal	10.8	N/A	Caltech, 2000	[1-27]
	5	0.5	UGent, 2016	[1-28]
	4.4	N/A	UGent, 2016	[1-29]
Liquid prism, lens	4	N/A	UCF, 2009	[1-30]
	15	N/A	UNT, 2011	[1-31]
	19.9	N/A	SCU, 2012	[1-32]
	±39	N/A	CU Boulder, 2016	[1-33]
OPA	1.5	0.36	UGent, 2010	[1-34]
	45	0.03	USC, 2018	[1-35]
	180	1.6	Columbia Univ. 2018	[1-36]
FPA	N/A	N/A	Toyota Central R&D Labs, 2019	[1-37]

Table 1.2 Performance comparison of OPA and FPA configurations.

Structure	Number of antennas	FOV [°]	Resolution [°]	Group & Year	Ref.
2D OPA	16	1.5	0.36	UGent, 2010	[1-34]
	64	6 × 6	N/A	MIT, 2013	[1-41]
	64	1.6 × 1.6	N/A	USC, 2015	[1-42]
	16	1.5 × 1.5	0.5 × 0.5	CIT, 2015	[1-43]
	64	7 × 7	N/A	UPenn, 2019	[1-44]
	128	16 × 16	0.8 × 0.8	CIT, 2019	[1-45]
1D OPA + Grating	16	2.3 × 14.1	2.3 × 2.4	UGent, 2009	[1-47]
	16	20 × 14	1.6 × 0.6	UC, 2011	[1-48]
	16	20 × 15	1.2 × 0.5	UT Austin, 2014	[1-49]
	32	23 × 3.6	1 × 0.6	UCSB, 2015	[1-50]
	50	46 × 36	0.85 × 0.18	MIT, 2017	[1-55]
	512	56 × 15	0.04 × N/A	Analog Photonics, 2019	[1-56]
	125	16 × 18.5	0.25 × 0.15	UC Berkeley, 2019	[1-57]
	512	70 × 6	0.15 × 0.08	Columbia Univ., 2020	[1-58]
	8192	100 × 17	0.01 × 0.039	Analog Photonics, 2020	[1-59]
2D FPA	16	2.07 × 4.12	0.06 × 0.06	SJTU, 2019	[1-60]
	16	12.4 × 26.8	0.8 × 0.8	Columbia Univ., 2021	[1-61]
	512	N/A	N/A	pointcloud, 2021	[1-62]
	16384	70 × 70	0.6 × 0.6	UC Berkeley, 2022	[1-63]
1D FPA + Grating	32	4.4 × 40	0.1 × 0.15	YNU, 2020	[1-64]
	16	0.9 × 8.1	0.1 × 0.5	SJTU, 2021	[1-65]

1.2.2 Optical phased array

An OPA consists of optical antennas, an optical distributing tree for each antenna, and phase shifters, where each phase shifter can be adjusted to form an arbitrary beam without a lens. Although 2D beam scanning is possible by arranging the antennas in a 2D array, the first reported OPAs were not equipped with phase shifters and scanned only in a 1D direction by wavelength sweep [1-34]. Later, 2D beam scanning was realized only by phase adjustment; however, all of them had narrow FOV and were not practical [1-41, 42, 43]. In general, the number of phase shifters is proportional to the number of

antennas, making it more difficult to adjust the phase shifters as the number of antennas increases. Although some OPAs have been reported to reduce the number of phase shifters [1-44], the problem of FOV limitation is more serious than that of large-scale integration because narrowing the pitch between antennas in a 2D OPA is difficult due to the limitation of optical wiring. OPAs using sparse array configurations have also been reported to suppress grating lobes. However, a concern is that the effective antenna aperture area will be reduced in LiDAR applications [1-45, 46].

Currently, the most common configuration for 2D beam scanning using OPA is a combination of an OPA in one dimension and beam scanning using a grating waveguide and wavelength sweep in the other dimension [1-47, 48, 49, 50]. Although a separate tunable wavelength light source is required, the FOV is wider than that of a 2D OPA because the antenna spacing can be relatively narrow. The angular sensitivity of a grating waveguide to wavelength change is typically about 0.1°/nm; therefore, large angular changes cannot be expected. A configuration that combines a lens to expand the angular range has been proposed [1-51] to overcome this problem. The beam angle can be changed not only by changing the wavelength but also by the thermo-optic effect. However, changing the angle to become as large as the wavelength change is difficult [1-52]. Conversely, an OPA that achieves 2D beam scanning by only wavelength sweep has been reported. However, the FOV in the direction of the grating waveguide is similarly narrow, and the fabrication error has a large impact on beam quality because it is a completely passive device [1-53]. One structure uses an aperiodic arrangement similar to 2D OPAs. However, the effect on the effective aperture has been the subject of concern [1-54]. The first FMCW LiDAR operation on a silicon photonics chip was reported by a group at MIT [1-55], and later, LiDAR operation that includes velocity detection and beam scanning in large-scale integration was reported [1-56, 57].

1.2.3 Focal plane array

In the past few years, LiDAR chips with FPA configuration using silicon photonics and OPA have been actively studied [1-60, 61, 62, 63]. As with OPA, 2D beam scanning can be achieved by arranging optical antennas in a 2D array. However, because the number of resolution points depends on the number of antennas, large-scale integration is required to achieve high resolution. Attempts have been made to increase the number of resolution points by using microlens arrays to split the beam for transmission, but some necessary steps are to separate the transmitter and receiver and provide a receiver for the number of resolution points split for transmission in the receiver section [1-62]. Currently, 1D OPA and grating waveguide configurations, which require phase adjustment and a variable wavelength light source, have high resolution but narrow FOV, while 2D FPA, which is a simple configuration and requires a lens, provides high sensitivity because of the lens. However, the number of resolution points is an issue.

Our group has studied and developed a LiDAR system realizing 2D beam scanning using an FPA configuration in one dimension and the slow light effect of a photonic crystal waveguide in the other dimension [1-64]. This system is simpler than an OPA and is expected to achieve higher resolution than a 2D FPA. The slow light effect allows a large change in beam angle with only a small change in the refractive index or wavelength of light, resulting in a larger FOV compared with a conventional grating waveguide [1-65].

1.3 Photonic Crystal Antenna for LiDAR Application

1.3.1 Photonic crystal waveguide

Photonic crystal waveguides (PCWs) for propagating slow light are expected to have various device

applications such as optical buffers [1-66, 67], compact optical modulators [1-68, 69, 70], optical pulse control [1-71, 72], and optical detectors [1-73, 74], and have been actively studied in our laboratory. A photonic crystal (PC) is a structure with a periodic refractive index distribution on a scale equivalent to the wavelength of light, in which light of a certain wavelength band is not allowed to propagate or exist in any direction; this condition is called a photonic band gap (PBG). The basic concept of a PBG was described by Otaka in 1979 [1-75], and structures with PBGs were later studied by Yablonovich [1-76, 77]. When a defect is placed in a PC, light propagates through the defect and functions as a waveguide based on total reflection due to the refractive index difference in the direction orthogonal to the Si slab and Bragg reflection due to PBGs in the in-plane direction of the Si slab.

As shown in Fig. 1.5(a), the PCWs discussed in this study are 2D PCWs with SiO_2 circular holes arrayed on a thin Si slab and SiO_2, where the Si slab was sandwiched between the upper and lower SiO_2 layers. Removing the circular holes and installing line defects, as shown in Fig. 1.5(b), enables light to be propagated using PBGs for TE polarization in the plane and total reflection above and below the slab. Compatible with silicon photonics, commercially available high-quality, large-area SOI substrates are used for fabrication and have been widely studied [1-78, 79, 80]. To operate in the optical communication wavelength band, the thickness of Si slab, lattice constant a, and circular hole diameter $2r$ must be in the order of 200, 400, and 200 nm, respectively. Electron beam lithography and photolithography are used for pattern formation, and reactive ion etching is used for circular hole fabrication. As shown in the band diagram in Fig. 1.5(d), the fundamental propagation mode in PCW is slow light with small group velocity [1-81, 82], and the slope of the band curve becomes smaller at low frequencies. In our laboratory, we demonstrated that, as shown in Fig. 1.16(a), the band is straightened, as shown in Fig. 1.16(b), and low-dispersion slow light with a wide bandwidth is obtained by applying a shift of s_3 in the waveguide direction to the third row of circular holes from the line defect [1-83]. In addition, more broadband low-dispersion slow light has been demonstrated by optimization of informatics technology [1-84].

1.3.2 Optical antenna using PCW

PCWs can function as optical antennas through the introduction of a doubly periodic structure [1-85, 86], as shown in Fig. 1.7(a), where the circular hole diameter is repeated in small and large sizes with a period of $\Lambda = 2a$, which is twice the lattice constant, or by providing a diffraction grating with a period of $\Lambda = 2a$, as shown in Fig. 1.7(b). Such structure enables the propagating mode band in the PCW to fold around the wavenumber 0.25 and appear above the light line between the air and the SiO_2 cladding. Therefore, the propagation mode is combined with the radiation mode. As a result, light propagates through the PCW while radiating into space. Figure 1.8 shows a schematic of the light emitted from the PCW optical antenna. In the waveguide direction of the PCW (z-direction), a narrow beam is formed by an aperture of some length according to the radiation coefficient. The radiation angle, beam divergence, and FOV are defined as θ, $\delta\theta$, and $\Delta\theta$, respectively, where β is the propagation constant in the PCW. In the orthogonal direction of the PCW, light is confined within a lattice constant of about two periods, and when light is emitted, the effective aperture is narrower than that in the waveguide direction, Therefore, the beam diverges at a larger angle $\delta\phi$ than $\delta\theta$ to form a fan-shaped beam, as shown in Fig. 1.8(b). θ can be changed by wavelength change or by the refractive index change of the waveguide due to the thermo-optic effect. The sensitivity of θ to wavelength λ and waveguide refractive index n is expressed as follows:

$$\frac{d\theta}{d\lambda} = -\frac{n_g - n_{eq}}{\lambda\sqrt{1 - n_{eq}^2}} \tag{1.4}$$

$$\frac{d\theta}{dn} = \frac{n_g - n_{eq}}{n\sqrt{1 - n_{eq}^2}} \tag{1.5}$$

,where n_g and n_{eq} are the group refractive index and equivalent refractive index, respectively. θ is proportional to n_g, which is why the high group index produced by slow light can change the beam angle widely for small changes in wavelength or refractive index. Fig. 1.9(a) shows the band diagram for a doubly periodic structure similar to that in Fig. 1.7(a), with a circular hole diameter difference Δr, where slow light of about $n_g = 20$ is obtained in the wide bandwidth and the angular sensitivity to wavelength change is approximately 1°/nm, which is 10 times greater than that of an ordinary grating waveguide, and a FOV of more than 20° is obtained. Furthermore, when light is input into the waveguide from the opposite direction, the beam is also emitted at the opposite angle, thus doubling the FOV by switching the input direction. The band diagram for temperature change is shown in Fig. 1.10(a), and the same angular change as the wavelength change is obtained for a change in temperature of about 200 K, enabling single-wavelength beam scanning. To obtain the same FOV with ordinary diffraction grating, a temperature change of 1000 K or more is required, which is not realistic. We have investigated thermo-optic heaters for PCW, such as a TiN heater in a SiO$_2$ cladding and a p-i-p heater in which the PCW line defect is sandwiched by p-type doping [1-87]. These p-i-p heaters, which can heat the PCW area more directly than TiN heaters located away from the slab, have more than two times greater heating efficiency with an operating speed of up to about 1 MHz when $\Delta\theta$ is evaluated at 3 dB width (Fig. 1.12).
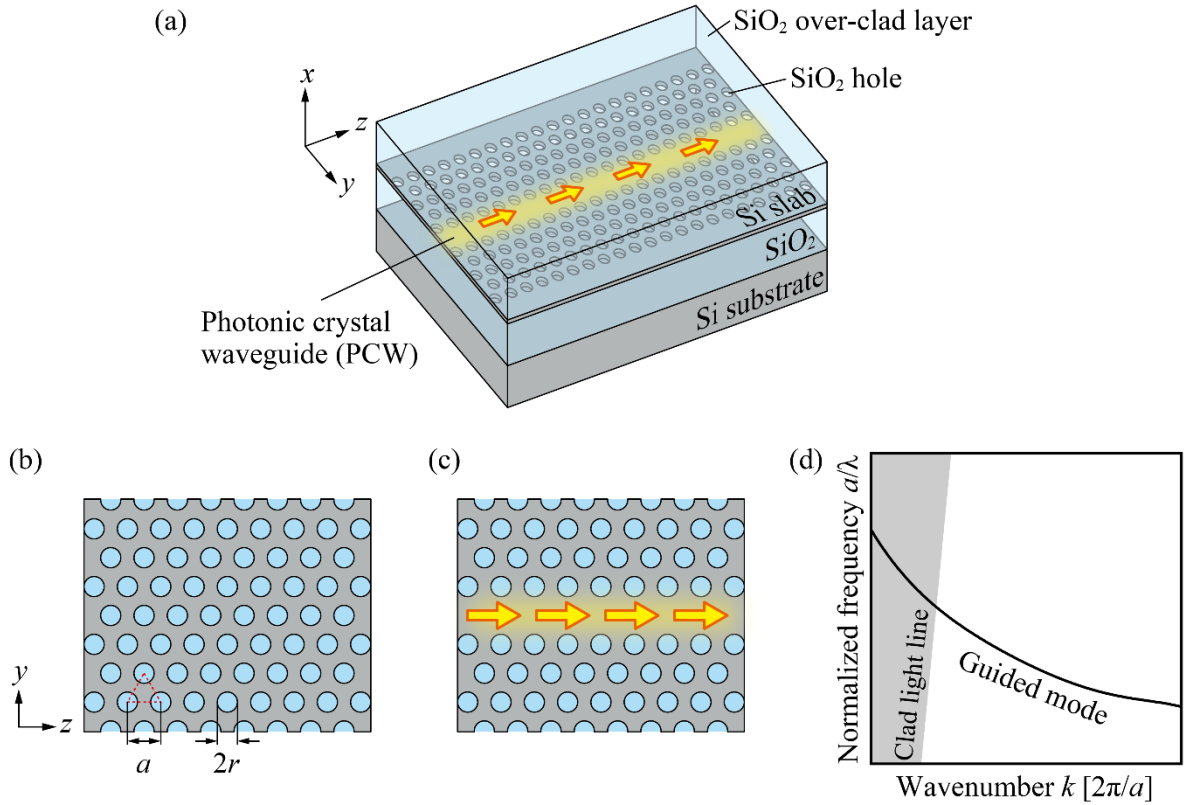

Fig. 1.5 (a) PCW. (b) Top view of 2D photonic crystal Si slab. (c) 2D photonic crystal with line defects. (d) Photonic band of guided mode in PCW.

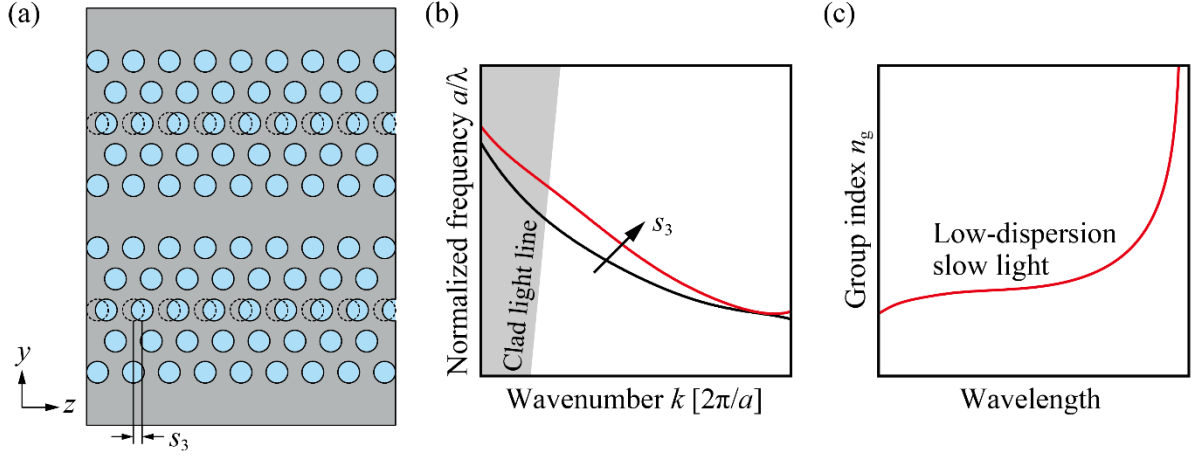Fig. 1.6 (a) PCW where the third row of circular holes is shifted. (b) Photonic band of PCW. (b) Group index with wavelength in PCW.
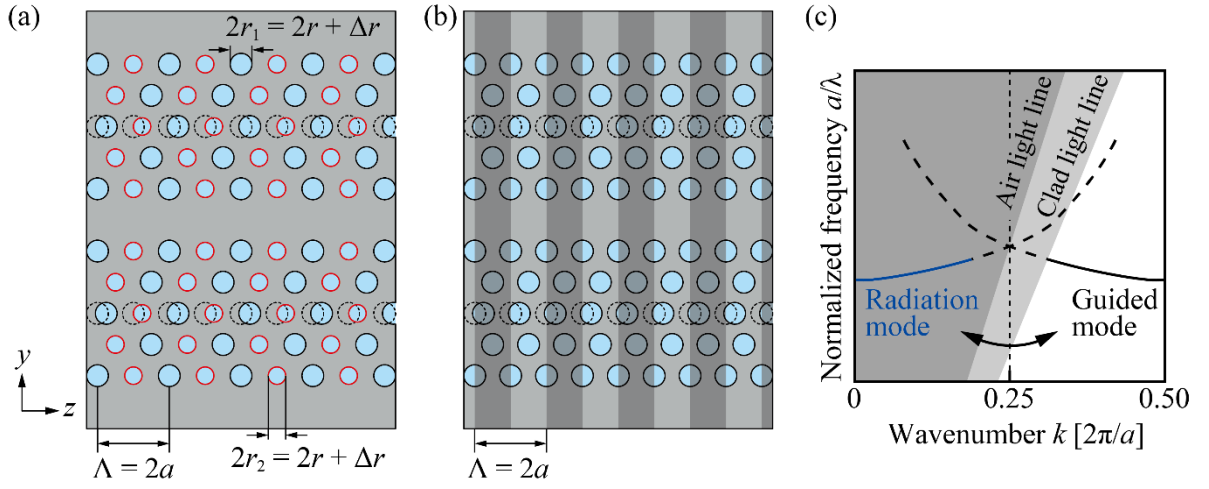
Fig. 1.7 (a) Top view of PCW with doubly periodic structure. (b) Top view of PCW with grating. (c) Band diagram of PCW with doubly periodic structure or grating.

Fig. 1.8 (a) Beam shape radiated in the direction of the PCW. (b) Fan-shaped beam orthogonal to the PCW.

(a)

(b)

(c)

Fig. 1.9 (a) Photonic band of doubly periodic PCW. (b) Group index calculated with wavelength. (c) Radiation angle θ calculated with wavelength.

(a)

(b)

Fig. 1.10 (a) Dependence of PCW photonic band on temperature. (b) Calculated radiation angle with temperature.

Fig. 1.11 (a) TiN heaters above Si slab. (b) p-i-p heater in Si slab.

Fig. 1.12 (a) Radiation angle with heating power. (b) Radiation angle range with frequency of heater operation.
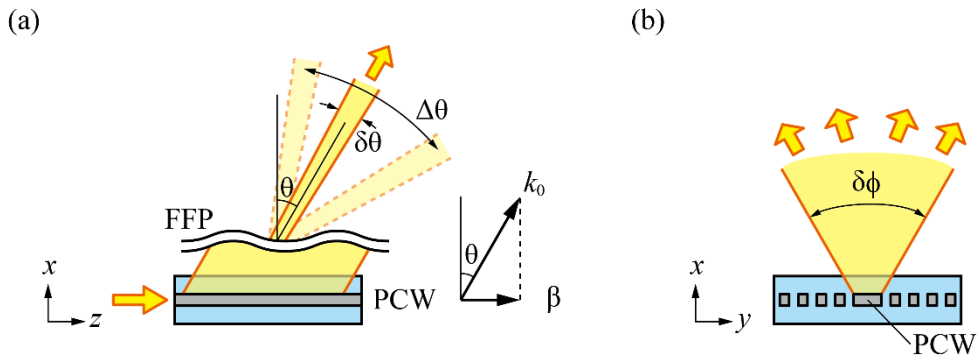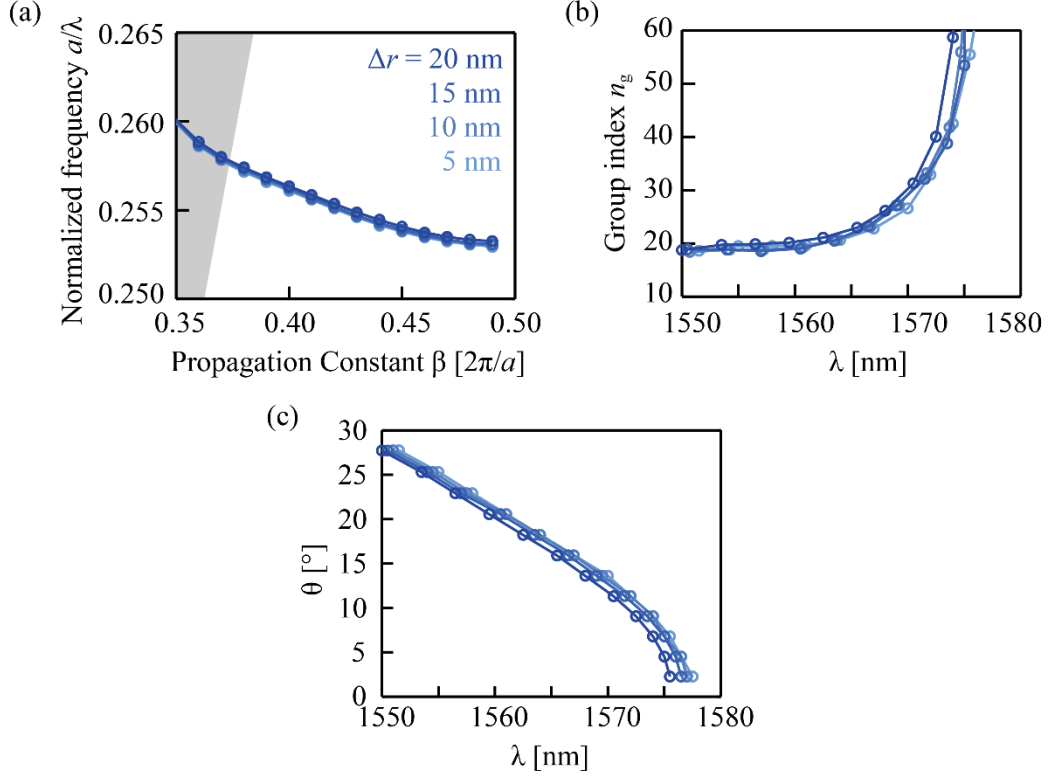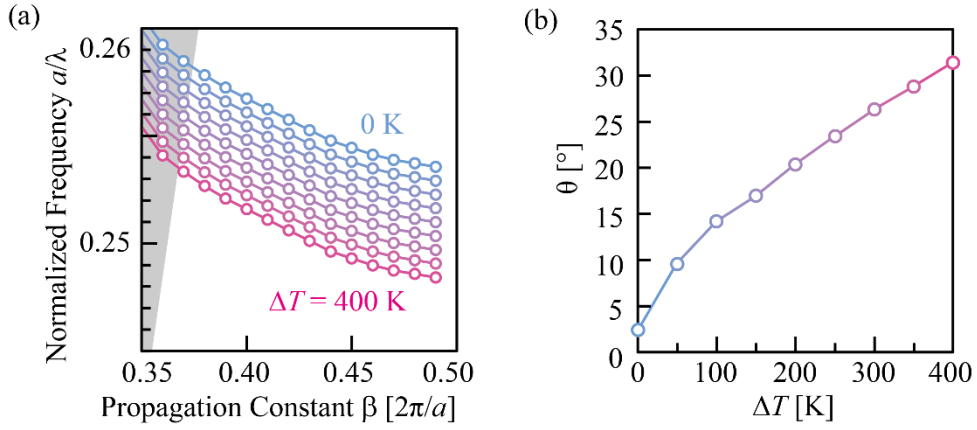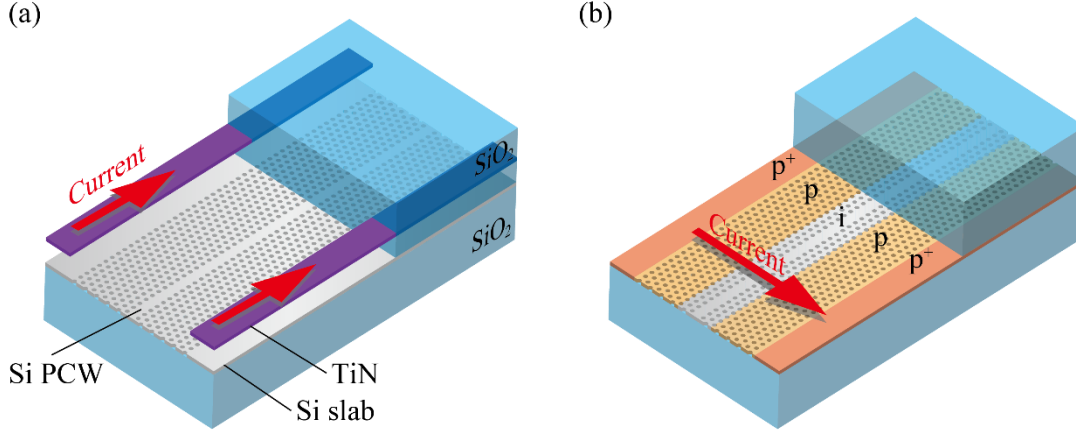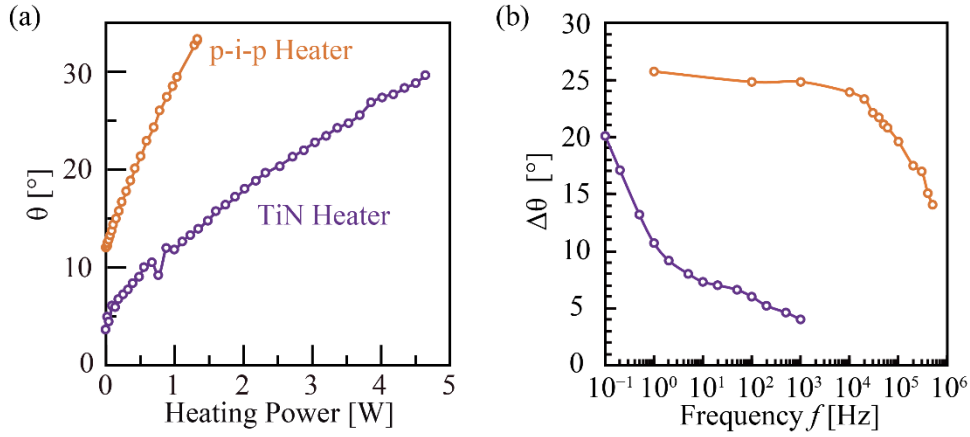
1.3.3 Comparison of silicon photonics LiDAR

Figure 1.13 compares the number of resolution points with the number of integrated optical antennas for the beam scanning and LiDAR devices fabricated by the aforementioned silicon photonics. For the configuration that combines OPAs with grating waveguides (GWs), the number of resolution points was evaluated by dividing the FOV by the beam divergence. Therefore, some studies may not be able to demonstrate the number of calculated resolution points. For 2D OPAs, narrowing the spacing between optical antennas to avoid crosstalk, including switches and waveguides up to the optical antennas, is a challenging task, which makes securing a wide FOV difficult. Large-scale integration to increase the aperture and improve beam quality is also difficult. Therefore, high resolution has not been achieved. The combination of 1D OPAs and GWs can provide a narrow beam with a wide FOV by relaxing the limitation on the pitch between the antennas. However, the FOV in the waveguide direction using wavelength sweep is narrower than that in the beam direction using phase control, requiring large-scale integration of OPAs.

The number of resolution points in a 2D FPA configuration corresponds to the number of antennas. Therefore, increasing the number of resolution points inevitably requires large-scale integration. Unlike OPAs, FPAs require lenses, which affect system miniaturization. However, they also have the advantage of allowing the beam divergence and FOV to be controlled by the lenses. Figure 13 shows the theoretical
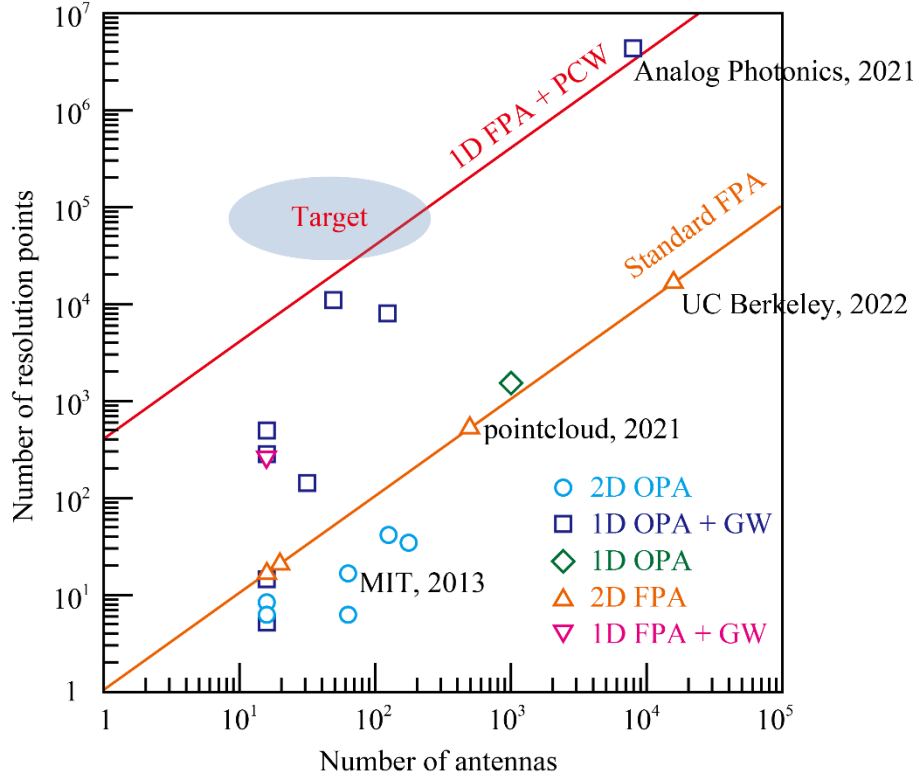
Fig. 1.13 Comparison of the number of resolution points with the number of optical antennas integrated on a chip.

line of the number of resolution points of the FPA, which is higher than that of the 2D OPA but lower than that of the 1D OPA and GW configurations. The combination of 1D FPA and GW is equivalent to pushing the theoretical line of FPA upward because the angular range is expanded by the wavelength sweep. However, because a large FOV cannot be obtained with an ordinary grating waveguide, there is not much difference compared with the combination of 1D OPA and GW.

To overcome these problems, we have studied a high-resolution LiDAR system that can be configured with far fewer optical antennas than OPA by using a configuration that combines a 1D FPA and PCW optical antennas. The theoretical line shown in Fig. 1.13 is obtained when the FOV and beam divergence of the PCW optical antenna are set to 20° and 0.1°, respectively, switching the input direction to the PCW. In addition, the combination of 1D OPA and GW requires a wavelength tunable light source, whereas our configuration can obtain the same FOV as wavelength sweep by beam scanning with thermo-optic control, thus reducing the burden on the light source.

1.3.4 Objective of this study

The purpose of this study is to improve the transmission and reception characteristics of PCW optical antennas in silicon photonics, especially for LiDAR, and to expand their applications. To suppress the effect of waveguide loss in PCWs, we first investigated a subarray configuration to improve the transmission and reception characteristics. Next, I confirmed the effectiveness of the PCW in LiDAR operation through experimental evaluation of transmission and reception in the FMCW method. The beam shape degradation caused by the non-uniformity of the PCW during fabrication was compensated by thermo-optic control, and the transmission and reception performance were confirmed to be improved by FMCW LiDAR transmission and reception experiments. Furthermore, we estimated the

signal intensity when the modulated light was emitted from the PCW optical antenna, and confirmed the limitation of the modulation frequency by conducting free-space optical transmission experiments. Finally, we fabricated a LiDAR chip that includes a subarray configuration and acquired point cloud images by 2D beam scanning and FMCW LiDAR transmission and reception experiments.

A. Subarray configuration

The PCW optical antenna transmission and reception performance can be improved and scaled by using a subarray configuration. In LiDAR applications, if the light beam emitted from the PCW optical antenna hits an object and some of the scattered light is returned, then a necessary step to prepare as long a PCW as possible, because the light intensity decreases inversely proportional to the square of the distance. Generally, the transmission and reception performance of an antenna are scaled by increasing the aperture. However, the PCW fabricated by silicon photonics has a large waveguide loss of 10 dB/cm order. Therefore, even if the PCW is simply made longer, the received light will be lost while propagating through the PCW, making the transmission and reception performance of the PCW unscalable. This, I aimed to reduce the total waveguide loss by arranging multiple short PCWs in a subarray and configuring them with a tournament-type optical splitter that consists of a low-loss Si waveguide and 1 × 2 couplers. The transmission and reception efficiency, reception intensity, and beam shape were calculated for this array configuration, and the beam quality and beam scanning were evaluated using the fabricated devices.

B. FMCW LiDAR evaluation

LiDAR transmission and reception experiments using the FMCW method were implemented to realize a silicon photonic LiDAR chip with PCW optical antennas. In particular, the transmission and reception characteristics of the PCW optical antennas in a subarray configuration were evaluated. An external in-phase quadrature-phase (I-Q) modulator was used to generate the FMCW signal to obtain a single-side band modulation close to the ideal single frequency modulation signal, and the beam was emitted from the PCW optical antenna through a collimator lens, where the collimator lens was used to convert the diverged beam in the orthogonal direction to the PCW into a collimated beam. The beam was then reflected from a mirror and coupled back to the PCW by using an external balanced photodiode for coherent detection. Finally, the measurement system was improved by investigating the cause of the extra noise peaks in the spectrum.

C. Thermo-optic beam calibration control

In addition to the array configuration, the beam shape of the PCW optical antenna was adjusted by thermo-optic control to improve the transmission and reception performance. One problem in PCWs fabricated by silicon photonics in addition to the problem of waveguide loss is that the beam shape is sometimes degraded due to in-plane non-uniformity during fabrication. Thermo-optic control was investigated to suppress this problem and obtain a beam shape close to the theoretical value. In an initial experiment, the beam shape was improved by controlling the refractive index distribution and adjusting the beam radiation angle by applying a temperature gradient in the aperture plane of the PCW optical antenna. FMCW LiDAR transmission and reception experiment was also implemented to confirm that thermo-optic control is also effective in the performance of the PCW antenna in LiDAR applications.

D. Evaluation of modulation signal in PCW antenna

The modulation signal intensity of the radiated beam was evaluated when the modulation signal was

used in the PCW optical antenna. When frequency-modulated signal light with intensity modulation is radiated from the PCW, the slow light effect causes a mismatch between the phase of the modulated signal of the radiated light and the phase of the modulated signal propagating through the PCW, which reduces the signal intensity at far field. The signal intensity radiated from the PCW was calculated theoretically, and was evaluated using the fabricated devices. The radiated beam with modulation signal was switched at high speed to two fiber collimators set at two different locations by controlling the radiation beam angle with a thermo-optic heater. The eye pattern was then observed from each fiber collimator with an oscilloscope, demonstrating the potential of the PCW optical antenna for free-space optical communication.

E. Acquisition of point cloud image

A LiDAR chip containing a PCW optical antenna in a subarray configuration and a germanium balanced photodiode for coherent detection was fabricated, and point cloud images were acquired by combining 2D beam scanning and FMCW LiDAR transmission and reception experiments. A Mach−Zehnder-type switch tree was used to switch the light input to the 32 parallel integrated PCW antenna subarrays, and the PCW switching and signal detection were controlled by an external DAC operational amplifier circuit using electrical wiring wire-bonded to the printed circuit board. In addition to the high resolution of the beam by the PCW slow light and the subarray configuration, the feasibility of a silicon photonics LiDAR chip with a simple configuration and high resolution was demonstrated by using the FPA configuration.

1.4   Dissertation Outline

The outline of this dissertation is shown in Fig. 1.14. Chapter 2 describes the design, fabrication, and performance evaluation of optical integrated devices such as silicon waveguides, spot size converter, multimode interference (MMI) coupler, PCW, and germanium PD, which are essential for constructing a silicon photonic LiDAR with PCW optical antennas. Chapter 3 describes the theoretical and computational estimation of the transmission and reception performance of the PCW optical antenna in a subarray configuration, and the beam quality evaluation and beam scanning using the fabricated elements. Chapter 4 describes the LiDAR transmission and reception experimental system based on the FMCW method, which is important for the application of PCW optical antennas to LiDAR, and evaluates the transmission and reception performance using PCW optical antennas in a subarray configuration. Furthermore, the measurement system was improved to eliminate unwanted noise in range detection. Chapter 5 discusses how the beam shape is improved by thermo-optic control using a normal PCW antenna without the subarray configuration, and the beam quality was evaluated before and after the adjustment is compared with the signal intensity in the FMCW LiDAR experiment. Chapter 6 presents the theoretical calculation of the signal intensity when using modulated signal light with a PCW optical antenna and evaluates the signal intensity using the fabricated device. In addition, free-space optical transmission experiment was implemented by switching the beam angle to fiber collimators set at two different locations. Chapter 7 describes the point cloud image acquisition by 2D beam scanning using a fully integrated LiDAR chip that includes a subarray configuration of the PCW. Finally, Chapter 8 summarizes and concludes this study.
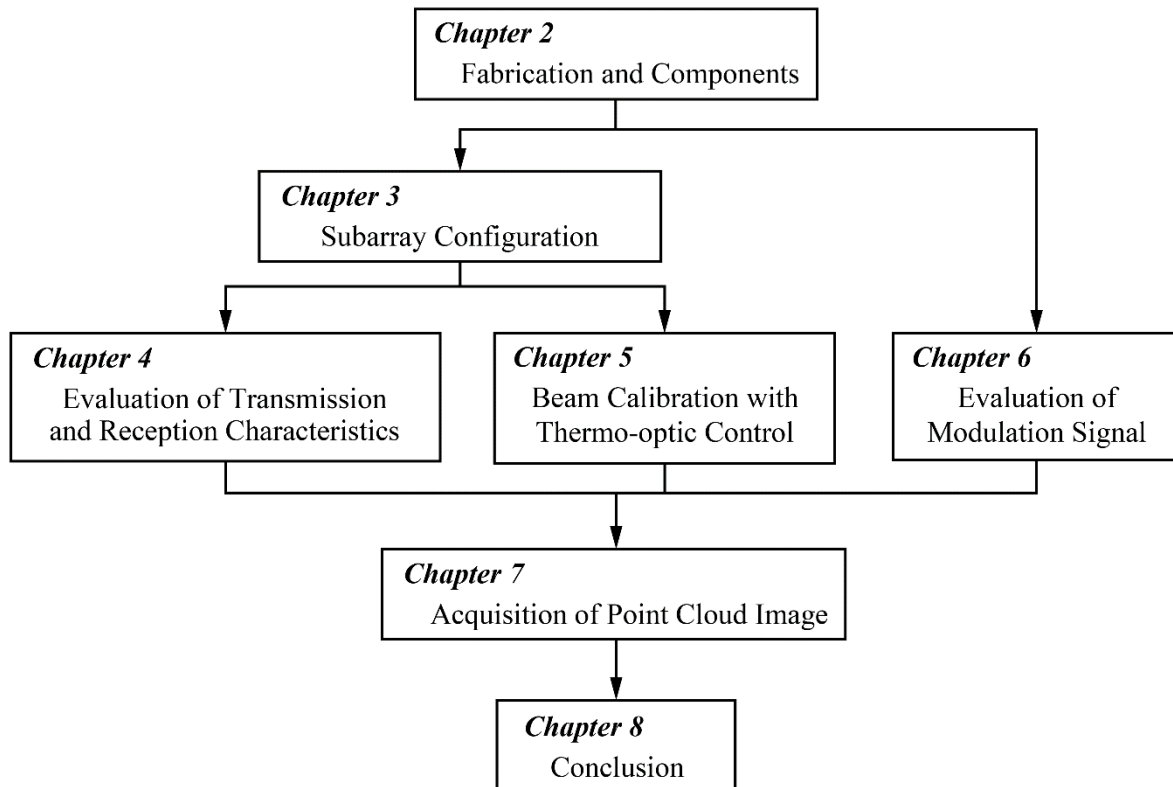
Fig. 1.14 Outline of this dissertation.

References

[1-1] B. Schwarz, "Mapping the world in 3D," Nature Photon. vol. 4, pp. 429–430, 2010.

[1-2] I. Puente, H. Gonzalez-Jorge, J. Martinez-Sanchez, and P. Arias, "Review of mobile mapping and surveying technologies," Measurement, vol. 46, no. 7, pp. 2127–2145, 2013.

[1-3] J. Hecht, "Lidar for Self-Driving Cars," Optics & Photonics News vol. 29, no. 1, pp. 26–33, 2018.

[1-4] "LiDAR drives forwards," Nature Photon. vol. 12, no. 441, 2018.

[1-5] https://www.sae.org/blog/sae-j3016-update, accessed on 2022-04-26.

[1-6] Z. Jia, J. Yang, W. Liu, F. Wang, Y. Liu, L. Wang, C. Fan, and K. Zhao, "Improved camera calibration method based on perpendicularity compensation for binocular stereo vision measurement system," Opt. Express vol. 23, no. 12, pp. 15205–15223, 2015.

[1-7] K. Genovese, Y. Chi, and B. Pan, "Stereo-camera calibration for large-scale DIC measurements with active phase targets and planar mirrors," Opt. Express, vol. 27, no. 6, pp. 9040–9053, 2019.

[1-8] F. Khan, S. Saqib, and J. Hossein, "Deep Learning-Based Monocular Depth Estimation Methods—A State-of-the-Art Review," Sensors, vol. 20, no. 8, pp. 2272, 2020.

[1-9] J. Geng, "Structured-light 3D surface imaging: a tutorial," Adv. Opt. Photon., vol. 3, pp. 128–160, 2011.

[1-10] J. Vargas, S. Alsweiss, O. Toker, R. Razdan, and J. Santos, "An Overview of Autonomous Vehicles Sensors and Their Vulnerability to Weather Conditions," Sensors, vol. 21, no. 16, pp. 5397, 2021.

[1-11] D. J. Yeong, G. Velasco-Hernandez, J. Barry, and J. Walsh, "Sensor and Sensor Fusion Technology in Autonomous Vehicles: A Review," Sensors, vol. 21, no. 6, pp. 2140, 2021.

[1-12] https://www.marketsandmarkets.com/Market-Reports/lidar-market-1261.html, accessed on

2022-02-09.

[1-13] P. Padmanabhan, C. Zhang, and E. Charbon, "Modeling and Analysis of a Direct Time-of-Flight Sensor Architecture for LiDAR Applications," Sensors, no. 19, vol. 24, pp. 5464, 2019.

[1-14] M. Perenzoni, and D. Stoppa, "Figures of Merit for Indirect Time-of-Flight 3D Cameras: Definition and Experimental Evaluation," Remote Sens., no. 3, vol. 11, pp. 2461–2472, 2011.

[1-15] A. Martin, D. Dodane, L. Leviandier, D. Dolfi, A. Naughton, P. O'Brien, T. Spuessens, R. Baets, G. Lepage, P. Verheyen, P. De Heyn, P. Absil, P. Feneyrou, and J. Bourderionnet, "Photonic integrated circuit-based FMCW coherent LiDAR," J. Lightwave Technol., vol.36, no.19, pp.4640–4645, 2018.

[1-16] https://velodynelidar.com/products/alpha-prime/, accessed on 2022-04-26.

[1-17] W. Piyawattanametha, R. P. J. Barretto, T. H. Ko, B. A. Flusberg, E. D. Cocker, H. Ra, D. Lee, O. Solgaard, and M. J. Schnitzer, "Fast-scanning two-photon fluorescence imaging based on a microelectromechanical systems two- dimensional scanning mirror," Opt. Lett., vol. 31, no. 13, pp. 2018–2020, 2006.

[1-18] J. Sun, S. Guo, L. Wu, L. Liu, S. W. Choe, B. S. Sorg, and H. Xie, "3D In Vivo optical coherence tomography based on a low-voltage, large-scan-range 2D MEMS mirror," Opt. Express, vol. 18, no. 12, pp. 12065–12075, 2010.

[1-19] H. Li, X. Duan, Z. Qiu, Q. Zhou, K. Kurabayashi, K. R. Oldham, and T. D. Wang, "Integrated monolithic 3D MEMS scanner for switchable real time vertical/horizontal cross-sectional imaging," Opt. Express, vol. 24, no. 3, pp. 2145–2155, 2016.

[1-20] X. Duan, H. Li, X. Li, K. R. Oldham, and T. D. Wang, "Axial beam scanning in multiphoton microscopy with MEMS-based actuator," Opt. Express, vol. 25, no. 3, pp. 2195–2205, 2017.

[1-21] T. K. Chan, M. Megens, B. W. Yoo, J. Wyras, C. J. Chang-Hasnain, M. C. Wu, and D. A. Horsley, "Optical beamsteering using an 8 × 8 MEMS phased array with closed-loop interferometric phase control," Opt. Express, vol. 21, no. 3, pp. 2807–2815, 2013.

[1-22] B. W. Yoo, M. Megens, T. Sun, W. Yang, C. J. Chang-Hasnain, D. A. Horsley, and M. C. Wu, "A 32 × 32 optical phased array using polysilicon sub-wavelength high-contrast-grating mirrors," Opt. Express, vol. 22, no. 16, pp. 19029–19039, 2014.

[1-23] Y. Wang, G. Zhou, X. Zhang, K. Kwon, P. A. Blanche, N. Triesault, K. Yu, and M. C. Wu, "2D broadband beamsteering with large-scale MEMS optical phased array," Optica, vol. 6, no. 5, pp. 557–562, 2019.

[1-24] https://www.baraja.com/en/spectrum-hd-coming-soon, accessed on 2022-04-26.

[1-25] X. Gu, T. Shimada, A. Matsutani and F. Koyama, "Miniature Nonmechanical Beam Deflector Based on Bragg Reflector Waveguide With a Number of Resolution Points Larger Than 1000," IEEE Photonics Journal, vol. 4, no. 5, pp. 1712–1719, 2012.

[1-26] X. Gu, T. Shimada, A. Fuchida, A. Matsutani, A. Ishimura, and F. Koyama, "Beam steering in GaInAs/GaAs slow-light Bragg reflector waveguide amplifier," Appl. Phys. Lett., vol.99, no.21, pp. 211107-1–3, 2011.

[1-27] X. Wang, D. Wilson, R. Muller, P. Maker, and D. Psaltis, "Liquid-crystal blazed-grating beam deflector," Appl. Opt., vol. 39, no. 35, pp. 6545–6555, 2000.

[1-28] X. Shang, A. M. Trinidad, P. Joshi, J. De Smet, D. Cuypers and H. De Smet, "Tunable Optical Beam Deflection Via Liquid Crystal Gradient Refractive Index Generated By Highly Resistive Polymer Film," IEEE Photonics Journal, vol. 8, no. 3, pp. 1–11, 2016.

[1-29] O. Willekens, X. Jia, M. Vervaeke, X. Shang, T. Baghdasaryan, H. Thienpont, H. D. Smet, K. Neyts, and J. Beeckman, "Reflective liquid crystal hybrid beam-steerer," Opt. Express, vol. 24, no. 19, pp. 21541–21550, 2016.

[1-30] Y. J. Lin, K. M. Chen, and S. T. Wu, "Broadband and polarization-independent beam steering using dielectrophoresis-tilted prism," Opt. Express, vol. 17, no. 10, pp. 8651–8656, 2009.

[1-31] J. Cheng, and C. L. Chen, "Adaptive beam tracking and steering via electrowetting-controlled liquid prism," Appl. Phys. Lett., vol. 99, pp. 191108, 2011.

[1-32] C. Liu, L. Li, and Q. H. Wang, "Liquid prism for beam tracking and steering," Optical Engineering, vol. 51, no. 11, pp. 114002, 2012.

[1-33] M. Zohrabi, R. H. Cormack, and J. T. Gopinath, "Wide-angle nonmechanical beam steering using liquid lenses," Opt. Express, vol. 24, no. 21, pp. 23798–23809, 2016.

[1-34] K. V. Acoleyen, H. Rogier, and R. Baets, "Two-dimensional optical phased array antenna on silicon-on-insulator," Opt. Express, vol. 18, no. 13, pp. 13655–13660, 2010.

[1-35] S. Chung, H. Abediasl and H. Hashemi, "A Monolithically Integrated Large-Scale Optical Phased Array in Silicon-on-Insulator CMOS," IEEE Journal of Solid-State Circuits, vol. 53, no. 1, pp. 275–296, 2018.

[1-36] C. T. Phare, M. C. Shin, S. A. Miller, B. Stern, and M. Lipson, "Silicon optical phased array with high-efficiency beam formation over 180 degree field of view," arXiv:1802.04624, 2018.

[1-37] D. Inoue, T. Ichikawa, A. Kawasaki, and T. Yamashita, "Demonstration of a new optical scanner using silicon photonics integrated circuit," Opt. Express, vol. 27, no. 3, pp. 2499–2508, 2019.

[1-38] B. Jalali and S. Fathpour, "Silicon Photonics," Journal of Lightwave Technology, vol. 24, no. 12, pp. 4600–4615, 2006.

[1-39] A. Rickman, "The commercialization of silicon photonics," Nature Photon., vol. 8, pp.579–582, 2014.

[1-40] S. Y. Siew, B. Li, F. Gao, H. Y. Zheng, W. Zhang, P. Guo, S. W. Xie, A. Song, B. Dong, L. W. Luo, C. Li, X. Luo, and G.-Q. Lo, "Review of Silicon Photonics Technology and Platform Development," J. Lightwave Technol. vol. 39, no. 13, pp. 4374–4389, 2021.

[1-41] J. Sun, E. Timurdogan, A. Yaacobi, E. S. Hosseini, and M. R. Watts, "Large-scale nanophotonic phased array," Nature, vol. 493, pp. 195–199, 2013.

[1-42] H. Abediasl, and H. Hashemi, "Monolithic optical phased-array transceiver in a standard SOI CMOS process," Opt. Express, vol. 23, no. 5, pp. 6509–6519, 2015.

[1-43] F. Aflatouni, B. Abiri, A. Rekhi, and A. Hajimiri, "Nanophotonic projection system," Opt. Express, vol. 23, no. 16, pp. 21012–21022, 2015.

[1-44] F. Ashtiani, and F. Aflatouni, "N × N optical phased array with 2N phase shifters," Opt. Express, vol. 27, no. 19, pp. 27183–27190, 2019.

[1-45] R. Fatemi, A. Khachaturian, and A. Hajimiri, "A Nonuniform Sparse 2-D Large-FOV Optical Phased Array With a Low-Power PWM Drive," IEEE Journal of Solid-State Circuits, vol. 54, no. 5, pp. 1200–1215, 2019.

[1-46] T. Fukui, R. Tanomura, K. Komatsu, D. Yamashita, S. Takahashi, Y. Nakano, and T. Tanemura, "Non-redundant optical phased array," Optica, vol. 8, no. 10, pp. 1350–1358, 2021.

[1-47] K. V. Acoleyen, W. Bogaerts, J. Jágerská, N. L. Thomas, R. Houdré, and R. Baets, "Off-chip beam steering with a one-dimensional optical phased array on silicon-on-insulator," Opt. Lett. vol. 34, no. 9, pp. 1477–1479, 2009.

[1-48] J. K. Doylend, M. J. R. Heck, J. T. Bovington, J. D. Peters, L. A. Coldren, and J. E. Bowers, "Two-dimensional free-space beam steering with an optical phased array on silicon-on-insulator," Opt. Express, vol. 19, no. 22, pp. 21595–21604, 2011.

[1-49] D. Kwong, A. Hosseini, J. Covey, Y. Zhang, X. Xu, H. Subbaraman, and R. T. Chen, "On-chip silicon optical phased array for two-dimensional beam steering," Opt. Lett., vol. 39, no. 4, pp. 941–944, 2014.

[1-50] J. C. Hulme, J. K. Doylend, M. J. R. Heck, J. D. Peters, M. L. Davenport, J. T. Bovington, L. A. Coldren, and J. E. Bowers, "Fully integrated hybrid silicon two dimensional beam scanner," Opt. Express, vol. 23, no. 5, pp. 5861–5874, 2015.

[1-51] C. S. Im, S. M. Kim, K. P. Lee, S. H. Ju, J. H. Hong, S. W. Yoon, T. Kim, E. S. Lee, B. Bhandari, C. Zhou, S. Y. Ko, Y. H. Kim, M. C. Oh, and S. S. Lee, "Hybrid Integrated Silicon Nitride–Polymer Optical Phased Array For Efficient Light Detection and Ranging," Journal of Lightwave Technology, vol. 39, no. 13, pp. 4402–4409, 2021.

[1-52] S. H. Kim, J. B. You, Y. G. Ha, G. Kang, D. S. Lee, H. Yoon, D. E. Yoo, D. W. Lee, K. Yu, C. H. Youn, and H. H. Park, "Thermo-optic control of the longitudinal radiation angle in a silicon-based optical phased array," Opt. Lett., vol. 44, no. 2, pp. 411–414, 2019.

[1-53] N. Dostart, B. Zhang, A. Khilo, M. Brand, K. A. Qubaisi, D. Onural, D. Feldkhun, K. H. Wagner, and M. A. Popović, "Serpentine optical phased arrays for scalable integrated photonic lidar beam steering," Optica, vol. 7, no. 6, pp. 726–733, 2020.

[1-54] T. Komljenovic, R. Helkey, L. Coldren, and J. E. Bowers, "Sparse aperiodic arrays for optical beam forming and LIDAR," Opt. Express, vol. 25, no. 3, pp. 2511–2528, 2017.

[1-55] C. V. Poulton, A. Yaacobi, D. B. Cole, M. J. Byrd, M. Raval, D. Vermeulen, and M. R. Watts, "Coherent solid-state LIDAR with silicon photonic optical phased arrays," Opt. Lett., vol. 42, no. 20, pp. 4091–4094, 2017.

[1-56] C. V. Poulton, M. J. Byrd, P. Russo, E. Timurdogan, M. Khandaker, D. Vermeulen, and M. R. Watts, "Long-Range LiDAR and Free-Space Data Communication With High-Performance Optical Phased Arrays," IEEE Journal of Selected Topics in Quantum Electronics, vol. 25, no. 5, pp. 1–8, 2019.

[1-57] T. Kim, P. Bhargava, C. V. Poulton, J. Notaros, A. Yaacobi, E. Timurdogan, C. Baiocco, N. Fahrenkopf, S. Kruger, T. Ngai, Y. Timalsina, M. R. Watts, and V. Stojanović, "A Single-Chip Optical Phased Array in a Wafer-Scale Silicon Photonics/CMOS 3D-Integration Platform," IEEE Journal of Solid-State Circuits, vol. 54, no. 11, pp. 3061–3074, 2019.

[1-58] S. A. Miller, Y. C. Chang, C. T. Phare, M. C. Shin, M. Zadka, S. P. Roberts, B. Stern, X. Ji, A. Mohanty, O. A. J. Gordillo, U. D. Dave, and M. Lipson, "Large-scale optical phased array using a low-power multi-pass silicon photonic platform," Optica, vol. 7, no. 1, pp. 3–6, 2020.

[1-59] C. V. Poulton, M. J. Byrd, B. Moss, E. Timurdogan, R. Millman and M. R. Watts, "8192-Element Optical Phased Array with 100° Steering Range and Flip-Chip CMOS," Conference on Lasers and Electro-Optics (CLEO), pp. 1–2, 2020.

[1-60] C. Li, X. Cao, K. Wu, X. Li, and J. Chen, "Lens-based integrated 2D beam-steering device with defocusing approach and broadband pulse operation for Lidar application," Opt. Express, vol. 27, no. 23, pp. 32970–32983, 2019.

[1-61] Y. C. Chang, M. C. Shin, C. T. Phare, S. A. Miller, E. Shim, and M. Lipson, "2D beam steerer based on metalens on silicon photonics," Opt. Express, vol. 29, no. 2, pp. 854–864, 2021.

[1-62] C. Rogers, A. Y. Piggott, D. J. Thomson, R. F. Wiser, I. E. Opris, S. A. Fortune, A. J. Compston, A. Gondarenko, F. Meng, X. Chen, G. T. Reed, and R. Nicolaescu "A universal 3D imaging sensor on a silicon photonics platform," Nature, vol. 590, pp. 256–261, 2021.

[1-63] X. Zhang, K. Kwon, J. Henriksson, J. Luo, and M. C. Wu, "A large-scale microelectromechanical-systems-based silicon photonics LiDAR," Nature, vol. 603, pp. 253–258, 2022.

[1-64] H. Ito, Y. Kusunoki, J. Maeda, D. Akiyama, N. Kodama, H. Abe, R. Tetsuya, and T. Baba, "Wide beam steering by slow-light waveguide grating and prism lens," Optica, vol. 7, no. 1, pp. 47–52, 2020.

[1-65] C. Li, X. Cao, K. Wu, G. Qiu, M. Cai, G. Zhang, X. Li, and J. Chen, "Blind zone-suppressed hybrid beam steering for solid-state Lidar," Photon. Res. vol. 9, no. 9, pp. 1871–1880, 2021.

[1-66] F. Long, H. Tian, and Y. Ji, "A Study of Dynamic Modulation and Buffer Capability in Low Dispersion Photonic Crystal Waveguides," J. Lightwave Technol., vol. 28, no. 8, pp. 1139–1143, 2010.

[1-67] Y. Zhai, H. Tian, and Y. Ji, "Slow Light Property Improvement and Optical Buffer Capability in Ring-Shape-Hole Photonic Crystal Waveguide," J. Lightwave Technol., vol. 29, no. 20, pp. 3083–3090, 2011.

[1-68] L. Gu, W. Jianga, X. Chen, L. Wang, and R. T. Chen, "High speed silicon photonic crystal waveguide modulator for low voltage operation," Appl. Phys. Lett., vol. 90, no. 7, pp. 071105, 2007.

[1-69] H. C. Nguyen, S. Hashimoto, M. Shinkawa and T. Baba, "Compact and fast photonic crystal silicon optical modulators," Opt. Express, vol. 20, no. 20, pp. 22465–22474, 2012.

[1-70] A. Hosseini, X. Xu, H. Subbaraman, C. Y. Lin, S. Rahimi, and R. T. Chen, "Large optical spectral range dispersion engineered silicon-based photonic crystal waveguide modulator," Opt. Express, vol. 20, no. 1, pp. 12318–12325, 2012.

[1-71] N. Ishikura, R. Hayakawa, R. Hosoi, T. Tamanuki, M. Shinkawa and T. Baba, "Photonic crystal tunable slow light device integrated with multi-heaters," Appl. Phys. Lett., vol. 100, no. 22, pp. 221110, 2012.

[1-72] K. Kondo, N. Ishikura, T. Tamura and T. Baba, "Temporal pulse compression by dynamic slow-light tuning in photonic crystal waveguides", Phys. Rev. A, vol. 91, no. 02, pp. 023831, 2015.

[1-73] R. Hayakawa, N. Ishikura and T. Baba, "Two-photon-absorption photodiodes in photonic-crystal slow-light waveguides", Appl. Phys. Lett., vol. 102, no. 3, pp. 031114, 2013.

[1-74] Y. Terada, K. Miyasaka, H. Ito and T. Baba, "Slow-light effect in a silicon photonic crystal waveguide as a sub-bandgap photodiode", Opt. Lett., vol. 41, no. 2, pp. 289–292, 2016.

[1-75] K. Ohtaka, "Energy band of photons and low-energy photon diffraction," Phys. Rev. B, vol. 19, no. 10, pp. 5057–5067, 1979.

[1-76] E.Yablonovitch, "Inhibited Spontaneous Emission in Solid-State Physics and Electronics," Phys. Rev. Lett., vol. 58, no. 20, pp. 2059–2062, 1987.

[1-77] E.Yablonovitch and T. J. Gmitter, "Photonic band structure: the face-centered-cubic case," Phys. Rev. Lett., vol. 63, no. 18, pp. 1950–1953, 1989.

[1-78] M. Notomi, A. Shinya, K. Yamada, J. Takahashi, C. Takahashi and I. Yokohama, "Structural tuning of guided modes of line-defect waveguides of silicon-on-insulator photonic crystal slabs," Journal of Quantum Electronics, vol. 38, no. 7, pp. 736–742, 2002.

[1-79] C. Jamois, R.B.Wehrspohn, L. C. Andreani, C. Hermann, O. Hess, U. Gösele, "Silicon-based two-dimensional photonic crystal waveguides," Photonics and Nanostructures-Fundamentals and Applications, vol. 1, no. 1, pp. 1–13, 2003.

[1-80] E. Kuramochi, S. Hughes, A. Shinya and M. Notomi, "Si based photonic crystal components: relationship between performance and structural disorder," NTT Technical Review, vol. 3, no. 12, pp. 69–74, 2005.

[1-81] M. Notomi, K. Yamada, A. Shinya, J. Takahashi, C. Takahashi, and I. Yokohama, "Extremely large group-velocity dispersion of line-defect waveguides in photonic crystal slabs," Phys. Rev. Lett., vol. 87, no.25, pp. 253902–1–4, 2001.

[1-82] Y. A. Vlasov, M. O'Boyle, H. F. Hamann, and S. J. McNab, "Active control of slow light on a chip with photonic crystal waveguides," Nature, vol. 438, no.11, pp. 65–69, 2005.

[1-83] T. Tamura, K. Kondo, Y. Terada, Y. Hinakura, N. Ishikura and T. Baba, "Silica-clad silicon

photonic crystal waveguides for wideband dispersion-free slow light," J. Lightwave Technol., vol. 33, no. 7, pp. 3034–3040, 2015.

[1-84] K. Hirotani, R. Shiratori and T. Baba, "Si photonic crystal slow-light waveguide optimized by informatics technology," Opt. Lett., vol. 46, no. 17, pp. 4422–4425, 2021.

[1-85] K. Kondo, T. Tatebe, S. Hachuda, H. Abe, F. Koyama and T. Baba, "Fan beam steering device using a photonic crystal slow-light waveguide with surface diffraction grating," Opt. Lett., vol. 42, no. 23, pp. 4990–4993, 2017.

[1-86] H. Abe, M. Takeuchi, G. Takeuchi, H. Ito, T. Yokokawa, K. Kondo, Y. Furukado and T. Baba, "Two-dimensional beam-steering device using a doubly periodic Si photonic-crystal waveguide," Opt. Express, vol. 26, no. 8, pp. 9389–9397, 2018.

[1-87] G. Takeuchi, Y. Terada, M. Takeuchi, H. Abe, H. Ito and T. Baba, "Thermally controlled Si photonic crystal slow light waveguide beam steering device," Opt. Express, vol. 26, no. 9, pp.11529–11537, 2018.

Chapter 2
Fabrication and Components

2.1 Fabrication

2.1.1 Silicon photonics foundry service

In this study, we designed, fabricated, and evaluated devices using the foundry service of silicon photonics. Recently, silicon photonics foundry services that can fabricate photonic integrated chips following the already mature CMOS technology have been enhanced [2-1, 2]. With this development, researchers do not need to purchase and maintain their own expensive fabrication equipment and can concentrate on design and evaluation of silicon photonics devices. Figure 2.1 shows the concept of a silicon photonics chip on an SOI wafer and examples of optical elements. Silicon photonics chips are cut from the reticle pattern by dicing. The multi-project wafer, in which the reticle pattern is shared among multiple users, is economical because it reduces the cost per user. However, foundries need to standardize recipes and dicing lines among users, thus reducing the freedom of device design on the user side.

Major optical elements that can be integrated include waveguides, spot size converters (SSCs), multimode interference (MMI) couplers, phase shifters, and photodetectors (PDs). Silicon is an indirect-transition semiconductor and is generally difficult to use as a light source, which is why hybrid integration is used, in which another light emitting device made of a compound semiconductor is attached to a silicon photonic integrated circuit. Grating couplers are generally used for coupling light into waveguides on the chip, which are the most basic optical devices. Light can be coupled into and out vertically from the chip surface, thus having the advantage of enabling wafer-scale testing of optical device characteristics before the chip is cut out. However, it generally has a narrow wavelength bandwidth. In this study, an inverse-tapered SSC with a narrow tip formed at the end of a chip is used, and the device is evaluated using an optical system with an objective lens and a lensed fiber. The phase shifter consists of a resistive heater above the waveguide to utilize the phase change caused by the thermo-optic effect. PIN photodiodes and avalanche photodiodes made of germanium epitaxially grown on Si are used as photodetectors. Some components such as light sources and PDs are not included in the recipe depending on the foundry.

In this study, two foundry services are used to fabricate devices, which are referred to here as Foundries A and B. The wafers that include chips fabricated by each of the two foundries are shown in Fig. 2.2, where Foundries A and B are silicon photonics CMOS processes with minimum line widths of 130 and 80 nm, respectively, and wafer sizes of 200 and 300 mm, respectively. The former uses a KrF excimer laser and phase-shift mask exposure, while the latter is the foundry of the National Institute of Advanced Industrial Science and Technology, which uses ArF excimer laser immersion exposure to achieve narrower minimum linewidths.
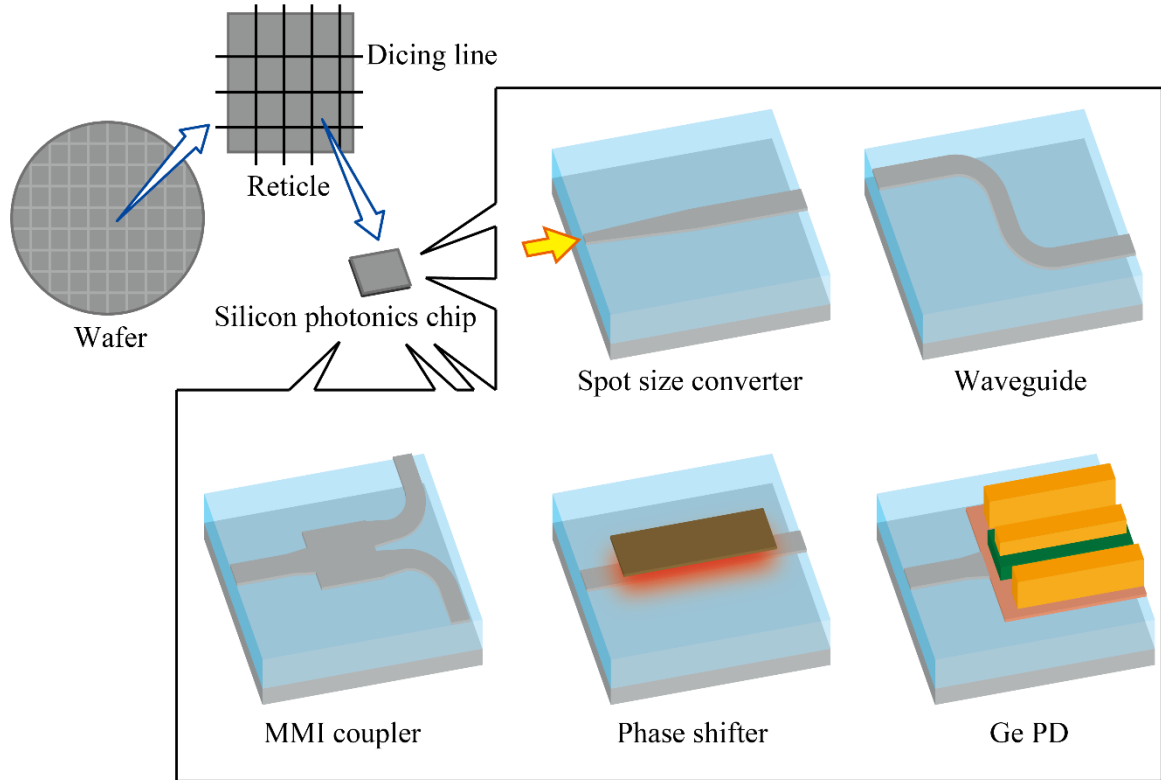
Fig. 2.1 Concept of silicon photonics chip integrated on SOI wafer and examples of optical elements such as spot size converter and waveguide, MMI coupler, phase shifter, and Ge PD.
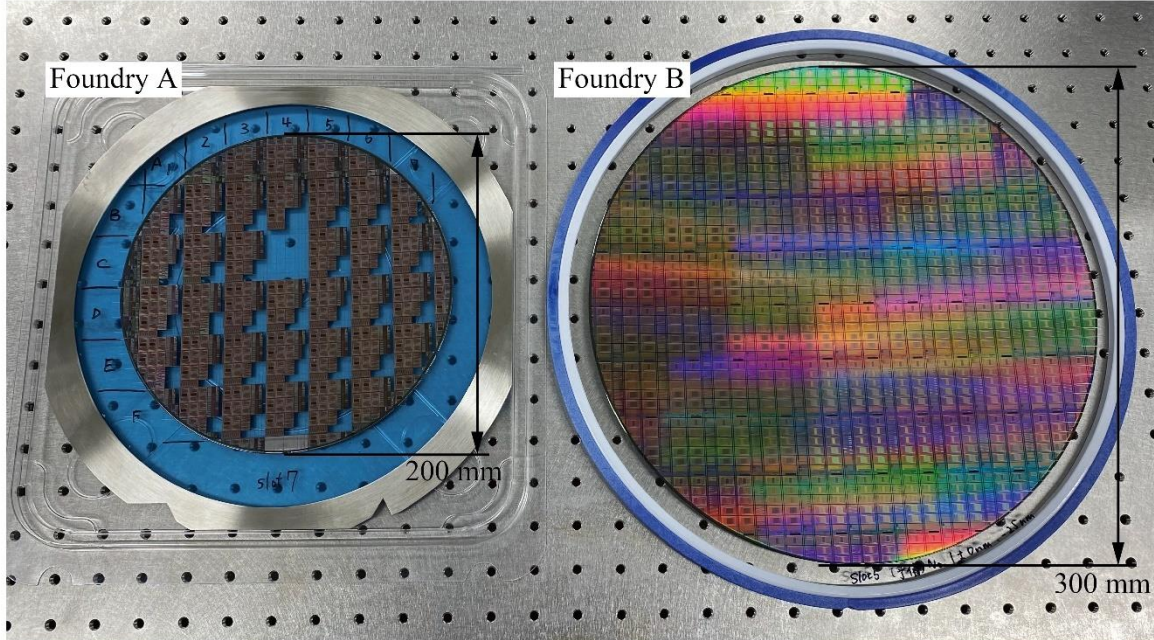

Fig. 2.2 Fabricated devices integrated on SOI wafers of Foundries A and B.

2.1.2 Design rule and fabrication process

Table 2.1 summarizes the differences in design rules between Foundries A and B. Foundry A used a 200 mm diameter SOI wafer with a Si slab thickness of t_{slab} = 210 nm, and Foundry B used a 300 mm diameter SOI wafer with t_{slab} = 220 nm to fabricate the devices. The thicknesses of the SiO$_2$ box layers

are different, being 2 and 3 μm for Foundries A and B, respectively. Heater isolation trench, silica trench for SSC, and Ge PD can be fabricated in Foundry A, but cannot be fabricated in Foundry B. Table 2.2 summarizes the doping concentration of Si in each foundry. n- and p-type Si are formed using phosphorus and boron as dopants, respectively, and two different doping concentrations can be selected, where n^+- and p^+-Si have 100 times higher concentration than n- and p-Si.

The structures of Si waveguide and TiN heater, PCW optical antenna, and Ge PD are shown in Fig. 2.3 as examples of devices fabricated in each foundry. The Si waveguide, which is the most basic element, was fabricated by determining the waveguide width w to obtain optimal single-mode propagation, because t_{slab} differs from foundries. TiN heaters are fabricated for phase shifters for optical switches and heaters of the PCWs, where the TiN layer is formed in the SiO_2 cladding about 1.2 μm away from the Si slab and is connected to the Al formed further up by contact holes. In Foundry A, a heater isolation trench can be formed by etching through the SiO2 layer to the Si substrate layer to improve heating efficiency. PCW was formed by etching circular holes on a Si slab, and then these holes were filled with SiO_2 when forming the oxide layer. A doubly periodic structure with a circular hole diameter or a diffraction grating structure with a shallow etching of 10 nm depth was introduced to enable the PCW to act as an optical antenna. The thermo-optical heaters used to heat the PCW were TiN heaters on both sides of the PCW or p-i-p heaters where the Si layer, which is the center of the PCW sandwiched by p-Si, is connected to p^+-Si and the Al layer by contact holes to apply voltage. Ge PD functioning as a PIN-type PD is fabricated by epitaxial growth of Ge on p-Si, which was formed by special doping concentration is selected for Ge PD fabrication, followed by n-type doping on Ge, where light is coupled into the p-Si layer from the Si waveguide through the tapered structure. The area where the SiO_2 layer is etched through from the surface to the Al layer is the probing/bonding Pad, which is used to drive the thermo-optical heater and to detect signals from the Ge PD. To prevent light scattered in the fabricated chip from affecting the beam shape and transmission and reception signal light, an n^+-Si layer is provided in the area other than the fabricated device in the LiDAR chip described in Chapter 7.

Table 2.1 Comparison of Foundries A and B.

Foundry	A	B
Lithography	KrF	ArF immersion
Diameter of SOI wafer [mm]	200	300
Thickness of Si slab t_{slab} [nm]	210	220
Thickness of SiO_2 box layer t_{box} [μm]	2	3
Heater isolation trench	Yes	No
Silica trench for SSC	Yes	No
Ge PD	Yes	No

Table 2.2 Doping concentration.

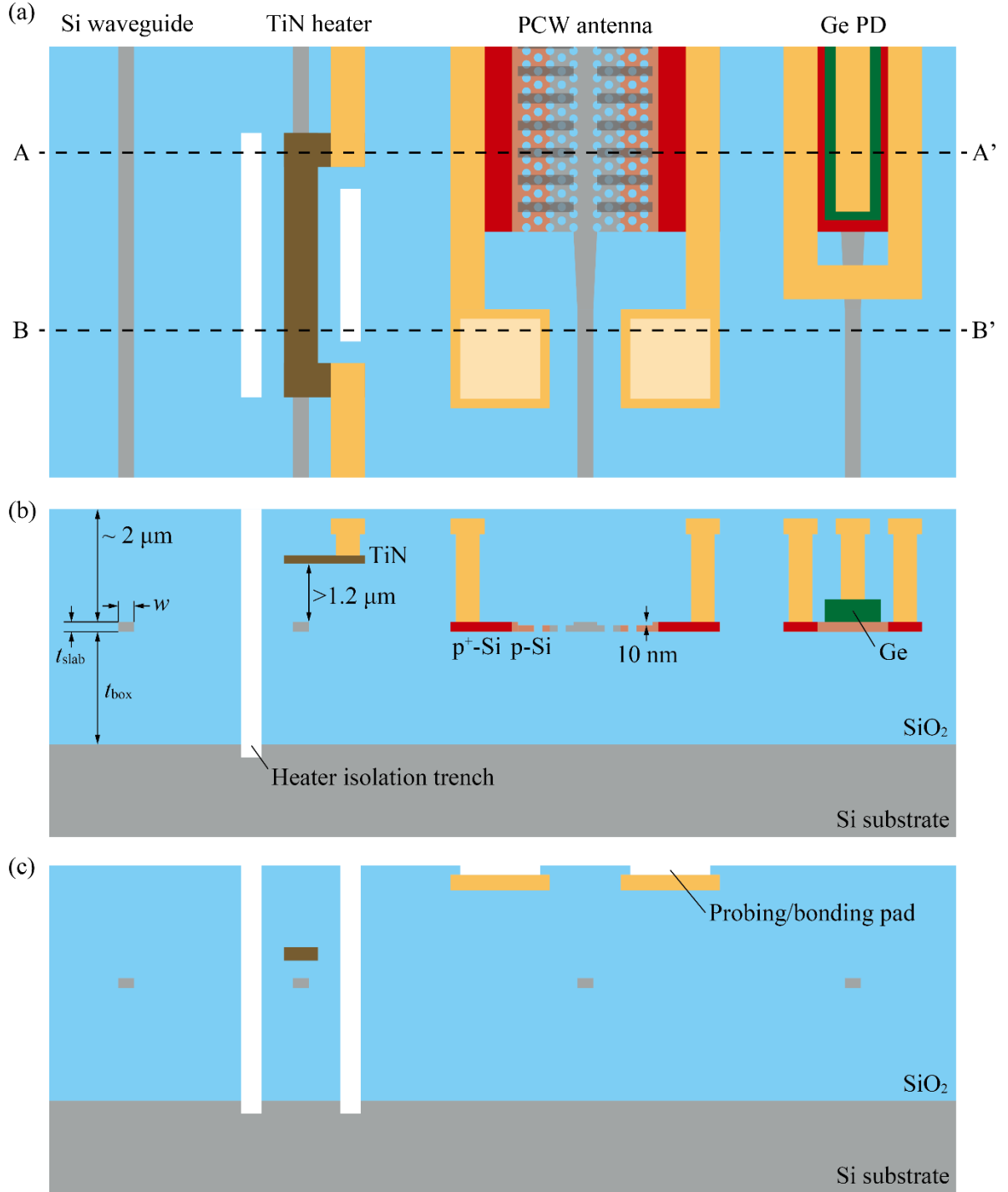|		n-Si	n^+-Si	p-Si	p^+-Si
	Dopant	Phosphorus		Boron	
Foundry A	Concentration [cm^{-2}]	1.3×10^{13}	4.0×10^{15}	2.2×10^{13}	4.0×10^{15}
Foundry B	Concentration [cm^{-2}]	1.12×10^{13}	5.0×10^{15}	1.05×10^{13}	5.0×10^{15}

Fig. 2.3 Examples of structures obtained in the fabrication process of silicon photonics foundries. (a) Top view of structures. (b) Cross section at A-A' line. (c) Cross section at B-B' line.

2.1.3 Creation of CAD data

CAD data for photomask fabrication to be submitted to each foundry must be in Graphic Design System II (GDSII) format, and the data were created according to the flow chart shown in Fig. 2.4. First, Drawing Interchange Format (DXF) data were created using Autodesk's AutoCAD, a commercial CAD software, according to the photomask layer numbers specified by each foundry, as shown in Table 2.3. Next, the DXF files were converted to GDSII files using Astron's DXF/GDS conversion software

program, Dvogue. GDS does not have the concept of hollowing out a shape; thus, the hollowed-out shape needs to be realized with a single drawing line to express it. In addition, circles are converted into inscribed polygons. Therefore, the hollowing-out of the PCW circular hole is represented by a regular 16-sided polygon. Each foundry has its own rules regarding the gaps and shapes between layers and layers; thus, whether the created layers conform to these rules or not after GDS files are created needs to be checked. Design rule check (DRC) was performed using KLayout, an open-source CAD layout software, where a new layer is created as shown in Fig. 2.4 if a layer does not meet the rules in DRC. The design should be reviewed again to prevent this DRC layer from being displayed. A GDS file that satisfied the DRC was created and submitted to the foundry to fabricate the devices.
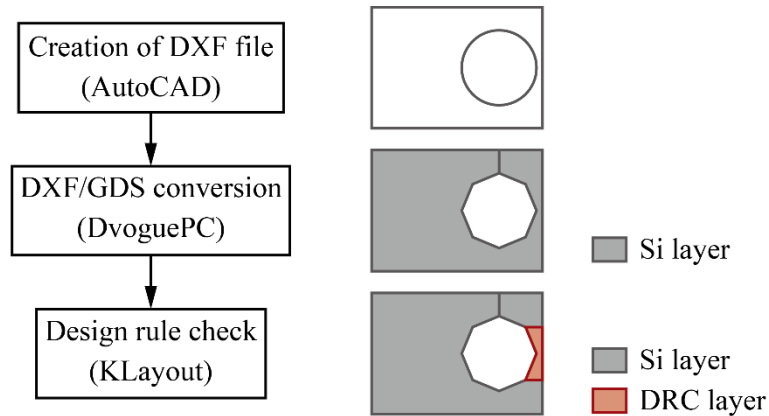
Fig. 2.4 Procedures for creating CAD data to be submitted to foundries.

Table 2.3 Photomask layer.

Device	Layer no.	
	Foundry A	Foundry B
Si	1	30
Holes of photonic crystal	3	-
Silica trench at SSC	4	-
Facet deep trench	7	-
Heater isolation trench	8	-
Al	9	36
Contact hole (heater)	10	39
TiN heater	11	38
Contact hole (pn)	13	35
n-Si	14	31
p-Si	15	32
n^+-Si	16	33
p^+-Si	17	34
n-Ge	18	-
p-Si for Ge PD	19	-
Ge window	20	-
Probing/bonding pad	21	41
Grating	32	29

2.2 Fundamental Components

2.2.1 Silicon waveguide

Si waveguides are fundamental elements in silicon photonics that form optical circuits on chips, playing an important role in connecting SSCs, optical switches, PCW optical antennas, optical detectors, and other elements. A PCW that operates with TE polarization is used in this study, which is why a waveguide design with single-mode propagation of TE polarization is also required. The Si slab thicknesses in Foundries A and B are different; hence, w was optimized as 0.4 and 0.44 μm, respectively, by previous research in our laboratory to provide conditions for single-mode propagation of TE polarization, where w was analyzed using commercial FDTD calculation software from Ansys Lumerical [2-3]. The propagation loss of the fabricated waveguide was 2−3 dB/cm, and most of the loss was caused by the roughness of the waveguide sidewalls during fabrication. The minimum waveguide bending radius for the device in this study was designed to be 5.0 μm, as shown in Fig. 2.5(b), and the loss of the fabricated device was 0.06−0.07 dB/bend.

2.2.2 Spot size converter

An inverted tapered SSC formed at the edge of the chip was used to couple the light into the Si waveguide inside the chip. Objective lenses and lensed fibers were used for fundamental characterization of the fabricated devices. For the fully integrated LiDAR chip described in Chapter 7, a polarization-maintaining core-shrunk fiber array block was directly fixed to the chip end for light input and output. As shown in Fig. 2.6, in Foundry A, the SSC is surrounded by the SiO_2 cladding with the width of 4 μm, which is further surrounded on both sides by air cladding with trenches etched through the SiO_2 layer to the Si substrate layer. A deep trench layer is etched at the edge of the chip to a depth of about 50 μm down to the Si substrate to suppress scattering loss. The tapered structure extends linearly from a tip width of 180 nm to 400 nm with a length of 200 μm and a 2 μm SiO_2 layer gap between the chip edge and the taper. A microscopic image of the fabricated SSC structure is shown in Fig. 2.7, and the coupling efficiency was 2−3 dB/facet. As shown in Fig. 2.8, the SSC structure of Foundry B has no air cladding structure, and a straight section with a width of 210 nm and a length of 100 μm is formed from the edge of the chip to the tapered structure, and the tapered structure has a length of 200 μm, similar to that in Foundry A. Figure 2.9 shows a microscopic image of the fabricated SSC, whose edge was formed without any cracks, and the coupling efficiency was 1.4 dB/facet.
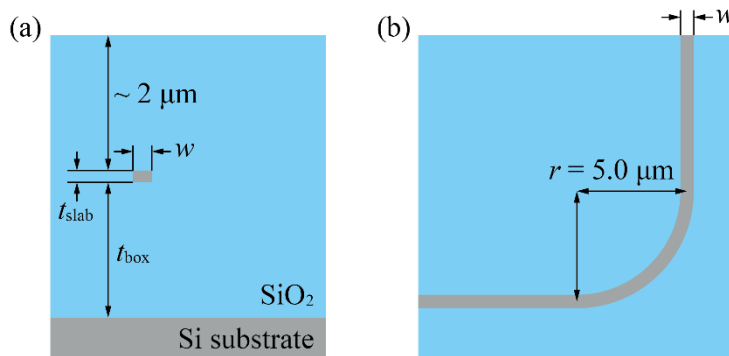
Fig. 2.5 (a) Cross section of silicon waveguide. (b) Bending structure of silicon waveguide.

(a)

(b)

(c)

(d)
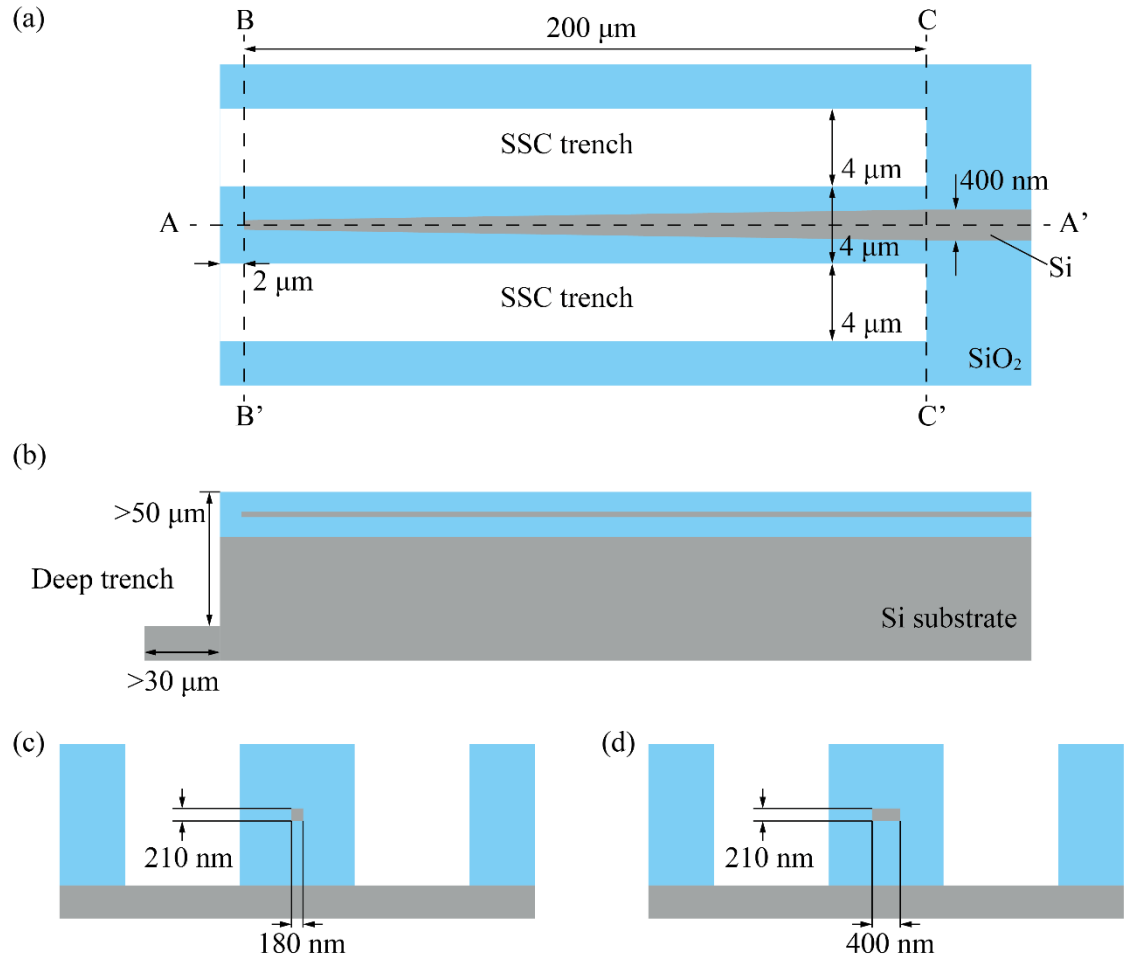
Fig. 2.6 Structure of SSC in Foundry A. (a) Top view. (b) Cross section at A-A' line. (c) Cross section at B-B' line. (d) Cross section at C-C' line.
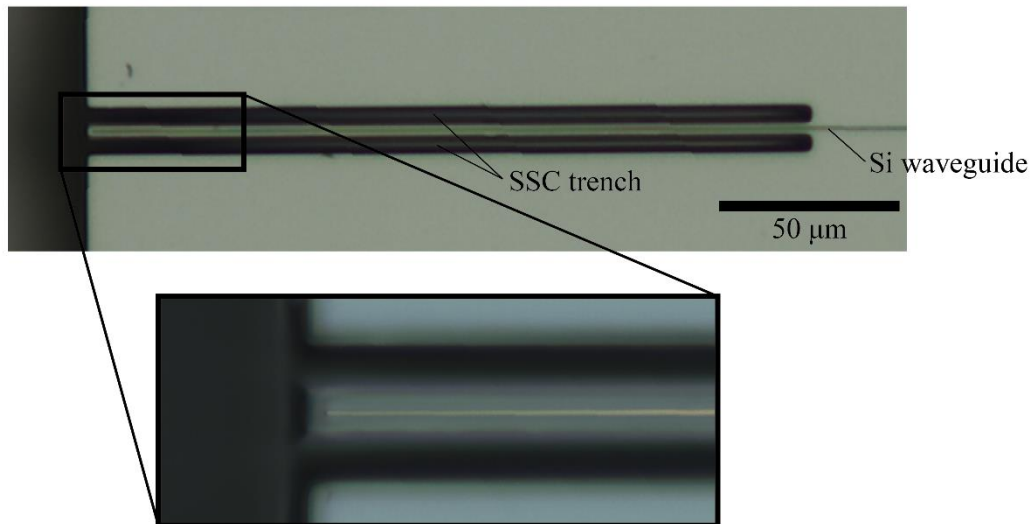

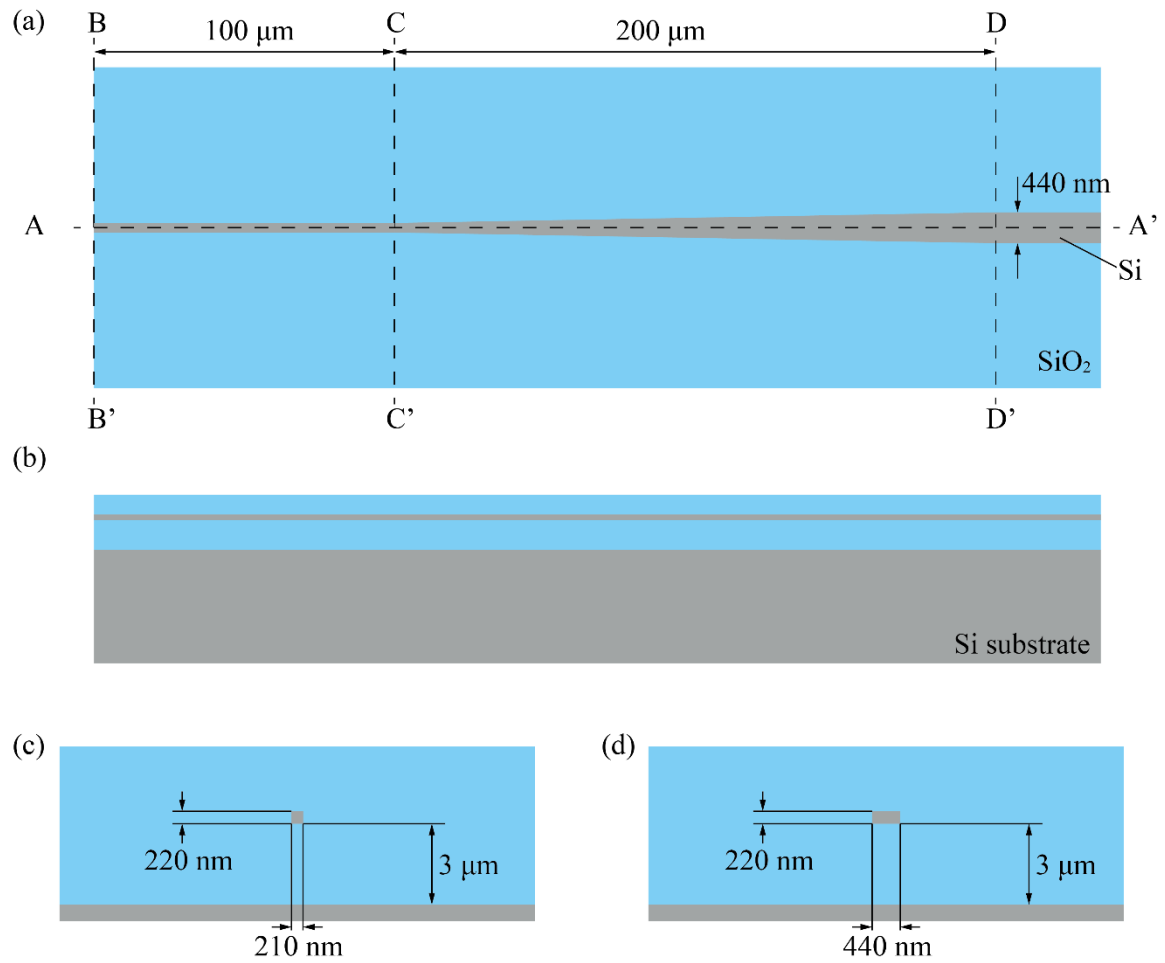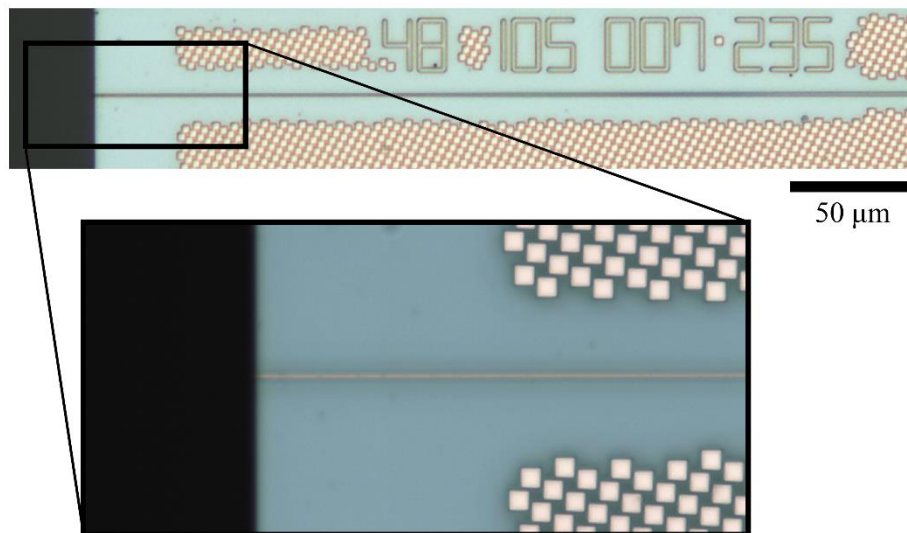Fig. 2.7 Microscopic image of fabricated SSC in Foundry A.

Fig. 2.8 Structure of SSC in Foundry B. (a) Top view. (b) Cross section at A-A' line. (c) Cross section at B-B' line. (d) Cross section at C-C' line.

Fig. 2.9 Microscopic image of fabricated SSC in Foundry B.

2.2.3 Multimode interference coupler

MMI couplers were used to configure the tournament-type splitter for the subarray configuration of PCW antenna described in Chapter 3 and Mach−Zehnder interferometer (MZI) type optical switch, which is the interference system for FMCW LiDAR operation. Figure 2.10 shows the design of a 1 × 2 MMI coupler and a 2 × 2 MMI coupler optimized by FDTD calculations based on previous research in our laboratory. The 1 × 2 MMI coupler has a tapered connection from the Si waveguide at the input and a tapered and bending structure with a radius of 5 μm at the output. The 2 × 2 MMI coupler has a tapered and bending structure for both input and output, which is optimized for the thickness of Si slab and the width of Si waveguide for foundries, respectively. The 2 × 2 MMI coupler fabricated by Foundry B was not used in this study and is omitted here. Microscopic images of the MMI couplers fabricated by each foundry are shown in Fig. 2.11. The insertion loss of the 1 × 2 and 2 × 2 MMI couplers fabricated by Foundry A and the 1 × 2 MMI coupler fabricated by Foundry B were 0.2, 0.4, and 0.3 dB, respectively.

2.2.4 Phase shifter

The optical switch integrated in the LiDAR chip described in Chapter 7 is an MZI-type switch consisting of MMI couplers and a thermo-optic heater with a TiN resistor. The design and microscope image of the fabricated device are shown in Fig. 2.12. A 1 × 2 MMI coupler was used for the input part, and the output ratio from the 2 × 2 MMI on the output side was adjusted by controlling a thermo-optic heater on one arm. A heater isolation trench was fabricated to increase the heating efficiency, and the power required for switching was 13 mW.
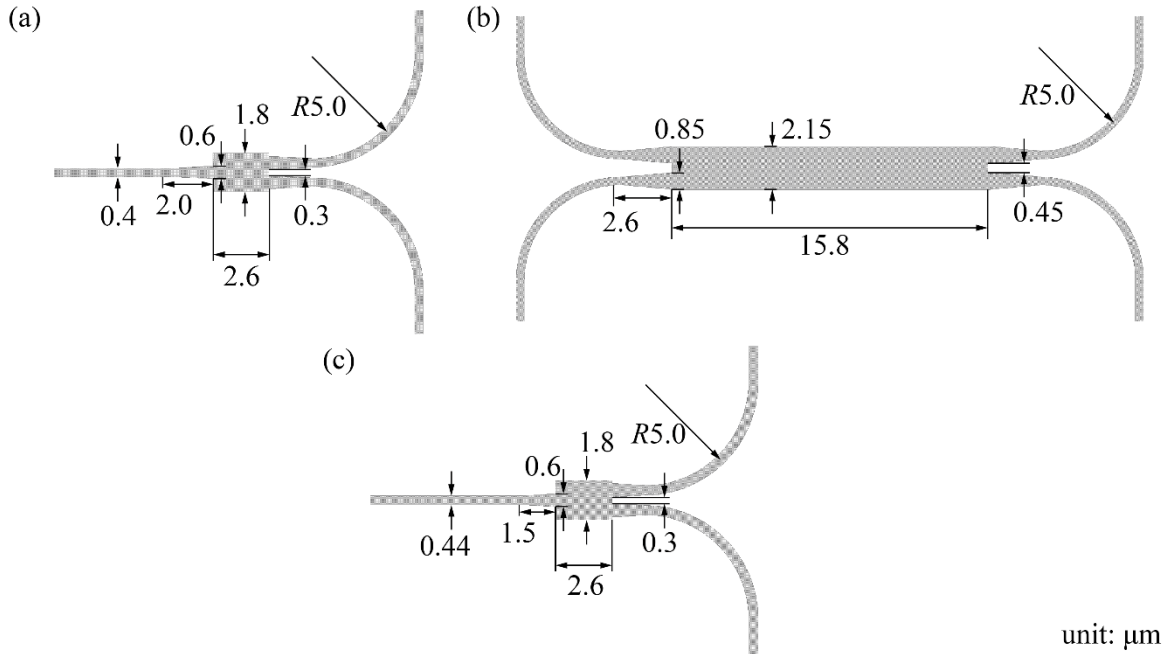
Fig. 2.10 Design of MMI couplers optimized by FDTD calculations. (a) 1 × 2 and (b) 2 × 2 MMI couplers for Foundry A, respectively. (c) 1 × 2 MMI coupler for Foundry B.

(d) (e)

(f)

5.0 μm
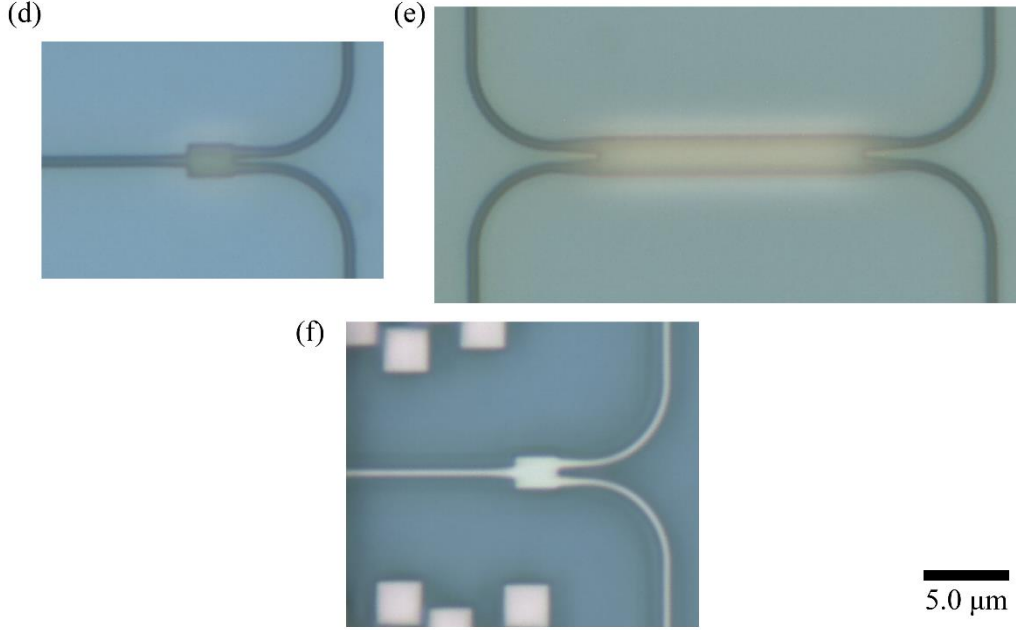
Fig. 2.11 Microscopic images of fabricated MMI couplers. (a) 1 × 2 and (b) 2 × 2 MMI couplers fabricated by Foundry A, respectively. (b) 1 × 2 MMI coupler fabricated by Foundry B.

(a)

Al wire

Heater isolation trench

170 μm

TiN heater

1 × 2 MMI coupler

2 × 2 MMI coupler

(b)

50 μm
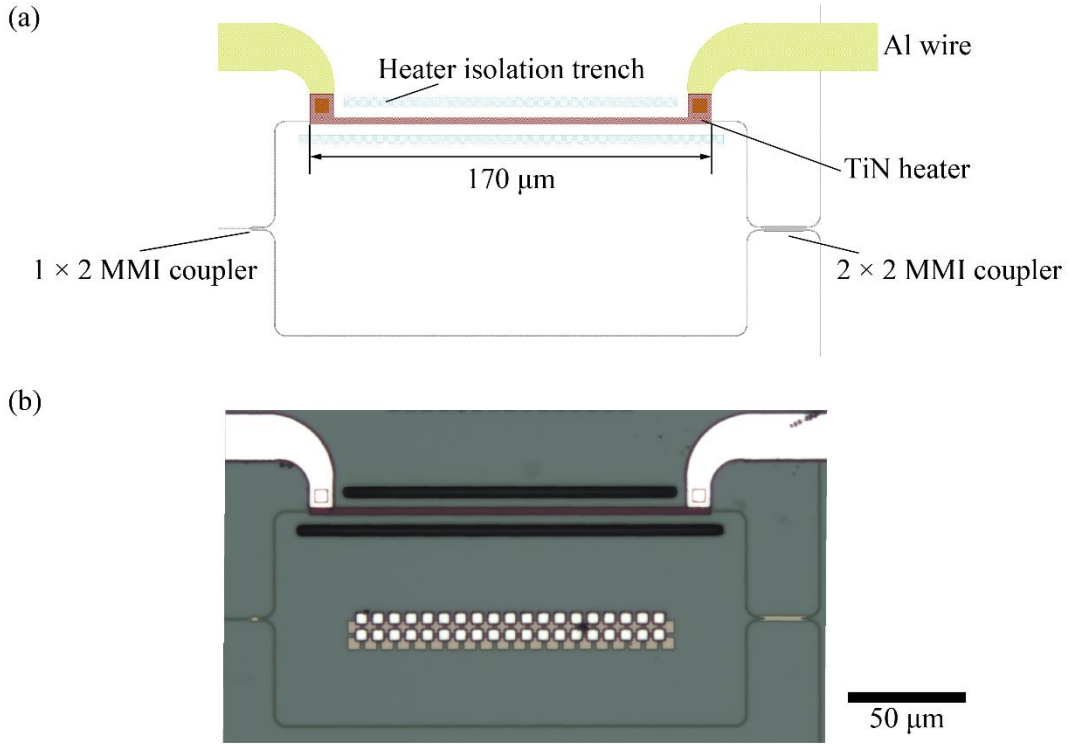
Fig. 2.12 (a) CAD data and (b) fabricated device of optical switch.

2.2.5 Lattice-shifted PCW

A lattice-shifted PCW as an optical antenna was designed and fabricated to propagate low-dispersion slow light, as shown in Fig. 2.13. If the third row of circular holes from the line defect is shifted by s_3 in the waveguide direction, then the band diagram is straightened, enabling low-dispersion slow light. In this study, $s_3 = 95$ nm, the group index $n_g = 15$, and the target operating wavelength was designed to

33

be 1550 nm. As shown in Fig. 2.13, the connection from the Si waveguide to the PCW consisted of a tapered structure that gradually widens the width of the waveguide at the L_{taper} length to the Si slab including the PCW, and the PCW was also tapered such that it gradually widened toward the slab edge; the coupling loss between Si waveguide and PCW was estimated to be 0.28 dB by the calculation [2-4]. The optimization of the position of the circular hole in the tapered structure lowered the coupling loss to 0.12 dB, increasing the usefulness of the slow light device in the PCW [2-5]. Figure 2.14 shows a confocal laser microscopic image of the connection structure between the Si waveguide and the PCW fabricated in Foundry B. $L_{taper} = 10$ μm and the coupling loss was approximately 0.5 dB. The fabrication of a doubly periodic structure of circular holes and a shallow-etched grating structure for optical antennas using PCWs are described in a later chapter.

2.2.6 Germanium photodiode

In the FMCW LiDAR chip described in Chapter 7, a Ge balanced PD was used for signal detection. The design and microscopic image of the Ge PD are shown in Fig. 2.15. A 40 μm long tapered structure was expanded from the Si waveguide to a width of 3.6 μm and connected to p-Si. A PIN-type PD was fabricated using Ge epitaxially grown on p-Si and n-Ge, where contact holes and Al were connected on p$^+$-Si and n-Ge. The sensitivity of the fabricated PD was approximately 0.5 A/W.
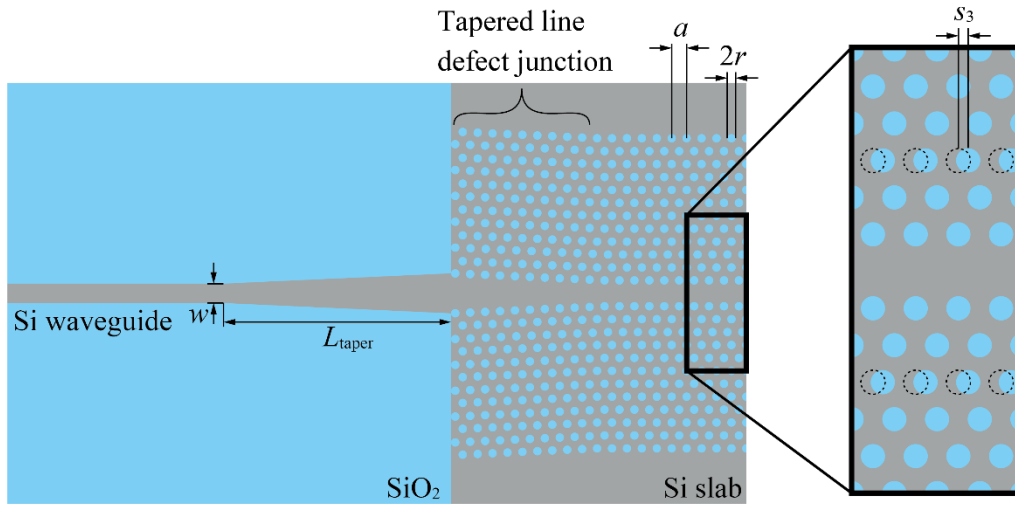
Fig. 2.13 Connection structure between the Si waveguide and the PCW.
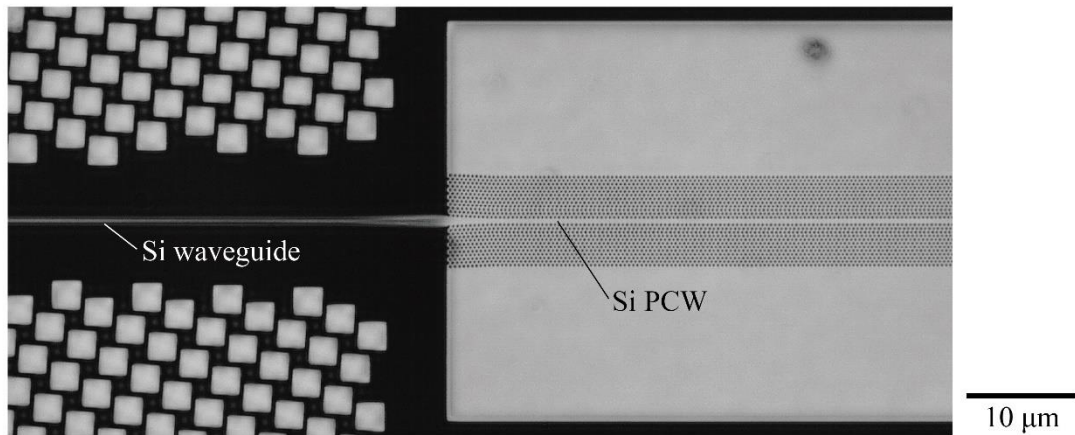
Fig. 2.14 Fabricated connection structure between the Si waveguide and the PCW.
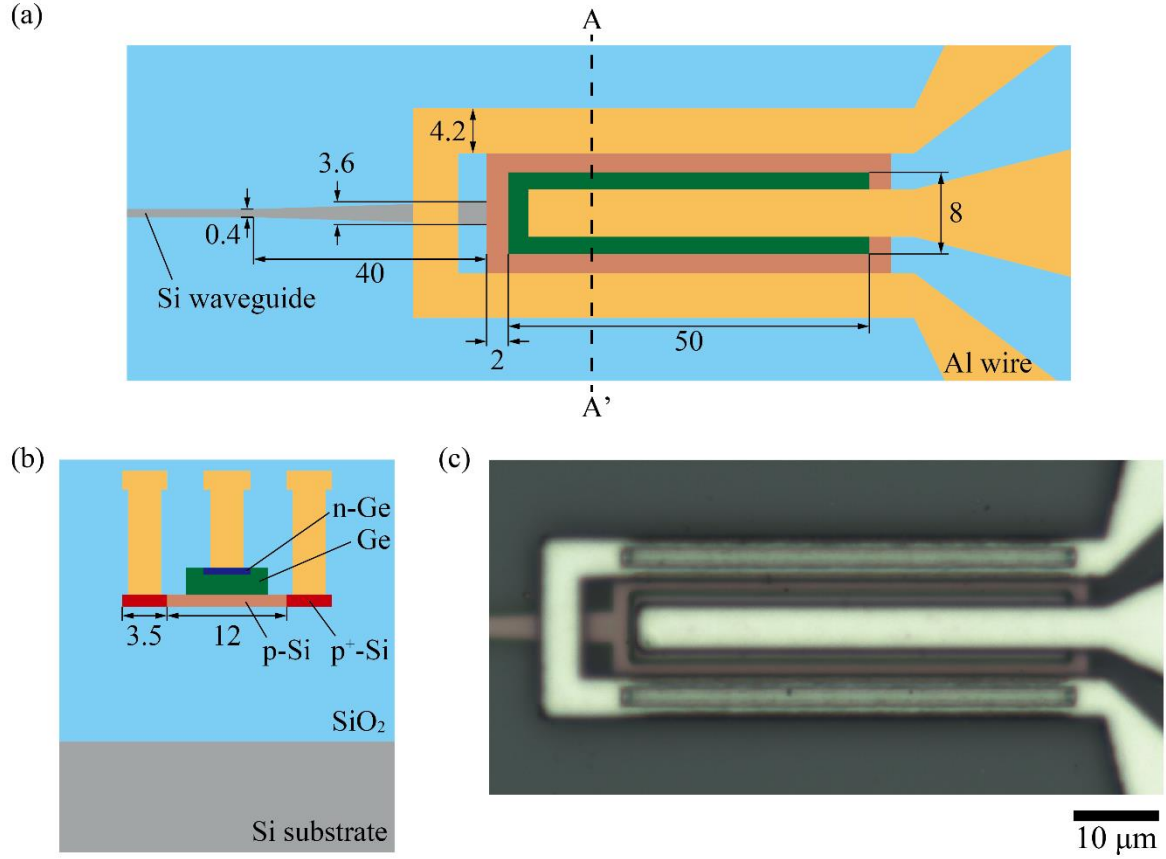
Fig. 2.15 Structure design of Ge PD in Foundry A. (a) Top view. (b) Cross section at A-A' line. (c) Fabricated Ge PD.

2.2.7 Setup for transmission spectrum measurement

To evaluate the transmission loss of the fabricated device, the transmission spectrum was measured using the system shown in Fig. 2.16. The output from a tunable wavelength laser (Santec, TSL-210F) was coupled into the device's SSC with TE-polarized mode using 5× and 20× objective lenses after the polarization-maintaining fiber (PMF). To check whether light was coupled into the SSC, the position of the device was adjusted while observing by using an infrared (IR) camera mounted on top of the device and an IR camera on the output side of the SSC. The output light from the SSC was partially coupled into an IR camera and partially into a single-mode fiber (SMF) through an optical system, and the power was observed by using an optical power meter (OPM). The tunable wavelength laser and OPM were connected via GPIB, and the transmission spectrum was measured by controlling the laser and OPM by using a PC program and by observing the power when the wavelength was changed.
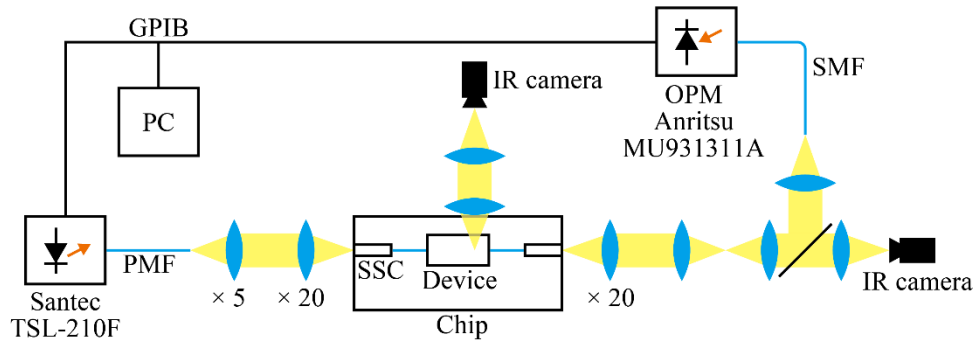
Fig. 2.16 Setup for transmission spectrum measurement.

References

[2-1]   K. Giewont, K. Nummy, F. A. Anderson, J. Ayala, T. Barwicz, Y. Bian, K. K. Dezfulian, D. M. Gill, T. Houghton, S. Hu, B. Peng, M. Rakowski, S. Rauch III, J. C. Rosenberg, A. Sahin, I. Stobert, and A. Stricker, "300-mm Monolithic Silicon Photonics Foundry Technology," IEEE Journal of Selected Topics in Quantum Electronics, vol. 25, no. 5, pp. 1−11, 2019.

[2-2]   S. Y. Siew, B. Li, F. Gao, H. Y. Zheng, W. Zhang, P. Guo, S. W. Xie, A. Song, B. Dong, L. W. Luo, C. Li, X. Luo, and G.-Q. Lo, "Review of Silicon Photonics Technology and Platform Development," J. Lightwave Technol. vol. 39, no. 13, pp. 4374−4389, 2021.

[2-3]   H. Ito, "Wavelength division multiplexing in Si photonics and its applications," Doctoral Dissertation, Yokohama National University, 2019.

[2-4]   Y. Terada, K. Miyasaka, K. Kondo, N. Ishikura, T. Tamura and T. Baba, "Optimized optical coupling to silica-clad photonic crystal waveguide," Opt. Lett., vol. 42, no. 22, pp. 4695−4698, 2017.

[2-5]   R. Shiratori, M. Nakata, K. Hayashi and T. Baba, "Particle swarm optimization of silicon photonic crystal waveguide transitions," Opt. Lett., vol. 46, no. 8, pp. 1904−1907, 2021.

Chapter 3
Subarray Configuration

3.1 Overview

A subarray configuration to suppress the effect of waveguide loss of the PCW was first investigated to improve the transmission and reception characteristics of the PCW optical antenna. When LiDAR applications are considered, the light scattered when the beam hits an object diverges in a hemispherical shape, and the intensity of the light returned to the receiver decreases in proportion to the square of the distance [3-1]. Therefore, PCW should be lengthened to enhance the reception intensity as much as possible. However, the PCW fabricated by silicon photonics usually has a propagation loss of 10 dB/cm order [3-2], which is why the transmission and reception performance is unscalable even if we lengthen the PCW. Therefore, to suppress the total PCW loss in both transmission and reception, this work considers a subarray configuration that consists of a short PCW and a tournament-type splitter composed of low loss Si waveguides and 1 × 2 MMI couplers, as shown in Fig. 3.1 [3-3, 4]. In this chapter, the transmission and reception efficiency of the PCW antenna and beam characteristics of a PCW subarray are calculated theoretically. Findings show that this configuration is effective in improving the transmission and reception characteristics. In addition, this chapter describes the evaluation of beam characteristics and beam scanning with wavelength tuning and thermos-optic control using the fabricated devices.
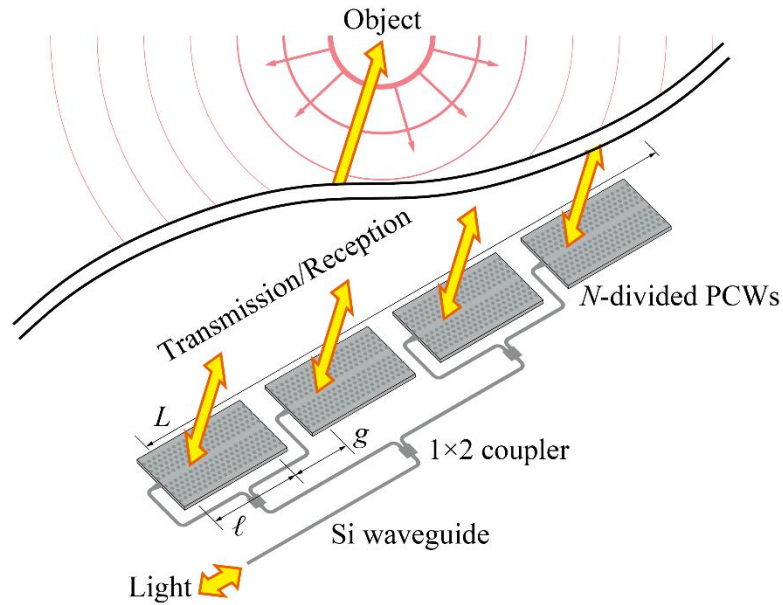
Fig. 3.1 Subarray configuration of PCW optical antenna consisting of *N*-divided PCWs and a tournament-type splitter composed of Si waveguides and 1 × 2 couplers.

3.2 Theoretical Analysis

3.2.1 Transmission and reception efficiency

As shown in Fig. 3.1, a calculation model of the PCW optical antenna that propagates light while radiating it into space is considered, where N is the number of PCW antennas, ℓ is the length of the transmission and reception aperture of each PCW with doubly periodic structure or shallow-etched grating, and g is the gap between the PCWs including the non-radiation area and connection structure between the Si waveguide and the PCW. Therefore, the total length of the subarray is $L = N(\ell + g)$. With the assumption that the radiation coefficient is α_{rad} [cm^{-1}] and the propagation loss of the PCW is α_{loss} [cm^{-1}], the attenuation coefficient of light propagating through the PCW is expressed as $\alpha = \alpha_{rad} + \alpha_{loss}$. When a power of P_0 is input to a PCW of length ℓ, the relationship between the power $P(z)$ at z and the power $P(z + dz)$ at $z + dz$, a small distance dz away, can be expressed as the following equation:

$$P(z+dz) - P(z) \equiv dP = -P(z)(\alpha_{rad} + \alpha_{loss})dz \tag{3.1}$$

With Eq. (3.1) transformed, the following differential equation is obtained:

$$\frac{dP}{dz} = -P(z)(\alpha_{rad} + \alpha_{loss}) \tag{3.2}$$

With Eq. (3.2) solved for $P(z)$, the following equation can be obtained:

$$P(z) = P_0 e^{-(\alpha_{rad}+\alpha_{loss})z} \tag{3.3}$$

The input power to each PCW divided into N is expressed as P_{in}/N, where P_{in} is the input power. The transmission efficiency η_{Tx} for an effective aperture of α_{rad}^{-1} at an ideal PCW with no propagation loss is expressed as

$$\eta_{Tx} = \xi\zeta \frac{\int_0^\ell \alpha_{rad}(P_{in}/N)e^{-(\alpha_{rad}+\alpha_{loss})z}dz}{\int_0^\infty \alpha_{rad}(P_{in}/N)e^{-\alpha_{rad}z}dz} = \xi\zeta\left(\frac{\alpha_{rad}}{\alpha_{rad}+\alpha_{loss}}\right)\left[1 - e^{-(\alpha_{rad}+\alpha_{loss})\ell}\right] \tag{3.4}$$

where ξ is the efficiency of inputting light to each PCW via a tournament-type splitter that consists of a Si waveguide and a 1 × 2 coupler, and ζ is the ratio of upper and lower radiation in the PCW. With the propagation loss of the Si waveguide and the loss per 1 × 2 coupler defined as α_{SiWG} [cm^{-1}] and A [dB], respectively, ξ can be expressed as

$$\xi = e^{-\alpha_{SiWG}(N-1)(\ell+g)} \cdot 10^{-\frac{A\log_2 N}{10}} \tag{3.5}$$

$\alpha_{SiWG} = 1$ dB/cm = 0.23 cm^{-1} and A = 0.1 dB were assumed. For a vertically symmetric structure such as a doubly periodic structure, $\zeta = 0.5$. However, for a vertically asymmetric structure such as a shallow-etched grating, ζ is larger than 0.5 [3-5]. For simplicity, $\zeta = 1$ is assumed here. Figure 3.3 shows the calculated transmission efficiency and transmission loss when $g = 30$, $\alpha_{rad} = 100$ dB/cm = 23.0 cm^{-1}, and $\alpha_{loss} = 35$ dB/cm = 8.05 cm^{-1}. The maximum transmission efficiency is 74% when $N = 1$ and L is

greater than 0.1 cm. As N increases, L becomes larger where the efficiency is maximized, and the maximum value becomes smaller than when $N = 1$ because the Si waveguide and coupler losses are increased. When a subarray configuration is introduced, the length of each PCW needs to be set so that enough light is radiated according to the radiation coefficient.

Next, the reception efficiency and the reception intensity are calculated. Transmission efficiency corresponds to reception efficiency. Therefore, for the power density p_{ret} of the light returned to the PCW, which was assumed to be a plane wave, with the power of the light coupled into the effective aperture of α_{rad}^{-1} defined as $P_{\text{ret}} = p_{\text{ret}}\alpha_{\text{rad}}^{-1}$ using the power P_{Rx} received at the PCW, the reception efficiency η_{Rx} is expressed as

$$\eta_{\text{Rx}} = \frac{P_{\text{Rx}}}{P_{\text{ret}}} = \frac{\xi\zeta\alpha_{\text{rad}}}{\alpha_{\text{rad}} + \alpha_{\text{loss}}}\left[1 - e^{-(\alpha_{\text{rad}} + \alpha_{\text{loss}})\ell}\right] \tag{3.6}$$

The efficiency of light coupled into N-divided PCW is expressed by the following equation:

$$\eta_{\text{Rx}} = \frac{P_{\text{Rx}}}{p_{\text{ret}}\ell} = \frac{N\xi\zeta}{(\alpha_{\text{rad}} + \alpha_{\text{loss}})\ell}\left[1 - e^{-(\alpha_{\text{rad}} + \alpha_{\text{loss}})\ell}\right] \tag{3.7}$$
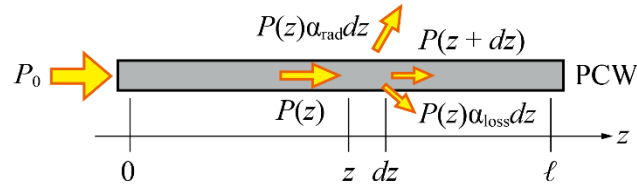
Fig. 3.2 Calculation model for transmission and reception efficiency of PCW antenna.
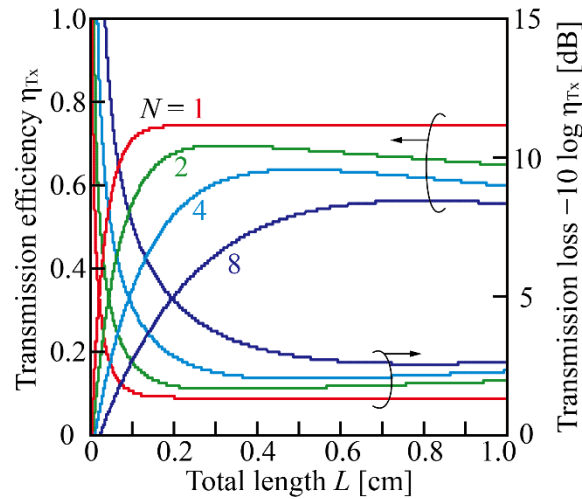
Fig. 3.3 Transmission efficiency η_{Tx} calculated with the total length of the PCW subarray. The vertical axis on the right side shows the transmission loss.
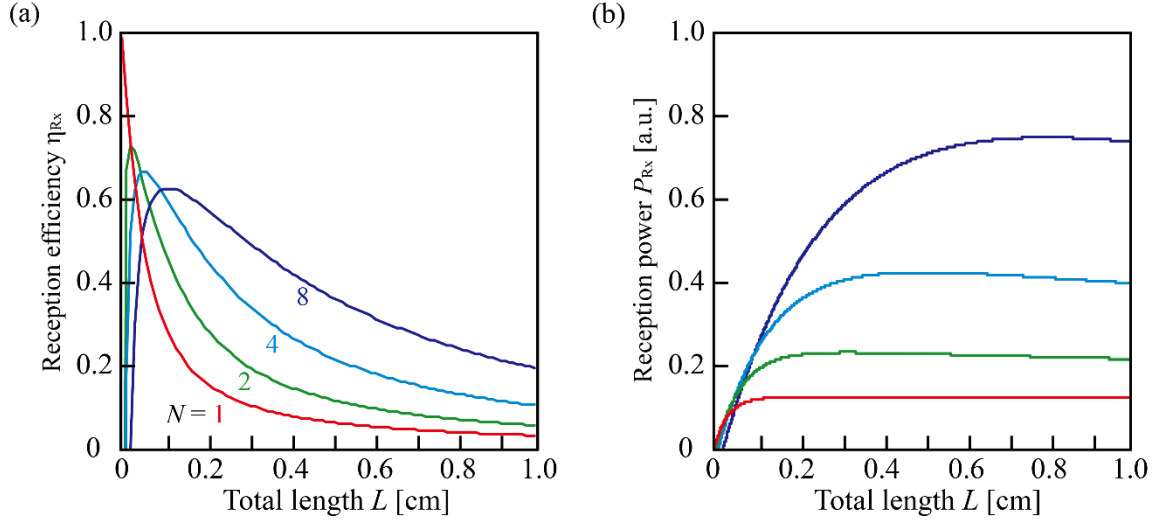
Fig. 3.4 (a) Reception efficiency and (b) reception power calculated with total length of the PCW subarray.

Figure 3.4 shows the reception efficiency and intensity calculated from Eq. (3.7). As L increases, the effect of waveguide loss increases, and the reception efficiency decreases regardless of N. However, the decrease in efficiency is mitigated by the fact that each PCW is shortened by dividing the PCW, thus suppressing the effect of waveguide loss. The reception intensity also saturates at $L = 0.1$ cm when $N = 1$, and lengthening the PCW further will not increase the intensity and take advantage of the aperture. However, the saturation of the intensity can be mitigated by increasing the length of the antenna while dividing it into subarrays, thus scaling the reception performance of the PCW antenna, where the intensity increases up to 3.4 and 5.3 times larger than $N = 1$ for $N = 4$ and 8, respectively.

3.2.2 Beam characteristics

This section describes the beam characteristics of the PCW antenna in transmission. In the previous section, how much power is radiated relative to the input light in transmission and is received when a plane wave with a constant intensity distribution is coupled into the PCW in reception was calculated. Knowing what the beam characteristics are is important. Considering LiDAR application, the beam hits an object and some of the scattered light returns to the PCW. A narrow beam shape that concentrates the power as much as possible is desirable for transmission, thereby increasing the number of resolution points.

The far-field intensity distribution of light emitted from an N-divided PCW subarray can be calculated from the guided mode light intensity in the waveguide, as shown in Fig. 3.5, and is expressed as follows for angle θ:

$$I(\theta) = \left| \sum_{n=0}^{N-1} \int_{n(\ell+g)}^{\ell+n(\ell+g)} E(z) e^{-jk_0 z \sin(\theta - \theta_{\mathrm{rad}})} dz \right|^2 \tag{3.8}$$

,where $k_0 = 2\pi/\lambda$ is the wavenumber of propagation light in space, θ_{rad} is the principal radiation angle of the beam, and $E(z)$ is the near-field electric field intensity distribution of guided mode in the PCW. From this relationship of $P(z) = |E(z)|^2$, Eq. (3.8) can be rewritten as

$$I(\theta) = \left| \sum_{n=0}^{N-1} \int_{n(\ell+g)}^{\ell+n(\ell+g)} \sqrt{\alpha_{\text{rad}} P_{\text{in}}} e^{-(\alpha_{\text{rad}}+\alpha_{\text{loss}})(z-n(\ell+g))} e^{-jk_0 z \sin(\theta-\theta_{\text{rad}})} dz \right|^2 \tag{3.9}$$

With the use of $\theta = \theta - \theta_{\text{rad}}$ for simplicity, Eq. (3.9) can be rewritten as follows:

$$I(\theta) = \frac{2\alpha_{\text{rad}} P_{\text{in}}}{(\alpha/2)^2 + (k_0 \sin\theta)^2} e^{-\alpha\ell/2} \left\{ \cosh(\alpha\ell/2) - \cos(\ell k_0 \sin\theta) \right\} \frac{\sin^2\left[\frac{N}{2}(\ell+g)k_0 \sin\theta \right]}{\sin^2\left[\frac{1}{2}(\ell+g)k_0 \sin\theta \right]} \tag{3.10}$$

If the terms in Eq. (3.10) are set as follows:

$$F_{\text{element}} = \frac{2\alpha_{\text{rad}} P_{\text{in}}}{(\alpha/2)^2 + (k_0 \sin\theta)^2} e^{-\alpha\ell/2} \left\{ \cosh(\alpha\ell/2) - \cos(\ell k_0 \sin\theta) \right\} \tag{3.11}$$

$$F_{\text{array}} = \frac{\sin^2\left[\frac{N}{2}(\ell+g)k_0 \sin\theta \right]}{\sin^2\left[\frac{1}{2}(\ell+g)k_0 \sin\theta \right]} \tag{3.12}$$

Then $I(\theta)$ can be expressed as the product of F_{element} and F_{array}, which are called the element factor and the array factor, respectively.

$$I(\theta) \approx \frac{2\alpha_{\text{rad}} P_{\text{in}}}{(\alpha/2)^2 + (k_0 \sin\theta)^2} e^{-\alpha\ell/2} \left\{ \cosh(\alpha\ell/2) - \cos(\ell k_0 \sin\theta) \right\} N^2 \tag{3.13}$$

The calculated distribution of the guided mode intensity and beam characteristics for different N subarrays are shown in Fig. 3.6, where $L = 0.4$ cm and wavelength $\lambda = 1550$ nm, normalized by the value obtained by substituting $\theta = 0$ into Eq. (3.13). The intensity disappears at $L = 0.2$ cm and the aperture length cannot be fully utilized when $N = 1$. Therefore, the beam characteristics are determined only by the combined coefficient of radiation and propagation loss. When $N = 2$, the effect of the element factor in addition to the element factor is multiplied, resulting in a smaller beam divergence. Sidelobes derived from the grating lobe of the array factor are generated. As N increases, the pitch between each PCW becomes narrower and the grating lobes move away from the center, thereby suppressing of the sidelobes by multiplying by the element factor.

The calculated beam divergence for the total length of the PCW array and the radiation coefficient are shown in Fig. 3.7, where beam divergence was evaluated as the full width at half maximum. At $N = 1$, the beam divergence decreases as L increases. However, it saturates at $L = 0.3$ cm due to the propagation loss, and the beam divergence does not change even if the L is lengthened further. The array factor is dominant in a subarray configuration, which is why the beam divergence can be reduced while taking advantage of the aperture length. The beam divergence does not change significantly with respect to the radiation coefficient. Thus, the radiation coefficient should be set to ensure a large transmission efficiency in the device design.
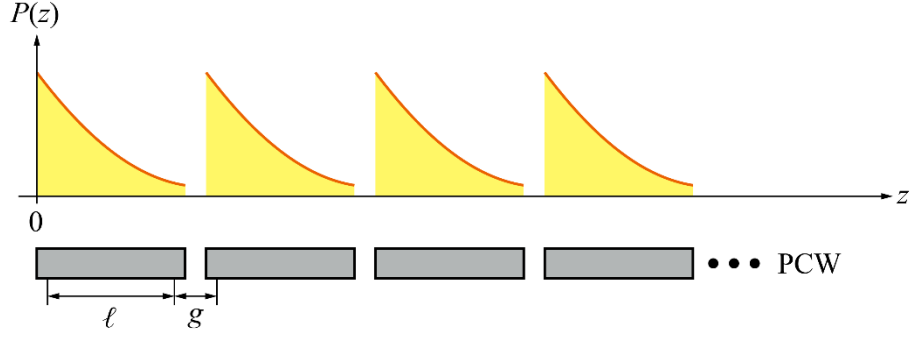
Fig. 3.5 Calculation model of guided mode intensity in the PCW subarray.
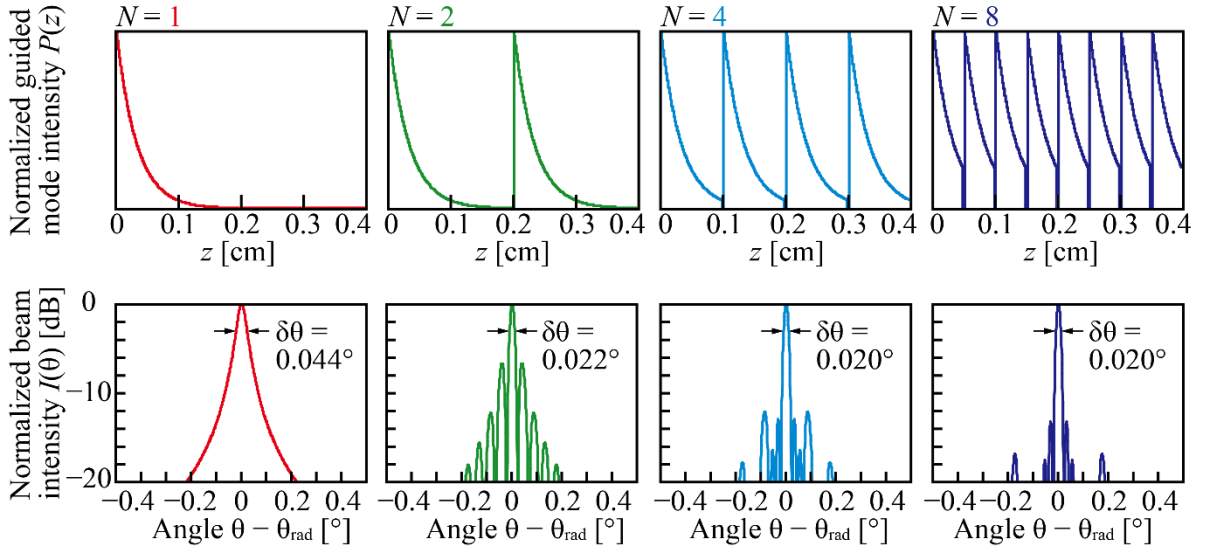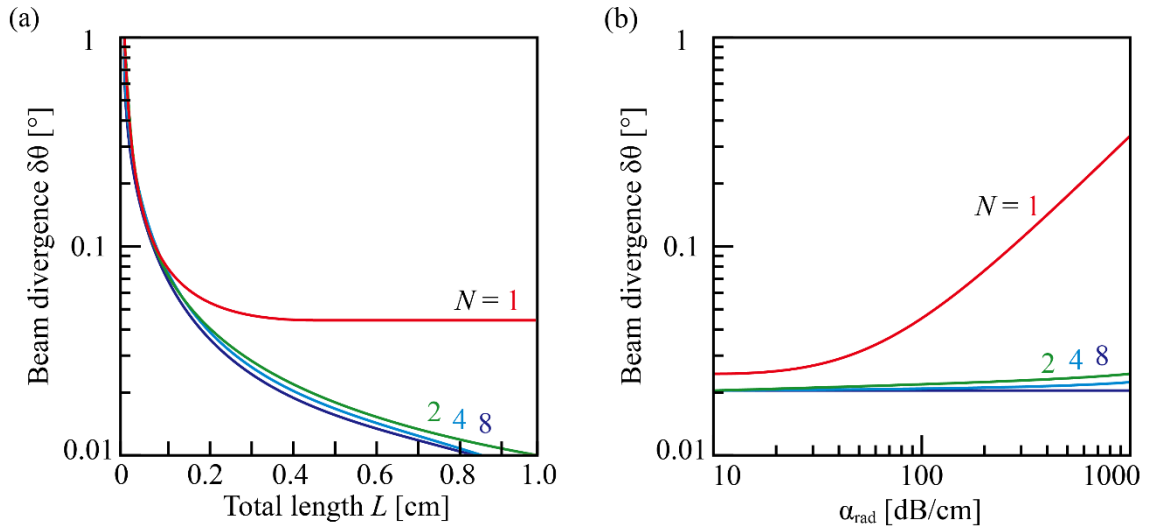

Fig. 3.6 Normalized guided mode intensity and beam intensity calculated with PCW subarrays with different N.

Fig. 3.7 Beam divergence calculated with (a) total length of the PCW subarray and (b) radiation coefficient.

Next, the sidelobe level in a subarray configuration is discussed. Figure 3.8 shows the calculated beam profiles with each length of the PCW ℓ when $\alpha_{rad} = 100$ dB/cm, $\alpha_{loss} = 30$ dB/cm, $g = 38$ μm, where $\ell = 0.2$ mm to 1.2 mm is varied by 0.2 mm. The calculation results show that the beam is formed by the product of the beam shape determined by ℓ (element factor) and the array factor determined by N. As ℓ increases, the width of the main beam, which is the zeroth-order diffraction beam, decreases, while the grating lobes due to the array factor move closer to the main beam as the pitch between the arrays increases. The element factor no longer suppresses the grating lobes sufficiently, thus resulting in larger sidelobes. In general, optical phased arrays have a wide element factor. Therefore, the effect of grating lobes cannot be ignored. In this configuration, however, because the beam divergence is about 0.1° at $\ell = 1$ mm, which means that the element factor is relatively narrow, the advantage is that grating lobes can be suppressed and the field of view is not limited when the beam is scanned.

Figure 3.9 shows the calculated beam divergence and sidelobe level with ℓ. The sidelobe level is evaluated by the intensity of the next largest peak after the main peak. For $N = 1$, the beam divergence decreases with increasing ℓ, while the sidelobe level gradually increases because the peak of the first-order sidelobe increases as the beam moves closer to the main beam. As ℓ is lengthened from 1.5 mm, the peak value becomes smoother, and the sidelobes are shifted to the second and third orders, further away from the main beam, resulting in a narrower beam and smaller sidelobes. In contrast, for $N = 2$ and 4, the sidelobes increase because the grating lobes by the array factor approaches the main beam side as ℓ increases. Therefore, the length of each PCW needs to be set in such a way that the sidelobe level becomes small to expand the aperture of a PCW optical antenna in a subarray configuration.

To evaluate the aperture efficiency of the subarray configuration, the directive gain was calculated from the beam divergence. The directivity gain G_d can be approximated by the following equation when the beam divergence in the waveguide direction and orthogonal direction of the PCW are $\delta\theta$ and $\delta\varphi$, respectively.
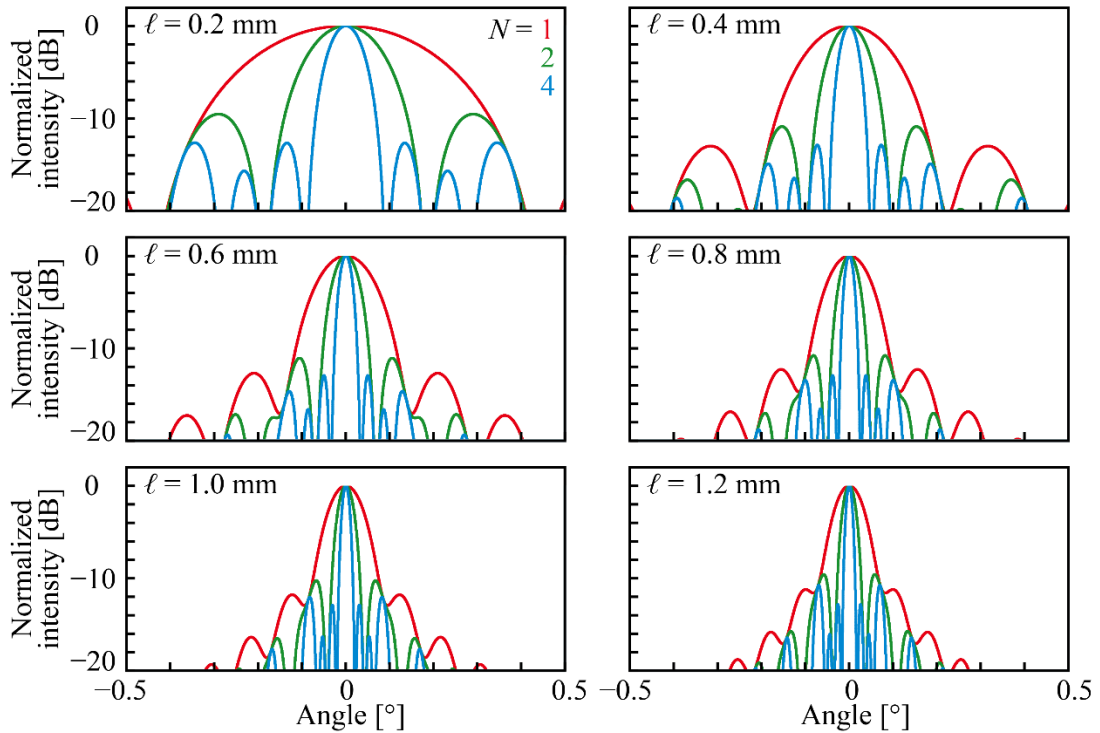
Fig. 3.8 Beam profile calculated with each length of PCW.

$$G_{\mathrm{d}} \approx \frac{4\pi}{\delta\theta\delta\varphi} \qquad (3.14)$$

Figure 3.10 shows the directive gain for the total length calculated from Eq. 3.14 when $\alpha_{\mathrm{rad}} = 100$ dB/cm, $\alpha_{\mathrm{loss}} = 35$ dB/cm, and $\delta\varphi = 30°$. For $N = 1$, the directive gain saturates because the aperture cannot be utilized due to waveguide propagation loss, and the beam divergence does not narrow even if L is lengthened. If the directive gain of an antenna with a uniform radiation aperture distribution is G_{u}, the aperture efficiency is defined as follows:

$$\eta_{\mathrm{a}} = \frac{G_{\mathrm{d}}}{G_{\mathrm{u}}} \qquad (3.15)$$

Figure 3.11 shows the aperture efficiency for the total length calculated from Eq. 3.15. For simplicity, we assume $\zeta = 1$ here. When $N = 1$, the maximum value is obtained at $L = 0.1$ cm. However, as N is increased, L, where the efficiency is maximum, becomes longer. Therefore, α_{rad} must be set appropriately to maximize η_{a}.
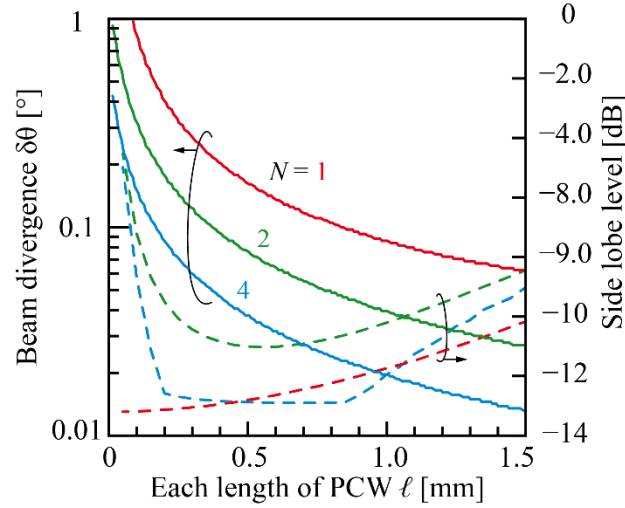
Fig. 3.9 Beam divergence and side lobe level calculated with each length of PCW.
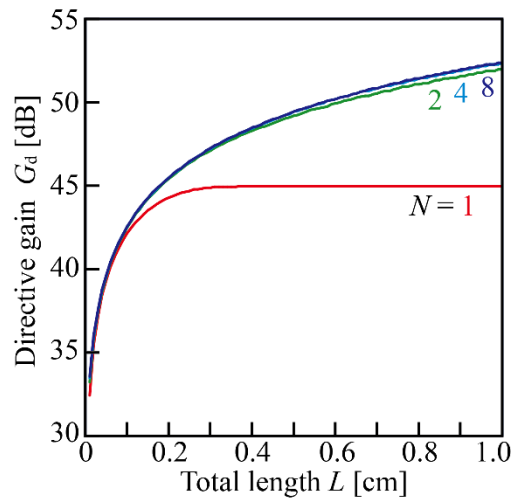
Fig. 3.10 Directive gain calculated with total length of the PCW subarray.
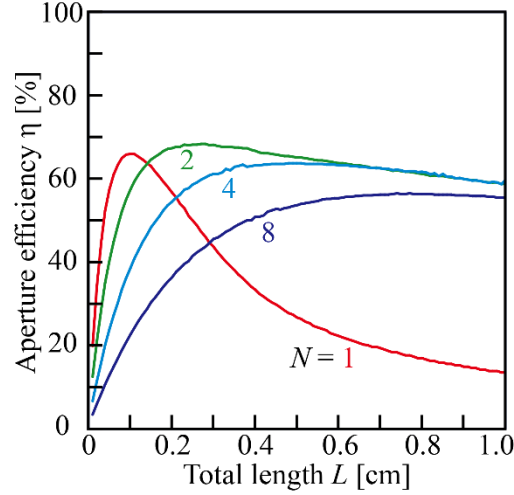
Fig. 3.11 Aperture efficiency calculated with total length of the PCW subarray.

3.3   Evaluation of Beam Profile

3.3.1   Fabricated devices

To evaluate the beam profile of the PCW optical antenna in a subarray configuration, devices were fabricated at Foundry B. The CAD layout of the fabricated devices is shown in Fig. 3.12. A normal PCW optical antenna with $N = 1$ and PCW optical antenna subarrays with $N = 2$ and 4 were designed. The doubly periodic structure was adopted as a radiation structure with $\ell = 1.17$ mm for $N = 1$ and $\ell = 0.97$ mm for $N = 2$ and 4. The input light was coupled into the PCW through the tapered structure of the Si waveguide and the PCW, as shown in Fig. 3.13(a). The design parameters of the PCW were $a = 400$ and $s_3 = 95$ nm. Twelve rows of photonic crystal holes were arranged from the line defects in the PCW, with the outer Si slab being doped with n^+ to absorb light and thus prevent the light leaking from the PCW from creating extra reflections. The end of the PCW was also doped with n^+, as shown in Fig. 3.13(b). The tapered structure of the PCW is followed by about 10 rows of circular holes in a regular PCW without a radiation mechanism. The parameters in the doubly periodic structure were $r_1 = 234$ nm and $r_2 = 219$ nm. For devices with $N = 2$ and 4, TiN heaters were provided on both sides of the PCW so that each PCW can be heated individually, as shown in Fig. 3.14. The gap between the PCWs had a tapered or bending structure of the Si waveguide and was designed to have a certain margin to avoid optical crosstalk, where the gap g between the radiation aperture was 38 μm. Fig. 3.15(a) shows a microscopic image of the fabricated device, and Fig. 3.15(b) shows an image of the doubly periodic structure of the PCW observed with a confocal laser microscope.

The wafer of the device fabricated at Foundry B has a mirror surface on the backside. The light emitted downward from the PCW optical antenna is reflected on the backside and interferes with the light emitted from the top surface, thereby affecting the beam profile. Therefore, the beam characteristics were improved by forming a rough surface on the backside of the chip by backside polishing. The tool shown in Fig. 3.16 was used for backside polishing. The polishing procedure is shown in Fig. 3.17. First, the tool used to fix the chip was heated with a heater to melt the wax, and then the surface of the chip was attached to the waxed area. After cooling and removing excess wax with dichloromethane, the chip was fixed with another tool and polished on a glass plate with a water-soluble abrasive. After polishing, the tool was again heated by a heater and the chip was removed. To remove wax from the chips, the chips were first heated in dichloromethane at 100 °C for 5 minutes, replaced with acetone three times, heated in resist stripper at 200 °C for 5 minutes, replaced with xylene three times, replaced with acetone

three times, and replaced with methanol three times. After polishing, a rough surface was formed on the chip, as shown in Fig. 3.17(g).
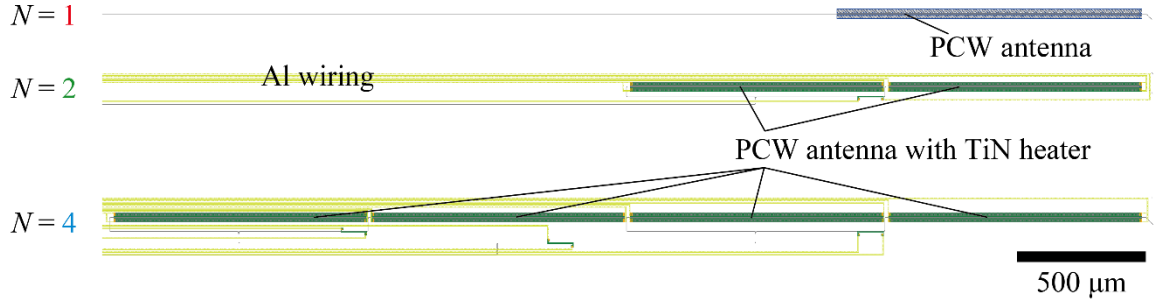

Fig. 3.12 CAD layout of PCW antenna ($N = 1$) and PCW antenna subarrays ($N = 2, 4$).
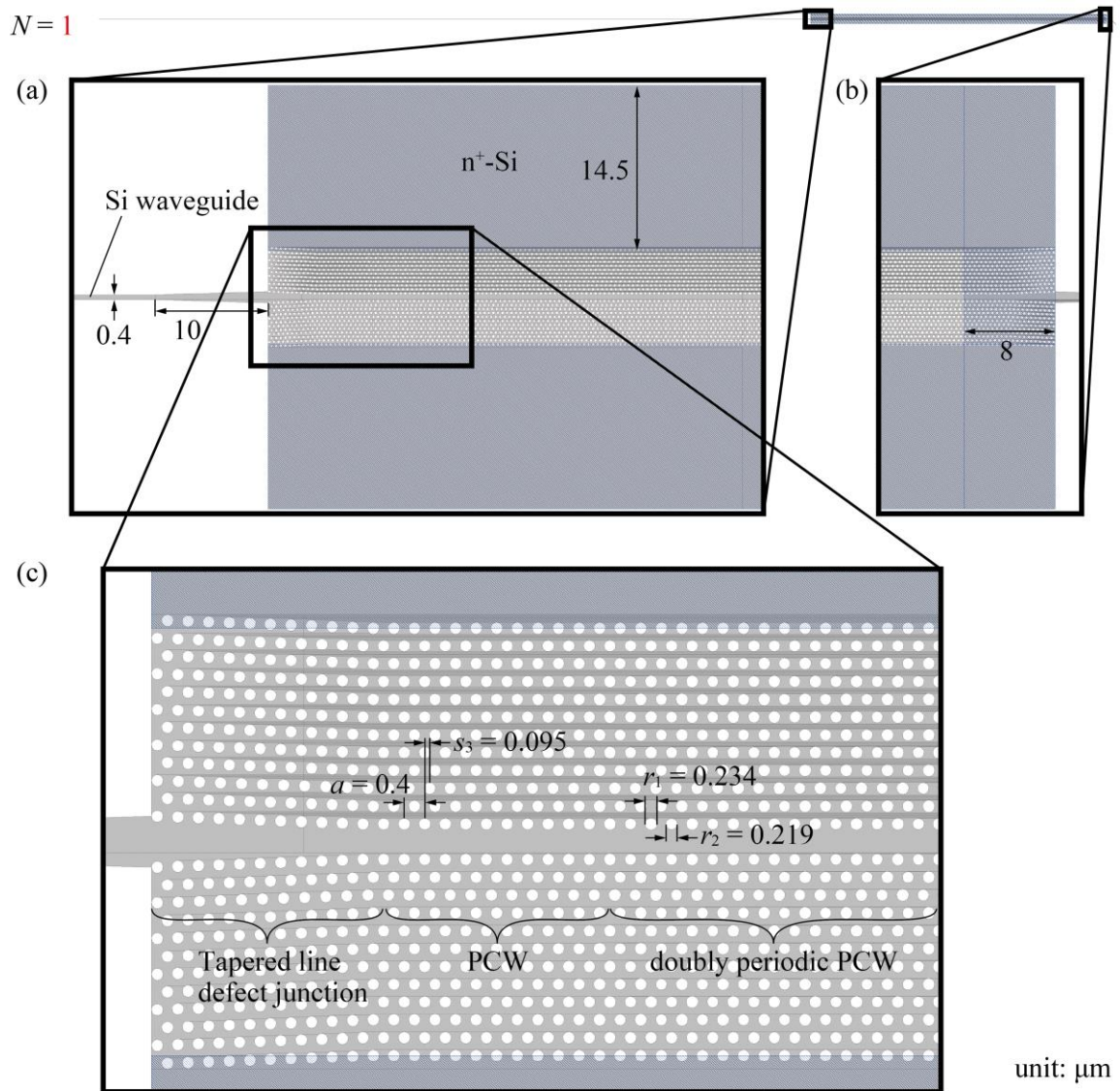

Fig. 3.13 CAD layout of PCW antenna ($N = 1$). (b) Input part of PCW antenna. (b) End part of PCW antenna. (c) Connection structure of PCW antenna between Si waveguide and PCW.
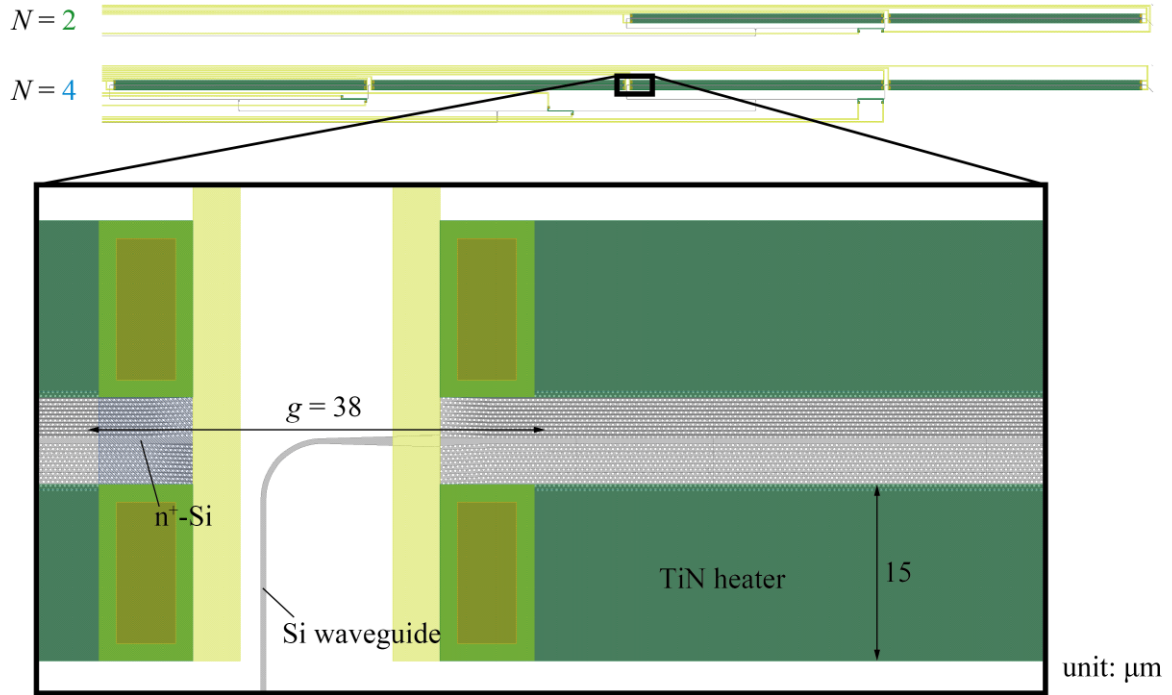
Fig. 3.14 CAD layout of PCW antenna arrays. The inset shows the magnified view of the gap between PCW antennas.
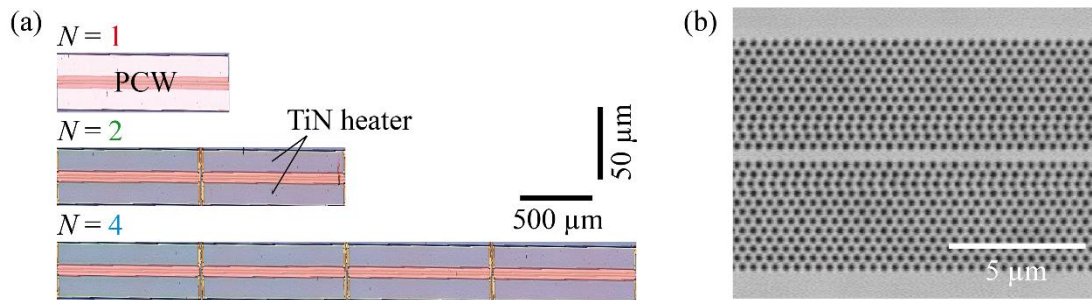
Fig. 3.15 (a) Fabricated devices. (b) Doubly periodic PCW observed by the confocal laser microscope.
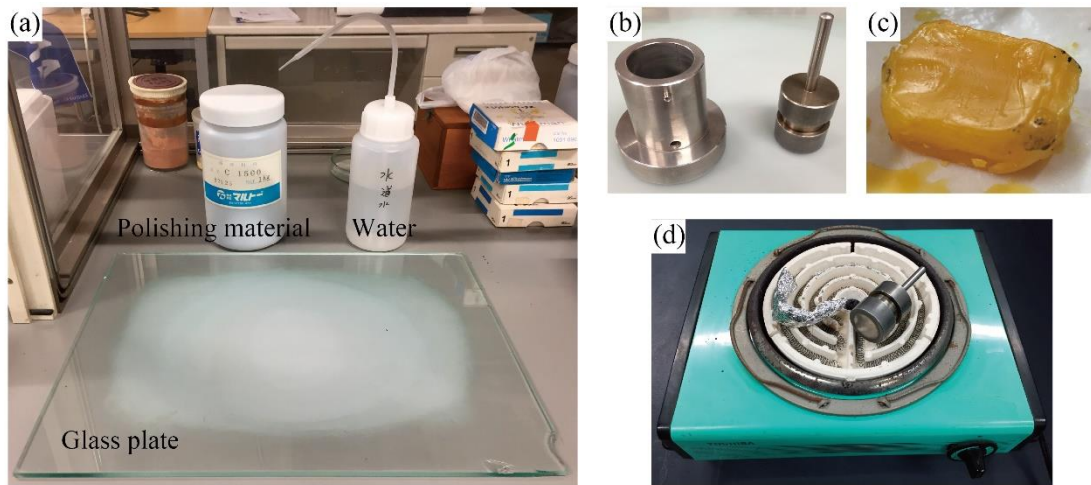
Fig. 3.16 (a) Workspace for polishing the backside of the chip. (b) Polishing tools. (c) Wax for fixing the chip to the tool. (d) Heater to melt the wax.
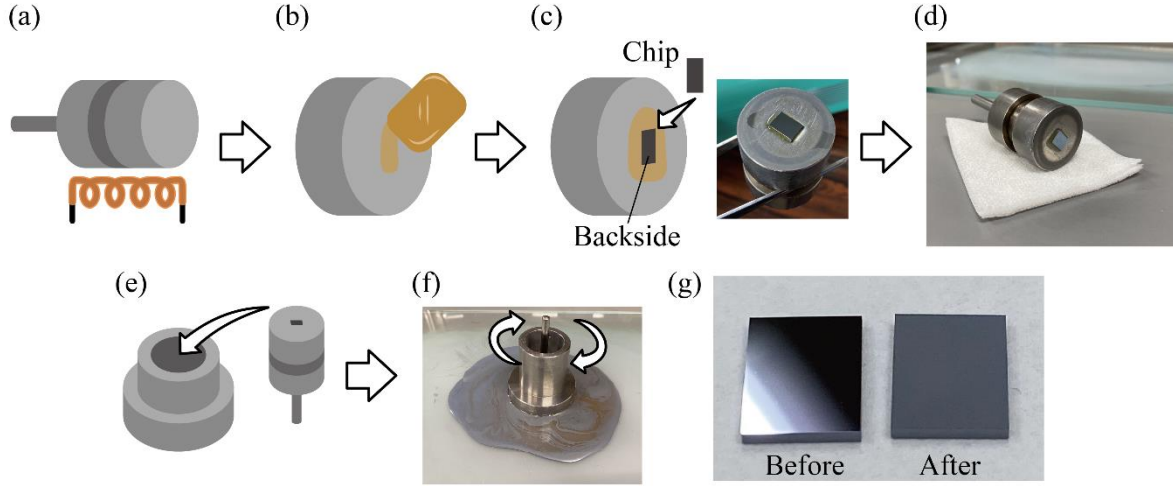
Fig. 3.17 Procedure of polishing the backside of the chip. (a) Heating the tool for melting the wax. (b) Melting the wax. (c) Attaching the front of the chip to the wax. (d) Cooling the tool. (e) Assembling the tools. (f) Dissolving abrasive powder in water and polish. (g) Comparison of backsides of the chips before and after polishing.

3.3.2 Setup for observing beam profile

Two main methods were used to observe the beam profile of the PCW antenna. One is a combination of lens-based optics, as shown in Fig. 3.18, and the other is a direct observation of the beam profile in the far field by illuminating the beam on a screen, as shown in Fig. 3.19.

In the former method, the output light from the tunable wavelength laser (Santec, TSL-550) was coupled into the SSC of the device by using a lensed fiber. The light radiated from the PCW was split through an objective lens into near-field pattern (NFP) and far-field pattern (FFP) optics, and observed by an InGaAs camera. NFP optics was used to align the light coupling from the lensed fiber into the SSC and to check the near-field image of radiation from the PCW. The FFP optics incorporates an fθ lens that converts the beam angle into a focal position, allowing the far-field image of the beam to be observed with a camera. This optics can be fully tilted, allowing the entire camera to be adjusted to the beam angle for observation. In observing the beam profile in this optics, the NA of the objective lens mounted above the device limits the observation range. The beam profile of light radiated in the range of about 600 μm in the near field can be observed in this system. Therefore, the beam profile could not be observed accurately in this system because the device fabricated in this study had an aperture of 1 mm or larger.

In the latter method, the beam profile was evaluated by illuminating the beam onto a screen and observing the scattered light directly with an InGaAs camera, as shown in Fig. 3.19. A collimator lens was inserted to convert the beam emitted from the PCW from a beam expanding in the orthogonal direction of the PCW to a collimated beam, and a mirror was used to change the optical axis and aim the beam at the screen. The beam profile was obtained through angular conversion of the distance between pixels in the image acquired by the camera after the distance from the device to the screen was measured, where the screen needs to be placed far enough away so that the distance is in the far-field area relative to the aperture length of the device.
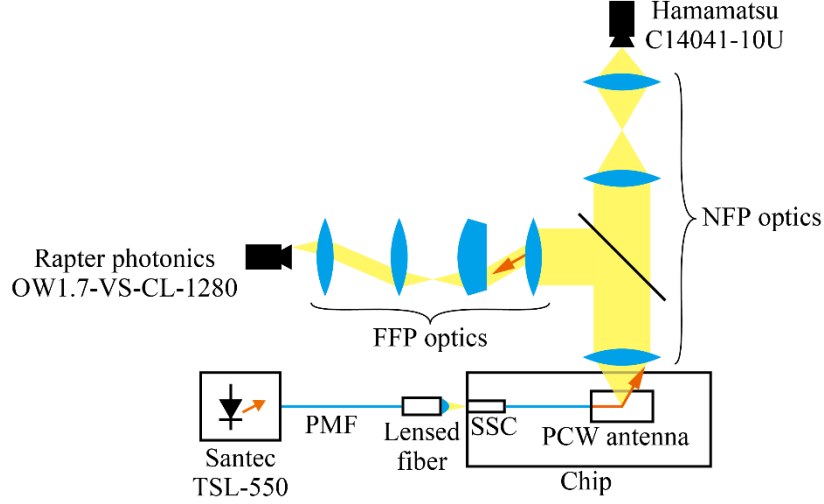
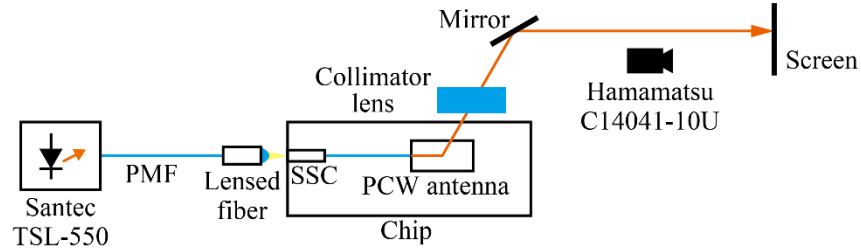Fig. 3.18 Setup for observing the beam profile using FFP optics.

Fig. 3.19 Setup for directly observing the beam profile using the screen.

3.3.3 Beam profile

The beam profiles and beam scanning were demonstrated with $N = 2$ PCW subarrays using the measurement system shown in Fig. 3.20. As shown in Fig. 3.21, the PCW subarray radiated a beam into space through a collimator lens, and a mirror was redirected the optical axis to hit an acrylic screen, where a cylindrical lens (Thorlabs, LJ1878L2-C) with a focal length of 10 mm was used as a collimator lens, and transmitted light was observed from the opposite side of the screen 250 cm away from the devices with an InGaAs camera. In the PCW subarray, each PCW is equipped with a TiN heater, and when voltage is applied to S_1 and S_2, respectively, the PCWs can be heated individually. G was connected to ground, and a DC voltage source was connected via a DC probe to control the TiN heater.

Figure 3.22 shows a superimposition of photographs taken by an InGaAs camera after 1D beam scanning by changing the wavelength from 1549 nm to 1577 nm in 1 nm steps. The beam spot scanned with and without TiN heater control are shown, and beam scanning was realized with a field of view of nearly 30°, where the collimator lens was adjusted so that the focal length was 10 mm for each beam. The beam profiles corresponding to these beam spots are shown in Fig. 3.23. Without heater control, sidelobes strongly appeared; with heater control, sidelobes were suppressed and the beam divergence was narrower in each beam angle. The sidelobes tend to be larger at longer wavelengths than at shorter because the group index near the band edge is larger and more sensitive to fabrication errors of the photonic crystal.
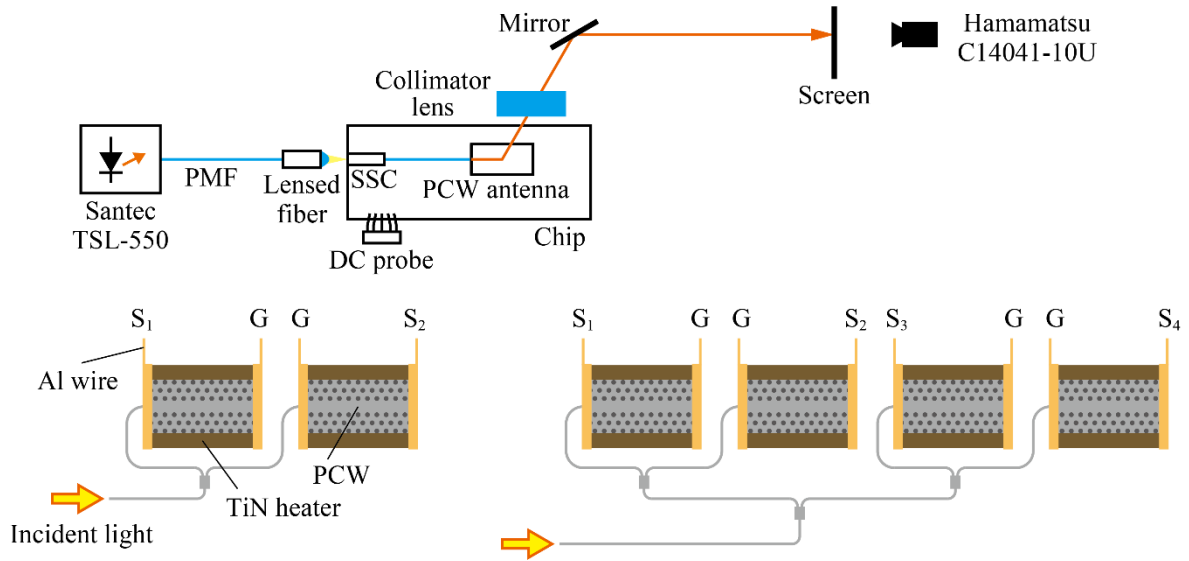
Fig. 3.20 Setup for observing the beam profile of PCW arrays.
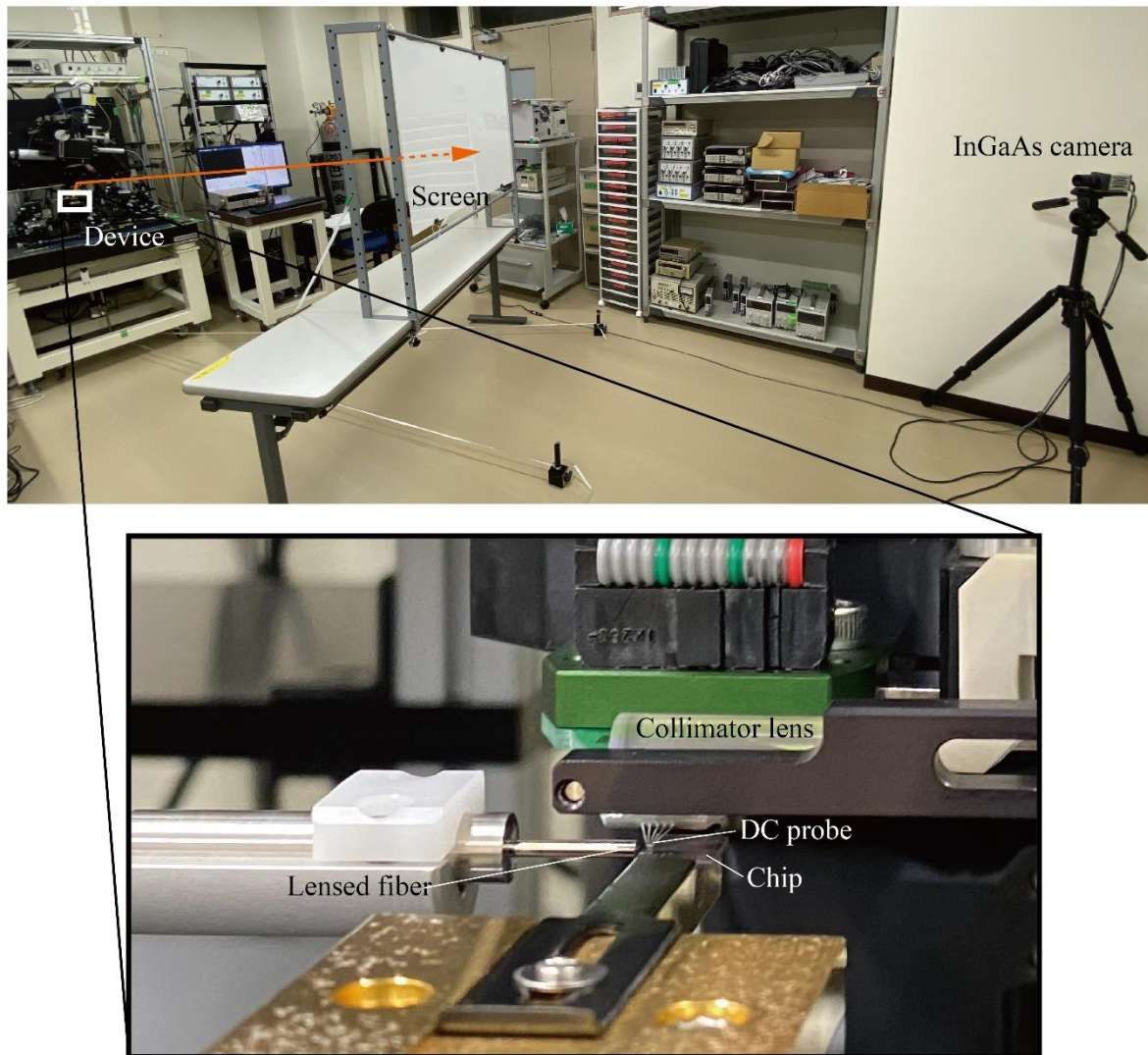
Fig. 3.21 Setup for observing the beam profile through the screen by using an InGaAs camera. Inset shows the magnified view of the setup around the chip.

(a)

(b)

5°
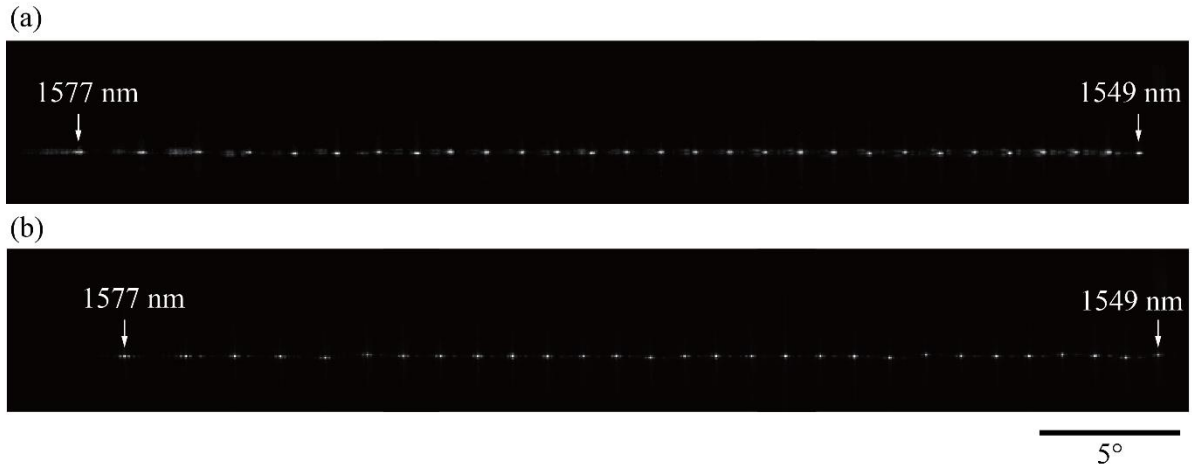
Fig. 3.22 Beam spots obtained by InGaAs camera when changing the wavelength of the input light. (a) without heater control. (b) with heater control.
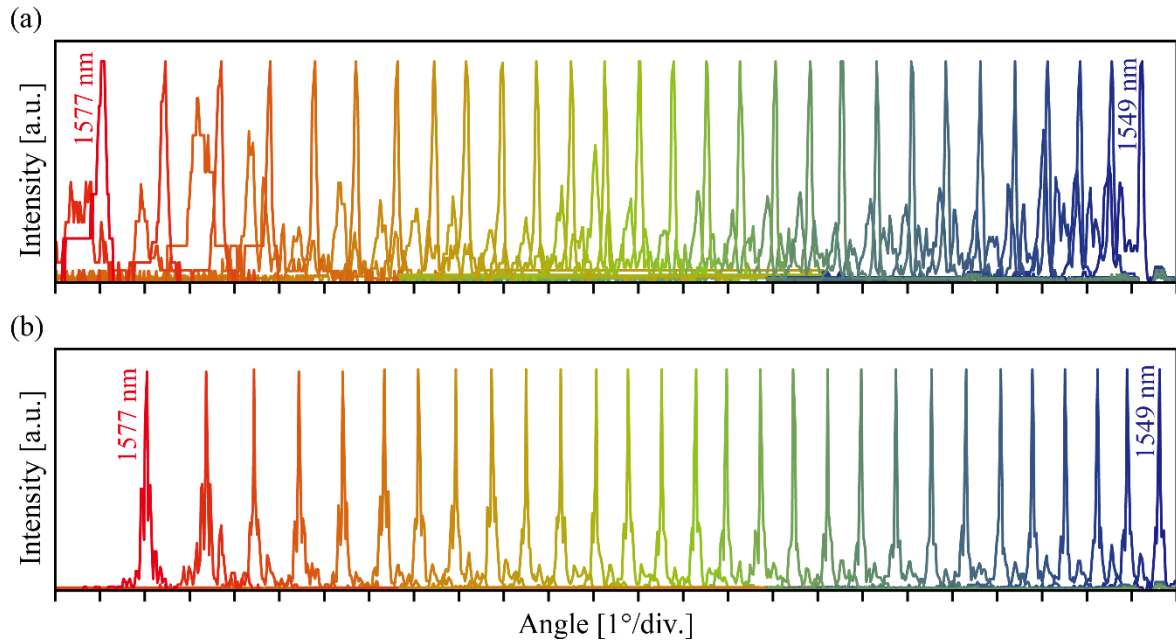
(a)

(b)

Angle [1°/div.]

Fig. 3.23 Beam profiles. (a) without heater control. (b) with heater control.

Figure 3.24 shows a graph that compares the beam profile before and after heater control at a wavelength of 1559 nm. Before the control, the beam was split due to non-uniformity during fabrication. However, a profile with a beam divergence of 0.053°, which was close to the theoretical value of 0.041°, was obtained after the control. Figure 3.25 compares the beam divergences of all beam spots before and after heater control. Before the heater control, most of the beams exceeded 0.1°; after the heater control, the average value was 0.06°. The applied voltage at each spot during control is shown in Fig. 3.26. The applied voltage was increased because the beam splitting tended to widen at longer wavelengths.

(a)

(b)
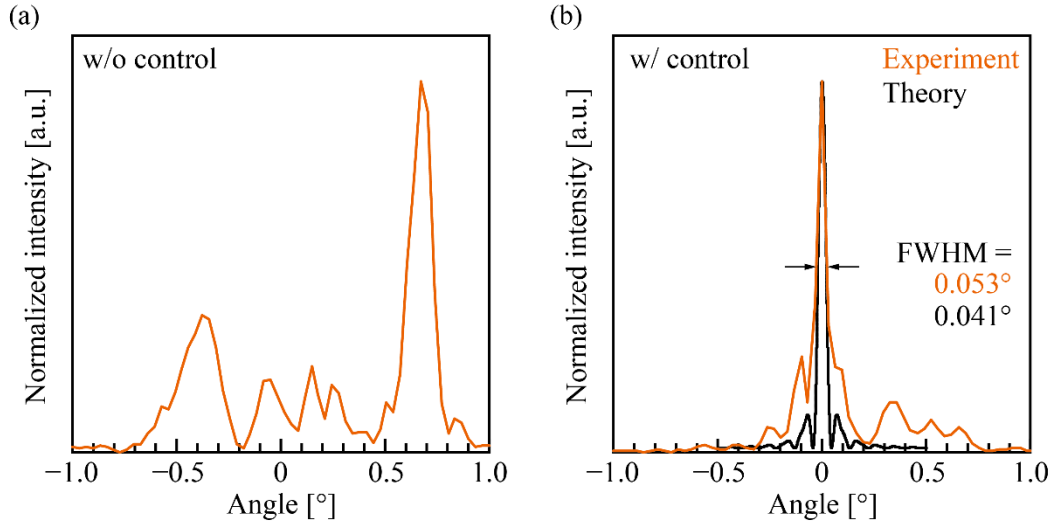
Fig. 3.24 Beam profiles at wavelength of 1559 nm (a) without heater control and (b) with heater control.
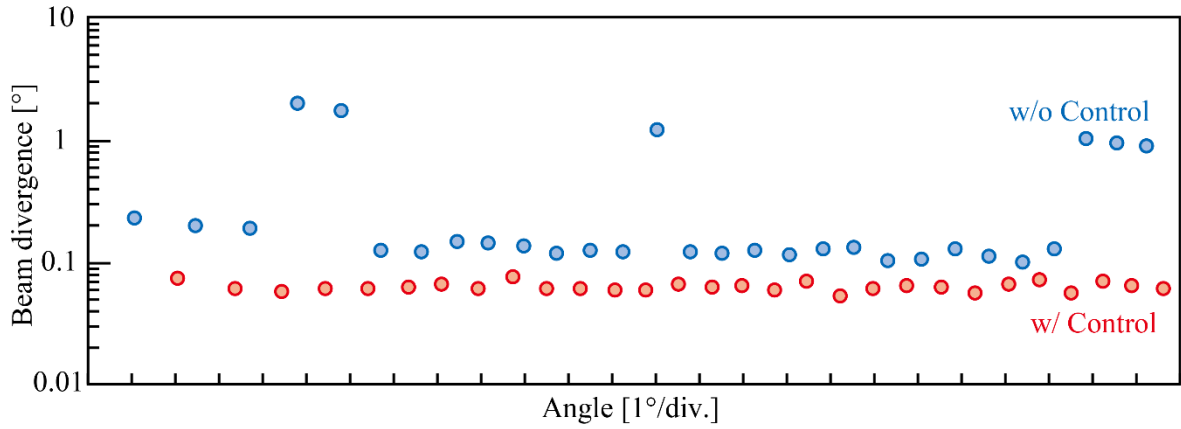
Fig. 3.25 Beam divergence at each wavelength with and without heater control.
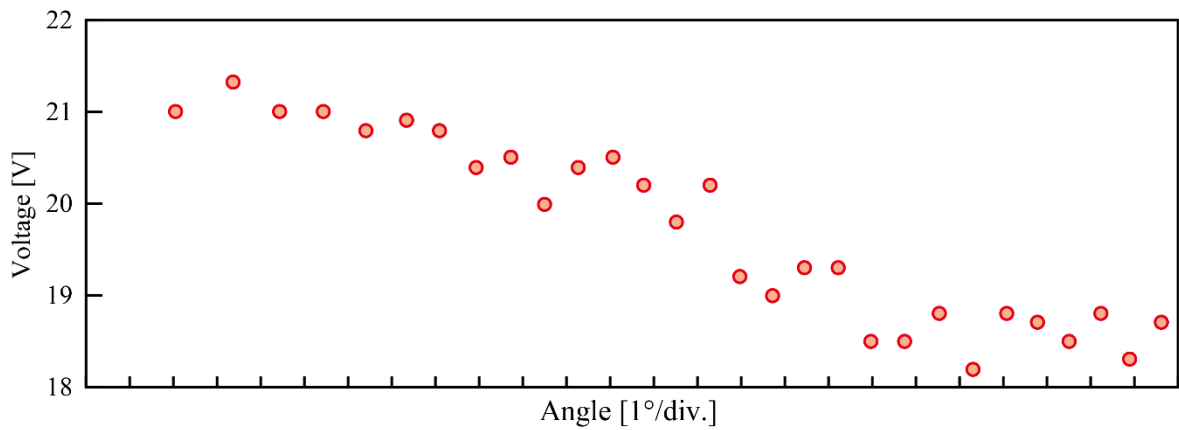
Fig. 3.26 Applied voltage at each beam spot when controlling the heater.

Next, the beam profiles of the PCW subarrays with $N = 1$, 2, and 4 were compared. The beam profile was observed using the measurement system shown in Fig. 3.27, and FMCW LiDAR transmission and reception experiments were implemented using the same system described in the next chapter. The $N = 4$ device had a radiation aperture of about 4 mm with an operation wavelength of 1555 nm, resulting in

a required distance of about 10 m to obtain a far-field beam. Therefore, the beam profile was observed at a distance of 10.6 m from the device. A cylindrical lens (Thorlabs, LJ1728L1-C) with a focal length of 50 mm, as shown in Fig. 3.28(a), was used as the collimator lens. As shown in Fig. 3.28(b), the beam was focused on the filter paper and the scattered light was observed by an InGaAs camera to obtain a beam profile. The beam shape was disrupted by a slight shift in the radiation angle of each PCW due to non-uniformity during fabrication. Therefore, TiN heaters were used to adjust the beam to maximize the maximum peak intensity. Table 3.1 shows the voltage applied to each TiN during adjustment.

Fig. 3.27 Setup for observing beam profiles of PCW arrays.
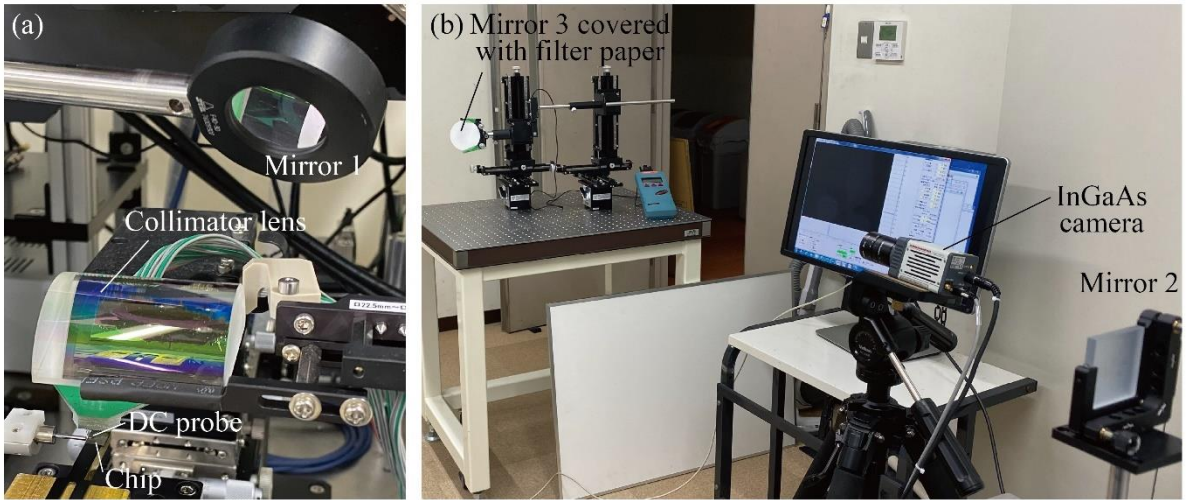
Fig. 3.28 (a) Collimator lens and mirror mounted above the chip. (b) Beam profiles were obtained by observing the light scattered at the filter paper by using an InGaAs camera.

Table 3.1 Condition of TiN heaters.

TiN heater	Power [mW]
S_1 of $N = 2$	279
S_1 of $N = 4$	51.4
S_2 of $N = 4$	99.7
S_3 of $N = 4$	246
S_4 of $N = 4$	12.6
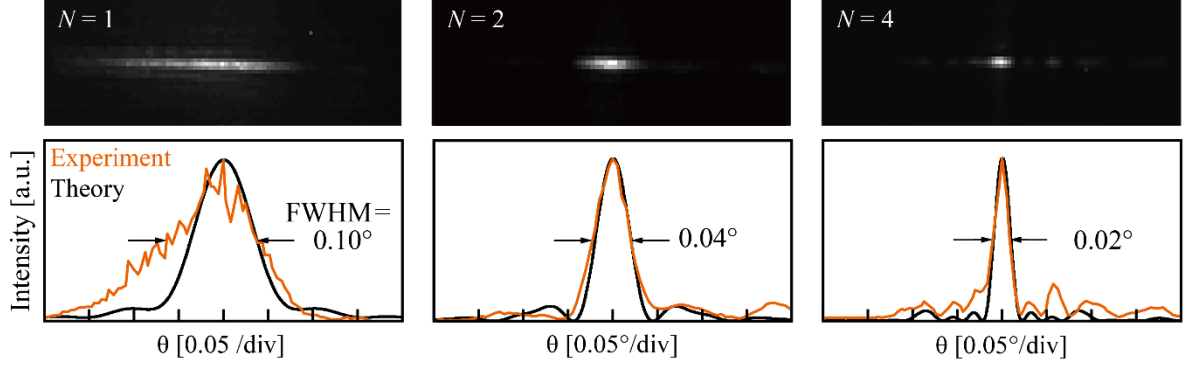
Fig. 3.29 Beam spots and beam profiles when using PCW arrays of $N = 1, 2, 4$.

The observed beam spots and the corresponding theoretical and experimental profiles are shown in Fig. 3.29. The $N = 1$ device shows a slightly wider beam compared with the theoretical value, which may be due to non-uniformity in the fabrication process. For $N = 2$ and 4 devices, the array factor effectively obtained a beam divergence close to the theoretical value, and the element factor suppressed the grating lobe, resulting in smaller sidelobes.

3.4   Discussion

In this chapter, the theoretical transmission and reception efficiency of the PCW optical antenna were calculated first to confirm that the subarray configuration is useful for improving the transmission and reception characteristics of the PCW. Theoretical calculations predicted that the reception intensity could be scaled by arranging short PCWs in series to suppress the total waveguide loss. For transmission, the beam divergence can be narrowed and the aperture is enlarged by effectively using the element factor and array factor. Although the beam profiles of the fabricated devices were degraded by the slight difference in the beam radiation angle between each PCW due to non-uniformity of the fabrication process, experiments confirm that beam profiles close to the theoretical values could be obtained by thermo-optic control of the TiN heaters. Beam divergences of 0.04° and 0.02° were obtained with $N =$ 2 and 4 devices, respectively, and more than 1,000 antenna integrations were required to achieve the same beam divergences in the OPA configuration [1-35]. Therefore, a high-resolution beam can be achieved with an overwhelmingly small number of antennas. Moreover, beam scanning is possible while adjusting the beam profiles by wavelength sweep and heater control. This experiment required a total of 279 and 410 mW of power at the TiN heaters for $N = 2$ and 4, respectively. The p-i-p type heaters used in later chapters can operate at lower power because they have higher heating efficiency [3-6].

References

[3-1]   K. Sayyah, R. Sarkissian, P. Patterson, B. Huang, O. Efimov, D. Kim, K. Elliott, L. Yang, and D. Hammonet, "Fully Integrated FMCW LiDAR Optical Engine on a Single Silicon Chip," J. Lightwave Technol., vol. 40, no. 9, pp. 2763−2772, 2022.

[3-2]   T. P. White, L. O'Faolain, Juntao Li, L. C. Andreani, and T. F. Krauss, "Silica-embedded silicon photonic crystal waveguides," Opt. Express 16, 17076−17081, 2008.

[3-3]   R. Tetsuya, H. Abe, H. Ito and T. Baba, "Efficient light transmission, reception and beam forming in photonic crystal beam steering device in a phased array configuration," Jpn. J. Appl. Phys., vol. 58, no. 082002, pp. 1-5, 2019.

[3-4]   R. Tetsuya, T. Tamanuki, H. Ito, H. Abe, R. Kurahashi, M. Seki, M. Ohtsuka, N. Yokoyama, M. Okano and T. Baba, "Si photonic crystal optical antenna serial array and frequency-modulated

continuous-wave light detection and ranging action," Appl. Phys. Lett., vol. 119, no.23, pp.231103 (1-5), 2021.

[3-5]   S. Suyama, R. Shiratori and T. Baba, "Unidirectional emission in engineered slow light beam scanner", Optoelectronic and Commun. Conf., Toyama, 2022 (To be presented).

[3-6]   T. Tamanuki, H. Ito and T. Baba, "Thermo-optic beam scanner employing silicon photonic crystal slow-Light waveguides", J. Lightwave Technol., vol. 39, no. 4, pp. 904−911, 2021.

Chapter 4
Evaluation of Transmission and Reception Characteristics

4.1 Overview

In this chapter, the transmission and reception characteristics of the PCW antenna subarrays were evaluated through LiDAR transmission and reception experiments using the FMCW method. In the previous chapter, beam profiles close to the theoretical values using the fabricated devices were observed, and findings show that a subarray configuration is useful for improving the transmission and reception characteristics with high-resolution beam. The FMCW LiDAR experimental system has two possible configurations: one with separate transmitter and receiver antennas, and the other with shared transmitter and receiver antennas. In the former configuration, the transmitter and receiver antennas need to be calibrated and controlled so that they have the same directivity. In this study, the latter configuration was adopted, which is simpler to implement. The experimental system was configured as follows. The FMCW signal was generated outside the chip and radiated from the PCW, and the reflected light from an object was mixed with reference light split before coupling into the PCW, detected by a balanced photodiode, and analyzed by an electrical spectrum analyzer. In the latter half of the chapter, the beat signal spectrum is included, and attempts to investigate the undesired noise in the beat signal spectrum and improve the setup are described. Noise signals with undesired peaks can cause false detection, which is why only the beat signal derived from desired reflected light from the object needs to be obtained as much as possible.

4.2 Setup for Evaluation of Transmission and Reception Characteristics

4.2.1 Setup for FMCW LiDAR

Figure 4.1 shows a schematic of the FMCW LiDAR experimental system that was first constructed to evaluate the transmission and reception characteristics of the PCW antenna subarrays. A tunable wavelength laser (Santec, TSL-550) with a linewidth of 200 kHz was used as the light source. The FMCW signal was generated by a lithium niobate (LN) in-phase/quadrature-phase (I-Q) modulator (MOD) which was a dual-parallel MZI structure with two RF drive voltages and three DC voltages. The RF signal was generated by an arbitrary waveform generator (AWG, Keysight, M9502A), and DC voltage was applied by a DC voltage source (ITECH, IT6922A), where the parameters of the FMCW signal were set using GUI software called Keysight IQ tools on a PC, as shown in Fig. 4.2(a). In the "IQ & RF Signals" section, a button named "Radar Pulses/Chirps" is given, which opens a separate window
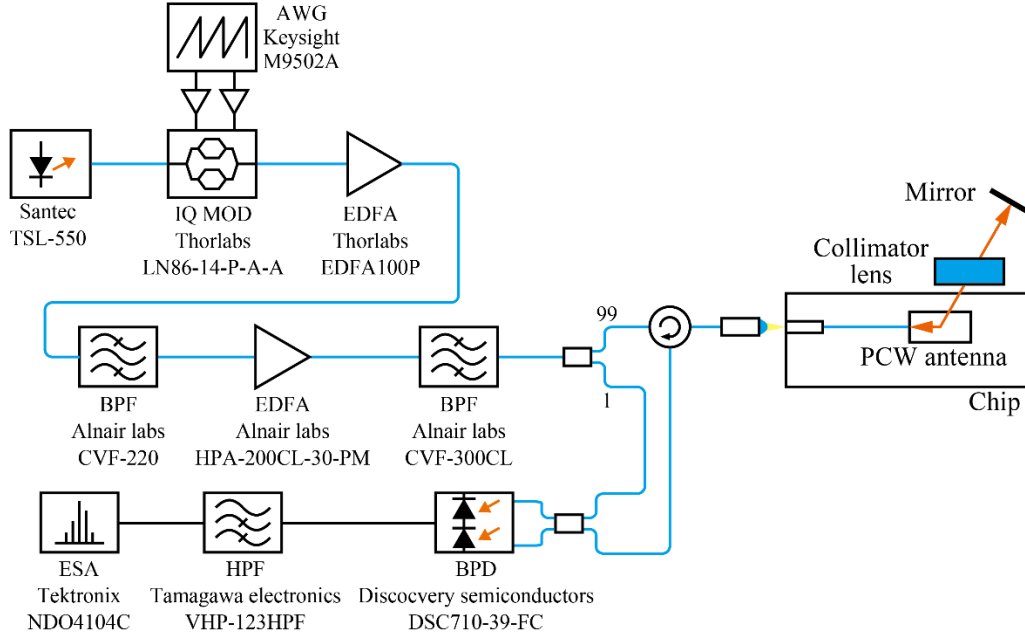
Fig. 4.1 Setup for evaluation of transmission and reception characteristics in PCW subarray configuration.
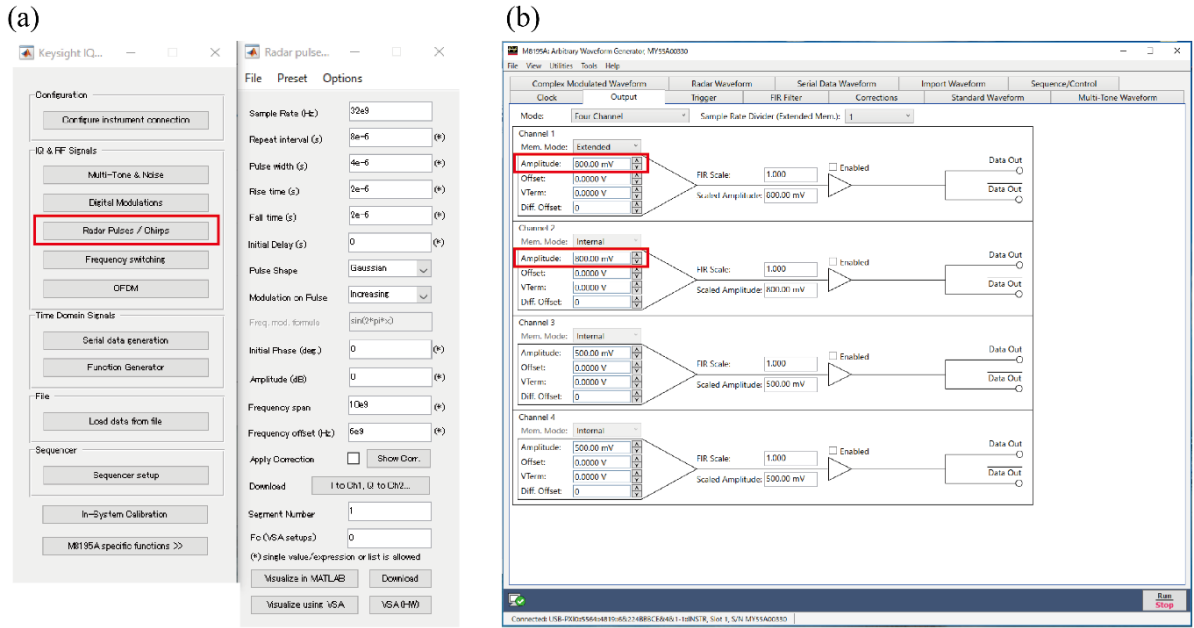

Fig. 4.2 (a) GUI of Keysight IQ tools. FMCW signal can be generated by the button surrounded by red lines. (b) Software GUI for adjusting the output of the signal. The red squares show the setting of the output amplitude.

where the parameters of the frequency chirp signal can be set. Pressing the "Download" button generates the signal, with a sampling rate of up to 32 GHz for I-Q signal generation. The electrical amplitude of the generated RF signal can be controlled using separate software as shown in Fig. 4.2(b), with output from channels 1 and 2 for I and Q, respectively, and can be set up to 1 V. If the "Modulation on Pulse" is set to "Increasing" in Fig. 4.2(a), then a sawtooth frequency chirp signal can be generated, as shown in Fig. 4.3(a). Although a sawtooth frequency chirp was used in this study, a triangular chirp enables

Doppler measurement that provides information on the velocity and vibration of the object [4-1, 2, 3]. The frequency modulation was performed in the range of frequency width f_{span} relative to the center frequency f_{offset}, with the frequency modulation period set to T. These can be set using "Repeat interval," "Frequency offset," and "Frequency span," respectively. As shown in Fig. 4.3(b), the generated signal can be windowed for the rise time t_{rise}, pulse width t_{width}, and fall time t_{fall} of the pulse signal, which can be set by "Rise time," "Pulse width," and "Fall time," respectively. The type of window function can be selected by "Pulse shape," including window types such as trapezoidal, Gaussian, and raised cosine. The trapezoidal window resulted in a large envelope hem of the desired beat signal spectrum; thus, a Gaussian or raised cosine window was used in this study. The generated RF signal was amplified by an electrical amplifier because the RF drive voltage of the I-Q MOD requires about 5 V.

The modulated light by the I-Q MOD was observed with an optical spectrum analyzer (OSA) (ADVANTEST, Q8384), and each DC voltage value of the I-Q MOD was adjusted to achieve single-sideband (SSB) modulation, which is close to pure frequency modulation. The SSB modulation was used in this study because pseudo-frequency modulation using intensity modulation of light amplitude produces a double side band (DSB), which interferes between DSB signals and produces an undesired beat signal [4-4, 5]. The spectrum of the modulated light observed by OSA is shown in Fig. 4.4. A single peak was seen only at the wavelength of the carrier wave, which is set by the laser without RF signal drive. When driven by an RF signal, a DSB was generated for the wavelength of the carrier wave, and the DC voltage was adjusted to ensure a small carrier wave and one side of the band. The obtained SSB modulated signal showed a carrier suppression ratio of −24.5 dB. An erbium-doped fiber amplifier (EDFA) (Alnair labs, HPA-200CL-30-PM) capable of amplifying up to 30 dBm was used to amplify the modulated light to couple into the device. The minimum input power of this EDFA was −10 dBm, and the modulated light was amplified by another EDFA (Thorlabs, EDFA100P) before input. A bandpass filter (BPF) (Alnair labs, CVF-220, CVF-300CL) was passed after the amplification of two EDFAs. The modulated light was then split by a 1:99 coupler, and the larger output was coupled into the SSC of the device from the lensed fiber through a circulator. The smaller output was mixed with the returned reflected light by a 2 × 2 coupler and received by a balanced photodiode (BPD) (Discovery Semiconductors, DSC710-39-FC) with a bandwidth of 10.3 GHz and sensitivity of 0.76 A/W. The RF output from the BPD was measured by an electrical spectrum analyzer (ESA) (Tektronix, NDO4104C) to observe the beat signal spectrum. A 30 MHz high-pass filter (HPF, Tamagawa Electronics, VHP-123HPF) was inserted into the RF output to cut the DC component of the signal.
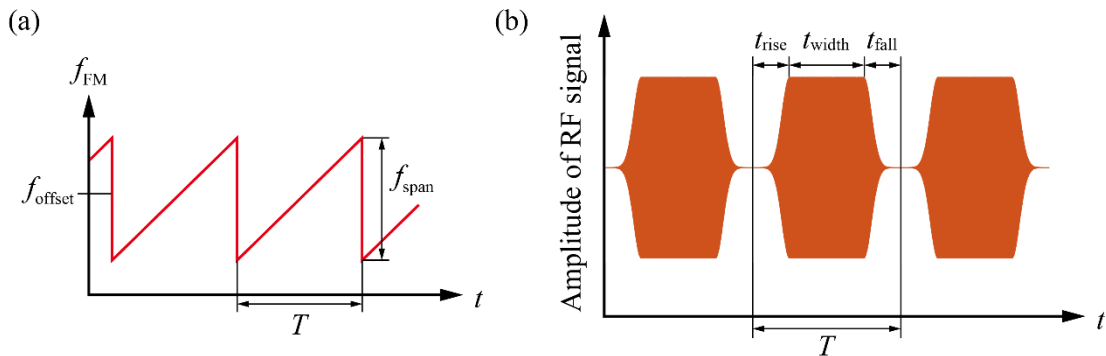

Fig. 4.3 (a) Sawtooth frequency chirp signal generated by AWG. (b) Amplitude of the signal generated by AWG.
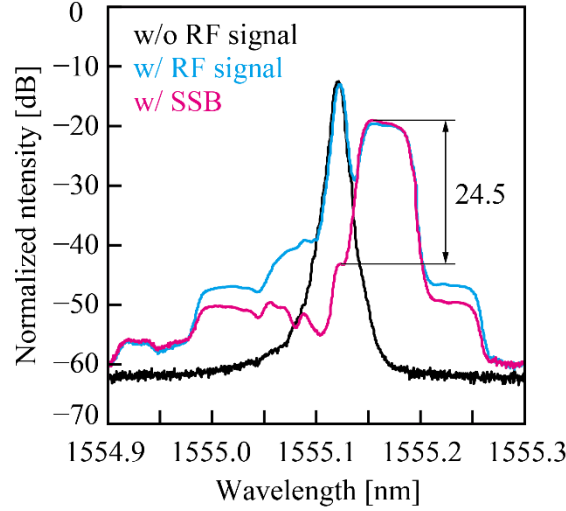
Fig. 4.4 Spectrum of the output from IQ MOD observed by OSA. SSB modulation can be obtained by adjusting the DC voltage whereas DSB can be seen without adjusting.

4.2.2 Beat signal spectrum

With the addition of the FMCW LiDAR measurement system shown in Fig. 4.1 to the optical system shown in Fig. 3.25 using the $N = 1, 2,$ and 4 devices described in the previous chapter, the transmission and reception signal intensities were evaluated from the beat signal spectrum observed at the ESA. The FMCW signal was generated by setting the AWG, as shown in Table 4.1. Figure 4.5(a) shows the beat spectrum observed for each device, and the peak signal intensity increased with increasing N. The plot of these peak intensities with N is shown in Fig. 4.5(b), where the received signal intensity increased by about 6 dB for each doubling of the total length of the PCW optical antenna, indicating experimentally that the transmission and reception characteristics of the PCW optical antenna can be scaled by the subarray configuration. This 6 dB increase in signal intensity corresponds to a halving of the beam divergence in transmission and a doubling of the aperture in reception.

The devices fabricated in this study required beam calibration due to fabrication errors, and the effect on the beat signal intensity with respect to changes in the applied voltage to the TiN heater was investigated. The SNR of the beat signal observed when the voltage values applied to S_1 and S_3 were changed for $N = 2$ and 4, respectively, is shown in Fig. 4.6. Over the range of voltages, SNR decreased up to 20, 10 dB for $N = 2$ and 4, respectively, indicating that the element factor, including fabrication error, suppressed the grating lobes due to the array factor more for the $N = 4$ device than for the $N = 2$ device [4-6]. Although calibration is required for each beam angle during beam scanning, it is less burdensome than OPA because the adjustment antennas are less than 1/100 of OPA.

Table 4.1 Setting of AWG.

Sample rate [Hz]	32×10^9	Modulation on pulse	Increasing
Repeat interval [s]	8×10^{-6}	Frequency span [Hz]	10×10^9
Pulse width [s]	4×10^{-6}	Frequency offset [Hz]	6×10^9
Rise time [s]	2×10^{-6}	Amplitude of Ch.1 [mV]	800
Fall time [s]	2×10^{-6}	Amplitude of Ch.2 [mV]	800
Pulse shape	Gaussian		

(a)

(b)
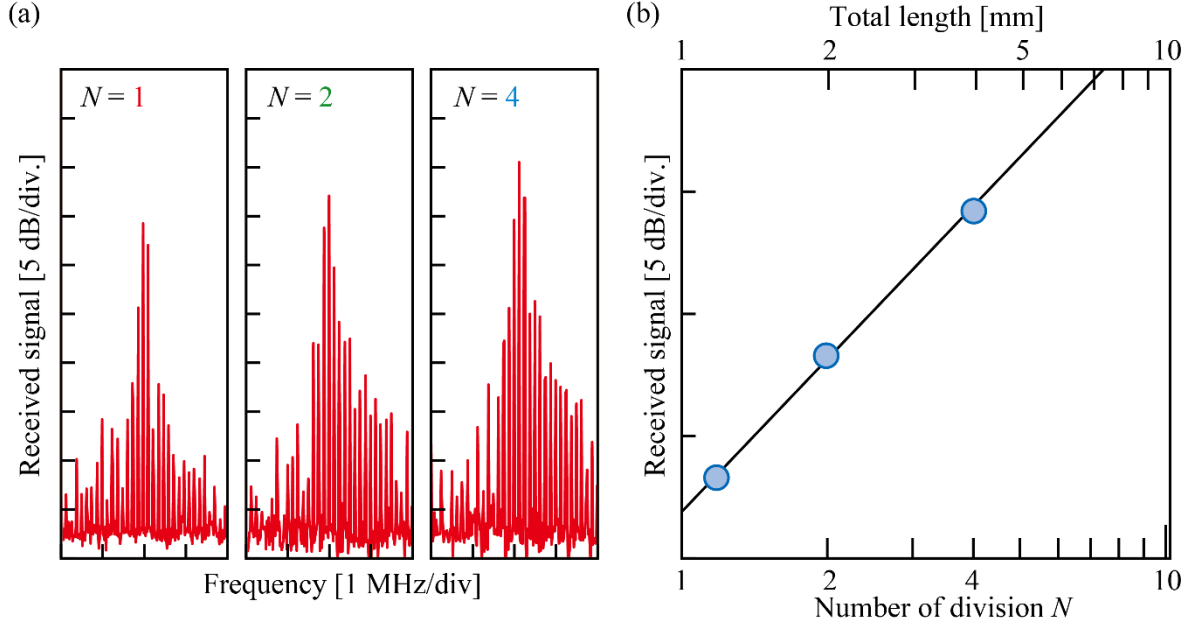
Fig. 4.5 (a) Observed beat spectrum with PCW arrays of $N = 1, 2, 4$. (b) Relative received signal intensity plotted with the number of division and the total length of PCW arrays.

(a)

(b)
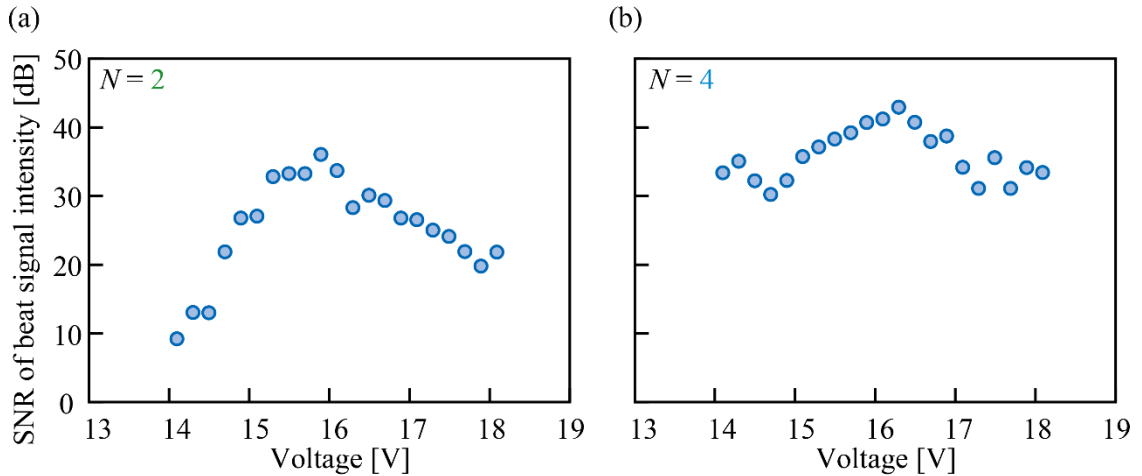
Fig. 4.6 SNR of beat signal intensity with voltage at (a) S_1 of $N = 2$ and (b) S_3 of $N = 4$.

4.3 Improvement of Setup for FMCW LiDAR

4.3.1 Evaluation of AWG signal

The signal generated by the AGW with and without the electrical amplifier was first investigated using the measurement system shown in Fig. 4.7 to remove undesired noise from the beat signal obtained in the FMCW LiDAR experiment. The spectrum were investigated for two cases where the frequency chirp period was set to 8 and 100 µs. In the case of 8 µs, the "Pulse width," "Rise time," and "Fall time" were set to 50, 25, and 25 µs, respectively, while these parameters were set to 50, 25, and 25 µs, respectively, in the case of 100 µs. A DC block (Anritsu, K261) was inserted immediately before the ESA (Rohde & Schwarz, FSW43) to remove the DC component of the signal. The results are shown in Fig. 4.8, where the frequency span was set from 0 to 40 MHz, and the reference level, attenuation level (Att), and

resolution bandwidth (RBW) were set to −30 dBm, 0 dB, 3 MHz, respectively. The modulation frequency band and harmonic components were observed. The modulation frequency ranges from 1 GHz to 11 GHz. However, the frequencies at both ends of the band were attenuated because of the window function applied to the signal by AWG. The suppression ratio of the harmonic components was amplified from about −40 dB to −20 dB when the preamplifier was set at ESA. Figures 4.8(c) and 4.8(d) show the spectrum range where the desired beat signal spectral peak occurs when the ranging objects were located within about 5 m with the FMCW LiDAR optical system in this study, showing that no noticeable noise peaks occurred. Figure 4.9 shows the result after the signal from the AWG is amplified by the electrical amplifier, confirming that no noise peak was generated from the electrical amplifier.
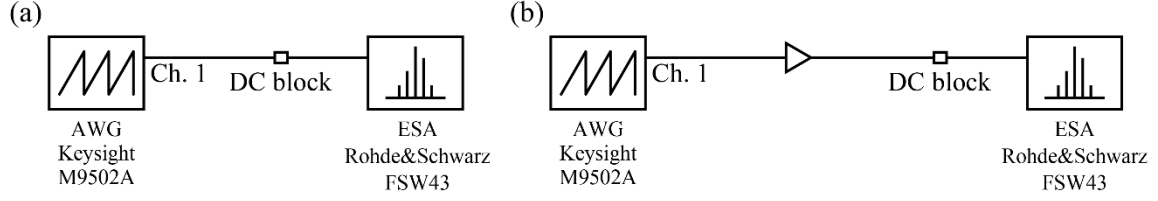
Fig. 4.7 (a) Setup for observing the signal from the AWG. (b) Setup for observing the amplified signal from the AWG.
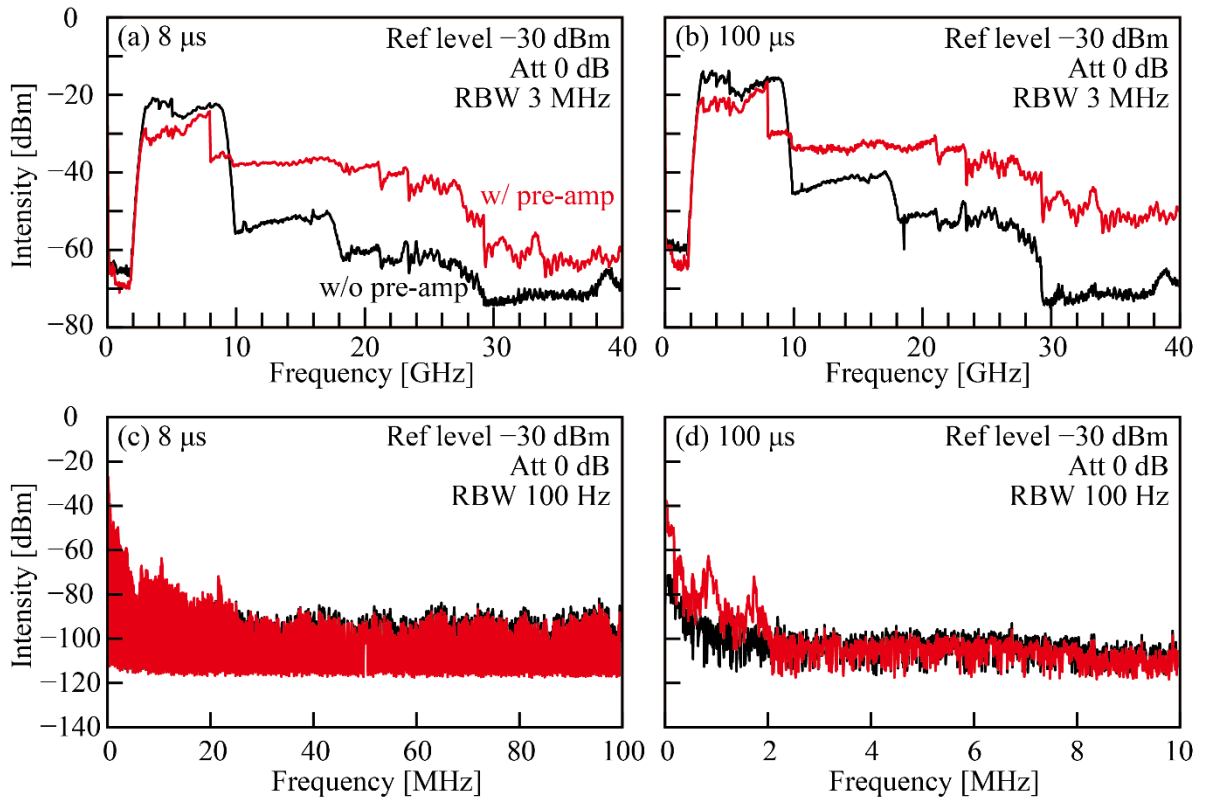
Fig. 4.8 Observed spectrum of AWG signal. (a) Repeat interval = 8 μs. (b) Repeat interval = 100 μs. (c), (d) Frequency span = 100, 10 MHz at (a) and (b), respectively.
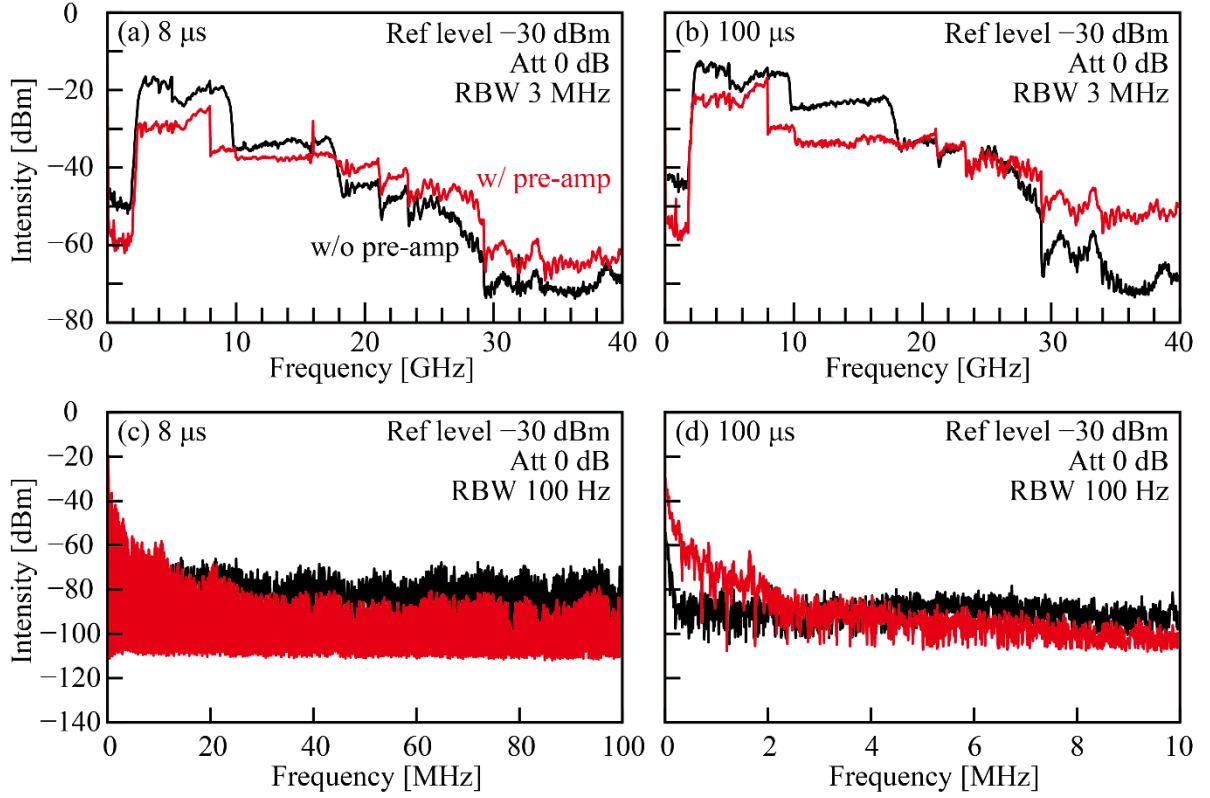
Fig. 4.9 Observed spectrum of amplified AWG signal. (a) Repeat interval = 8 μs. (b) Repeat interval = 100 μs. (c), (d) Frequency span = 100, 10 MHz at (a) and (b), respectively.

4.3.2 Evaluation of modulated light

Next, a measurement system was constructed, as shown in Fig. 4.10, and the spectrum of the light modulated by the I-Q MOD directly at the BPD and the RF signal obtained by the BPD at the ESA was observed. In Fig. 4.10(a), the modulated light was input to only one side of the BPD, while in Fig. 4.10(b), it was input to the BPD through a 1 × 2 coupler. The noise floor tended to increase when the preamplifier was set at 8 μs. However, when light was input to the BPD through the 1 × 2 coupler, the noise decreased, as shown in Figs. 4.11(c) and 4.11(d), confirming the effect of the balance detection. Another peak was observed around 10 and 1 MHz near the DC component in Figs. 4.11(c) and 4.11(d), respectively, indicating that the modulated light already had an extra peak at the stage of modulation by I-Q MOD, and the RF signal setting or modulator is considered to contain the cause of this noise peak.

To confirm the influence of a BPF, the spectrum was observed with a setup where the BPF inserted immediately after the I-Q MOD, as shown in Fig. 4.12. Figure 4.13 shows the results of the observed spectrum when a BPF was added to the setup. In addition to the noise derived from the modulated light, several extra spectral peaks caused by the BPF were observed. The BPF was used to suppress the amplified spontaneous emission noise generated when amplified by an EDFA. However, because the noise floor did not change with and without the BPF, the BPF was removed in the setup described in a later chapter. In addition, "Repeat interval" of 100 μs was used because the noise floor was larger at 8 μs than at 100 μs. As a longer period of frequency chirp shifts the beat frequency to the lower-frequency side, the required frequency bandwidth for the BPD to be used was reduced. As the chirp time increases, the Doppler shift detected from the object becomes more sensitive, resulting in the instability of the distance to be measured with respect to the object's velocity and vibration in sawtooth chirping.
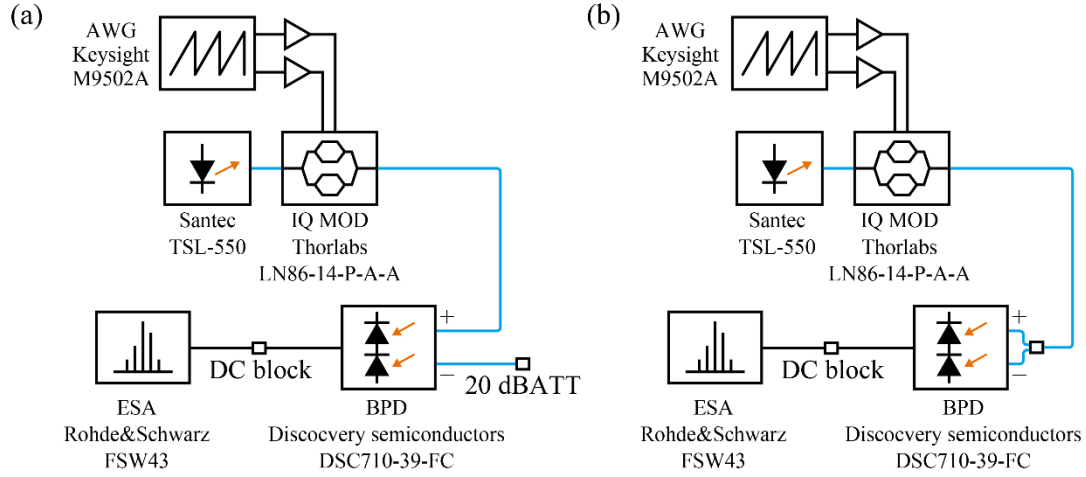
Fig. 4.10 Setup for observing the spectrum of the modulated light from LN IQ MOD. (a) Light was input to one side of the BPD with the other side attenuated by 20 dB. (b) Light was input to the BPD through the 1 × 2 coupler.
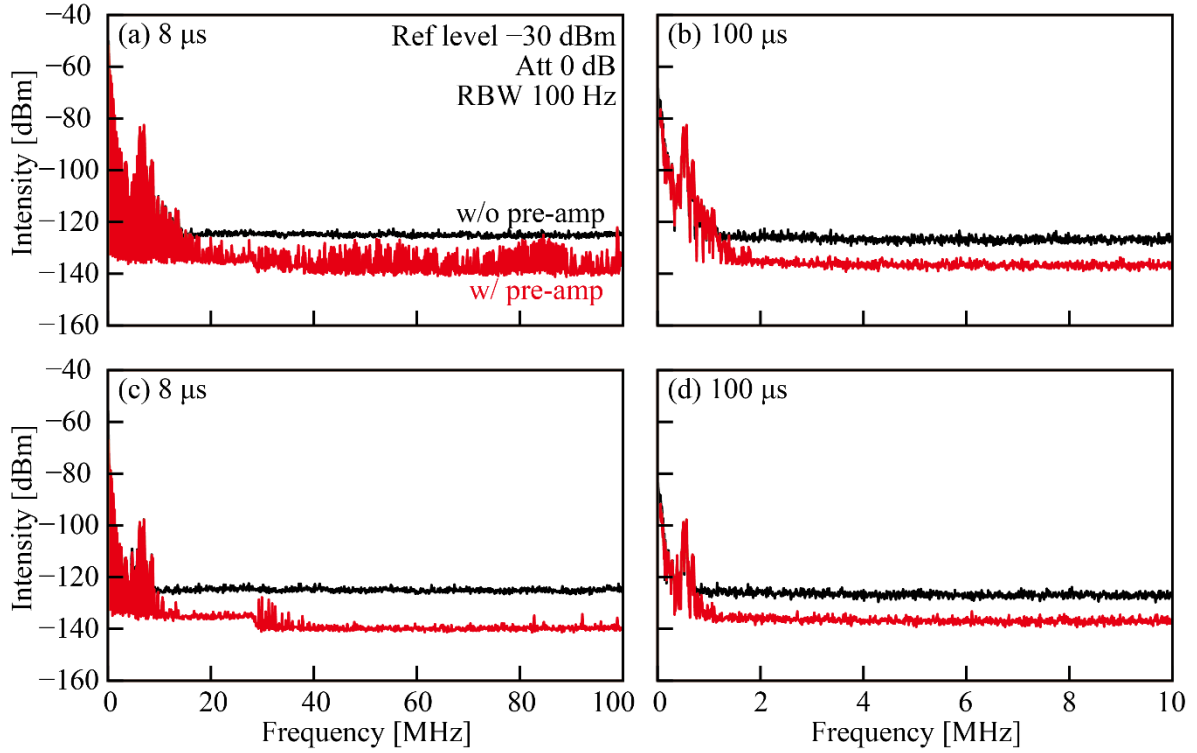
Fig. 4.11 Observed spectrum when modulated light was input to one side of the BPD. "Repeat interval" = (a) 8 and (b) 100 μs, respectively. Observed spectrum when modulated light was input to the BPD through the 1 × 2 coupler. "Repeat interval" = (c) 8 and (d) 100 μs, respectively.
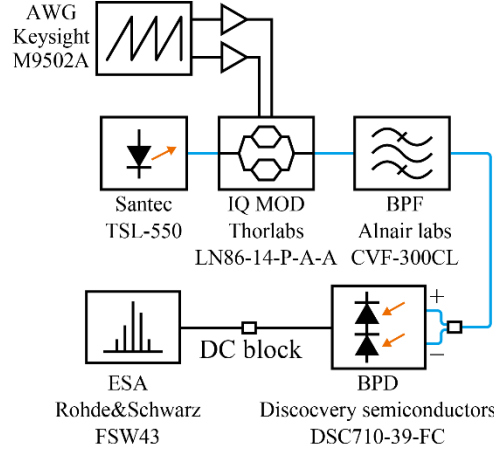
Fig. 4.12 Setup for observing the modulated light after the BPF.
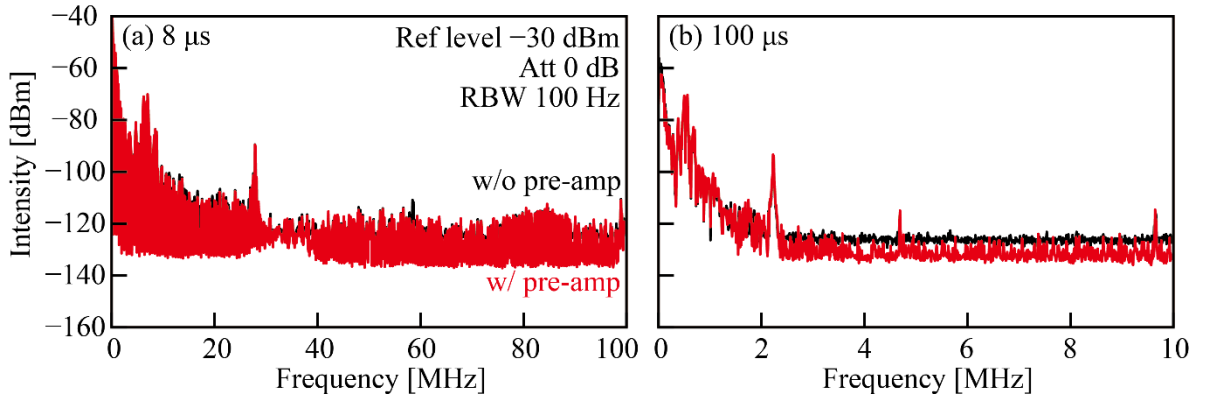
Fig. 4.13 Observed spectrum at the setup including the BPF. "Repeat interval" = (a) 8 and (b) 100 μs.

4.3.3 Evaluation of beat signal

Next, the noise in the beat spectrum was observed using the PCW. As shown in Fig. 4.14, a PCW optical antenna, a switch, an interference system for observing the beat signal, and a Ge BPD integrated on-chip device were used for the measurement. The light was input to the chip using a fiber block as described in Chapter 7, where the measured input power was 7.28 dBm. A portion of the input light was split and radiated from the PCW via a switch (SW) tree. The collimator lens and mirrors were aligned so that the light was coupled back into the PCW. The returned light interfered with the reference light and was received by a Ge BPD. An electrical signal was extracted from one of the BPDs and observed by ESA with an inserted DC block. The other BPD was terminated with a 50 Ω resistor. The observed beat spectrum is shown in Fig. 4.15. Ideally, only the beat spectrum generated from the reflected light from the mirror should be observed. However, several undesired noise peaks were observed.

Next, the kind of noise generated when the modulated light was input directly to the chip, as shown in Fig. 4.16(a), was checked. The measurement result is shown in Fig. 4.17(a), confirming that only the noise derived from the modulated light observed in Fig. 4.11(d) appeared, in addition to the beat spectrum from the mirror. Furthermore, as shown in Fig. 4.16(b), how the noise changed when an EDFA was inserted and amplified was checked. The injection current of the EDFA was adjusted to be the same as the power of the light input to the chip in the system shown in Fig. 4.14. The result is shown in Fig. 4.17(b), confirming that no extra noise peak appeared. Figure 4.18 summarizes the beat signal intensity, signal-to-noise ratio (SNR), and noise floor when the input power to the chip was changed under these

conditions.
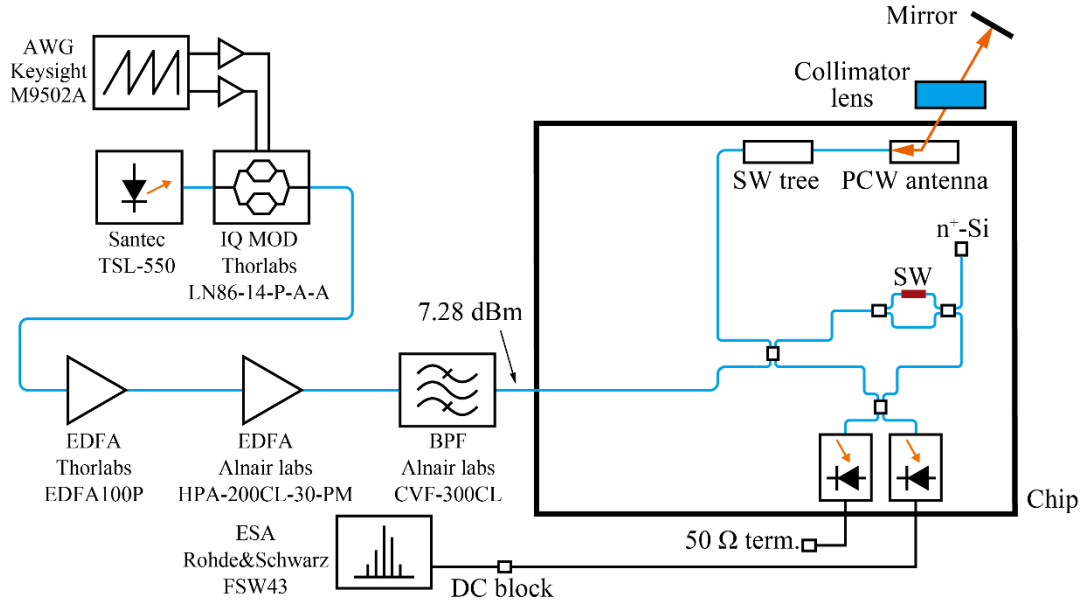
Fig. 4.14 Setup for observing the beat spectrum using the chip integrated with the PCW antennas and Ge BPD.
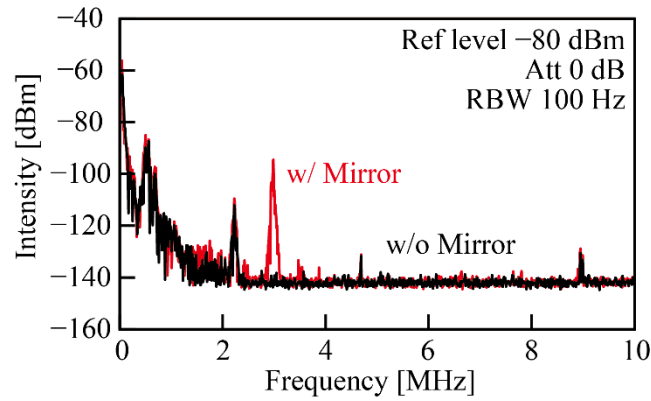
Fig. 4.15 Observed beat spectrum, where the red line shows the beat signal corresponding to the reflected light form the mirror.
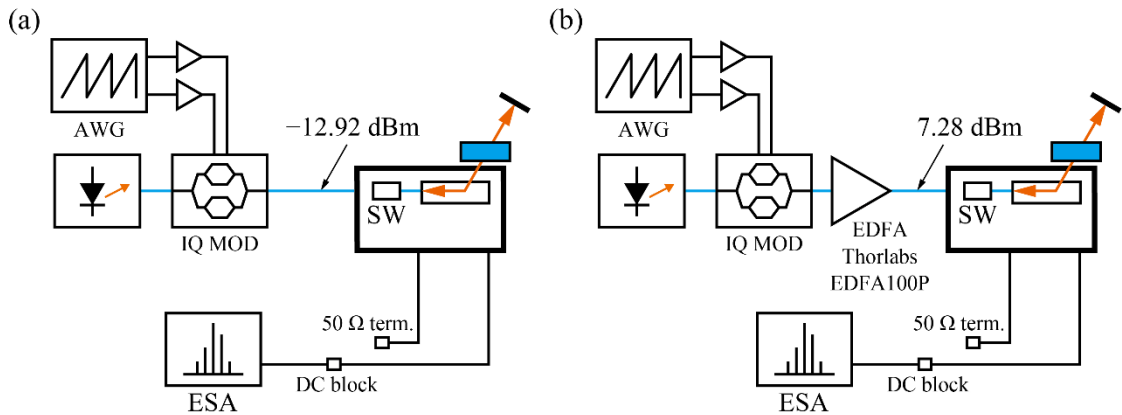

Fig. 4.16 (a) Setup for observing the beat spectrum without EDFAs and BPF at the setup of Fig. 4.14. (b) Setup with only one EDFA.
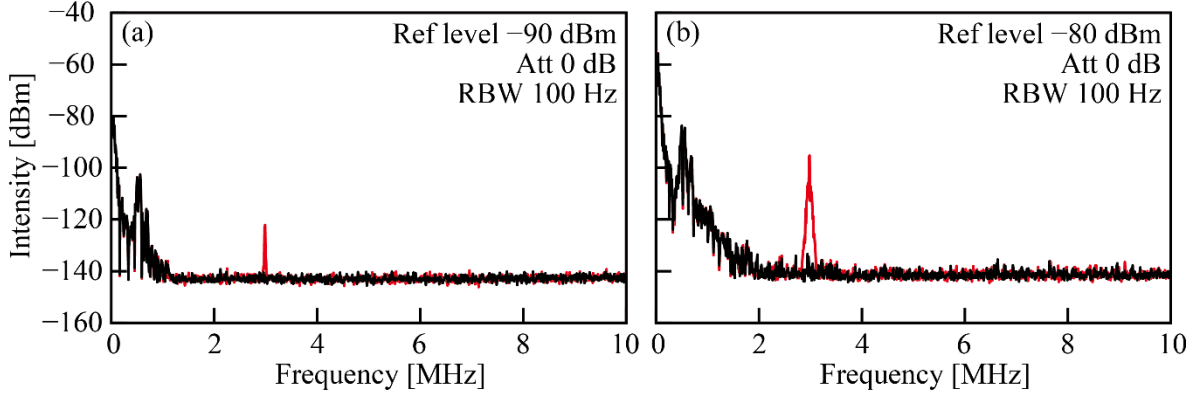
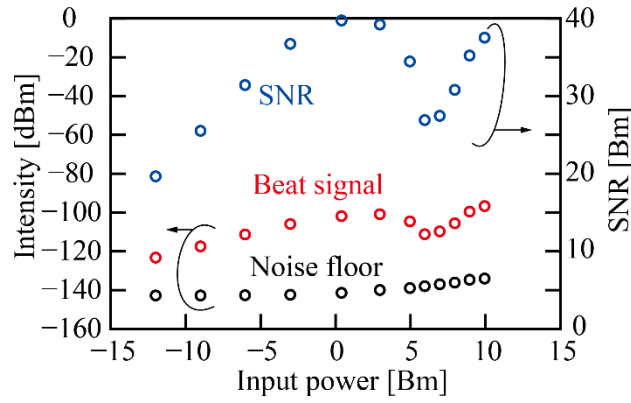Fig. 4.17 (a), (b) Observed beat spectrum at the setup of Figs. 4.16(a) and 4.16(b), respectively.

Fig. 4.18 Beat signal intensity, SNR, and noise floor with input power.

4.4 Discussion

In this chapter, an FMCW-based transmission and reception experimental system for LiDAR application of the PCW was constructed to evaluate the transmission and reception characteristics of the $N = 1, 2,$ and 4 PCW subarrays fabricated in the previous chapter. The PCW in LiDAR application exhibited scalability with the subarray configuration. In addition, the cause of undesired noise in the beat spectrum was investigated. This undesired noise may cause false detection when the distance in LiDAR operation is calculated. Findings confirm that no extra noise peaks were generated in the measurement system without inserting a BPF after amplification with an EDFA. Therefore, the point cloud image acquisition using LiDAR chip described in Chapter 7 employed this simplified measurement system.

References

[4-1] W. Zhang, W. Gao, L. Huang, D. Mao, B. Jiang, F. Gao, D. Yang, G. Zhang, J. Xu, and J. Zhao, "Optical heterodyne micro-vibration measurement based on all-fiber acousto-optic frequency shifter," Opt. Express, vol. 23, no. 13, pp. 17576−17583, 2015.

[4-2] Y. Xiong, Z. Peng, G. Xing, W. Zhang and G. Meng, "Accurate and Robust Displacement Measurement for FMCW Radar Vibration Monitoring," IEEE Sensors Journal, vol. 18, no. 3, pp. 1131−1139, 2018.

[4-3] S. Suyama, H. Ito, R. Kurahashi, H. Abe and T. Baba, "Doppler velocimeter and vibrometer FMCW LiDAR with Si photonic crystal beam scanner," Opt. Express, vol. 29, no. 19, pp. 30727−30734, 2021.

[4-4]   M. Kamata, Y. Hinakura, and T. Baba, "Carrier-suppressed single sideband signal for FMCW LiDAR using Si photonic crystal optical modulators," J. Lightwave Technol., vol. 38, no. 8, pp. 2315−2321, 2020.

[4-5]   P. Shi, L. Lu, C. Liu, G. Zhou, W. Xu, J. Chen, and L. Zhou, "Optical FMCW Signal Generation Using a Silicon Dual-Parallel Mach-Zehnder Modulator," IEEE Photonics Technology Letters, vol. 33, no. 6, pp. 301−304, 2021.

[4-6]   R. Tetsuya, T. Tamanuki, H. Ito, H. Abe, R. Kurahashi, M. Seki, M. Ohtsuka, N. Yokoyama, M. Okano and T. Baba, "Si photonic crystal optical antenna serial array and frequency-modulated continuous-wave light detection and ranging action," Appl. Phys. Lett., vol. 119, no.23, pp.231103 (1−5), 2021.

Chapter 5
Beam Calibration with Thermo-optic Control

5.1 Overview

In this chapter, the transmission and reception characteristics of the PCW optical antennas was improved by using thermo-optic control. The beam angle relative to the operating wavelength for each waveguide and left/right input switching was investigated by using a chip with 32 PCWs integrated in parallel. From these results, the angle variations among the waveguides were assumed to be due to slight refractive index gradients in the PCW caused by non-uniformity in the fabrication process, which resulted in the formation of a gradient distribution of beam angles. In this study, such beam shape degradation due to fabrication errors was compensated by using thermo-optic control. First, the intensity distribution of the radiated beam was calculated for the phase change in the PCW, and the effect on the beam shape when the gradient of the propagation constant exists due to fabrication errors was investigated. In addition, the beam profile when a phase distribution was formed to focus the beam on a certain point was calculated. For example, the focusing effect can be obtained by adjusting the phase of each antenna in OPA [5-1]. Liquid crystal lenses and metalenses can achieve a focusing effect by adjusting the direction of the liquid crystal and the nanopillar structure, respectively [5-2, 3]. Although adjusting the phase at each scattering point by using the diffraction grating in waveguide antennas is practically difficult, this work investigated whether a similar phase adjustment could be made in PCW by forming a temperature distribution in the waveguide and giving a refractive index distribution as a result. The objective was to improve the signal intensity in LiDAR transmission and reception experiments by focusing the light on the object [5-4]. Next, a blue laser was used to form a temperature distribution in the aperture of the PCW for thermo-optic control, and LiDAR transmission and reception experiments were implemented to compare the signal intensities.
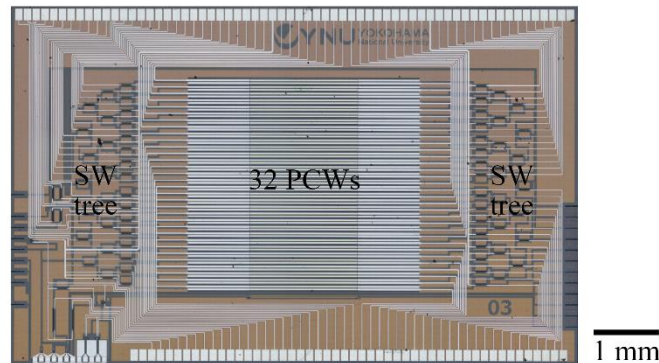
Fig. 5.1 Microscopic image of fabricated LiDAR chip that includes 32 PCWs.

Table 5.1 Parameters of PCW.

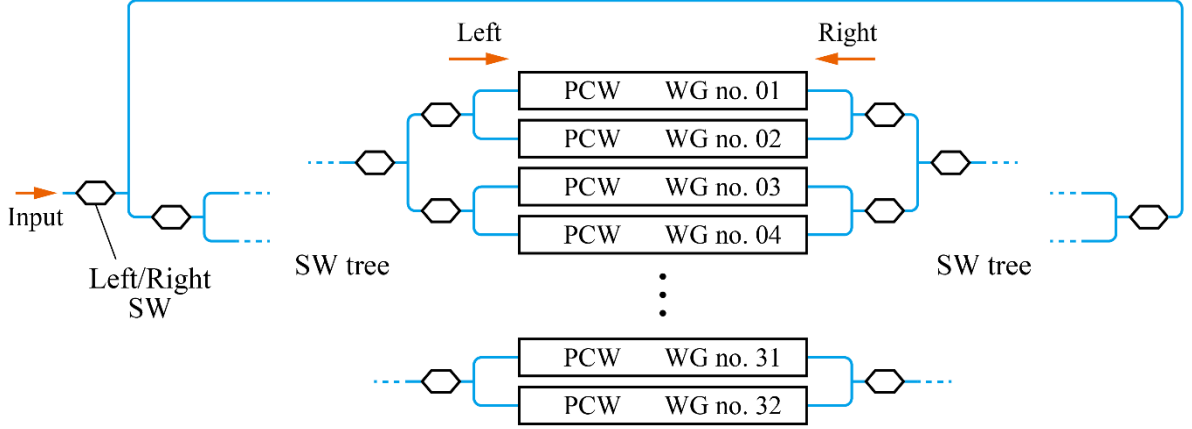|	
Lattice constant a [nm]	394
Hole diameter $2r$ [nm]	197
Third row shift s_3 [nm]	95
Width of shallow-etched grating [nm]	200
Aperture ℓ [μm]	1500

Fig. 5.2 Configuration of PCWs with SW trees.

5.2 Investigation of the Influence of Fabrication Error

5.2.1 Fabricated device

Figure 5.1 shows a microscopic image of the device used to investigate the effects of fabrication errors, which was fabricated at Foundry B. Thirty-two PCWs were integrated in parallel with 100 μm spacing, and an MZI-type optical switch (SW) tree was used for the input to the PCWs [5-5]. Other integrated devices include PCW optical modulators and Ge BPDs. However, these were not used in this study and are not described here. The main parameters of the PCW are shown in Table 5.1. For the target operation wavelength around 1550 nm, the lattice constant a, the circular hole diameter $2r$, the third row circular hole shift s_3, the width in the waveguide direction of the shallow-etched grating, and the radiation aperture length were designed as 394, 197, 95, 200, and 1500 nm, respectively. As shown in Fig. 5.2, the input light is first split to the SW trees located on the left and right sides of the PCW via the left-right input SW. The TiN heater used to drive the SW was wire-bonded to the chip and the printed circuit board (PCB) and controlled electrically from the outside. This SW operation selects one PCW to emit light. The waveguides (WG) are numbered from top to bottom as nos. 1, 2, and 3.

5.2.2 Beam angle deviation

Waveguide switching and left-right input switching were performed using 32 PCWs and SW trees to investigate the variation in operating wavelength and beam angle. First, a measurement system was set up, as shown in Fig. 5.3(a), to investigate the wavelengths near the band edge of each PCW. Light was input to the chip from a tunable wavelength laser (santec, TSL-550) and emitted from an PCW selected by SW. The radiated light was observed with an InGaAs camera (Hamamatsu, C14041-10U) through an NFP optical system with a ×10 objective lens attached. Figure 5.3(b) shows a photograph of the area where the PCW radiation started, showing the case when the input came from the left side, and the scattered light was found at the position where the PCW that includes the shallow grating started;

findings confirm that the light propagated through the PCW and was radiated into space by the grating. First, the wavelength was set to the longer wavelength side where radiation from the PCW could not be observed, and then the wavelength was changed to the shorter wavelength side by 0.1 nm increments until radiation could be observed. Here, the wavelengths at which radiation was observed were considered to be near the band edge. Next, a measurement system was constructed, as shown in Fig. 5.3(c), and the beam angle when the wavelength was fixed at 1537 nm was investigated. An InGaAs camera (Rapter Photonics, OW1.7-VS-CL-1280) was used through FFP optics to observe the beam angle. The optical system was tilted by 4° and −4° for the left and right inputs, respectively, because the observed beam angle was within the observation range of the objective lens.

The observed wavelengths near the band edge for each waveguide and left-right input switching are shown in Fig. 5.4. A periodic shift of about 1 nm for each of the five waveguides, and an overall shift toward the long wavelength side occurred. The observation of the beam angle with a fixed wavelength, as shown in Fig. 5.5, also confirmed the periodic shift where the band edge wavelength was on the long wavelength side, corresponding to a larger beam angle. No significant difference was observed for beam divergence, as shown in Fig. 5.6.
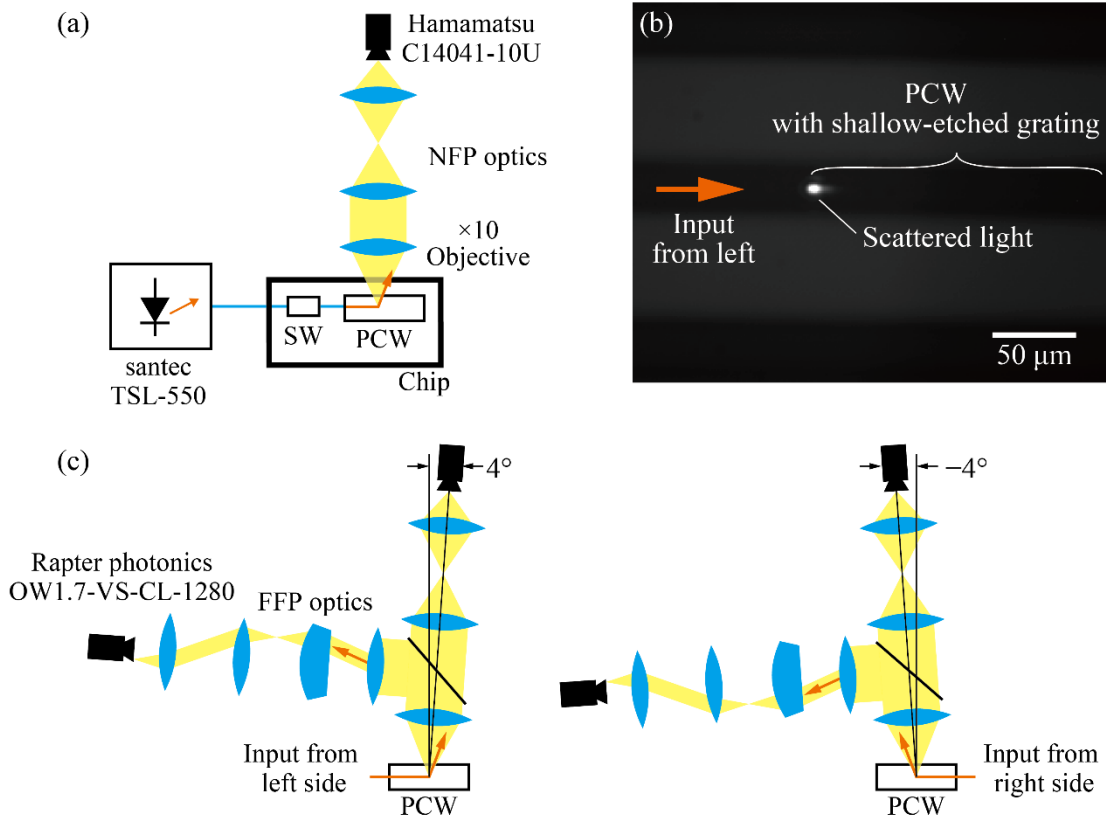
Fig. 5.3 (a) Setup for investigating wavelengths near the band edge. (b) Light emitted from the edge of the PCW observed by NFP optics. (c)
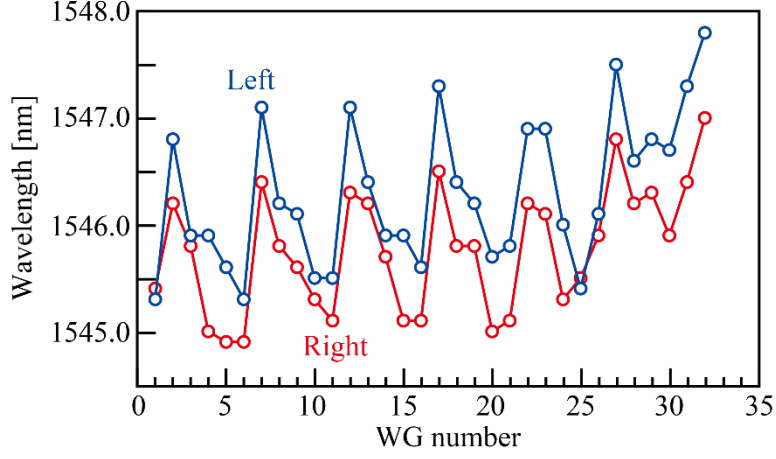
Fig. 5.4 Observed wavelengths near the band edge for each WG and for each left-right SW.
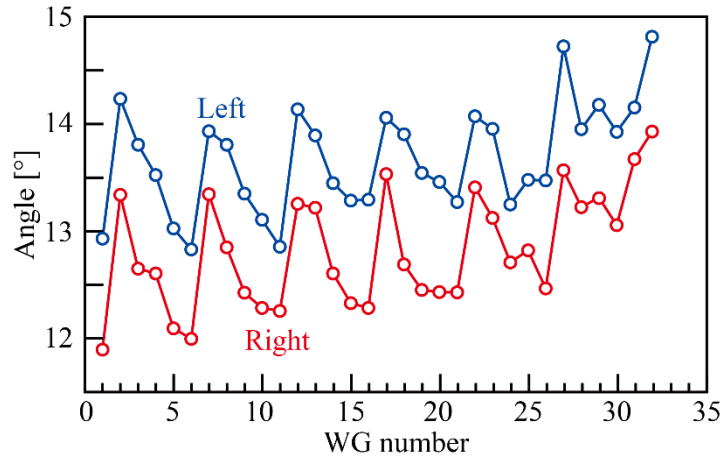
Fig. 5.5 Observed beam angles for each WG and for each left-right SW.
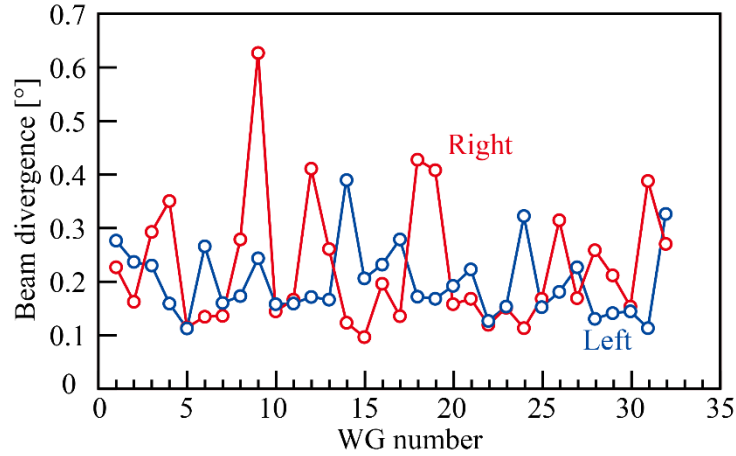
Fig. 5.6 Observed beam divergences for each WG and for each left-right SW.

5.2.3 Calculation of the beam intensity distribution

The phase distribution required to achieve a focusing effect in a waveguide type optical antenna such as PCW by adjusting the phase in the aperture as in an OPA was calculated. First, as shown in Fig. 5.7(a), the power P_{IN} input to the PCW is assumed to propagate while radiating light into space according to the radiation coefficient α_{rad} and propagation loss α_{loss}. Let ℓ be the aperture length of the PCW, and as

shown in Fig. 4.1(b), the electric field of the emitted beam at a position (y_2, z_2) distant by a range R from a certain position $(0, z_1)$ in the PCW is the superposition of the electric fields at the positions (y_2, z_2) of light emitted from each position of the waveguide. The power is expressed as follows:

$$P = \left| \int_0^\ell \sqrt{\alpha_{\mathrm{rad}} P_{\mathrm{IN}}} e^{-(\alpha_{\mathrm{rad}} + \alpha_{\mathrm{loss}})z} e^{-j(\Phi(z) + k_0 R(z))} dz \right|^2 \tag{5.1}$$

where $\Phi(z)$ is the amount of phase shift of the light within the PCW, and $R(z)$ is the distance of the PCW from position z. The attenuation of light intensity due to propagation in free-space was neglected because it was calculated only to check the beam profile. The conditional equation for the propagation constant of the PCW in the simulation is defined as follows:

$$\Phi(z) = \int_0^z (\beta_1 z + \beta_0) dz \tag{5.2}$$

The propagation constant in the PCW was taken as β_0, and $\beta_1 = 0$ if the propagation constant is ideally constant. As mentioned above, this term must be taken into account when the propagation constant is assumed to be skewed due to non-uniformity caused by fabrication errors in the PCW. To focus the light at a distance R, which means the condition for the electric fields to strengthen each other at this position, the condition for $\Phi(z)$ is expressed as follows:

$$\Phi(z) = k_0 \{ R(0) - R(z) \} \tag{5.3}$$

Figure 5.8 shows the calculation results of $\Phi(z)$ when $\ell = 1$ mm and the beam angle θ is varied, i.e., $\beta_0 = k_0 \sin\theta$ and $\beta_1 = 0$, where the wavelength is set to 1550 nm and the radiation coefficient is set to $\alpha_{\mathrm{rad}} = 20/(\ell\ln10)$ [dB/cm] so that the propagating light intensity is $1/e^2$ at a waveguide length ℓ. For simplicity, α_{loss} was set to be 0 dB/cm. If the propagation constant is ideally constant, then the phase changes linearly with respect to the waveguide direction, and the radiation angle of the beam varies with β_0. Next, when $\ell = 1$ mm, 1 cm, and 10 cm, $\alpha_{\mathrm{rad}} = 20/(\ell\ln10)$ [dB/cm], the beam intensity distribution at $\theta = 30°$ calculated for a 1.5 m square from the PCW is as shown in Fig. 5.9, where z is the direction of the PCW and y is the direction orthogonal to the PCW, each calculated at a position divided into 501 points.
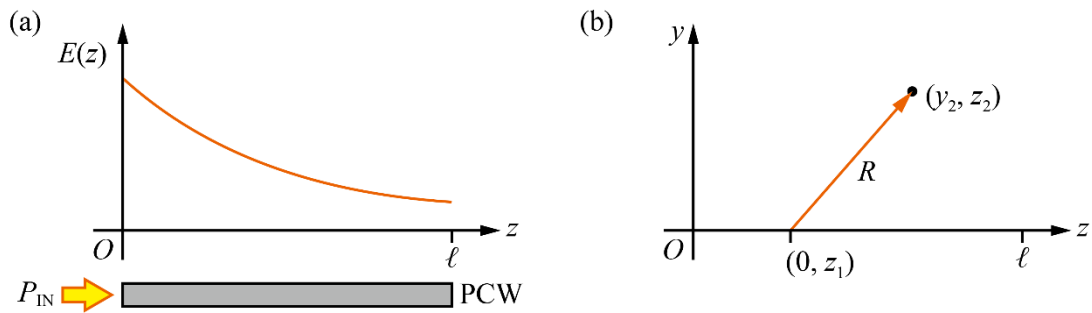
Fig. 5.7 Calculation model for the beam intensity distribution. (a) Electric field intensity distribution of guided mode in the PCW. (b) Distance R from the position of PCW $(0, z_1)$ to a point (y_2, z_2).
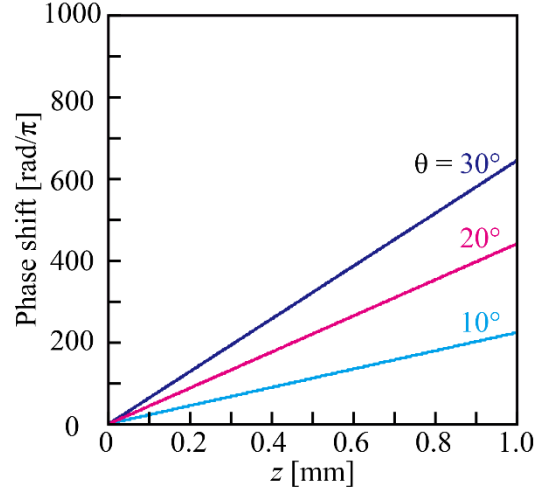
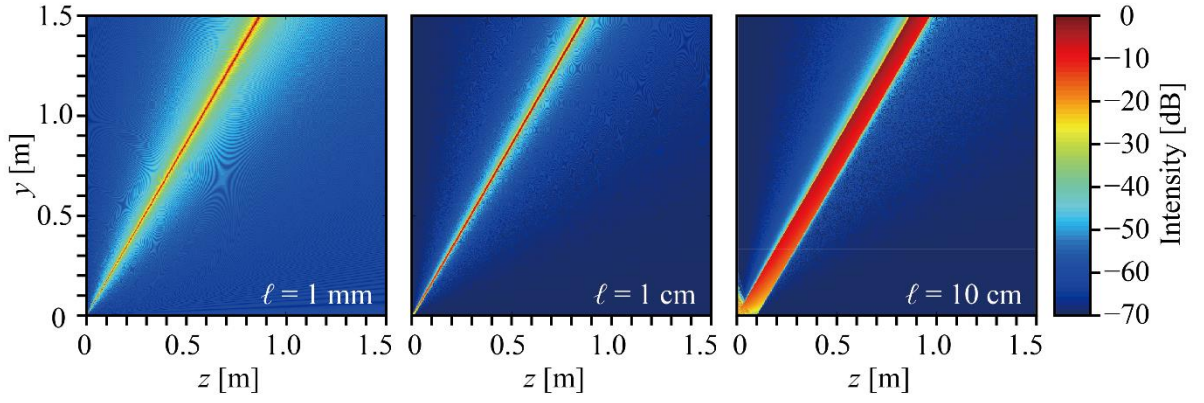Fig. 5.8 Phase shift $\Phi(z)$ calculated for the position of PCW z in ideal condition.

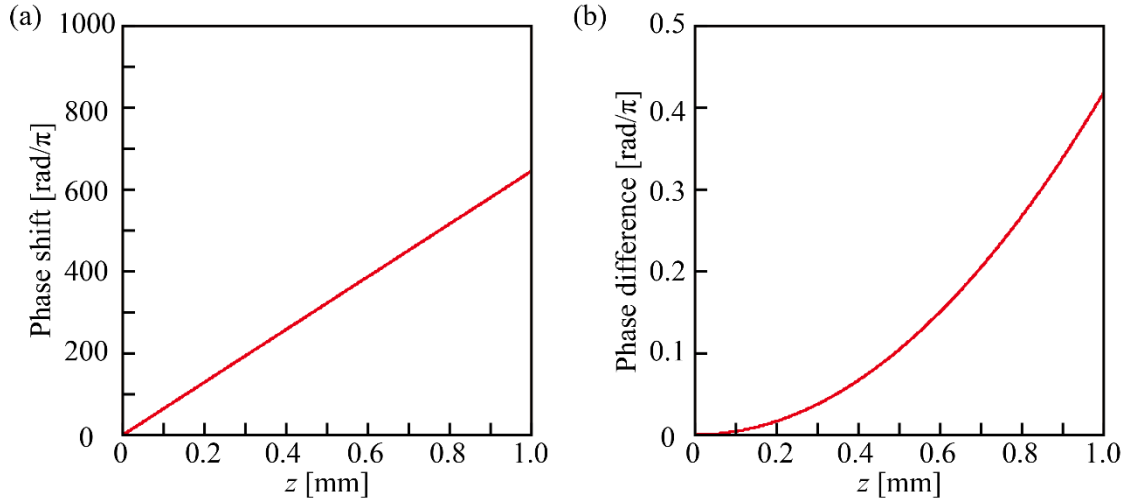Fig. 5.9 Beam intensity distribution calculated for ℓ.

Fig. 5.10 (a) Phase shift $\Phi(z)$ calculated for the position of PCW z in the condition that creates a focal point at a point (1, sin[30°]). (b) Calculated phase difference between with and without focusing conditions.
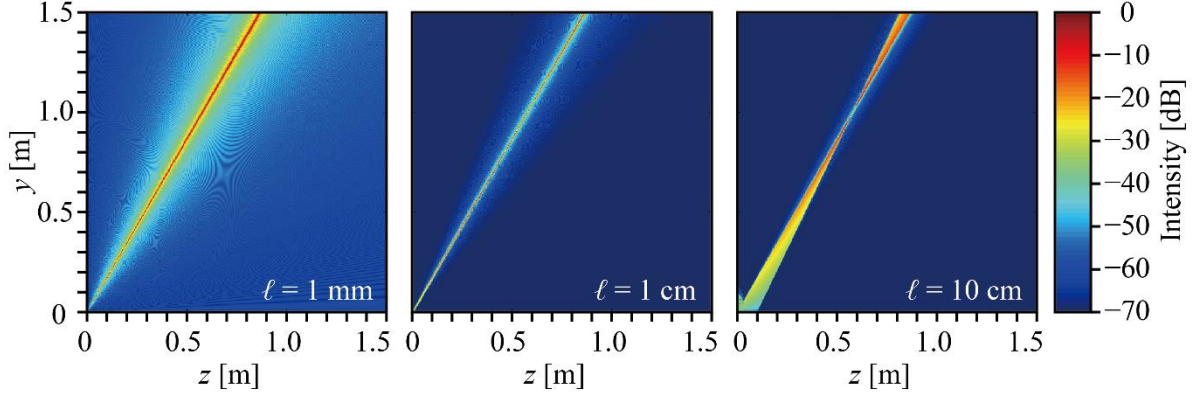
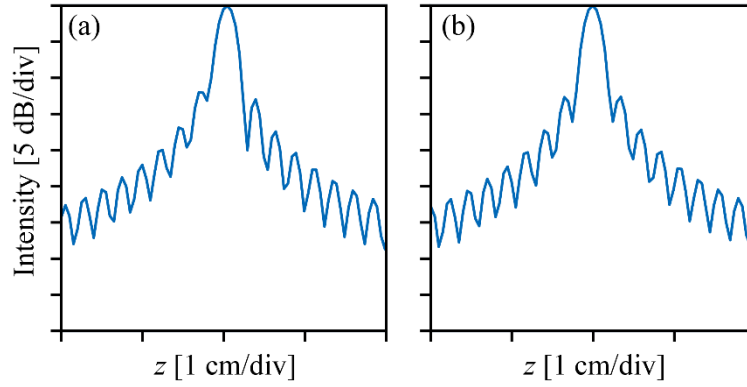Fig. 5.11 Beam intensity distribution calculated for the condition that creates a focal point at a point (1, sin[30°]).

Fig. 5.12 Beam profiles at the position of (1, sin[30°]). (a) Condition without focusing effect. (b) Condition with focusing effect.
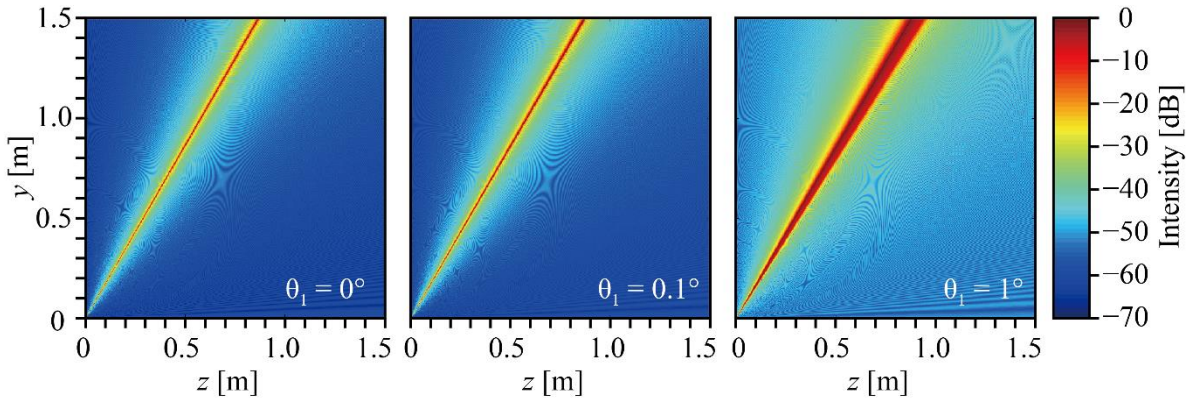
Fig. 5.13 Beam intensity distribution calculated for conditions where the inclination of the propagation constant exists in the PCW.

Figures 5.10 and 5.11 show the calculated phase shift and beam intensity distribution in the PCW for the phase condition of focusing at $(y, z) = (1, \sin[30°])$, respectively. To create a focal point, a quadratic phase difference needs to be provided with respect to the phase shift under normal non-focusing conditions. The longer the ℓ, the more clearly the focusing effect became apparent, which requires the focal point to be well within the near-field region determined by the length of the PCW aperture. However, Fig. 5.12 shows a magnified image of the beam shape at (1, sin[30°]) with and without the

focusing condition, confirming that the effect of focusing was effective, albeit slight.

Next, simulations were performed assuming the existence of a gradient in the propagation constant in the PCW, where the beam intensity distribution was calculated when a tilt of θ_1 occurred within the aperture $\ell = 1$ mm, i.e., $\beta_1 = \sin\theta_1$, compared with the case when no tilt occurred. The calculated results for $\theta_1 = 0°$, 0.1°, and 1° are shown in Fig. 5.13. The beam profile degraded as θ_1 increased, and if the angular sensitivity of the PCW optical antenna is 1°/nm, then even a small inclination of 1 nm has a negative effect on the beam profile. Such inclination must be compensated for. Therefore, this study attempts to improve this condition through thermo-optical control.

To focus the light and to compensate for the inclination of the propagation constant, a nonlinear phase shift must be applied to the normal PCW, and methods such as thermo-optic control and structural modulation of the PCW can be considered. The next section shows the improvement of the signal intensity in the FMCW LiDAR transmission and reception experiment by calibrating the beam profile and controlling the refractive index distribution in the waveguide by irradiating a blue laser beam to form a temperature gradient in the PCW.

5.3 Transmission and Reception Characteristics with Thermo-optic Control

5.3.1 Device

Figure 5.14 shows the design of the device used for thermo-optic control with a blue laser. An PCW with a shallow-etched grating was used, and the main parameters are shown in Table 5.2. The a, $2r$, s_3, the width of shallow-etched grating and the aperture ℓ in the waveguide direction were designed to be 394 nm, 208 nm, 95 nm, 200 nm, and 942 μm, respectively, to operate at a wavelength of 1550 nm. ℓ was shorter than that of the device used in the previous section because a long aperture caused the area irradiated by the blue laser to be smaller relative to the aperture. A p-i-p heater was used to heat the PCW, which could be operated via Al wiring by connecting a DC probe to the probing pad. Figure 5.15 shows a microscopic image of the fabricated device. The SSC was used to input light from the outside to the PCW, and because it also had an SSC on the other side of the chip, left and right inputs were possible. Figure 5.16 shows the beam angles observed by FFP optics using the fabricated device. The operating wavelength range was from about 1530 to 1560 nm, the angular range of the beam was about 25°, and the angular sensitivity to wavelength was −0.76°/nm.

5.3.2 Thermo-optic calibration of beam profile

To irradiate the chip that contains the fabricated device with a blue laser, light was emitted from the cut surface of the multimode fiber (MMF). A blue laser diode (LD) (Neoark, TCSQ-441W) with a wavelength of 441 nm was connected to the MMF and radiated from the cut surface of the MMF to the aperture of an optical power meter (OPM) (Ophir, PD300-3W-V1). The OPM was equipped with a filter and the measurement wavelength was set to 441 nm. The MMF was fixed on a stage, the end of the MMF was placed near the center of the OPM aperture plane, and the micrometer was adjusted to maximize the observed value of the OPM. The observed output radiated from the MMF for the current injected into the LD is shown in Fig. 5.18. The threshold current was 0.2 A, and 372 mW was obtained for a maximum injection current of 1 A.
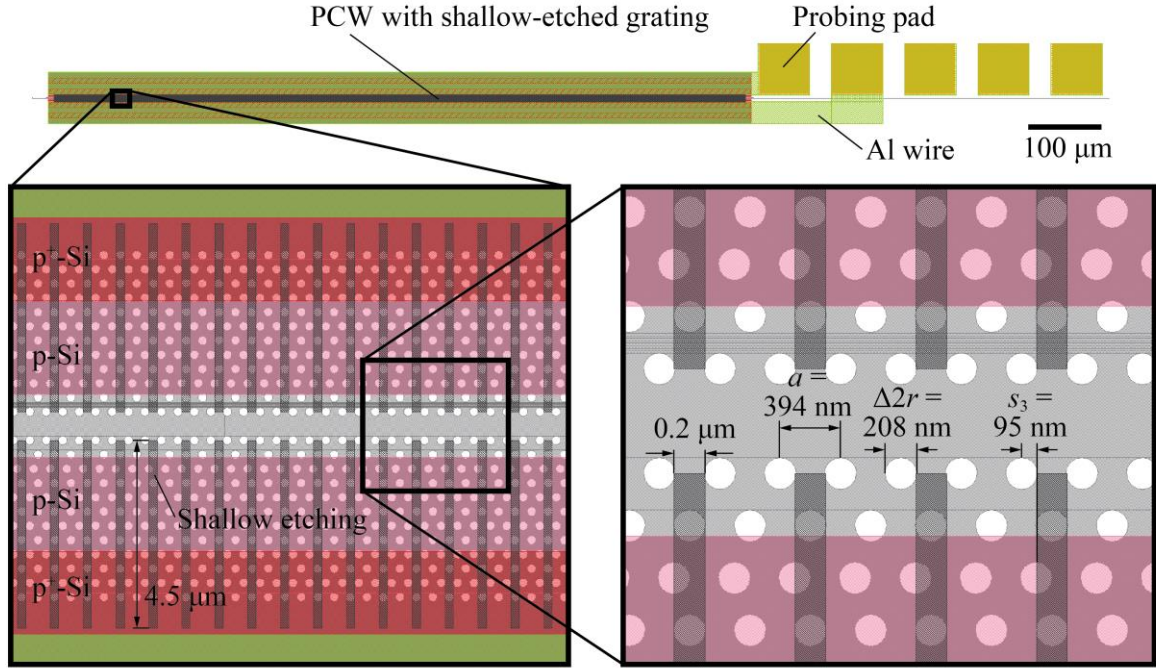
Fig. 5.14 CAD layout of PCW with shallow-etched grating fabricated in Foundry B. Insets show the magnified views of p-i-p heater of PCW and line defect of PCW.

Table 5.1 Parameters of PCW.

Lattice constant a [nm]	394
Hole diameter $2r$ [nm]	208
Third row shift s_3 [nm]	95
Width of shallow-etched grating [nm]	200
Aperture ℓ [µm]	942
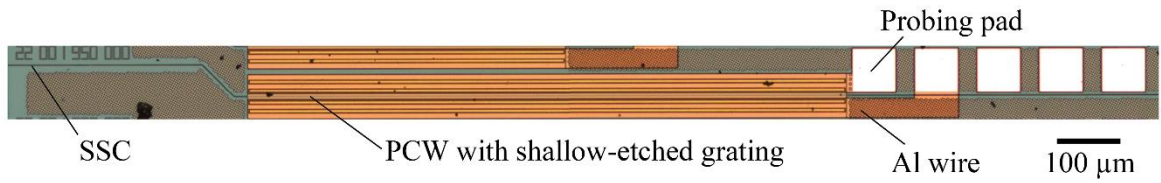
Fig. 5.15 Microscopic image of fabricated PCW in Foundry B.
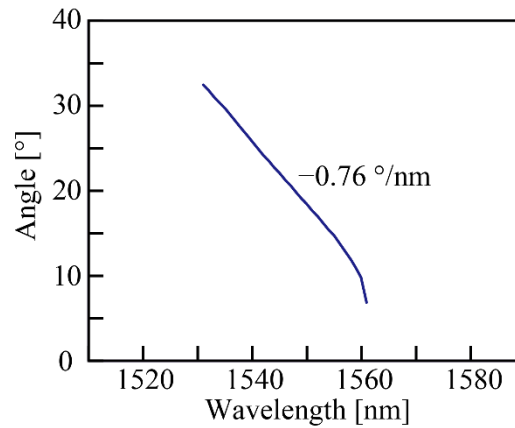
Fig. 5.16 Beam angle with wavelength of input light.
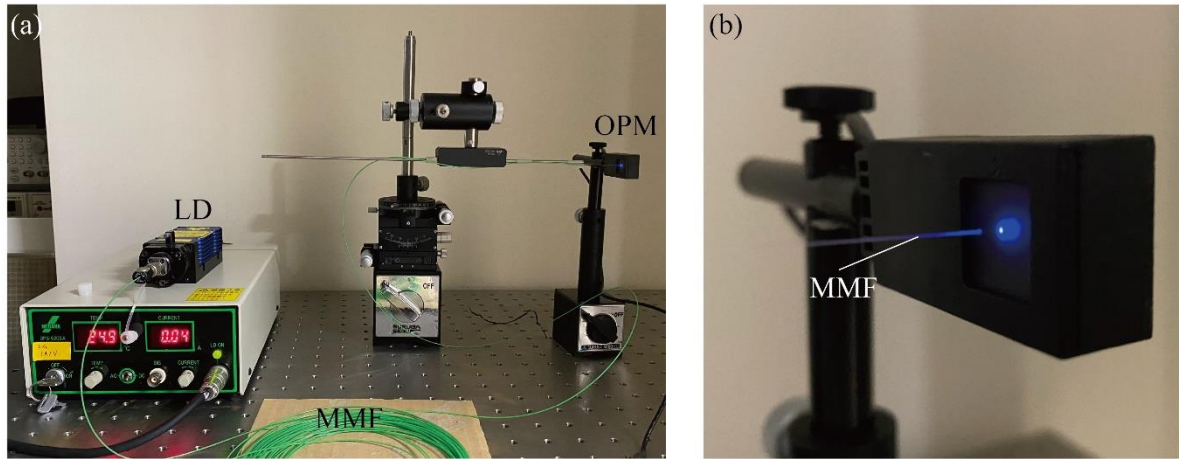
Fig. 5.17 (a) Setup for measuring the output power of MMF from the LD. (b) Magnified view of the aperture of the OPM, where the blue light was illuminated from the cut surface of the MMF.
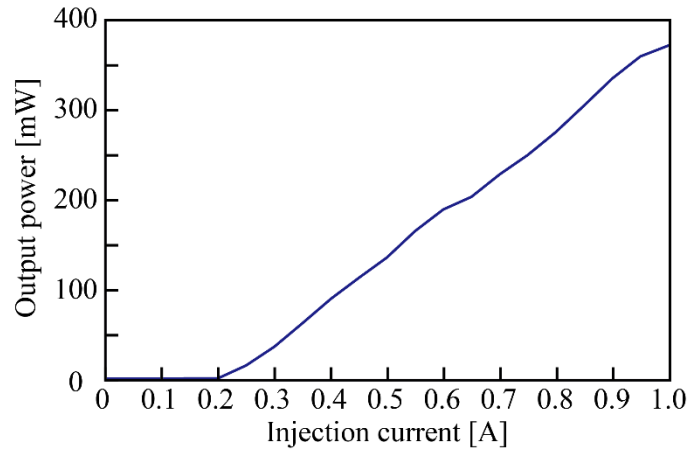
Fig. 5.18 Output power from the MMF with the injection current of the LD.
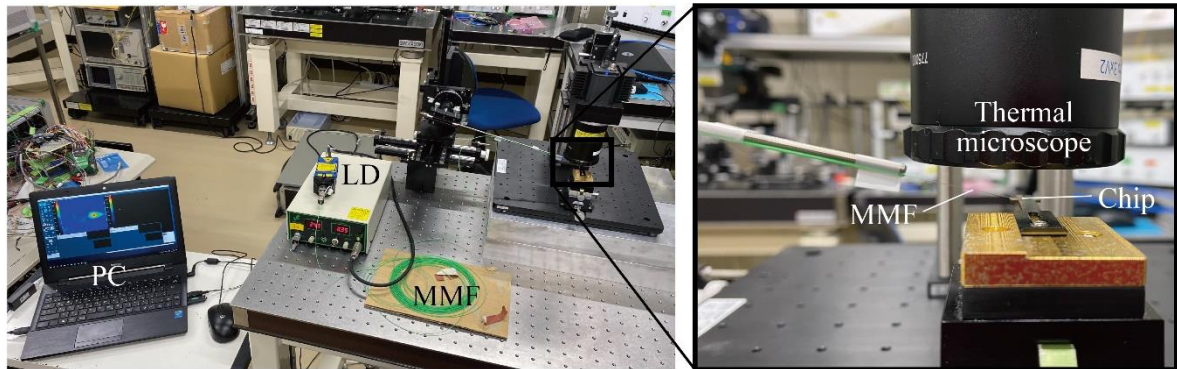
Fig. 5.19 Setup for observing the temperature distribution on the chip when illuminating the blue light. Inset shows the magnified view of the chip and the edge of the MMF, Thermal microscope.

After the output power in relation to the injection current into the LD was confirmed, a measurement system was set up as shown in Fig. 5.19 to check what kind of temperature distribution was formed when the chip was irradiated. The output from the LD was irradiated via MMF onto a chip fixed to a stage, where the angle of incidence of the MMF could be adjusted with a micrometer to enable the temperature distribution to be checked for any angle and output. The temperature distribution was analyzed using a thermal microscope (ViewOhre Imaging, XMCR32-SA0350-3XHT) placed above the

77

chip and software on a PC. The picture taken by a normal camera when the light was irradiated on the chip is shown in Fig. 5.20(a), and the light was irradiated near the edge of the PCW. The temperature distribution observed by thermal microscopy is shown in Fig. 5.20(b), confirming that a temperature gradient was formed around the edge of the PCW. The temperature profile in the waveguide direction at the center of the waveguide is shown in Fig. 5.20(c), where a temperature gradient of 3.5°C was formed over approximately 450 μm.

On the basis of the above conditions, a measurement system was constructed as shown in Fig. 5.21, and the beam profile and the beat signal spectrum from the FMCW LiDAR transmission and reception experiment before and after the beam calibration by the temperature gradient formation were observed and compared. The AWG settings for FMCW signal generation are shown in Table 5.3. The beam profile was obtained from an InGaAs camera by irradiating the beam onto a blank board, as shown in Fig. 5.22(a). As shown in Fig. 5.22(b), an MMF was inserted between the collimator lens and the chip and irradiated with a blue laser. The LD injection current and MMF position were adjusted to maximize the peak intensity in the beam profile. The beam profiles and corresponding beat spectrum before and after calibration are shown in Figs. 5.23 and 5.24, respectively. The slight sidelobes caused by fabrication errors were suppressed, a beam profile close to the theoretical value was obtained, and the signal intensity in the FMCW LiDAR experiment was improved by 4.1 dB.
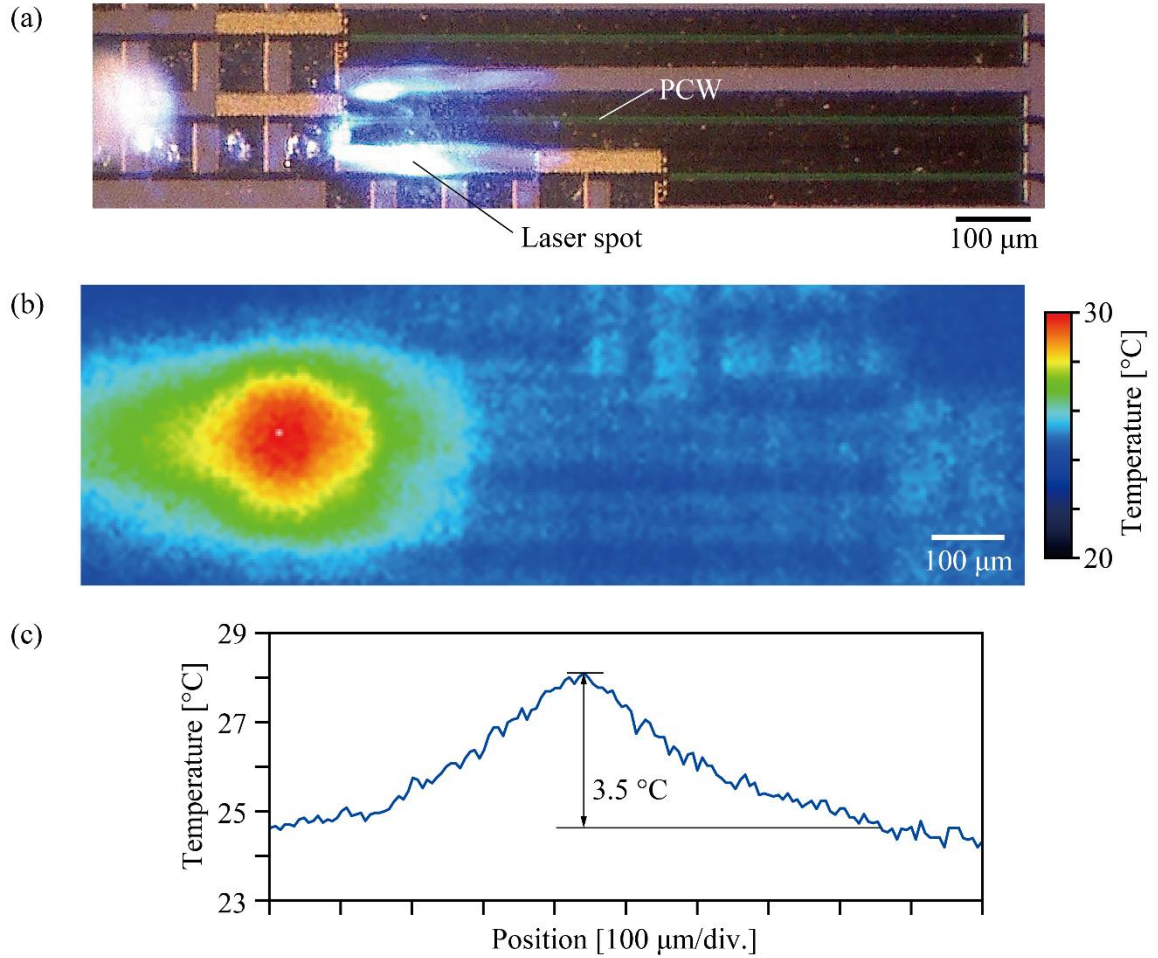
Fig. 5.20 (a) Image captured by a normal camera when illuminating blue light on the chip. (b) Temperature distribution obtained by the thermal microscope. (c) Temperature profile at the center of the PCW in the direction of the PCW.
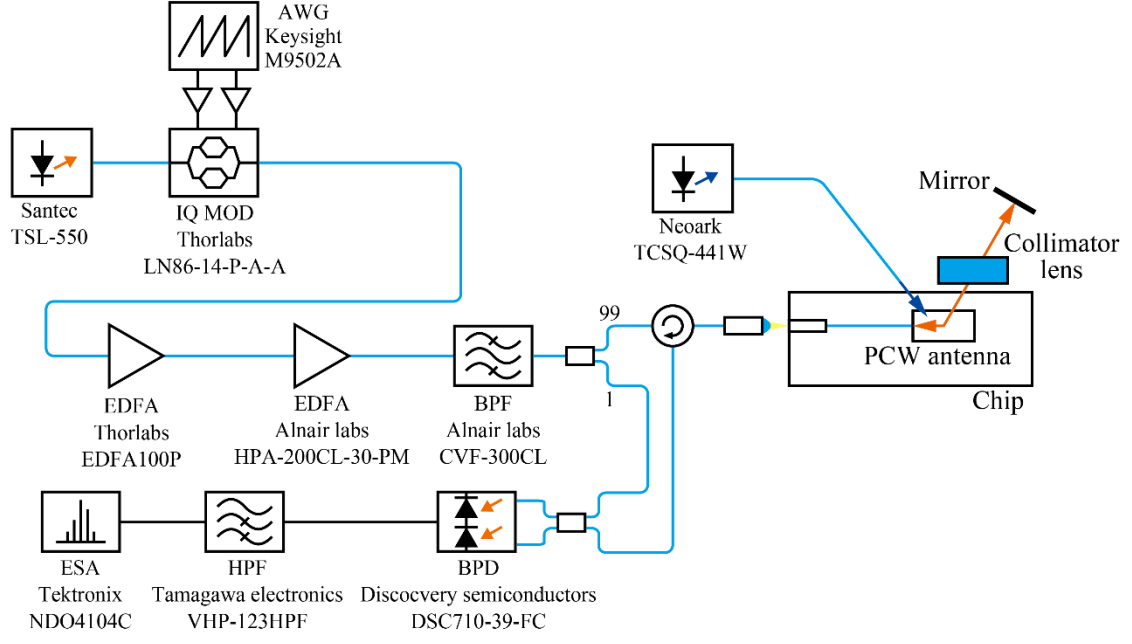
Fig. 5.21 Setup for FMCW LiDAR.

Table 5.3 Setting of AWG.

Sample rate [Hz]	32×10^9	Modulation on pulse	Increasing
Repeat interval [s]	8×10^{-6}	Frequency span [Hz]	10×10^9
Pulse width [s]	4×10^{-6}	Frequency offset [Hz]	6×10^9
Rise time [s]	2×10^{-6}	Amplitude of Ch.1 [mV]	800
Fall time [s]	2×10^{-6}	Amplitude of Ch.2 [mV]	800
Pulse shape	Gaussian		

Fig. 5.22 (a) Setup for observing the beam profiles. (b) Magnified view of the chip.

(a)   (b)
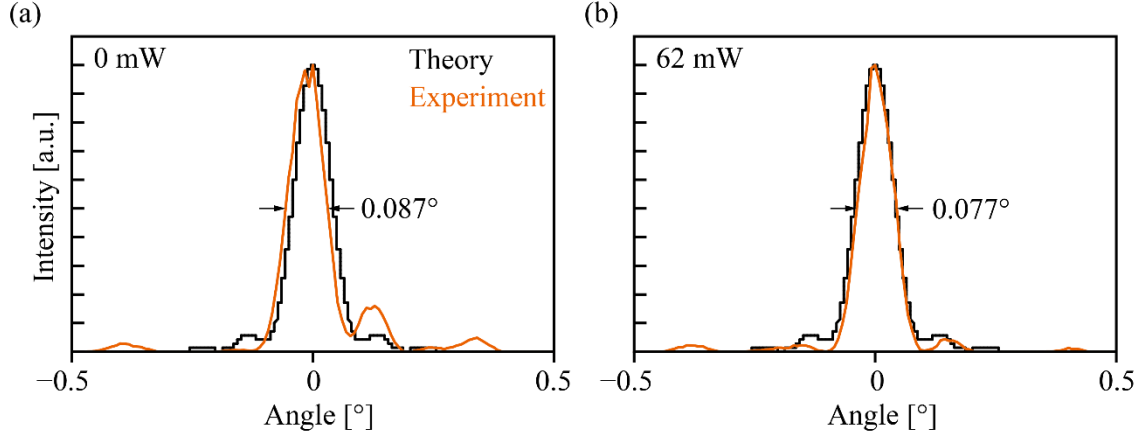
Fig. 5.23 Beam profiles (a) with and (b) without calibration.

(a)   (b)
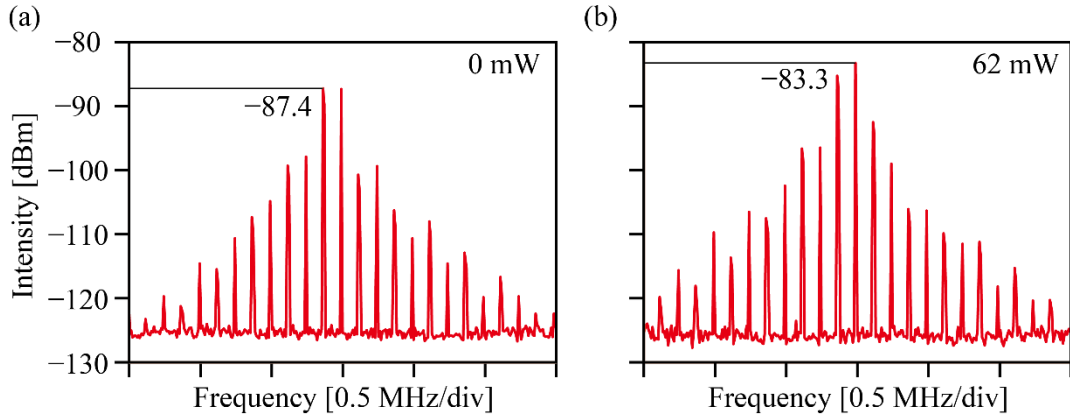
Fig. 5.24 Beat spectrum (a) with and (b) without calibration.

5.4 Discussion

This chapter demonstrates that the formation of a temperature gradient by thermo-optic control is effective in improving the transmission and reception characteristics of the PCW optical antenna. PCWs fabricated by silicon photonics were assumed to have an inclination of beam angle distribution due to non-uniformity during fabrication, and thermo-optic control was used in this study to compensate for this inclination. As demonstrated in the OPA, the phase distribution within the aperture of the PCW was calculated to obtain the focusing effect. The effects of fabrication errors and focusing effects could be compensated by additional thermo-optical heaters that provide phase distribution and structural modulation of the PCW. As an initial experiment, thermo-optic control by blue laser irradiation suppressed the sidelobes in the beam profile to obtain a profile close to the theoretical value, and the signal intensity was improved by 4.1 dB in the FMCW LiDAR experiment. In this measurement system, the beam was observed in the far field region. Therefore, the correction of fabrication errors had a greater effect on the improvement in signal intensity than the focusing effect.

References

[5-1]   J. Notaros, C. V. Poulton, M. Raval, and M. R. Watts, "Near-Field-Focusing Integrated Optical Phased Arrays," Journal of Lightwave Technology, vol. 36, no. 24, pp. 5912−5920, 2018.

[5-2]   S. Zhou, Z. Shen, X. Li, S. Ge, Y. Lu, and W. Hu, "Liquid crystal integrated metalens with dynamic focusing property," Opt. Lett. Vol.45, no. 15, pp. 4324−4327, 2020.

[5-3]   T. Chantakit, C. Schlickriede, B. Sain, F. Meyer, T. Weiss, N. Chattham, and T. Zentgraf, "All-dielectric silicon metalens for two-dimensional particle manipulation in optical tweezers," Photon. Res. vol. 8, no. 9, pp. 1435−1440, 2020.

[5-4]   P. Pentikäinen, E. J. O'Connor, A. J. Manninen, and P. Ortiz-Amezcua, "Methodology for deriving the telescope focus function and its uncertainty for a heterodyne pulsed Doppler lidar," Atmos. Meas. Tech., vol. 13, no. 5, pp. 2849–2863, 2020.

[5-5]   T. Baba, T. Tamanuki, H. Ito, M. Kamata, R. Tetsuya, S. Suyama, H. Abe, R. Kurahashi, "Silicon photonics FMCW LiDAR chip with slow light grating beam scanner," IEEE J. Sel. Top. Quantum Electron., vol. 28, no. 5, pp. 8300208, 2022.

Chapter 6
Evaluation of Modulation Signal

6.1 Overview

In this chapter, the modulation signal intensity of the radiated beam when modulated signal light is used for the PCW optical antenna is discussed. As a possible application to free-space optical communication, an experiment of free-space optical transmission to two points by fast beam switching is described. When an intensity-modulated signal is used for PCW, as shown in Fig. 6.1, the slow light effect of PCW slows down the RF signal propagation, causing phase mismatch due to the tilt of the RF signal wavefront relative to the wavefront of the light emitted into space. This condition reduces the modulation signal intensity in the far field. The velocity of the RF signal propagation corresponds to the group velocity v_g, which can be expressed as $v_g = c/n_g$ using the speed of light c and the group index n_g. DSB modulation is discussed, where frequency modulates the amplitude envelope of the light rather than SSB modulation with an I-Q modulator, as used in FMCW LiDAR experiments. First, the signal intensity of the beam when an intensity-modulated signal is used in the PCW was calculated, and estimations were made as to what constraints are imposed on the length, n_g, and modulation frequency of the PCW. Next, a free-space optical transmission experiment was demonstrated, in which modulated signal beams were sent to fiber collimators set at two locations by switching the beams. Free-space optical communication is attracting attention as one of the methods to reduce the load of wireless communication [6-1, 2]. Here a rectangular wave is applied to the p-i-p heater to switch beams at high-speed. The received light from the fiber collimator was observed to see if data were transmitted to each point by observing the eye pattern on an oscilloscope after OE conversion.
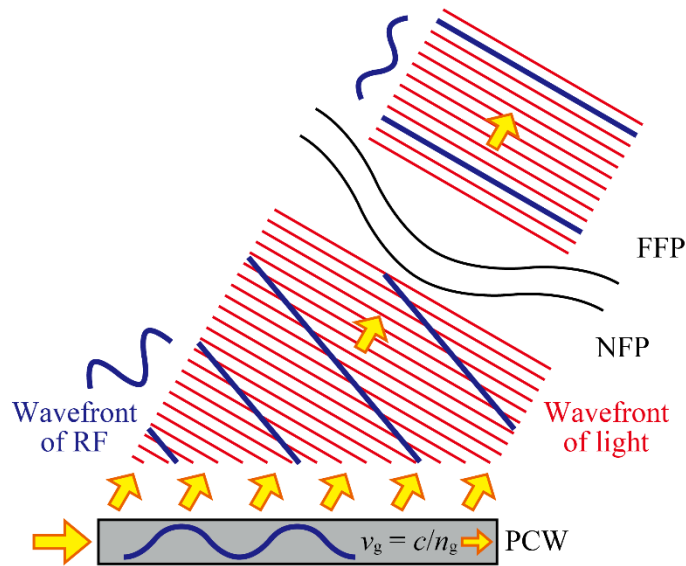

Fig. 6.1 Concept of phase mismatching between light and RF using PCW optical antenna.

6.2   Phase Mismatching Between Light and RF Signal

6.2.1   Calculation model

For the generation of the DSB signal, modulation with an MZI-type modulator was assumed. The output P_{mod} when light of power P_{IN} is input to an MZI-type modulator is defined as follows:

$$P_{mod} = P_{IN} \frac{1 + \cos(\phi_0 + m \sin 2\pi f_m t)}{2} \tag{6.1}$$

where ϕ_0 is the phase operating point, m is the modulation degree, and f_m is the modulation frequency. The modulated light intensity when $\phi_0 = \pi/2$ and $m = 1$, varying with respect to time t, is shown in Fig. 6.2. The modulation signal intensity was calculated from the time variation of the beam intensity in the far field of the radiated beam when the intensity-modulated light was input to the PCW. When determining the far field pattern, the modulated light power at the position z in the PCW needs to be described. Therefore, Eq. (6.1) can be rewritten using $v_g = c/n_g$ and expressed as follows:

$$P_{mod}(t,z) = \frac{P_{IN}}{2} \left\{ 1 + \cos\left[\phi_0 + m \sin 2\pi f_m \left(t - \frac{z}{v_g} \right) \right] \right\} \tag{6.2}$$

The far field intensity distribution of the light emitted from the PCW with respect to the angle θ is expressed as follows for the beam radiation angle θ_{rad}

$$I(t,\theta) = \left| \int_0^\ell \sqrt{\alpha_{rad}} \sqrt{P_{mod}(t,z)} \sqrt{e^{-(\alpha_{rad} + \alpha_{loss})z}} e^{-jk_0 \sin(\theta - \theta_{rad})z} dz \right|^2 \tag{6.3}$$

where the PCW aperture length, radiation coefficient, and waveguide propagation loss are ℓ, α_{rad}, and α_{loss}, respectively. By transforming Eq. (6.2), we obtain

$$P_{mod}(t,z) = P_{IN} \cos^2\left[\frac{\phi_0}{2} + \frac{m}{2} \sin 2\pi f_m \left(t - \frac{z}{v_g} \right) \right] \tag{6.4}$$

With Eq. (6.2) substituted into Eq. (6.3), the following equation can be obtained:

$$I(t,\theta) = \alpha_{rad} P_{IN} \left| \int_0^\ell \cos\left[\frac{\phi_0}{2} + \frac{m}{2} \sin 2\pi f_m \left(t - \frac{z}{v_g} \right) \right] e^{-\left\{ \frac{\alpha_{rad} + \alpha_{loss}}{2} + jk_0 \sin(\theta - \theta_{rad}) \right\} z} dz \right|^2 \tag{6.5}$$

From this equation, the change in peak intensity as t is varied was calculated, the difference between the maximum and minimum peak intensity was defined as the modulation signal intensity of the radiated beam, and the calculations when ℓ, f_m, and n_g are changed were compared to confirm the constraints on the parameters. The signal intensity was calculated by varying t in the range of $1/f_m$ or more to ensure that the amplitude change of the modulating signal was sufficiently expressed.

6.2.2   Modulation signal intensity

Figure 6.3 shows the calculated results of the modulation signal intensity when ℓ is varied, where the

wavelength is 1550 nm, α_{rad} = 100 dB/cm, and α_{loss} = 30 dB/cm. The results when f_m is varied from 1 to 10 GHz are shown. The calculations are normalized to the signal intensity at f_m = 0.1 GHz, when the decrease in signal intensity is sufficiently small. At n_g = 10, the decrease in intensity with increasing ℓ was more pronounced for higher f_m. At ℓ = more than 0.3, the signal intensity does not decrease any further because the light is not radiating through the aperture any further according to the emission coefficient and propagation loss. Therefore, the effective aperture remains constant. At n_g = 20, the slow light effect becomes more obvious, and the attenuation of the signal intensity is even larger. Moreover, a periodic change in signal intensity occurs, and the amplitude can be considered to reach a minimum when ℓ is N (a natural number) times the wavelength of the modulating signal, as expressed in the following equation:

$$\ell = N \frac{c}{n_g f_m} \tag{6.6}$$

From Eq. (6.6), ℓ is inversely proportional to the product of n_g and f_m. Therefore, a trade-off relationship exists between the two parameters. Figure 6.4 shows the modulation signal intensity calculated for f_m, where the parameter ℓ = 942 μm, which is the aperture length of the PCW optical antenna used in the experiments described in the next section. In accordance with Eq. (6.6), the signal intensity decreases significantly as n_g and f_m increase. When a fast modulation signal with a high slow light effect is used, the ℓ must be set short. When an intensity-modulated signal is used in PCW, the modulation frequency is restricted due to the slow light effect.
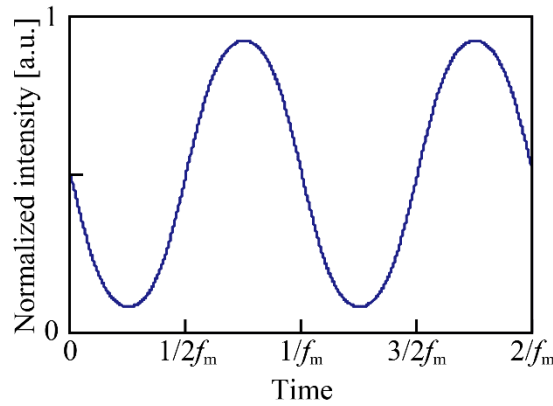
Fig. 6.2 Modulation signal intensity with time.
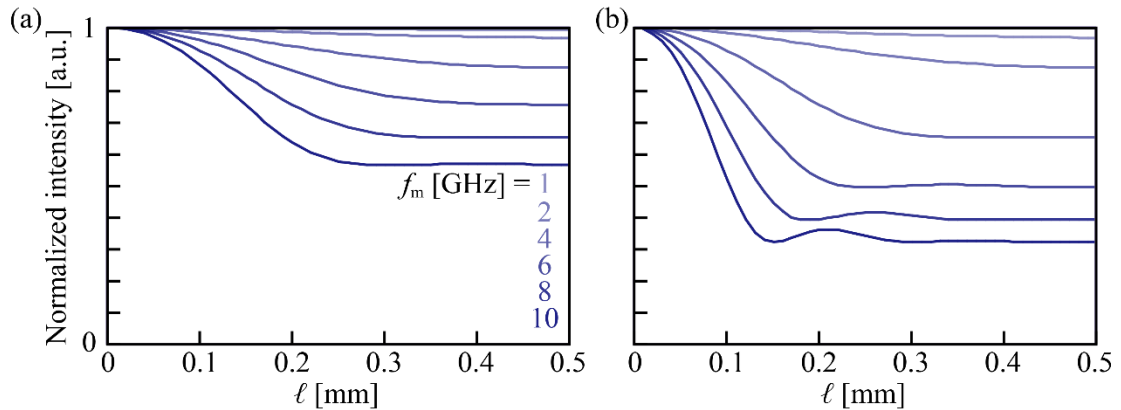
Fig. 6.3 Calculated modulation signal intensity with the aperture length of the PCW ℓ when modulation frequency f_m = from 1 to 10 GHz. (a) n_g = 10. (b) n_g = 20.
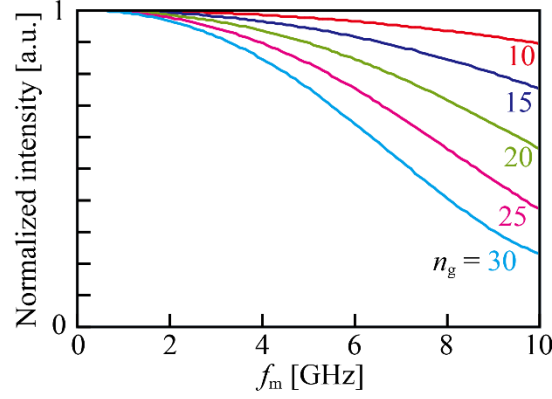
Fig. 6.4 Calculated modulation signal intensity with modulation frequency f_m.

6.3 Evaluation of Modulation Signal

6.3.1 Setup for observing modulation signal from the PCW

Figure 6.5 shows the measurement system used to observe the modulation signal intensity of the light emitted from the PCW. The output from the tunable wavelength laser (santec, TSL-550) was sinusoidally modulated by LN MOD (Alnair Labs, LNMOD-400), amplified by EDFA (Alnair Labs, CDA-100-CL), and then coupled through BPF (Alnair Labs, CVF-220CL) into the chip that includes PCW using a lensed fiber from SSC. The RF signal to drive the LN MOD was generated using AWG (Keysight, M9502A). After passing through the collimator lens, the light emitted from the PCW was extracted using an SMF from the fiber port attached to the NFP optical system for beam profile observation described in Chapter 3. The extracted signal light was input to an OPM (ADVANTEST, Q8221) through a channel selector (OPTOHUB, SY-0910-F) to confirm the light intensity. After the optical axis of the fiber with lens, the position of the NFP optics, and the position of the fiber port were adjusted to ensure a large output observed by the OPM, the waveform was switched by the channel selector, amplified by EDFA (Alnair Labs, LN-220-C), and connected to an oscilloscope (Agilent, 86100C) through BPF (Alnair Labs, CVF-220CL) for analysis, and the signal from the AWG was connected as the trigger source to the OSC.

6.3.2 Modulation signal

Figure 6.6 shows the signal waveforms observed by OSC when f_m is varied from 0.5 to 10 GHz. The amplitude of the waveform decreased as f_m increased. From this result, a graph that plots the experimental and theoretical values when the signal intensity is normalized at $f_m = 0.5$ GHz, is shown in Fig. 6.7. The theoretical values were calculated with $\alpha_{rad} = 100$ dB/cm and $\alpha_{loss} = 30$ dB/cm. When the experimental values were plotted, the signal generated by the AWG before modulation with LN MOD was observed by OSC to confirm only the effect of the modulated signal light on the PCW, and the experimental values were normalized by the amplitude characteristics of the waveform versus the modulation frequency. The experimental results showed that the signal intensity decreased as the modulation frequency increased, a tendency consistent with the theoretical value. The cutoff frequency of 3 dB was estimated to be approximately 10 GHz, confirming that the modulation frequency in the PCW optical antenna was constrained. In the next section, on the basis of this limitation to the modulation frequency, experiments on signal transmission to two points were conducted by combining the modulated signal light with high-speed beam switching of PCW as an application to free-space optical communications.
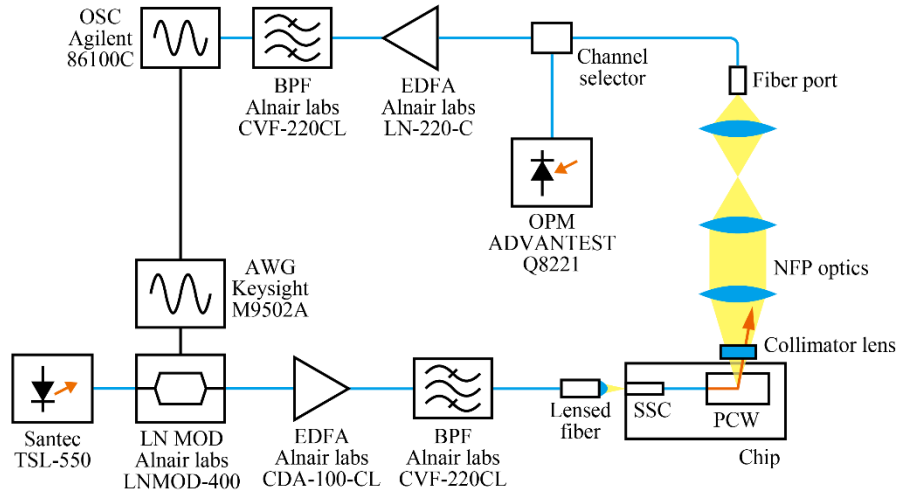
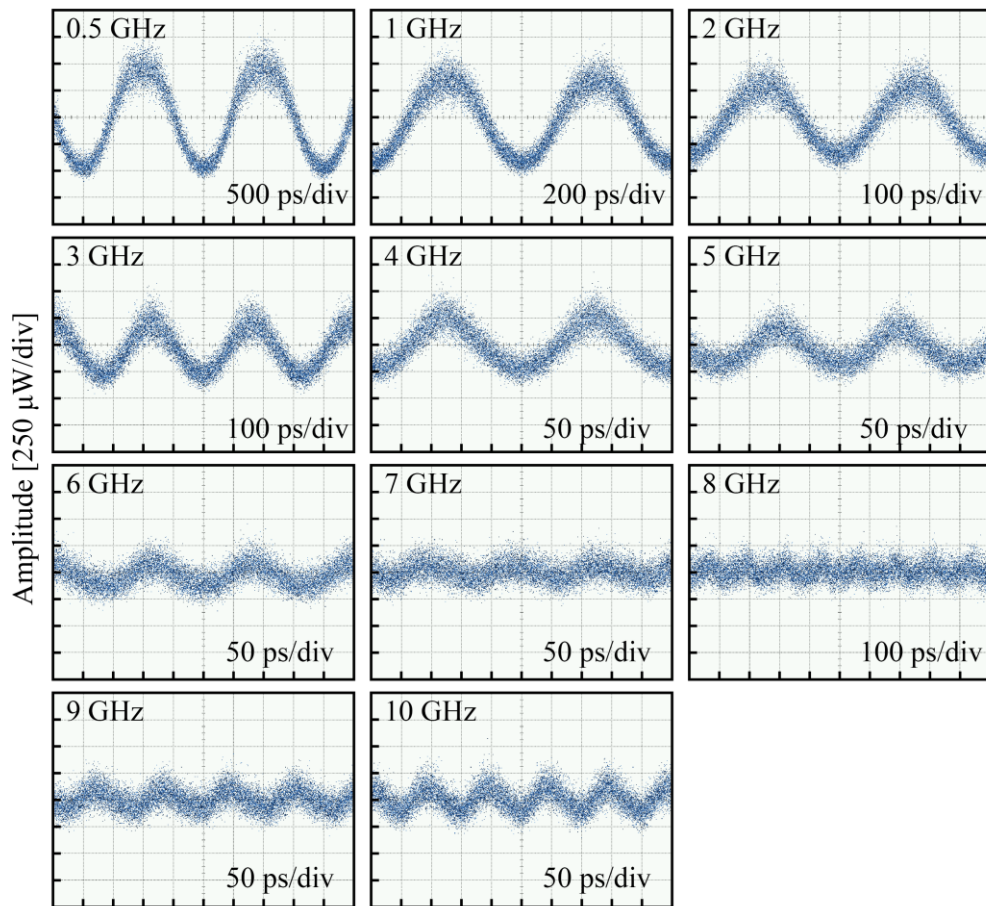Fig. 6.5 Setup for observing modulation signal intensity radiated from the PCW.

Fig. 6.6 Observed waveform of the modulation signal radiated from the PCW.
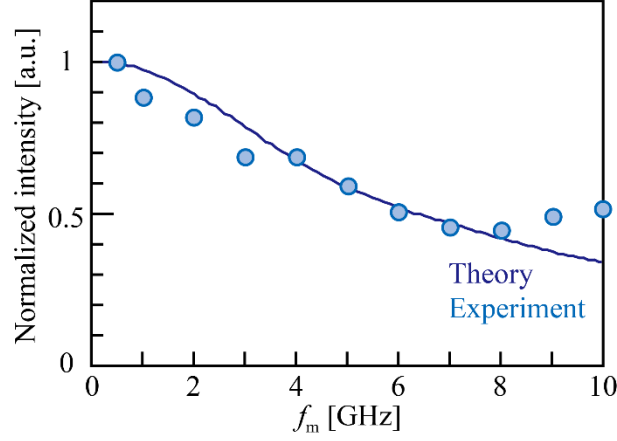
Fig. 6.7 Experimental and theoretical modulation signal intensity from the PCW with modulation frequency f_m.

6.4 Free-space Optical Transmission

6.4.1 Measurement of eye pattern

Before the free-space optical transmission experiment using PCW was conducted, the eye pattern of the modulated light was observed using the measurement system shown in Fig. 6.8. The output light from the tunable wavelength laser was set to 1550 nm, modulated by LN MOD, amplified by EDFA, and then input to an O/E converter (Agilent, 11982A). Here, the RF signal used to drive the LN MOD was a pseudo-random binary sequence (PRBS, $2^{15}-1$) generated by a pulse pattern generator (PPG) (Anritus, MP1800A) as the modulating signal, where the bit rate can be set from 2.4 to 32 Gbps. The injection current of EDFA was adjusted so that the input optical power to the O/E converter was 0 dBm.

Figure 6.9 shows the eye patterns observed when the bit rate is varied with the voltage measurement range of 35 mV/div. The bit rate supported by the O/E converter was up to 22 Gbps; thus, setting a bit rate higher than this value resulted in a narrower eye opening, and the bit rate limitation was confirmed in the measurement system before using PCW.

6.4.2 Setup for free-space optical transmission

Figure 6.10 shows the measurement system of the free-space optical transmission experiment using PCW. As in the measurement system shown in Fig. 6.8, the output light of 1550 nm wavelength was modulated by LN MOD using the PRBS signal by PPG as the modulation signal, amplified by EDFA, and then coupled into the SSC of the chip using a fiber with a lens, where the injection current of the EDFA was adjusted to achieve an output power of 15 dBm. The PCW was a device fabricated in Foundry B at $\ell = 942$ μm, as described in Chapter 5, which was equipped with a p-i-p type thermo-optical heater. A 1 kHz square wave signal generated by a function generator (FG) (Agilent, 33220A) was applied via a DC probe for fast switching between two beam angles. The emitted beam from the PCW passed through the prism lens shown in Fig. 6.11 and was reflected by a mirror to two fiber collimators (Thorlabs, F810FC-1559) located 1.5 m away. A photograph of the beam switching taken by an InGaAs camera is shown in Fig. 6.12. The output from the fiber collimator was −25 dBm after coupling into the SMF; thus, it was amplified to 0 dBm by the EDFA and then input to the O/E converter, and the signal was observed by the OSC.
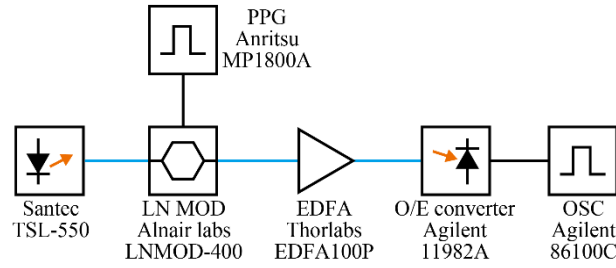
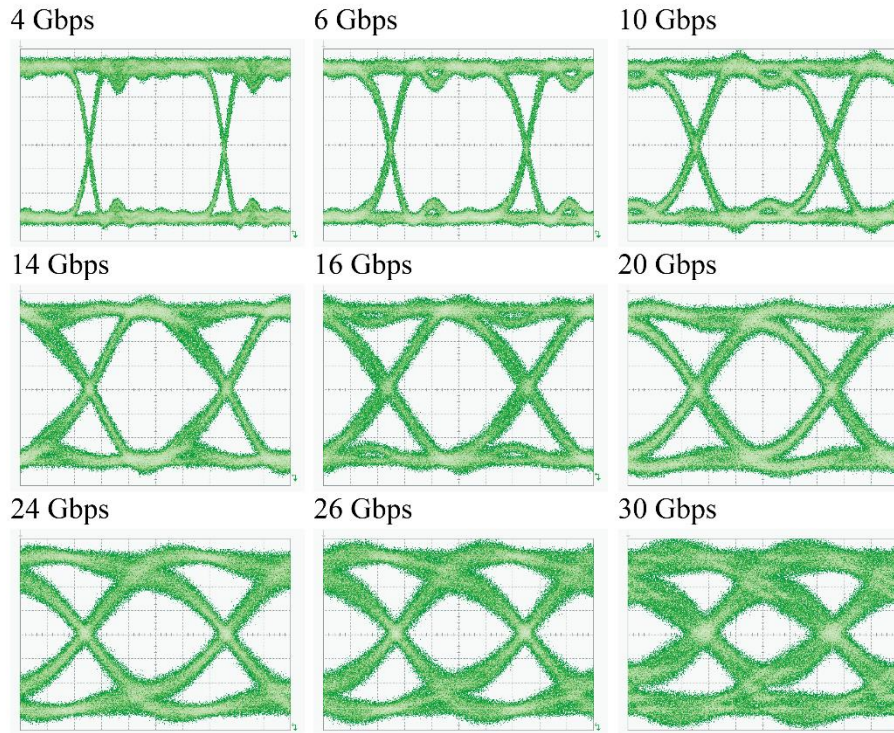Fig. 6.8 Setup for measuring eye patterns of modulation signal light.

Fig. 6.9 Measured eye patterns of modulation signal light from LN MOD. The voltage range was set as 35 mV/div.
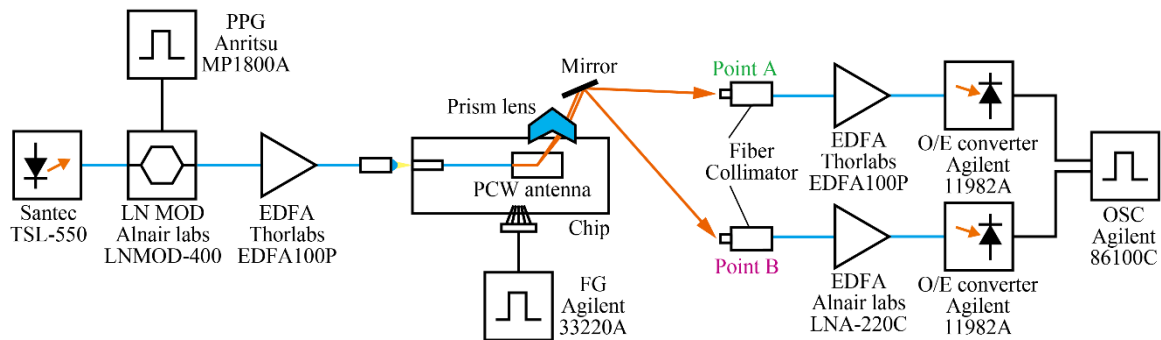

Fig. 6.10 Setup for demonstration of free-space optical transmission by using the PCW optical antenna with beam switching.
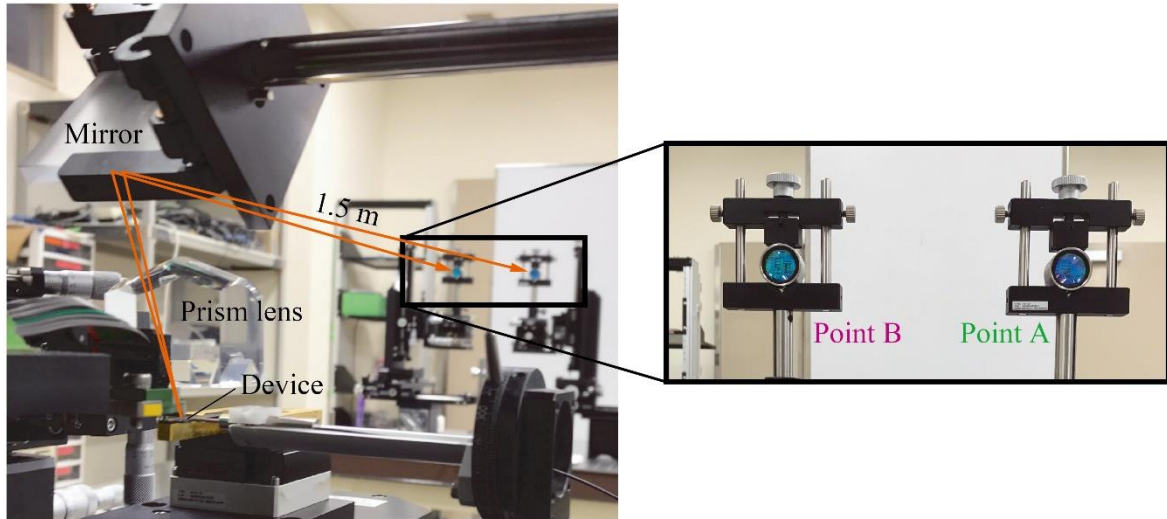
Fig. 6.11 Setup for free-space optical transmission. The inset shows the magnified view of two fiber collimators.
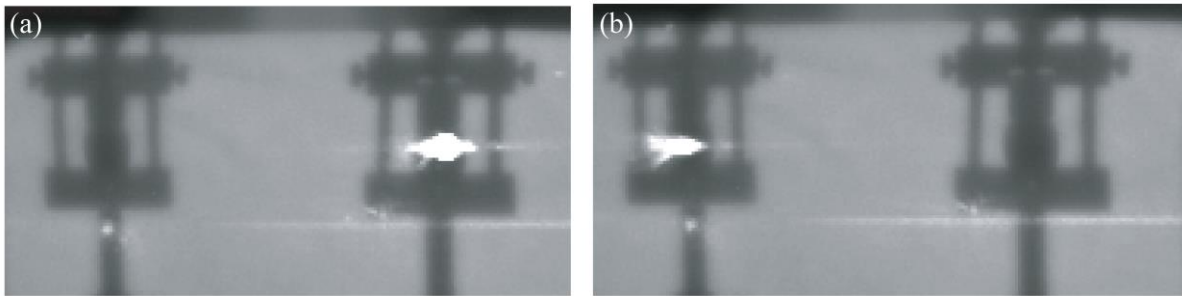

Fig. 6.12 Beam switching observed by InGaAs camera. (a) At point A. (b) At point B.

6.4.3 Demonstration of free-space optical transmission

The data sequence to each fiber collimator observed by the OSC is shown in Fig. 6.13. Data were transmitted to two points at a period corresponding to 1 kHz applied to the p-i-p heater. The eye patterns observed at each point are shown in Figs. 6.14 and 6.15. Eye opening up to 22 Gbps was confirmed for each point, demonstrating free-space optical transmission using PCW.
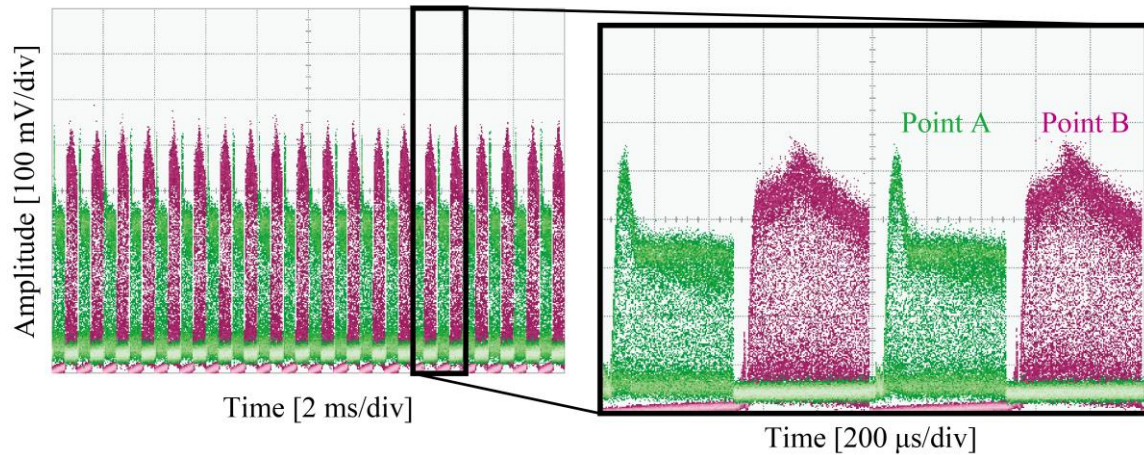
Fig. 6.13 Observed data sequence at each point.

10 Gbps   12 Gbps   14 Gbps   16 Gbps

18 Gbps   20 Gbps   22 Gbps   24 Gbps

26 Gbps   28 Gbps   30 Gbps   32 Gbps
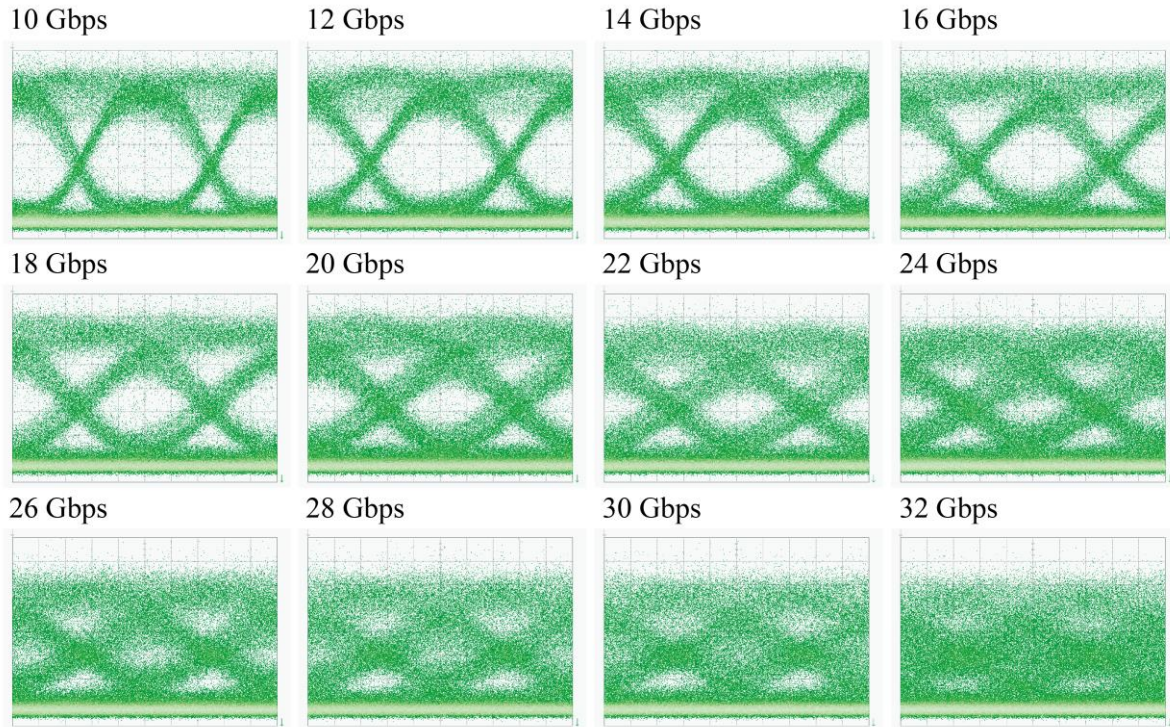
Fig. 6.14 Measured eye patterns at point A.

10 Gbps   12 Gbps   14 Gbps   16 Gbps

18 Gbps   20 Gbps   22 Gbps   24 Gbps

26 Gbps   28 Gbps   30 Gbps   32 Gbps
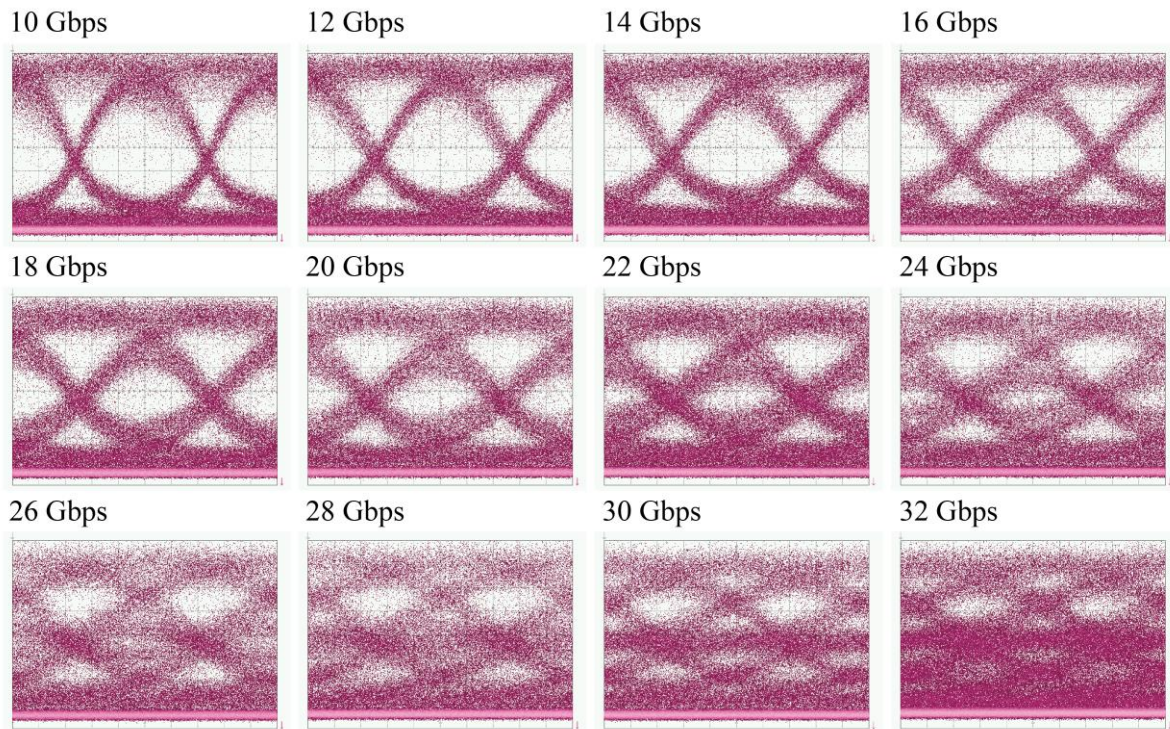
Fig. 6.15 Measured eye pattern at point B.

6.5   Discussion

In this chapter, the constraints on the modulation frequency when intensity-modulated signal light is used in PCW were estimated and experimentally confirmed. At a fixed length of PCW, the signal intensity decreases in proportion to the group index and the modulation frequency. The group index of

PCW, which was mainly designed in this study, was about 20, and in this case, the cutoff frequency is 10 GHz. As an application to free-space optical communication, data transmission up to 22 Gbps to two points was achieved by high-speed beam switching with a p-i-p heater driven at 1 kHz. At higher speeds, the amplitude component of the attenuated signal can be seen near the center of the eye pattern because of the bit rate limitation of the O/E converter, in addition to the attenuation of the high frequency component of the signal due to the slow light effect. The intensity of the data sequence observed at each location was not constant, which may represent beam drift due to the thermal response of the p-i-p heater. This issue can be corrected by using a waveform such as a pre-emphasis signal instead of a rectangular wave to fix the beam position [6-3].

References

[6-1]   T. Koonen, J. Oh, K. Mekonnen, Z. Cao, E. Tangdiongga, "Ultra-High Capacity Indoor Optical Wireless Communication Using 2D-Steered Pencil Beams," J. Lightwave Technol., vol.34, no. 20, pp. 4802−4809, 2016.

[6-2]   T. Koonen, "Indoor Optical Wireless System : Technology, Trends, and Applications," J. Lightwave Technol., vol.36, no. 8, pp1459−1467, 2018.

[6-3]   J. Gondo, H. Ito, T. Tamanuki, and T. Baba, "Space-time-domain observation of high-speed optical beam scanning in a thermo-optic Si photonic crystal slow-light beam scanner," Opt. Lett., vol. 46, no. 15, pp. 3600−3603, 2021.

Chapter 7
Acquisition of Point Cloud Image

7.1 Overview

This chapter describes a range image acquisition, i.e., point cloud image, based on the FMCW LiDAR method using a fully integrated LiDAR chip that includes a two-divided PCW subarray configuration and Ge BPD for signal detection. The configuration and parameters of the device fabricated for the LiDAR chip are first described, followed by the fiber connections used for optical input/output and wire bonding for electrical signals. A LiDAR driver composed of a DAC-controlled operational amplifier circuit was used for 2D beam scanning and for driving the thermo-optic heaters to heat the PCWs. The beam angles of the integrated PCWs differ slightly from each other due to fabrication errors; thus, the PCWs were calibrated using thermo-optic control. The wiring was modified so that only one of the PCW subarrays could be heated, because the PCW subarrays were configured to be heated simultaneously due to the wiring for integration. Finally, point cloud images were acquired for various objects by combining 2D beam scanning and FMCW LiDAR transmission and reception experiments using a LiDAR chip with a calibrated beam profile.

7.2 Fully Integrated LiDAR Chip

7.2.1 Design

The design of the PCW subarray with $N = 2$ integrated on a LiDAR chip, fabricated in Foundry A, is shown in Fig. 7.1. The main design parameters are shown in Table 7.1. An PCW with $s_3 = 95$ nm was used, and a shallow-etched grating was employed for radiation. The aperture length ℓ and the gap g between the apertures were 1208 and 58.6 μm, respectively, where the gap includes the bending of the Si waveguide and the tapered structure to connect the PCW. The taper length was designed to be 10 μm to keep the non-radiation area as short as possible. A p-i-p type thermo-optic heater was designed to heat the PCW that contains the shallow-etched grating, as shown in Fig. 7.2.

The configuration of 32 PCW subarrays integrated in parallel is shown in Fig. 7.3. One PCW subarray was equipped with a power splitter on both sides to allow input from either the left or right side. The 32 PCW subarrays had a thermo-optic MZI-type SW tree on the left and right sides, with additional SWs outside these arrays for switching the left and right inputs, enabling 2D beam scanning by switching PCW subarrays and wavelength sweep or thermo-optic control. The layout of the LiDAR chip is shown in Fig. 7.4. Three optical inputs and outputs exist; the first is the input to the PCW modulator, the second is a port to output a portion of the modulated light, and the third is a port to re-input the externally amplified light. In this study, an external modulator was used due to a malfunction of the PCW modulator. Therefore, the modulator inside the chip was not used. The modulated signal light needs to be split and the reference light and the reflected light are mixed to obtain the beat signal in the FMCW LiDAR; thus,

the modulated signal light was split externally, the reference light was input through the PCW modulator from port 1, and the main light to be emitted from the PCW was input through port 3. The light from port 3 passes through a 2 × 2 MMI coupler, half to the SW tree and the other half to the SSC at the chip end opposite the ports, which was used for optical axis adjustment to fix a fiber array block on the input port side. The reflected light returned from the PCW was input to the Ge BPD through a 2 × 2 MMI coupler and interfered with the reference light to detect electrical signals from two connectors out of the chip from two Ge PDs. Ideally, if the sensitivity of the two Ge PDs is the same, then balanced detection would be possible. However, considering the influence of fabrication errors, the system was configured so that the electrical signals can be taken out separately for balancing with an external attenuator. In this configuration, the main input light from port 3 passes through the 2 × 2 MMI coupler twice before being reflected from the object and received by the Ge PD, resulting in a loss of 6 dB in principle.
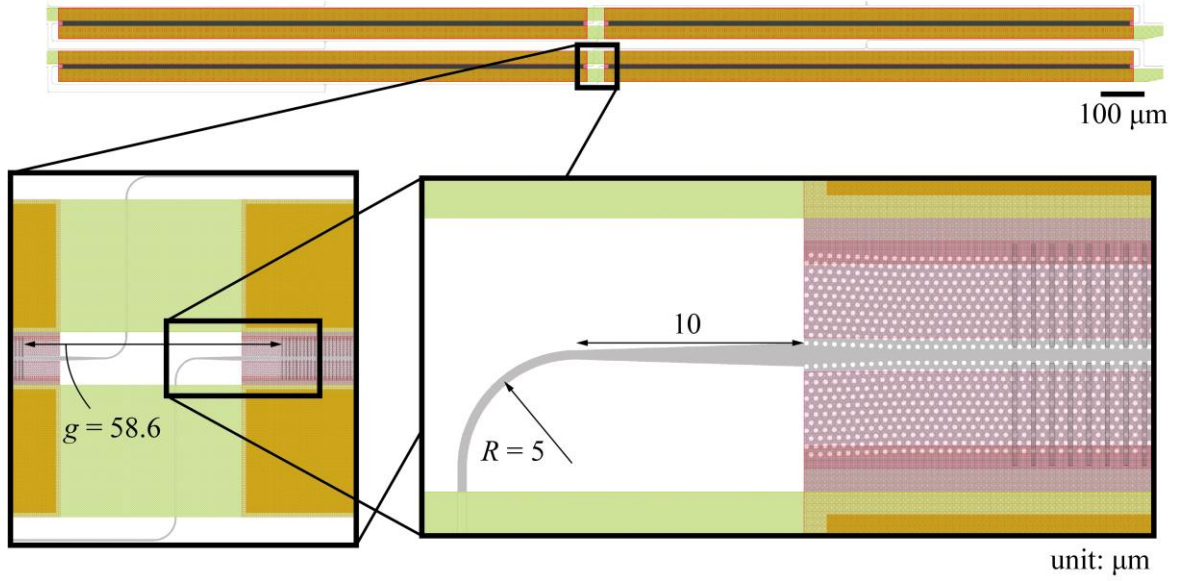
Fig. 7.1 CAD layout of the PCW subarray with $N = 2$. Magnified views show the gap between apertures including the bending and taper structures of Si waveguides.
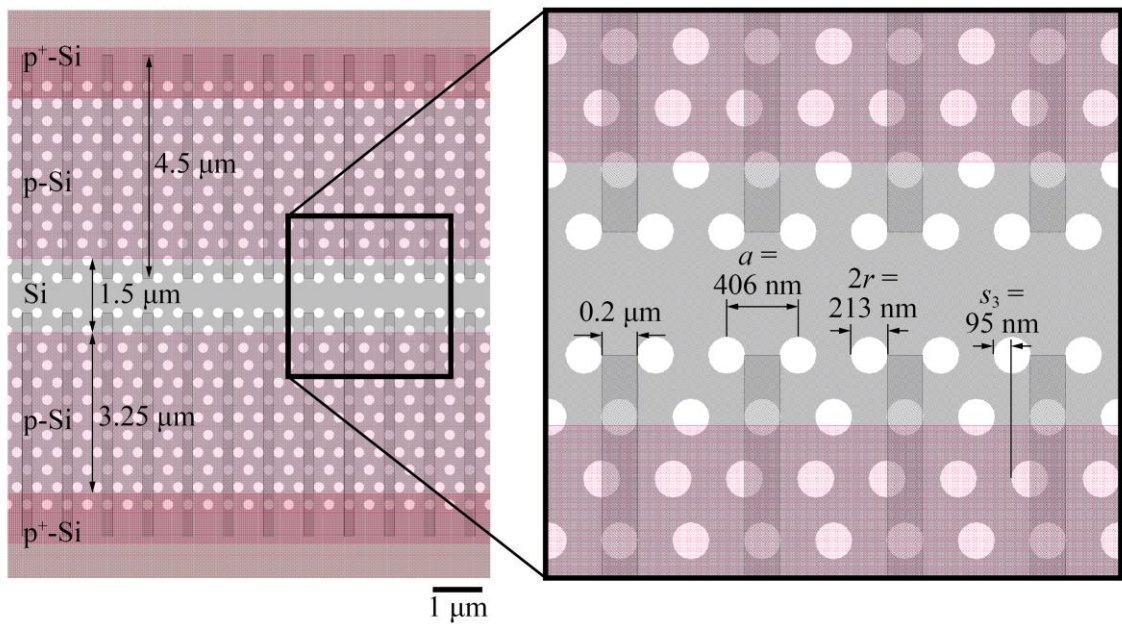
Fig. 7.2 CAD layout of PCW with shallow-etched grating and p-i-p heater.

Table 7.1 Parameters of PCW subarray.

Lattice constant a [nm]	406
Hole diameter $2r$ [nm]	213
Third row shift s_3 [nm]	95
Width of shallow-etched grating [nm]	200
Aperture ℓ [μm]	1208
Gap between apertures g [μm]	58.6
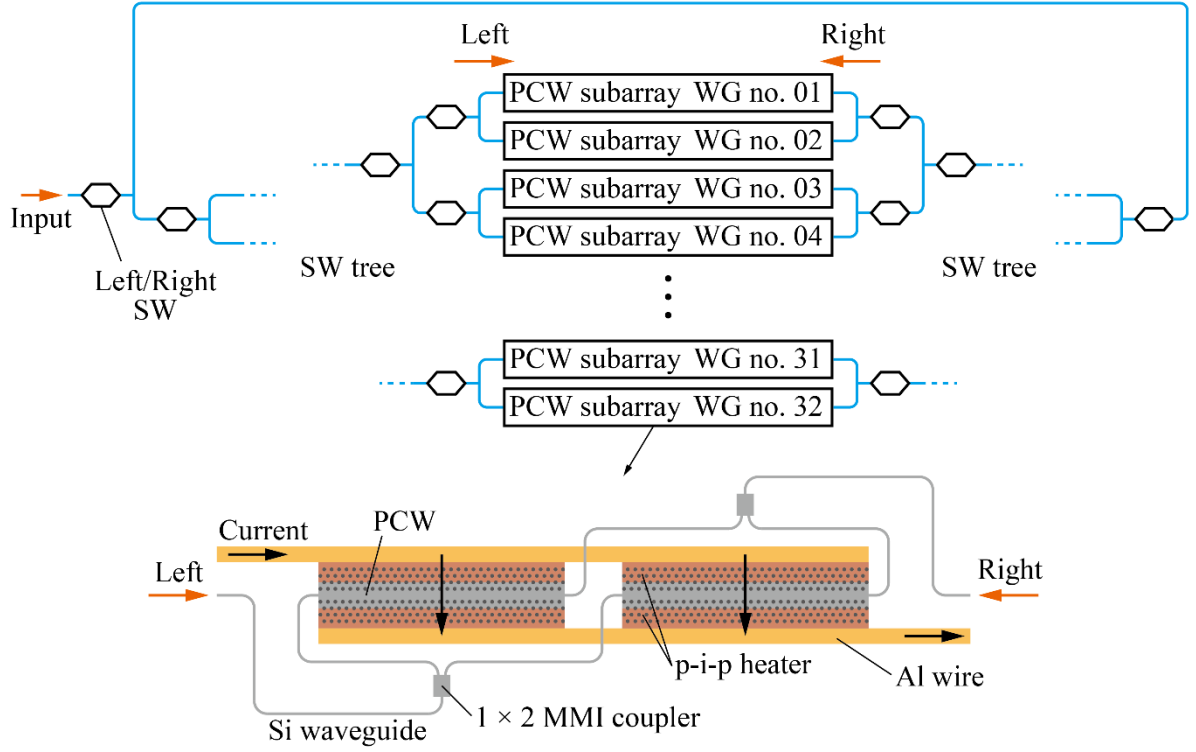
Fig. 7.3 Configuration of PCW subarrays integrated in parallel. Insets show each PCW subarray with p-i-p heater and tournament-type splitter.
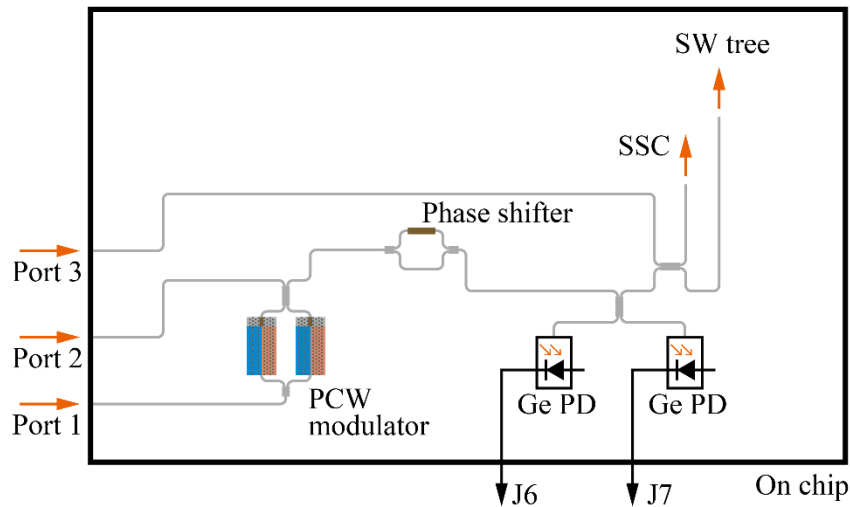

Fig. 7.4 Layout of LiDAR chip.

7.2.2 Fabricated device

A microscopic image of the fabricated LiDAR chip is shown in Fig. 7.5. Thirty-two PCW subarrays were integrated in the center, and SW trees for waveguide input switching were located on the left and right. Ge BPD for signal detection was integrated at the edge of the chip. Bonding pads connected to Al wiring were located on the top and bottom of the chip for waveguide switching, PCW heater control, and detection of electrical signals from Ge BPDs. These pads were connected to the PCB by wire bonding, the LiDAR driver was used to control the heater for waveguide switching and PCW, and the electrical signals from the Ge BPD were analyzed by ESA. A fiber block for optical input/output was attached to the left end of the chip. This fiber was a core-shrunk polarization-maintaining fiber fixed by using ultraviolet curing resin.

A magnified microscopic image of the optical circuit configuration for the SSC and PCW modulators for optical input/output, Ge BPD, and FMCW LiDAR operation is shown in Fig. 7.6. The PCW modulator was designed to generate a pseudo-frequency modulation using an intensity modulation of the amplitude of the light. However, it was not used as a modulator in this study, but rather as a reference light path. This approach resulted in restrictions on the transmission characteristics of PCW. The reference light intensity was adjusted for coherent detection with the reflected light by adjusting the power balance (PB) of the attenuator using a thermo-optic heater. The Ge BPD was configured to ensure common ground electrodes of the two Ge PDs and to enable the signal electrodes to be taken out separately.

Figure 7.7(a) shows a photograph of a LiDAR chip connected to an optical fiber and mounted on a PCB. Three optical fibers that correspond to the ports were connected, which were polarization-maintaining single-mode fibers with FC/APC connectors. As shown in Fig. 7.7(b), SMP connectors mounted in the form of PCBs were used to detect signals from the Ge PD.
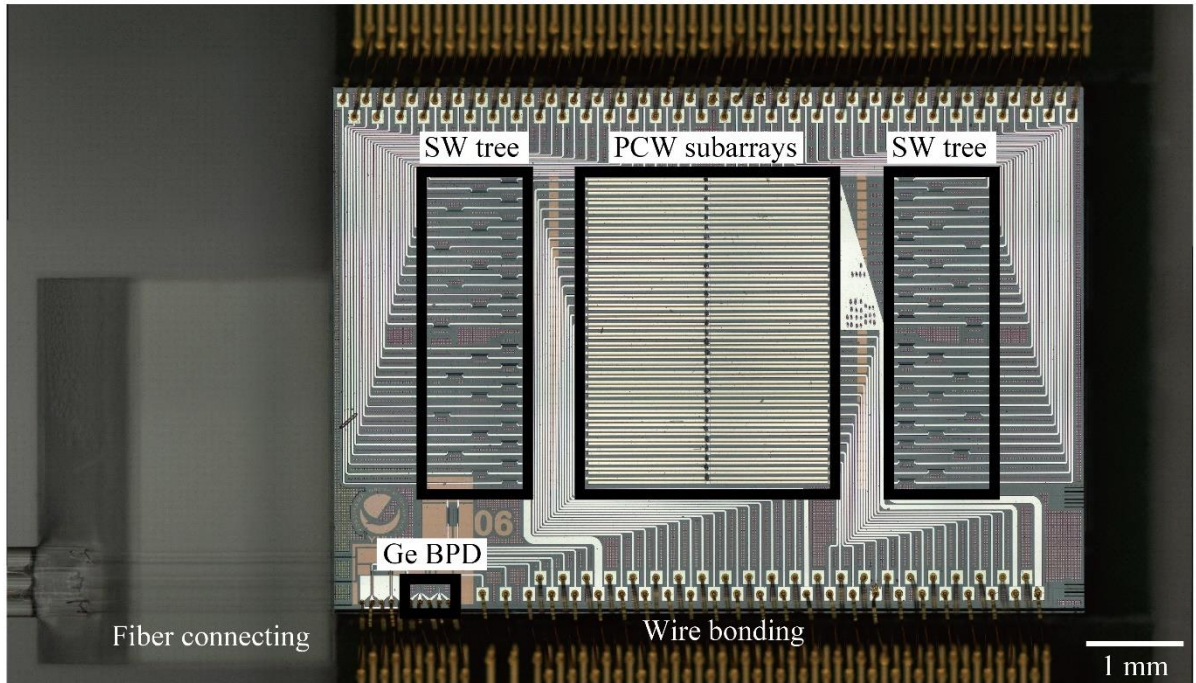

Fig. 7.5 Microscopic image of fabricated LiDAR chip that includes PCW subarrays and Ge BPD, which was connected with the fiber block and mounted on the PCB.
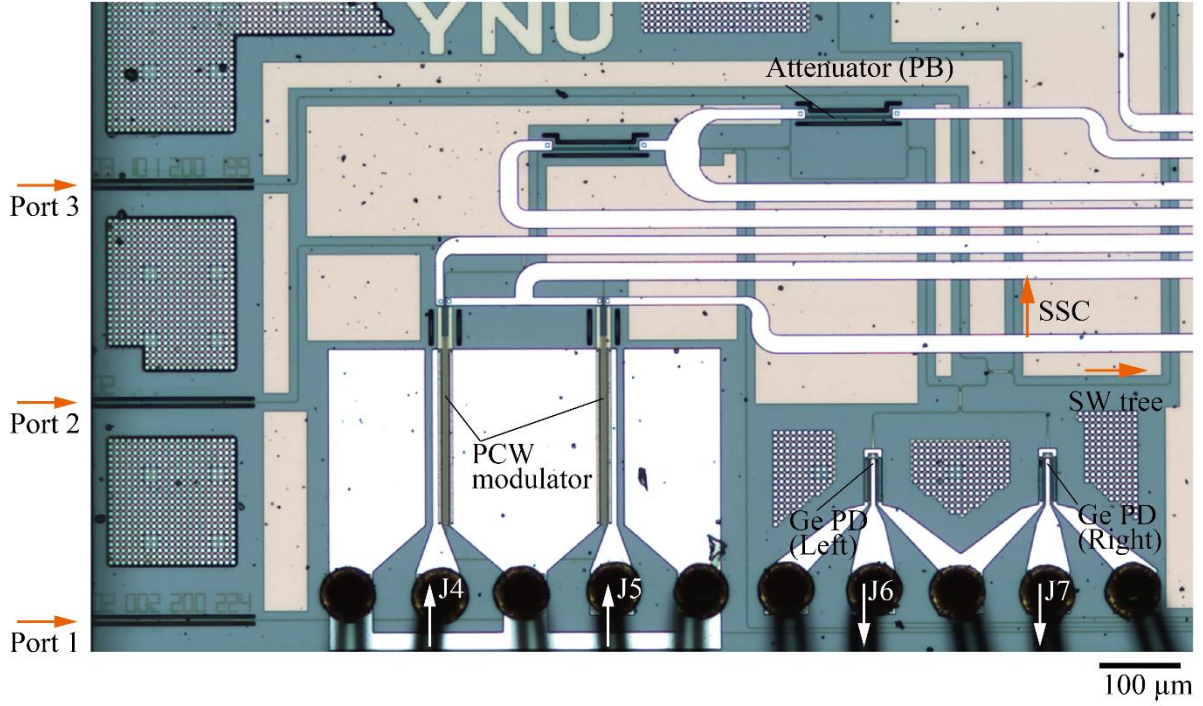
Fig. 7.6 Magnified view of the microscopic image of SSCs for input and output, and the PCW modulator, Ge BPD, and optical circuit for FMCW LiDAR.
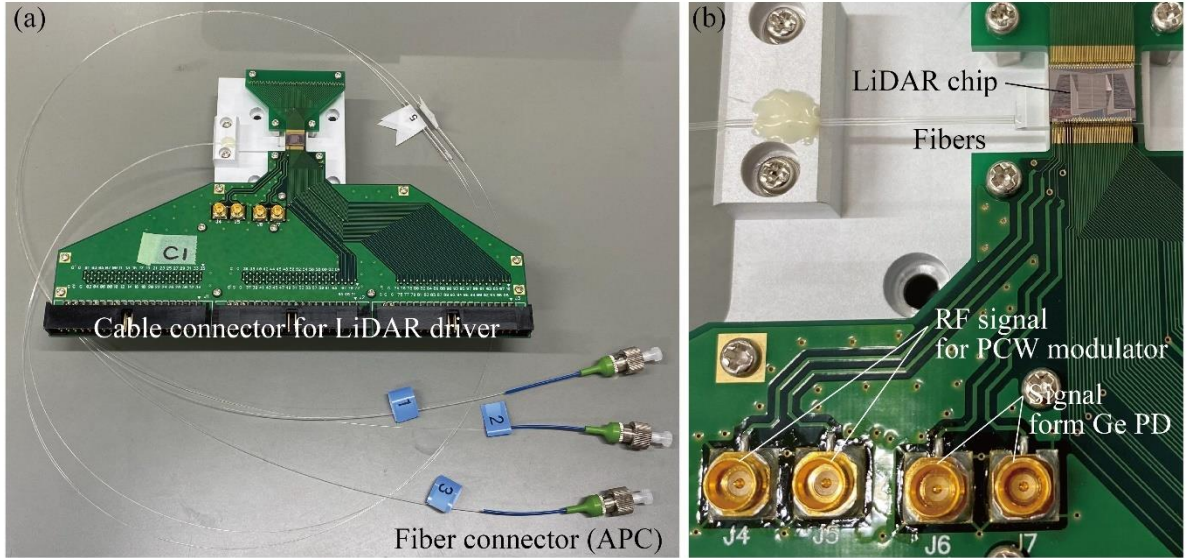

Fig. 7.7 (a) LiDAR chip connected to optical fibers and mounted on the PCB. (b) Magnified view of SMP connectors for the signal from Ge PD and the RF signal for the PCW modulator.

7.3 LiDAR Driver

Figure 7.8 shows the LiDAR driver configuration used for PCW input switching and PCW thermo-optic heater drive. The LiDAR driver system was constructed by a researcher in this laboratory. The TiN thermo-optic heaters used for input switching and the PCW p-i-p heaters were controlled by DC voltages, and an operational amplifier circuit with a DAC mounted on a PCB was used to generate these DC voltages. These DACs were controlled via serial peripheral interface (SPI) communication, and Digilent's Analog Discovery 2 (AD2) was used for signal generation. AD2 was connected to a PC with a USB cable and operated by Python on the PC. External DC 40, 20, and 5 V inputs were used as power

supplies to operate the DAC driver board. The DC outputs from each board were input to a PCB on which the LiDAR chip was mounted.

An overview of SPI communication for DAC control by AD2 is shown in Fig. 7.9. Eight driver boards had 16 DACs, and two driver boards were mounted on one PCB, for a total of four PCBs, as shown in Fig. 7.8. Data were sent to all driver boards, and eight signals from Sync-0 to Sync-07 were used to distinguish each DAC. Each board had 16 DAC outputs, for a total of 128 DAC outputs controlled.
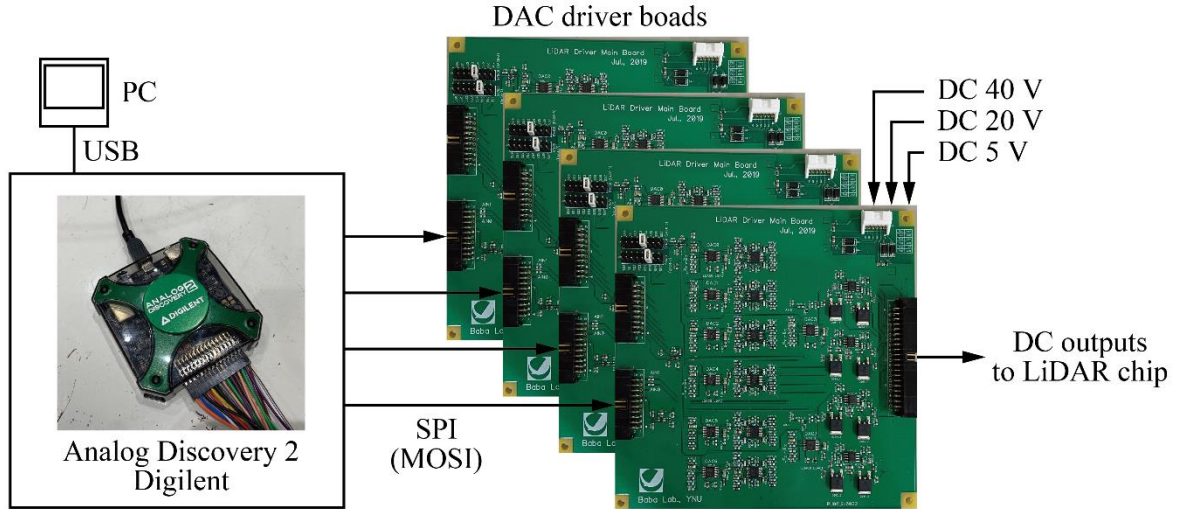
Fig. 7.8 Configuration of LiDAR driver.
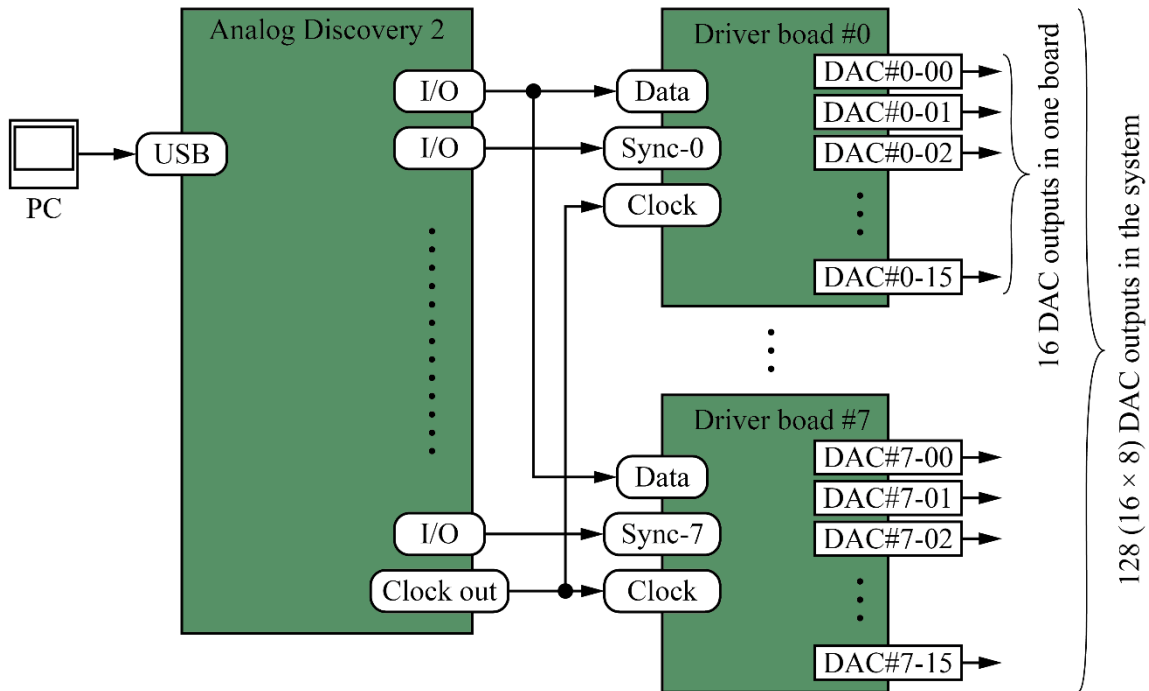
Fig. 7.9 Concept of SPI communication for DAC control by AD2.
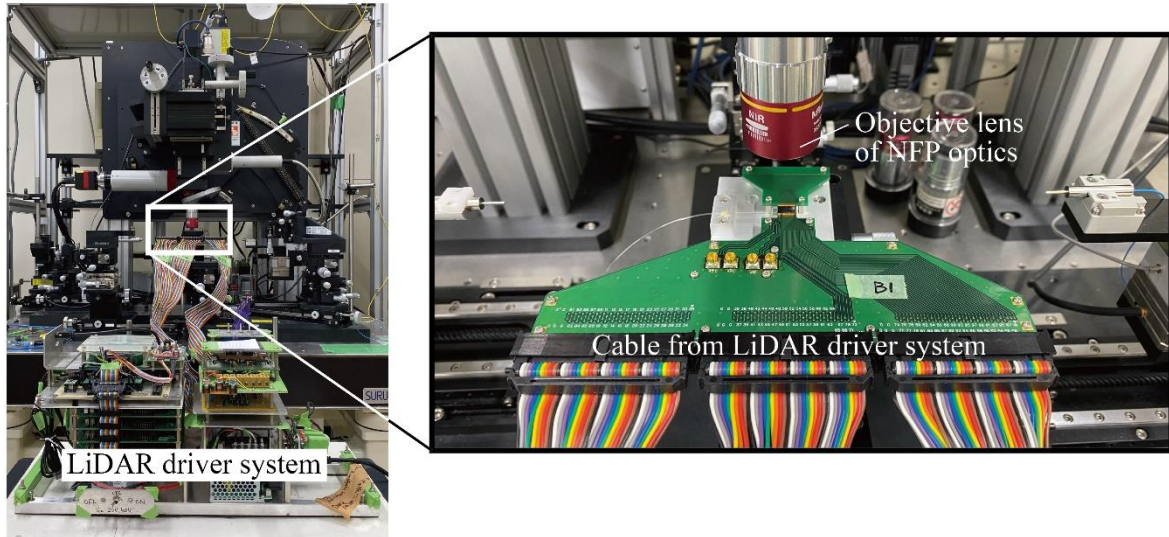
Fig. 7.10 LiDAR chip and LiDAR driver system.
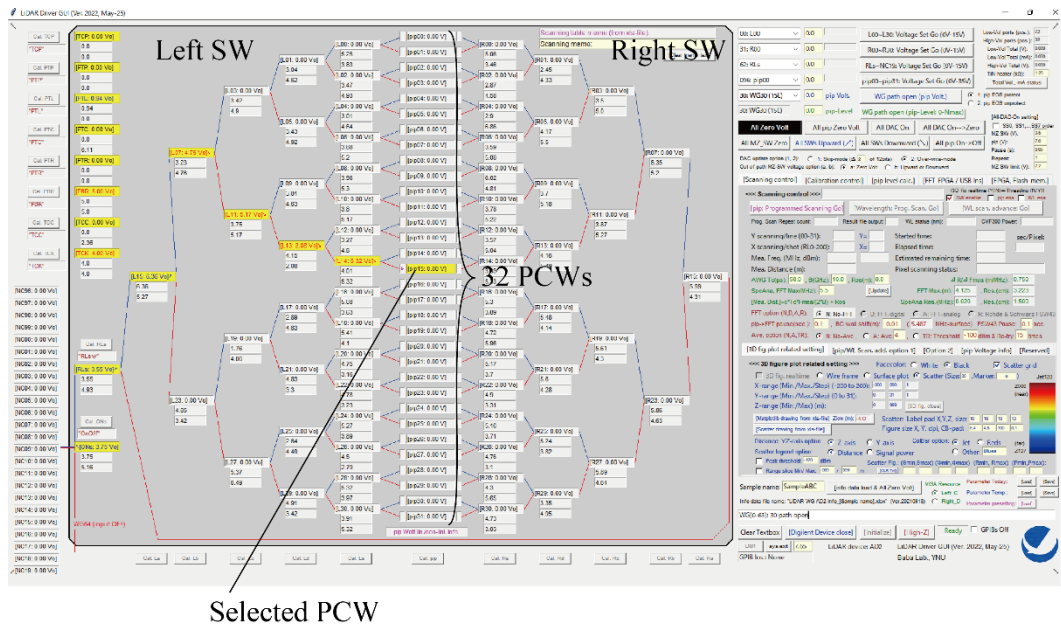
Fig. 7.11 GUI for LiDAR driver. The yellow underlined area represents the DAC at the control point.

Photographs of the LiDAR chip and LiDAR driver attached to the FFP and NFP optics are shown in Fig. 7.10. This system is the measurement system used to calibrate the PCW input switching with the objective lens of the NFP optical system installed above the chip. Each DAC was controlled by a GUI of the Python program on a PC, as shown in Fig. 7.11, where a schematic of the integrated PCW and SW tree is shown, and the DACs in the controlled areas are indicated by yellow underlines. For SW calibration, NFP optics was used to adjust the voltage applied to the thermo-optic heater of the SW while observing the light emitted from the PCW. To emit light only from the desired PCWs, the voltage values were determined starting from the SW at the top of the SW tree. The voltage values were adjusted at 0.1 V intervals, ranging from 0 to 7 V. Adjustments were started from the left and right SWs, and the voltage values were determined to minimize the intensity of the radiation by observing the other PCWs so that light was emitted from only one PCW. The input wavelength was set to the longer side of the operating wavelength to enable the radiation from the PCW to be clearly seen.

7.4 Calibration

7.4.1 Investigation of beam angle

To investigate the beam angle from each PCW in the PCW subarray, the NFP of the radiating area of the PCW was observed using the measurement system shown in Fig. 7.12. The fabricated devices have slightly different beam angles for each PCW due to non-uniformity during fabrication, and the beam profile split and widened. Therefore, thermo-optic compensation using p-i-p heaters was attempted in this study. The beam angle was investigated to confirm which PCW should be heated because this configuration heated two PCWs at the same time due to the limitation of heater control points and the pitch between the PCW subarrays integrated in parallel. When the beam angle with a normal PCW was observed, the FFP optics as shown in Fig. 3.16 was used. In the case of PCW subarrays, however, beams are emitted from both PCWs at the same time, thus posing difficulty in distinguishing which side the split beam was emitted from when the angles were slightly different. Therefore, the beam angle shift was confirmed by observing the wavelength near the band edge of each PCW using NFP optics. Here, the left end of each PCW was observed when inputting from the left side, and the right end was observed when inputting from the right side. The measurement method is the same as in Section 5.2.2.

   Figure 7.13 shows the wavelengths near the band edges of the left and right PCWs observed when switching the left and right inputs by using the 32 PCW subarrays of the fabricated LiDAR chip. The right PCW had a longer wavelength at the band edge than the left PCW at the left input. In addition, periodic wavelength shifts of approximately every five beams are observed, and these also require wavelength and heater adjustments to align the beam angle during beam scanning. In contrast, the band edge wavelength difference between the left and right PCWs was small when the right side input was used, and a similar periodic wavelength shift was observed. A comparison of the band edge wavelengths of the two PCWs shows that the shorter wavelength side corresponds to a smaller beam angle at the same wavelength. This relationship is shown schematically in Fig. 7.14(a), where the beam angles of the left and right PCWs are θ_L and θ_R, respectively. $\theta_L > \theta_R$ is estimated from the band edge wavelength measurement results and can therefore be adjusted so that $\theta_L = \theta_R$ by heating only the left PCW. As shown in Fig. 7.14(b), if the Al wire is cut at the scribing line indicated by the red line, then only the p-i-p heater of the PCW on the left side can be heated by the current. Next, an attempt was made to cut the Al wire of each PCW subarray.
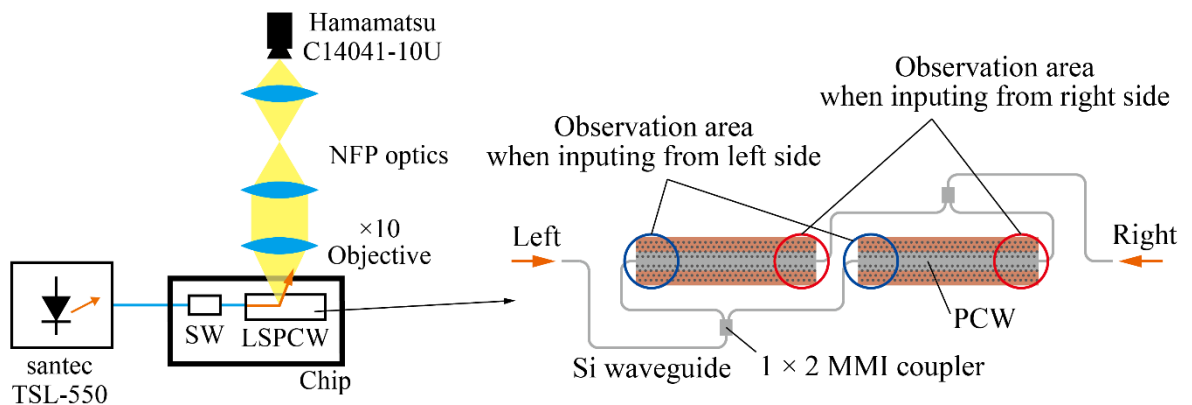

Fig. 7.12 Setup for the investigation of the beam angle. The inset shows the observation area of the PCW subarray. Blue and red circles show the observation area when inputting light from the left and right sides, respectively.
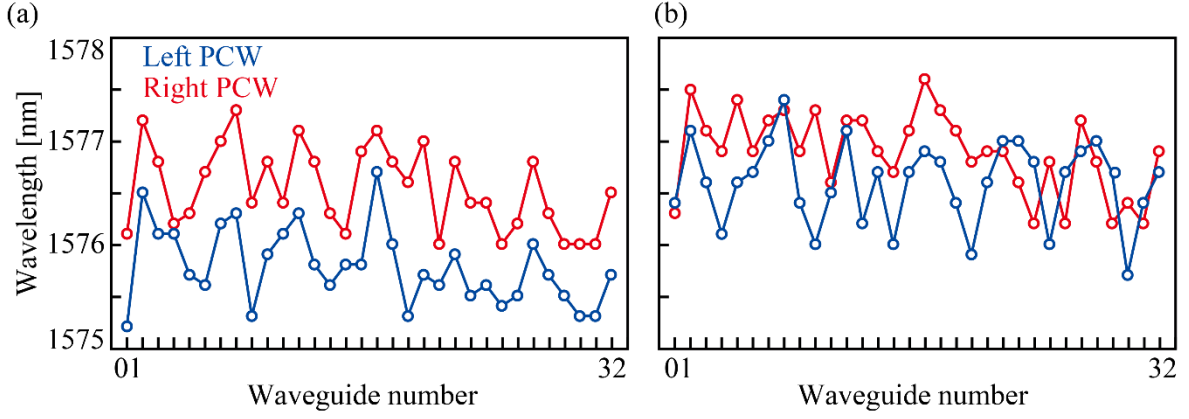
(a)

(b)

Fig. 7.13 Observed wavelengths near the band edge of left and right PCWs in the subarray. (a) When inputting from the left. (b) When inputting from the right.
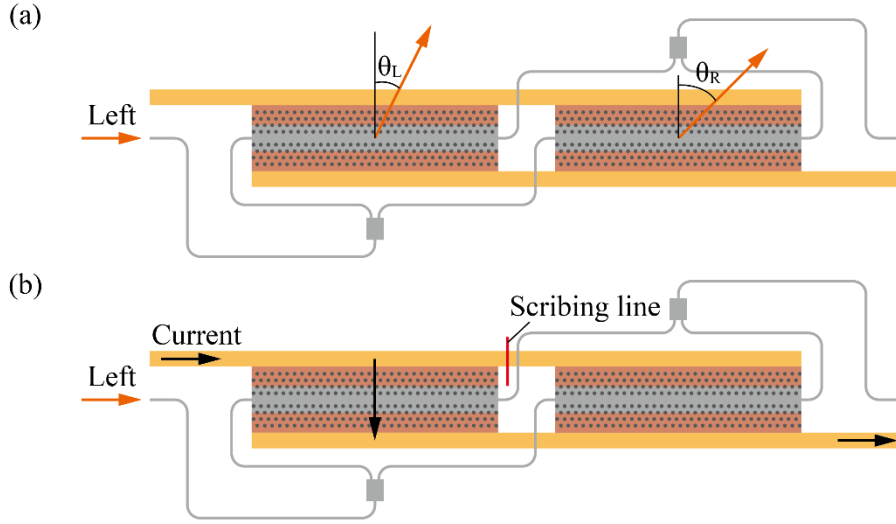
(a)

(b)

Fig. 7.14 When the beam angle of the left PCW θ_L is larger than that of the right PCW θ_R. (b) When the Al wiring is cut at the scribing line indicated by the red line, current flows only in the PCW on the left side and this PCW is heated.

7.4.2 Scribing of Al wire

With the use of the band edge wavelengths identified in the previous section as a reference, the Al wire of each PCW subarray was cut using an Opto System diamond scriber. A 3P-type needle with three contact points was used for the scriber needle. The attachment angle was determined using an angle adjustment tool, as shown in Fig. 7.15(a), and the scriber was attached to the main body of the scriber machine, as shown in Fig. 7.15(b). The needle was mounted at an angle of 51° from horizontal and adjusted to 39° in the tool's scale. Figure 7.16 shows a microscopic image of the fabricated LiDAR chip. The ground-side wiring of the p-i-p heater had a relatively large area, and this area was used to scratch the chip surface during the "wafer 0" operation to check the chip surface position. The scratch formed during this operation and intersection of the white line used for the target position is shown in the inset.

The chip surface position is not always constant at each cutting point; thus, a "wafer 0" operation was performed at each PCW subarray as shown in Fig. 7.17 to make the conditions as equal as possible at each cutting point. The cut length can be set when scribing. However, because the scratches on the chip in the "wafer 0" operation were larger than the width of Al wire, the Al wire was cut by setting the cut

length to 0, the load of scriber to 100 g, and the cut depth to 50 μm, and by adjusting the target position switch and the number of attempts.
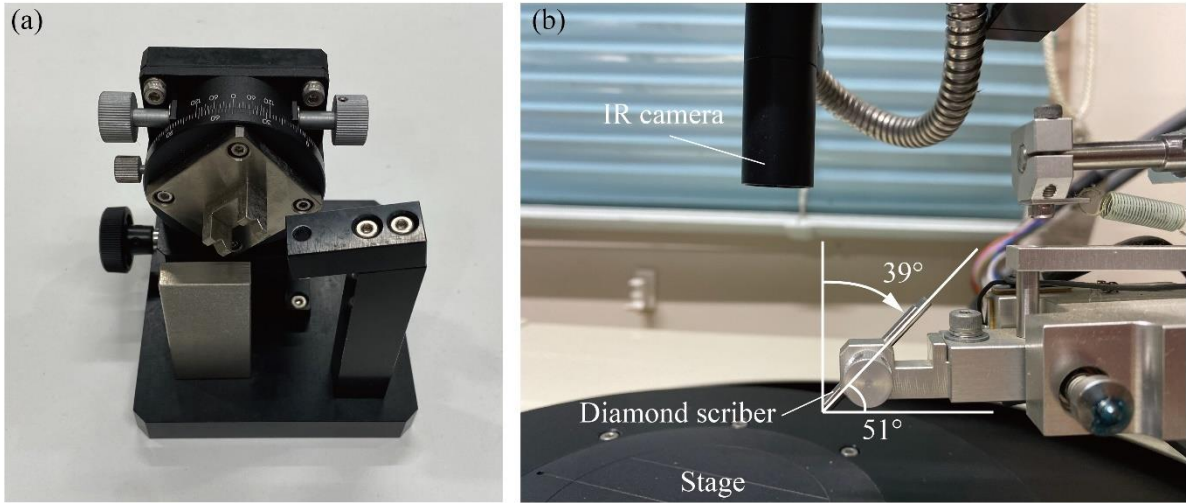

Fig. 7.15 (a) Tool for adjusting the mounting angle of the scriber needle. (b) Scriber needle mounted above the stage.
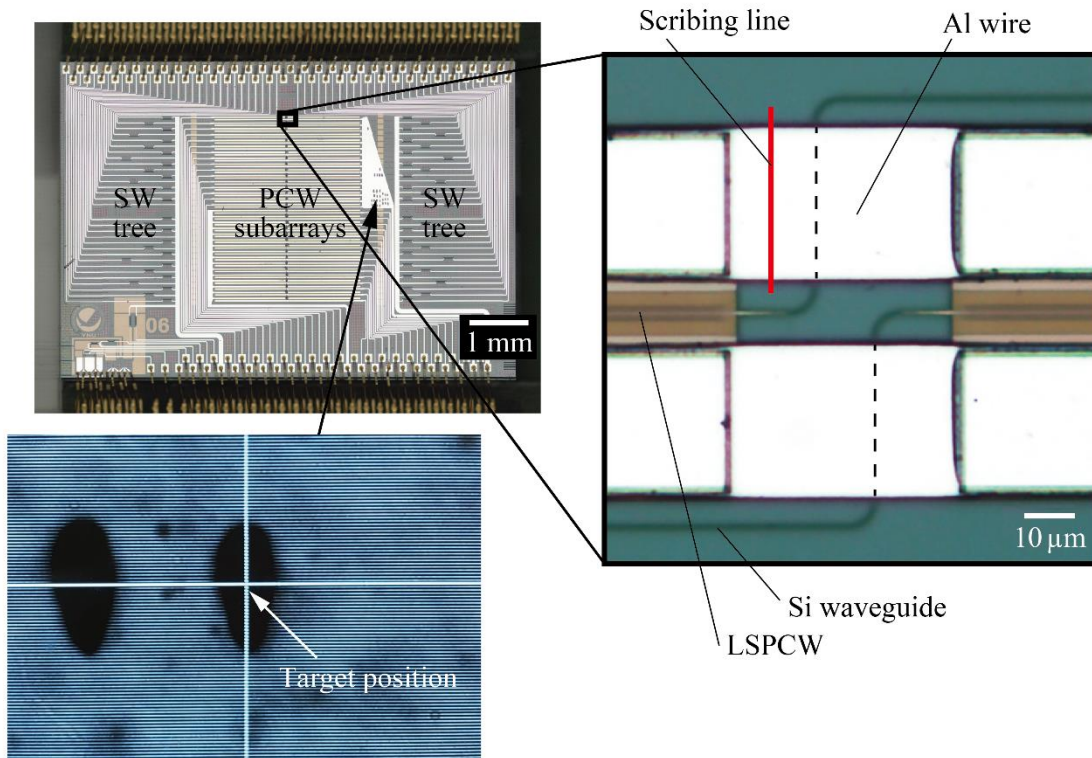

Fig. 7.16 Microscopic image of the fabricated LiDAR chip. Magnified view shows the gap between PCWs at each subarray. Red line indicates the scribing line, and dashed lines show the Si waveguides below Al wires. The inset shows a picture obtained by IR camera, where a white line intersection shows the target position of starting point for scribing. The black areas centered on the intersection represent scribing scratch.
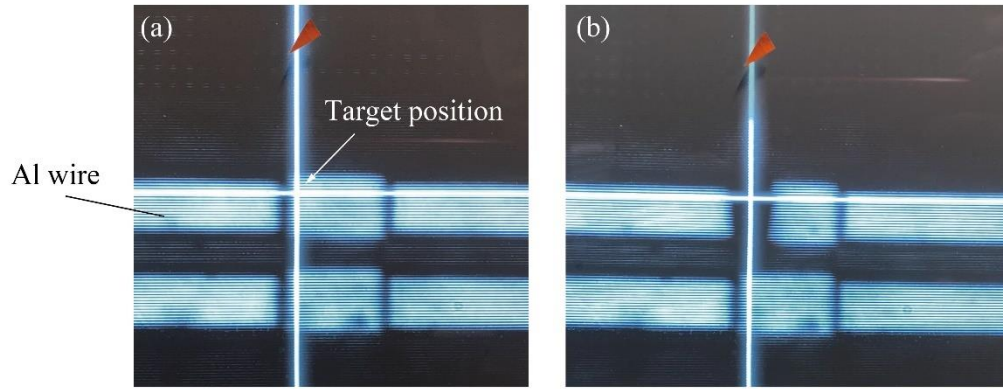
Fig. 7.17 (a) Target position of Al wire in the PCW subarray observed by IR camera. (b) Scratch on the chip formed after the "wafer 0" operation.
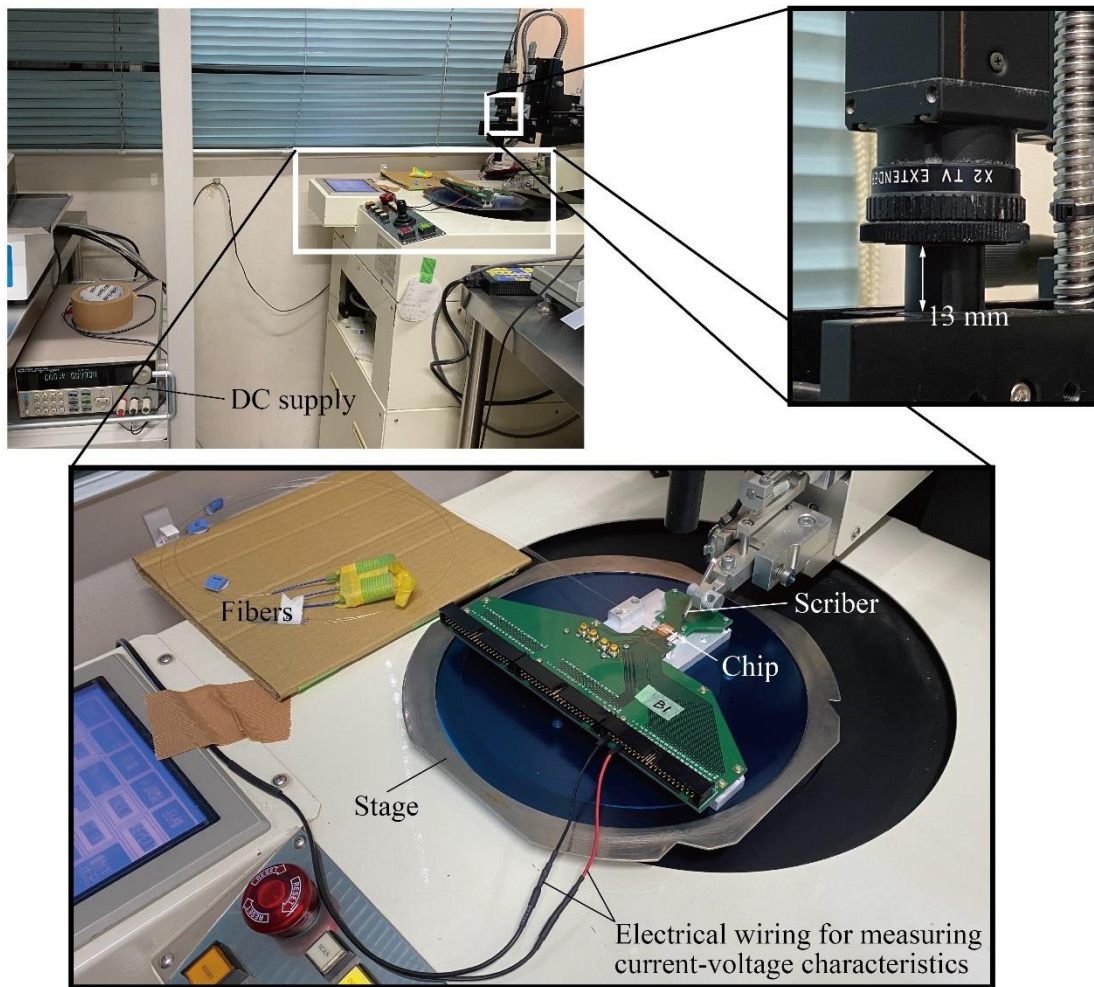
Fig. 7.18 Setup for scribing Al wires of the PCW subarrays. DC power supply was used for measuring the current-voltage characteristics of each PCW subarray. The IR camera was positioned according to the height of the chip. The device was fixed on the stage using dicing tape, and the fibers were evacuated to prevent unnecessary tension.

The setup that was constructed to cut the Al wire is shown in Fig. 7.18. First, the entire substrate, including the chip, was fixed on dicing tape attached to a metal ring. This was placed on the stage, and the entire surface was stabilized by suction from the back side of the tape on which the substrate was

placed. The fiber was moved out of the stage to avoid excessive force. The connector on the PCB to the LiDAR driver was wired and connected to a DC voltage source (ITECH, IT6922A) to measure the current-voltage characteristics of the p-i-p heater in each PCW subarray. The IR camera used to determine the scribing position was adjusted to be 13 mm higher than the height of the device.

The Al wire could not be cut with only one scribing operation, and the wound only widened as the Al dented and extended. Therefore, cutting was attempted by slightly changing the scribing position and repeating the process. As shown in Fig. 7.19(a), five scribing operations were performed in a 4 μm wide area with a 1 μm pitch from the center of the Al wire and back. The 7.5 μm shift from the center of the Al wire in the transverse direction was applied because the scribing scar was asymmetric with respect to the target position. Microscopic images of the results of the trials with dummy devices and different PCW subarrays are shown in Figs. 7.19(b)−7.19(g). Although the scribing position was varied, scribing was possible within the range that did not affect the Si waveguide and PCW.

On the basis of the above conditions, Fig. 7.20 shows the microscopic images of the results of scribing on each PCW subarray of the LiDAR chip for which point cloud images were acquired in this study. Table 7.2 summarizes the number of scribing trials for each waveguide. In all waveguides, the Al wires could be cut without damaging other Si layers. The current-voltage characteristics of each p-i-p heater before and after scribing are shown in Fig. 7.21. One of the heaters connected in parallel was disconnected, thereby confirming that the resistance had approximately doubled.
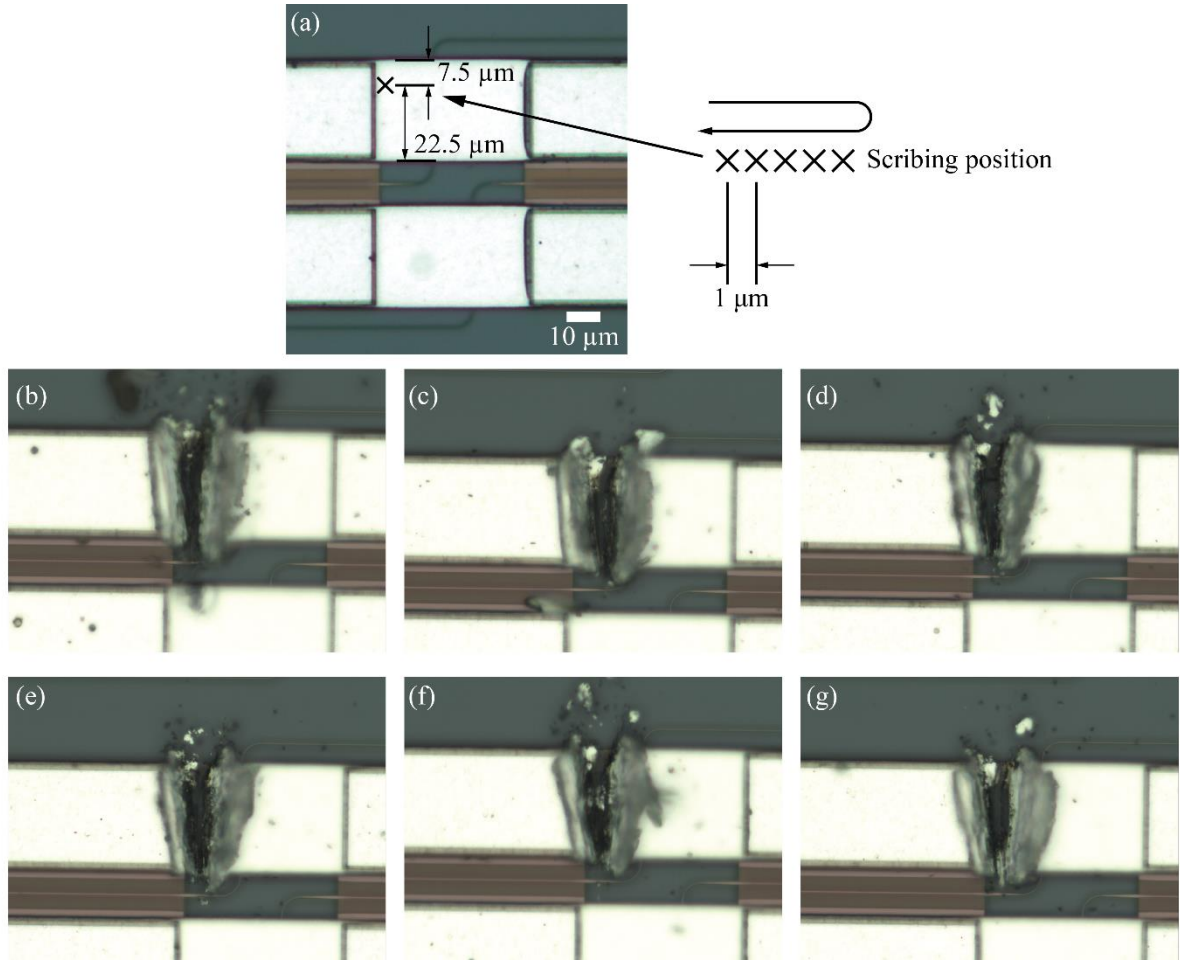

Fig. 7.19 (a) Target position of scribing. × marks show the respective scribing target positions. (b)−(g) Results in different PCW subarrays. Only (d) was attempted five times; all others were attempted 10 times.
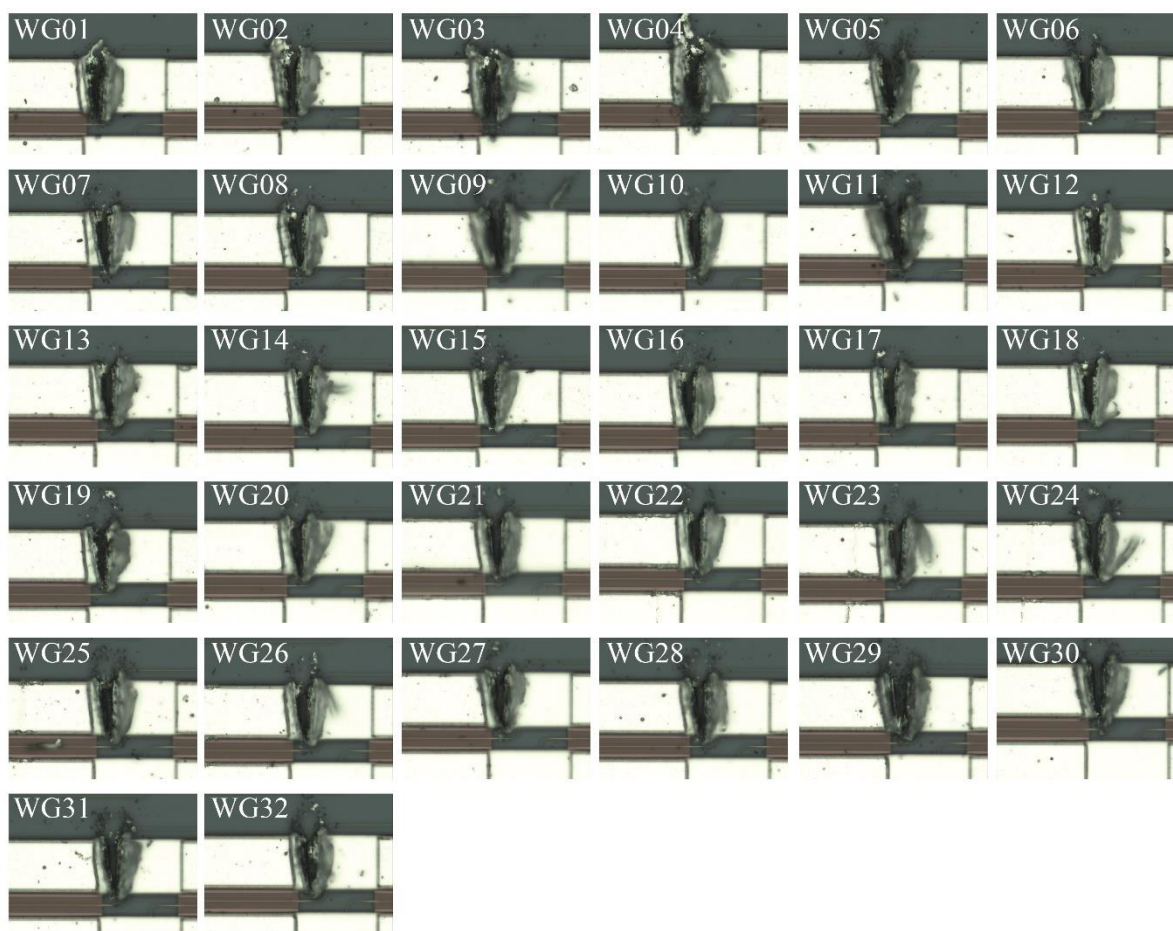
Fig. 7.20 Microscopic images of Al wires after scribing.

Table 7.2 Number of scribing attempts in each waveguide.

WG	Times	WG	Times	WG	Times	WG	Times
01	5	09	10	17	20	25	15
02	13	10	12	18	10	26	15
03	17	11	10	19	10	27	18
04	18	12	10	20	18	28	23
05	17	13	15	21	18	29	29
06	15	14	12	22	16	30	25
07	17	15	17	23	19	31	15
08	15	16	14	24	18	32	15
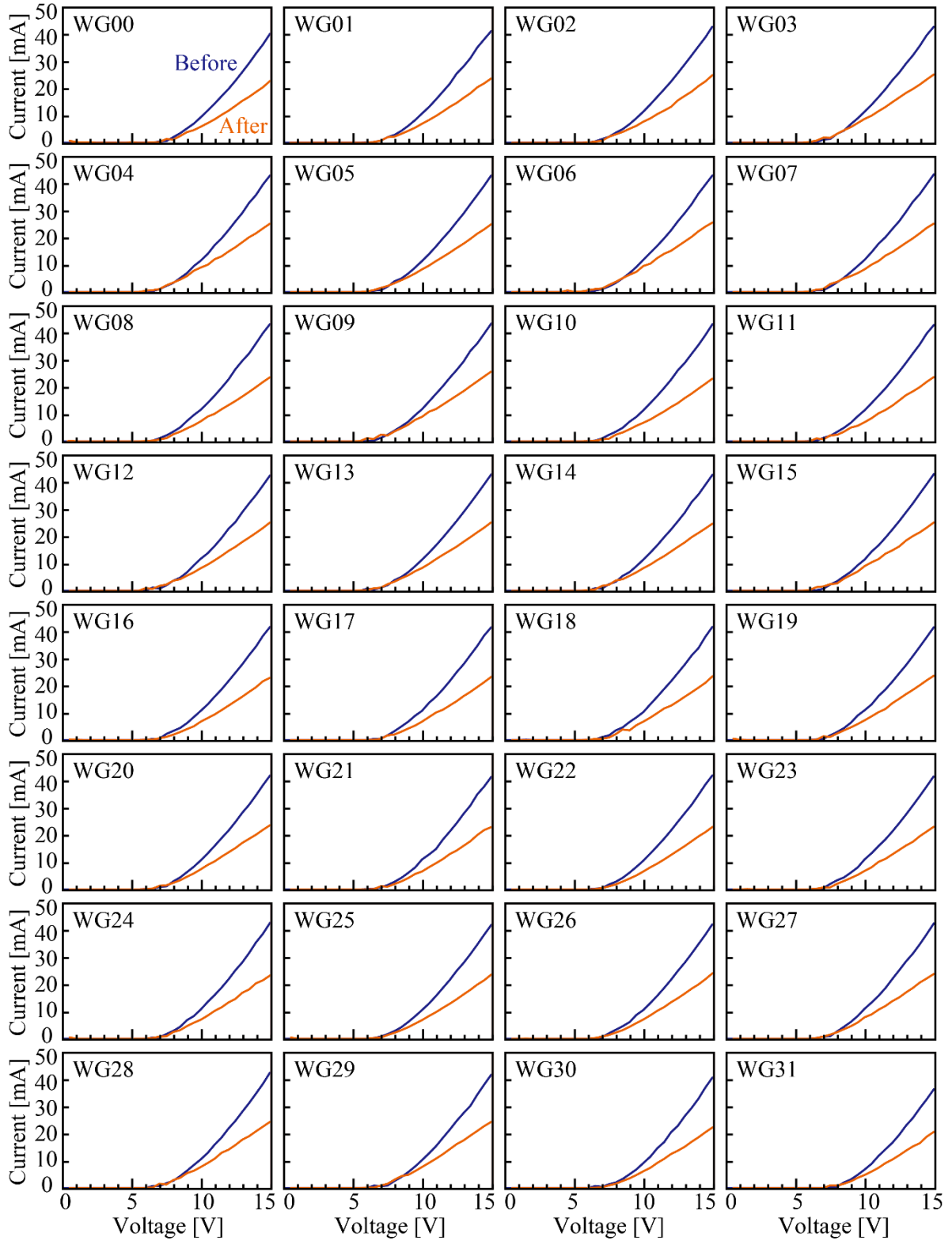
Fig. 7.21 Current-voltage characteristics for each p-i-p heater before and after scribing.

7.5   Acquisition of Point Cloud Image

7.5.1 Setup

With the use of a LiDAR chip with modified Al wires for beam profile calibration, point cloud images

were acquired for various objects by using the measurement system shown in Fig. 7.22. The output from the tunable wavelength laser (santec, TSL-550) was used to drive an I-Q MOD (Thorlabs, LN86-14-P-A-A) with RF signals generated by an AWG (Keysight, M9502A) to generate modulated light. The AWG settings are shown in Table 7.3. The modulated light was amplified by an EDFA (Thorlabs, EDFA100P) and split by a 99:1 coupler. The smaller output was input to port 1 as reference light, and the larger output was input to port 3 as the main light emitted from the PCW. The reference light was input through the PCW MOD to the Ge BPD via a 2 × 2 MMI coupler, and the voltage value of the heater was adjusted to increase the signal intensity using a phase shifter on the way. The aforementioned LiDAR driver was used to switch the input to each PCW and to control the p-i-p heaters mounted on the PCWs. 2D beam scanning was performed by input switching with a LiDAR driver via USB and laser wavelength sweep via GPIB. A prism lens, as shown in Fig. 7.23, was used to collimate the beam in the orthogonal direction of the waveguide [7-1, 2]. In the wavelength sweep of the beam scanning, the wavelength was set to compensate for the beam angle variation caused by the thermo-optic control of the p-i-p heater and for the beam angle variation in each original PCW.

   To detect the beat signal to obtain range information, the signal from the Ge PD was processed and analyzed by ESA (Rohde & Schwarz, FSW43), as shown in Fig. 7.24. A bias tee (Aeroflex, 8810EMF2-50,18) was inserted and a DC voltage source (Matsusada, P4K18-2) was connected and set to 0 V for AC coupling after Ge PD, excluding the DC component. The signal was then amplified by a TIA (Texas Instruments, THS4631) and input to a variable attenuator (VA; Analog Devices, HMC346) through a 1 MHz high-pass filter (HPF). The amplification was balanced to account for variations in the sensitivity of the two Ge PDs. A controller with a dial for adjusting the variable resistance, as shown in Fig. 7.24, was used to adjust the beat signal intensity to the maximum and the noise floor to the minimum. The output of the VA was input to a differential amplifier (Analog Devices, LTC6400), and the output was input to the ESA via a DC block. The ESA was connected to a PC via the same GPIB as the laser. For each beam at each wavelength during 2D beam scanning, the range was calculated from the maximum intensity of the spectrum observed by the ESA to obtain a point cloud image.
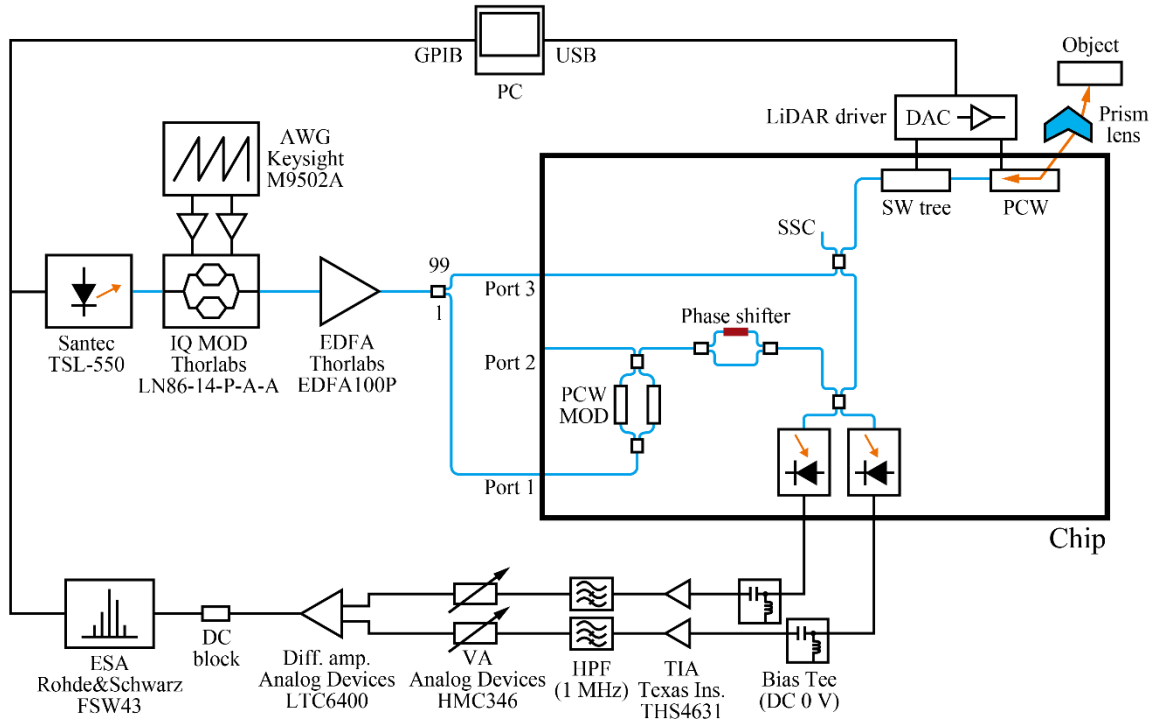

Fig. 7.22 Measurement system for point cloud image acquisition.

Table 7.3 Setting of AWG.

Sample rate [Hz]	32×10^9	Modulation on pulse	Increasing
Repeat interval [s]	100×10^{-6}	Frequency span [Hz]	10×10^9
Pulse width [s]	50×10^{-6}	Frequency offset [Hz]	6×10^9
Rise time [s]	25×10^{-6}	Amplitude of Ch.1 [mV]	800
Fall time [s]	25×10^{-6}	Amplitude of Ch.2 [mV]	800
Pulse shape	Raised cosine		
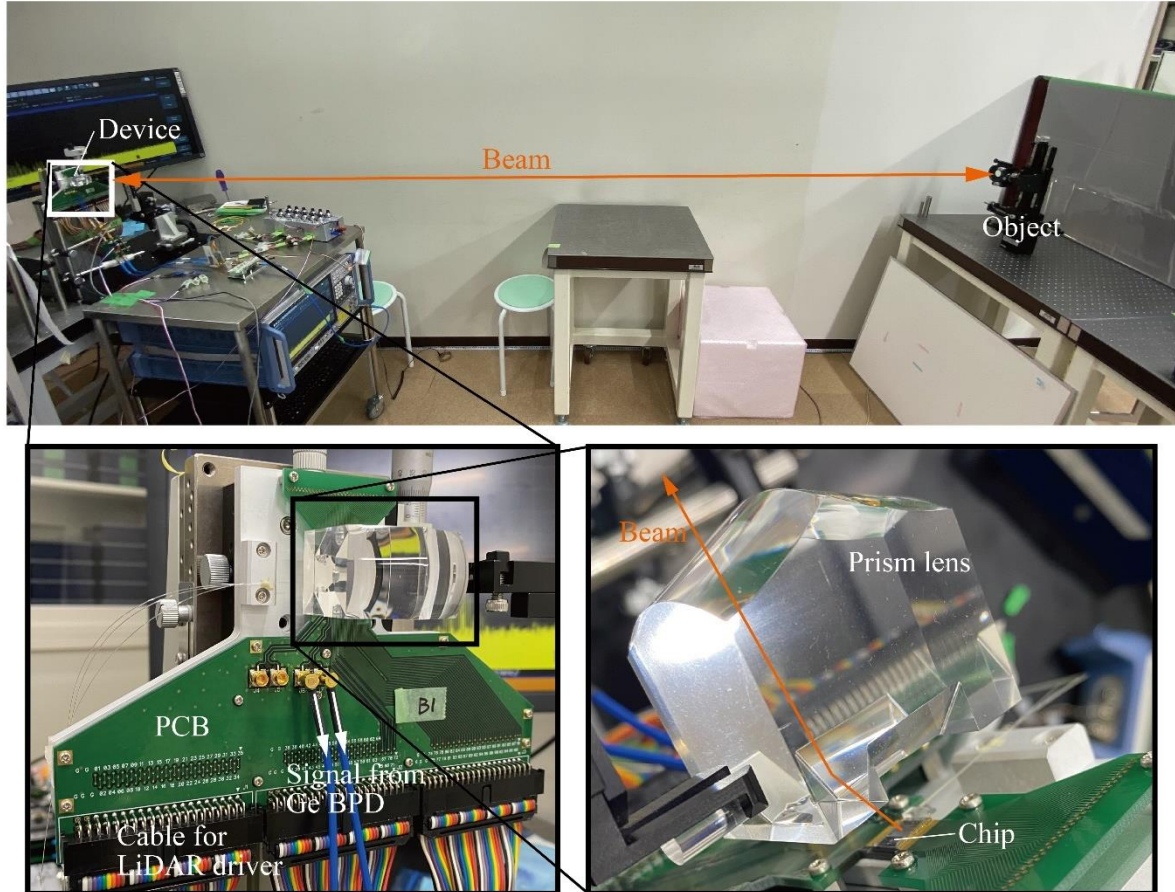
Fig. 7.23 Setup for point cloud image acquisition.

The target objects were objects to which retroreflective film (OEALITE, AP1000) was attached, as shown in Fig. 7.25. The first was an array of Al rods; the second was a film with gaps of 20, 10, 0.5, and 2.5 mm to confirm that the subarray configuration narrowed the beam and improved the resolution, and the third was a plate with the letters "YNU" hollowed out.

7.5.2 Beam profile

The beam spots observed by the InGaAs camera and the corresponding profiles before and after beam calibration are shown in Fig. 7.26. These images were obtained by selecting one of the 32 PCW subarrays, emitting the beam, placing a piece of paper near the object, and observing the scattered light with an InGaAs camera. When the p-i-p heater was not driven and the beam was not calibrated, the beam split and spread. However, a beam profile with a near-theoretical beam width of 0.035° was produced after the heater was adjusted to maximize the beam peak value.
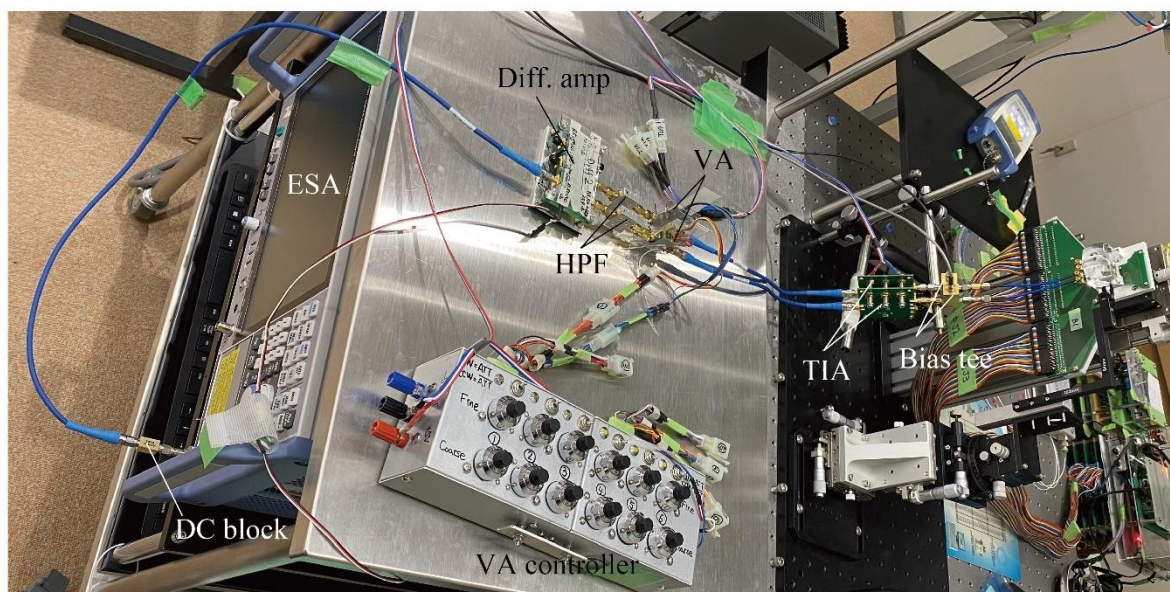
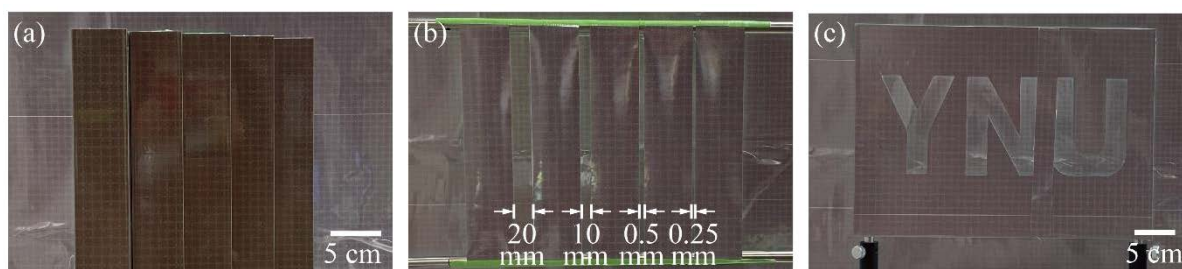Fig. 7.24 Setup for analyzing signals output from Ge PD with ESA.

Fig. 7.25 Objects covered with retroreflective film. (a) Array of Al rods. (b) Film with gaps of 20, 10, 0.5, and 0.25 mm. (c) Plate with the letters "YNU" hollowed out.
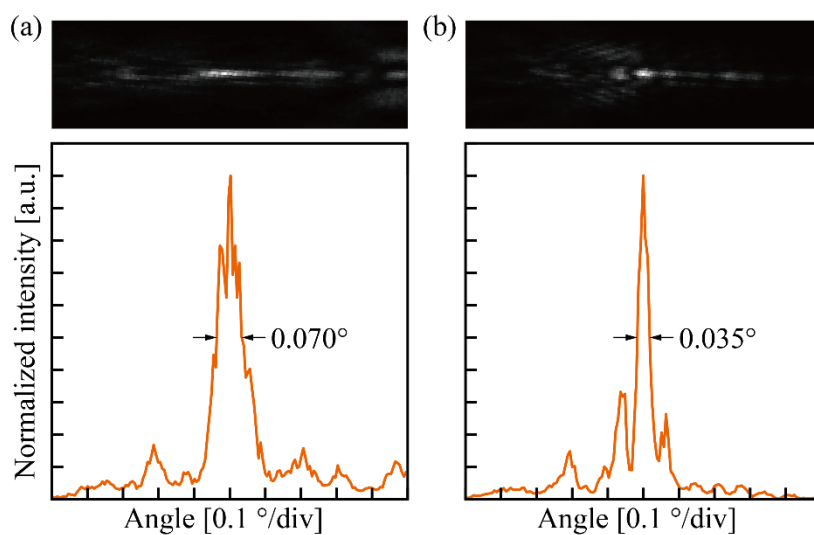

Fig. 7.26 Beam spots and corresponding profiles observed by the InGaAs camera. (a) Without calibration. (b) With calibration.
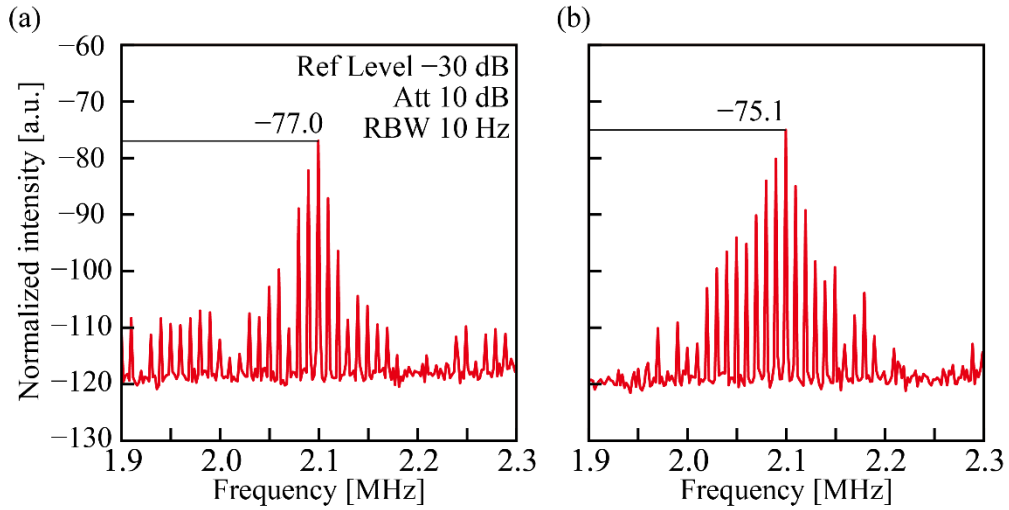
Fig. 7.27 Beat signal spectrum obtained in the FMCW LiDAR experiment when the object is a retroreflective film. (a) Without calibration. (b) With calibration.
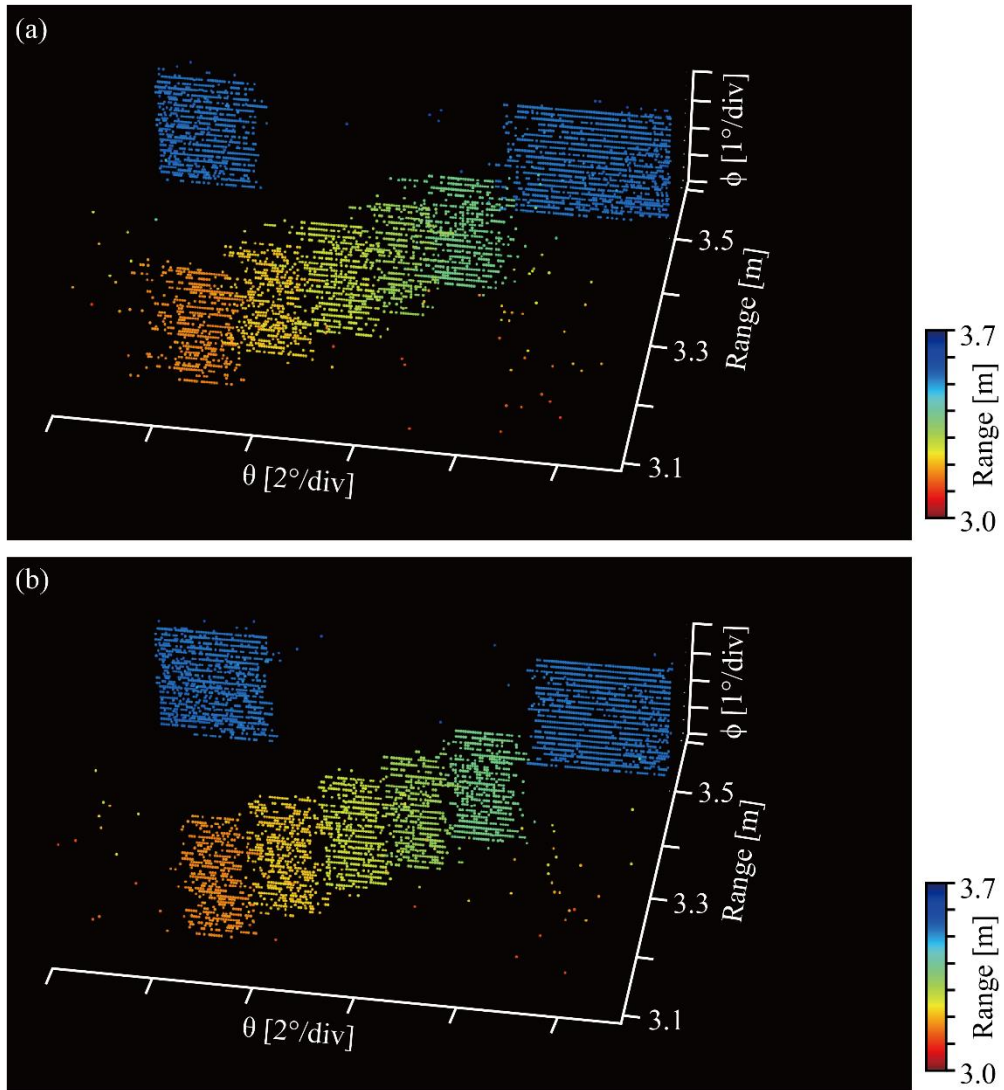
Fig. 7.28 Acquired point cloud images for Al rods. (a) Without calibration. (b) With calibration.
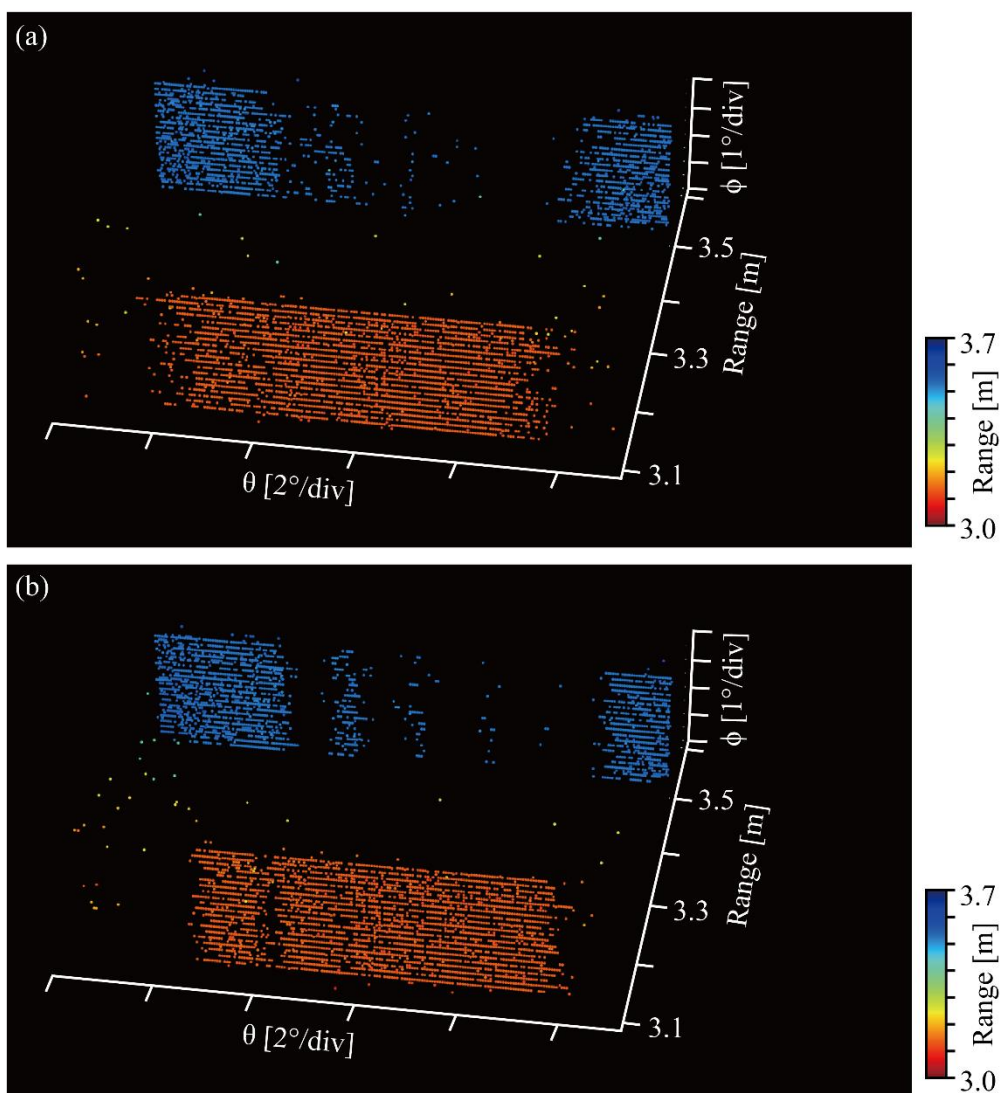
Fig. 7.29 Acquired point cloud images for film with gaps of 20, 10, 0.5, and 0.25 mm. (a) Without calibration. (b) With calibration.
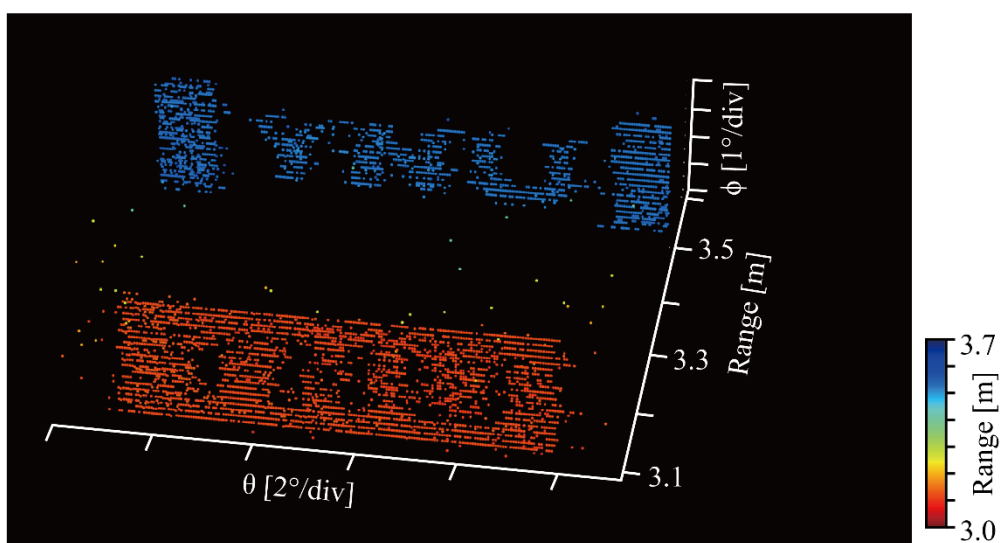

Fig. 7.30 Point cloud image for the plate with the letters "YNU" hollowed out, with calibration.

Table 7.4 Voltage values and wavelengths at each p-i-p heater in the experiments of 2D beam scanning and FMCW LiDAR.

WG	Voltage [V]	Wavelength [nm]	WG	Voltage [V]	Wavelength [nm]
00	9.6	1554.0 ~ 1565.0	10	9.8	1554.4 ~ 1565.4
01	10.1	1554.5 ~ 1565.5	11	10.1	1555.1 ~ 1566.1
02	10.0	1554.4 ~ 1565.4	12	9.1	1554.3 ~ 1565.3
03	9.1	1554.1 ~ 1565.1	13	9.1	1554.1 ~ 1565.1
04	9.4	1554.1 ~ 1565.1	14	9.0	1554.2 ~ 1565.2
05	9.7	1554.3 ~ 1565.3	15	9.0	1554.2 ~ 1565.2
06	9.0	1554.8 ~ 1565.8	16	9.2	1554.4 ~ 1565.4
07	9.8	1554.9 ~ 1565.9	17	9.3	1554.5 ~ 1565.5
08	9.7	1554.2 ~ 1565.2	18	10.4	1554.3 ~ 1565.3
09	9.2	1554.2 ~ 1565.2	19	9.7	1554.1 ~ 1565.1

7.5.3 Transmission and reception characteristics

Figure 7.27 shows the beat signal spectrum observed in the FMCW LiDAR experiment before and after beam calibration. The maximum intensity of the spectrum improved by about 2 dB. As a result of beam calibration. The retroreflective film is designed to reflect light in the same direction as the emitted beam angle; thus, the transmission characteristics were unlikely to be reflected in the improvement of beat signal intensity even if the beam was narrowed.

7.5.4 Point cloud image

With the beam profile calibrated by a p-i-p heater, 2D beam scanning was performed by wavelength sweep and PCW subarray switching, and point cloud images were acquired for each object by the FMCW LiDAR experimental system. The switch of the device used in this study was defective. Therefore, 20 waveguides were used for beam scanning. The set voltage values and wavelength sweep ranges of the p-i-p heaters in each PCW subarray are shown in Table 7.4. The voltage values were set to maximize the peak intensity of the beam profile in each waveguide, where the voltage was adjusted to minimize the beam divergence in addition to the peak intensity. The wavelength was varied by 0.05 nm, and the beam angle was calibrated to be equal for all waveguides with an InGaAs camera to compensate for beam angle variation and fabrication errors due to thermo-optic control. The point cloud image acquired for the array of Al rods is shown in Fig. 7.28. The different colors of each point indicate the range, with the Al rods placed in different positions and the background board at the back of the rods. The beam calibration improved the blurred boundaries of the rods, which were caused by beam splitting and expansion before calibration, and made them clearly visible. The point cloud image acquired for a film with gaps is shown in Fig. 7.29. The calibration resulted in a narrow beam divergence close to the theoretical value, thus enabling the gap to be captured. Figure 7.30 shows an image obtained for a plate with a complicated letter hollowed out during further calibration. The shape of the letter was clearly captured on the board in front and in the back. The number of resolution points obtained in this experiment was $221 \times 20 = 4{,}220$, and the field of view was $11° \times 3.8°$.

7.6   Discussion

In this study, point cloud image acquisition using a LiDAR chip with a two-divided PCW subarray configuration and integrated Ge BPDs for signal detection was demonstrated by performing 2D beam scanning by waveguide switching and wavelength sweeping, combined with FMCW LiDAR

transmission and reception experiments. Although beam splitting and expansion were observed in the beam profile as a result of fabrication errors, a beam profile close to the theoretical value could be obtained by calibrating the beam profile with the use of thermo-optic control. In the device used in this study, beam scanning was performed by combining thermo-optic control and wavelength sweep due to the convenience of modified electrical wiring. However, beam scanning at a single wavelength can be achieved by configuring the PCW to be individually heated, thereby allowing for a simpler configuration than the current mainstream 2D beam scanning configuration that combines an OPA and a grating waveguide. Beam calibration is also challenging because OPA has more phase adjustment points compared with this configuration [7-3, 4]. The field of view in the waveguide direction was 11°, which is less than half the theoretical performance of the PCW. However, this condition was due to bandwidth limitations caused by the PCW modulator used as the reference light path and the fact that the prism lens was not optimized for the subarray configuration; the field of view can be expanded by overcoming these limitations. The beam calibration enabled a profile close to the theoretical value to be obtained, resulting in the demonstration of a silicon photonics LiDAR chip with high resolution.

References

[7-1]   J. Maeda, D. Akiyama, H. Ito, H. Abe and T. Baba, "Prism lens for beam collimation in silicon photonic crystal beam-steering device," Opt. Lett., vol. 44, no. 23, pp. 5780−5783, 2019.

[7-2]   R. Kubota, M. Kamata, R. Tetsuya, T. Tamanuki and T. Baba, "High NA and size reduction in prism lens for silicon photonics SLG beam scanner," Conf. Laser and Electro-Opt. Pacific Rim, Sapporo, 2022 (To be presented).

[7-3]   T. Komljenovic, and P. Pintus, "On-chip calibration and control of optical phased arrays," Opt. Express, vol. 26, no. 3, pp. 3199−3210, 2018.

[7-4]   L. J. Li, W. Chen, X. Y. Zhao, and M. J. Sun, "Fast Optical Phased Array Calibration Technique for Random Phase Modulation LiDAR," IEEE Photonics Journal, vol. 11, no. 1, pp. 1−10, 2019.

Chapter 8
Conclusion

This work studied a silicon photonics LiDAR chip that uses PCWs as optical antennas, which can achieve high resolution with a small number of antennas, because the slow light effect enables wide field-of-view beam scanning. In this study, the objective was to improve the transmission and reception characteristics of PCW optical antennas and other applications. A subarray configuration was introduced to reduce total waveguide loss and enable scaling of PCWs fabricated by silicon photonics. Theoretical and experimental results demonstrated that the subarray configuration improves the transmission and reception characteristics. Furthermore, the transmission and reception performance was improved by forming a temperature distribution in the aperture of the PCW for thermo-optic control. In addition, as a potential free-space optical communication application of the PCW optical antenna, an optical transmission experiment to two points combined with high-speed beam switching was conducted. Finally, a LiDAR chip that contains a subarray composed of two antennas was fabricated, and 2D beam scanning was performed by combining waveguide switching and wavelength sweeping to acquire point cloud images, which includes range information, for various objects. The details of the conclusions for each item are described below.

8.1 Characteristic Improvement by Subarray Configuration

Subarrays were introduced to overcome the limitation of PCW optical antennas in scaling the transmission and reception characteristics due to waveguide loss. PCWs fabricated by silicon photonics typically have waveguide propagation losses of 10 dB/cm order. Simply lengthening the PCW will result in light loss as light propagates through the PCW for both transmission and reception, making it impossible to take advantage of the aperture. The subarray configuration suppresses the overall loss, allowing for narrower beams of 0.04° and 0.02° with 2 and 4 antennas, respectively, in the transmission. To achieve the same beam divergence with OPA, more than 1,000 antennas are required, whereas PCW subarrays can achieve a high resolution beam with far fewer antennas. Another feature is that the array factor is suppressed by the element factor of each PCW. Therefore, the field of view is not limited by the grating lobe. In reception, the saturation of reception intensity with respect to the aperture can be mitigated. A beam profile close to the theoretical value was obtained by using the fabricated PCW subarray consisting of two or four antennas. The FMCW LiDAR transmission and reception experimental system was introduced, and the observed signal intensity improved by 6 and 12 dB, indicating that the subarray configuration effectively improves the transmission and reception characteristics of the PCW optical antenna.

8.2 Thermo-optic Beam Calibration

In addition to the subarray configuration, the improvement of the transmission and reception

characteristics of the PCW optical antenna by thermo-optic control was demonstrated. PCWs fabricated by silicon photonics are subject to not only waveguide loss but also to in-plane non-uniformity. When the propagation constant in the PCW is not constant, the beam profile is degraded, thereby degrading the transmission and reception characteristics. Therefore, the transmission and reception characteristics were improved by forming a temperature distribution in the aperture of the PCW and calibrating the beam profile by using thermo-optic control to bring it close to the theoretical value. In this study, as an initial experiment, a blue laser was irradiated to the edge of the PCW to form a temperature distribution. Laser intensity and irradiation position were adjusted to maximize the peak intensity of the beam profile. In the FMCW LiDAR transmission and reception experiments, the signal intensity was improved, demonstrating that beam calibration by thermo-optic control effectively improves the transmission and reception characteristics of the PCW optical antenna. Although the practical design requires more control points, this can be achieved by incorporating a heater that can form a temperature distribution for calibration in addition to the p-i-p thermo-optical heater for beam scanning.

8.3   Free-space Optical Transmission

Experiments were conducted on high-speed beam switching optical transmission to two points for free-space optical communication as a new application of the PCW optical antenna. First, the modulation signal intensity of the radiated light was investigated when an intensity-modulated signal was used with the PCW. In a PCW, the wavefront of the RF signal propagating through the PCW is delayed relative to the wavefront of the emitted light due to the slow light effect, resulting in phase shift mismatch and decreased modulation signal intensity of the emitted beam at far field. When the group index is set to 20, the signal intensity is halved at a modulation frequency of 10 GHz, and similar results were obtained in the experiment. On the basis of these results, a rectangular wave was applied to the p-i-p heater to switch the beam, and an optical transmission experiment was conducted on fiber collimators set at two locations. Data transmission up to 22 Gbps at a switching speed of 1 kHz was demonstrated, showing the potential of PCW optical antennas for free-space optical communications.

8.4   Acquisition of Point Cloud Image

A LiDAR chip integrated with a PCW subarray that consists of two antennas and a Ge BPD for coherent detection was fabricated, and LiDAR by point cloud image acquisition was demonstrated. Thirty-two PCW subarrays were integrated in parallel, and each of which was input-switched by SW trees. 2D beam scanning was realized by combining this waveguide switching and wavelength sweep with a prism lens above the chip for collimation. Core-shrunk polarization-maintaining fibers fixed to the SSC with ultraviolet curing resin were used for optical input and output, while switches and signal reception were externally controlled by wire bonding to a PCB. With the combination of 2D beam scanning and FMCW LiDAR transmission and reception experiments, the range information was calculated and point cloud images were acquired for various objects to which retroreflective film was attached. Although large-scale integration is essential to achieve high resolution in both OPA and FPA, the combination of the FPA configuration and the wide beam steering angle due to the slow light effect in this configuration is expected to support a LiDAR device that achieves high resolution beam scanning with a small number of antennas. In this study, LiDAR operation with PCW antennas, which have a higher resolution due to their subarray configuration, was demonstrated.

Acknowledgments

I would like to thank secretaries of Baba Laboratory: Ms. Tomoko Mando, Ms. Masako Akaishi, and Makiko Koyanagi for their clerical support.

I would like to thank the members of The National Institute of Advanced Industrial Science and Technology (AIST) for fabrication of the devices.

I would like to thank the members of OPTO-SYSTEM Co., Ltd. For their cooperation in the scribing the Al wires of the devices.

Finally, I would like to thank my family for their mental and financial support.

鉄矢 諒

Publications

Journal Papers

[1] R. Tetsuya, H. Abe, H. Ito and T. Baba, "Efficient light transmission, reception and beam forming in photonic crystal beam steering device in a phased array configuration", Jpn. J. Appl. Phys., vol. 58, no. 082002, pp. 1-5, 2019.

[2] H. Ito, Y. Kusunoki, J. Maeda, D. Akiyama, N. Kodama, H. Abe, R. Tetsuya, and T. Baba, "Wide beam steering by slow-light waveguide grating and prism lens", Optica, vol. 7, no. 1, pp. 47-52, 2020.

[3] 馬場俊彦, 伊藤寛之, 阿部紘士, 玉貫岳正, 竹内悟朗, 古門優弥, 雛倉陽介, 前田惇, 秋山大地, 倉橋諒, 楠侑真, 鉄矢諒, 鎌田幹也, 白鳥遼, 近藤圭祐, 建部知紀, 竹内萌江, 板垣健祐, 児玉直也, 横川朋樹, "シリコンフォトニクススローライトライダの開発", 電子情報通信学会論文誌, vol. J103-C, no. 11, pp. 434-452, 2020 (招待論文).

[4] R. Tetsuya, T. Tamanuki, H. Ito, H. Abe, R. Kurahashi, M. Seki, M. Ohtsuka, N. Yokoyama, M. Okano and T. Baba, "Si photonic crystal optical antenna serial array and frequency-modulated continuous-wave light detection and ranging action", Appl. Phys. Lett., vol. 119, no.23, pp.231103 (1-5), 2021.

[5] T. Baba, T. Tamanuki, H. Ito, M. Kamata, R. Tetsuya, S. Suyama, H. Abe, R. Kurahashi, "Silicon photonics FMCW LiDAR chip with slow light grating beam scanner", IEEE J. Sel. Top. Quantum Electron., vol. 28, no. 5, pp. 8300208, 2022 (Invited Paper).

[6] J. Gondo, T. Tamanuki, R. Tetsuya, M. Kamata, H. Ito, T. Baba, "Step-like beam scanning in slow-light grating beam scanner for FMCW LiDAR", Opt. Lett., 2022 (To be published).

International Conferences

[1] R. Tetsuya, H. Abe and T. Baba, "Control of light emission characteristics from a serial array of Si photonic crystal beam steering devices", Int. Sympo. Photon. Electron. Convergence, Tokyo, 2018.

[2] R. Tetsuya, H. Abe, H. Ito, G. Takeuchi, Y. Furukado and T. Baba, "Efficient light emission and beam forming in Si photonic crystal beam steering device and its phased array configuration", SPIE Photonics West, San Francisco, no. 10922-68, 2019.

[3] H. Ito, Y. Kusunoki, D. Akiyama, R. Tetsuya, H. Abe and T. Baba, "Enhanced light emission from a Si optical beam steering device consisting of asymmetric photonic crystal waveguide", SPIE Photonics West, San Francisco, no. 10923-37, 2019.

[4] R. Tetsuya, H. Abe, H. Ito and T. Baba, "Transmission/reception efficiencies and modulation signal intensity in a serial array of Si photonic crystal beam steering devices", Int. Sympo. Photon. Electron. Convergence, Tokyo, 2019.

[5] T. Baba, H. Ito, H. Abe, T. Tamanuki, Y. Hinakura, R. Tetsuya, J. Maeda, M. Kamata, R. Kurahashi and R. Shiratori, "Si PIC based on photonic crystal for LiDAR application", Opt. Fiber Commun. Conf., San Diego, no. M4H.1, 2020 (Invited Paper).

[6] R. Tetsuya, H. Abe, H. Ito, T. Tamanuki a and T. Baba, "Controlled beam steering in serial array of Si photonic crystal waveguide optical antennas", Int. Symp. Photon. Electron. Convergence, Tokyo, 2020.

[7] M. Kamata, H. Abe, H. Ito, T. Tamanuki, R. Tetsuya, R. Kurahashi and T. Baba, "3D imaging and a consideration on sensitivity of Si photonics full-integrated LiDAR chip", Int. Sympo. Photon. Electron. Convergence, Tokyo, 2021.

[8] R. Tetsuya, T. Tamanuki, H. Ito and T. Baba, "Acquisition of point cloud image using LiDAR chip integrating serial array of Si photonic crystal optical antennas", Int. Sympo. Photon. Electron. Convergence, Tokyo, 2021.

[9] R. Tetsuya, T. Tamanuki, R. Kubota, M. Kamata and T. Baba, "Point cloud imaging using Si photonic crystal optical antenna serial array", Optoelectronic and Commun. Conf., Toyama, no. TuA4-2, 2022.

[10] J. Gondo, T. Tamanuki, R. Tetsuya, M. Kamata, H. Ito and T. Baba, "High-speed, step-like optical beam scanning using Si photonics SLG beam scanner for FMCW LiDAR", Conf. Laser and Electro-Opt. Pacific Rim, Sapporo, no. CThP8F-06, 2022.

[11] R. Kubota, M. Kamata, R. Tetsuya, T. Tamanuki and T. Baba, "High NA and size reduction in prism lens for silicon photonics SLG beam scanner", Conf. Laser and Electro-Opt. Pacific Rim, Sapporo, no. CWP17A, 2022.

[12] R. Tetsuya, N. Kodama, M. Kamata, T. Tamanuki and T. Baba, "Free-space optical transmission using Si photonics slow light grating beam switching device", Conf. Laser and Electro-Opt. Pacific Rim, Sapporo, no. CWP12A-03, 2022.

Domestic Conferences

[1] 鉄矢諒, 阿部紘士, 馬場俊彦, "縦列アレイ型 Si フォトニック結晶光偏向器の放射特性制御", 応用物理学会秋季講演会, no. 18a-212A-6, 2018.

[2] 鉄矢諒, 雛倉陽介, 阿部紘士, "馬場俊彦, Si フォトニック結晶光偏向器による送信での変調信号強度", 応用物理学会秋季講演会, no. 18a-212A-7, 2018.

[3] 鉄矢諒, 阿部紘士, 伊藤寛之, 馬場俊彦, "縦列アレイ型 Si フォトニック結晶光偏向器の送受信効率", 応用物理学会春季講演会, 12p-W631-6, 2019.

[4] 鉄矢諒, 阿部紘士, 伊藤寛之, 馬場俊彦, 縦列アレイ型 Si フォトニック結晶光偏向器の送受信効率と変調信号強度, 応用物理学会秋季講演会, no. 20a-E207-9, 2019.

[5] 倉橋諒, 阿部紘士, 鉄矢諒, 馬場俊彦, "Si フォトニック結晶光送受信アンテナを用いた空間光ビームによる FMCW LiDAR", 応用物理学会春季講演会, no. 15a-B415-7, 2020.

[6] 鉄矢諒, 阿部紘士, 伊藤寛之, 馬場俊彦, "縦列アレイ型 Si フォトニック結晶光偏向器の放射特性制御とビームステアリング," 応用物理学会秋季講演会, 2020.

[7] 鉄矢諒, 阿部紘士, 伊藤寛之, 倉橋諒, 馬場俊彦, "Si フォトニック結晶光偏向器の縦列アレイ構成による送受信特性改善", 応物春季講演会, no. 18p-Z10-4, 2021.

[8] 鎌田幹也, 玉貫岳正, 鉄矢諒, 阿部紘士, 伊藤寛之, 倉橋諒, 馬場俊彦 Si フォトニクスフル集積 LiDAR チップの感度に関する考察, 応用物理学会秋季講演会, no. 11p-N207-11, 2021.

[9] 鉄矢諒, 玉貫岳正, 伊藤寛之, 馬場俊彦, "縦列アレイフォトニック結晶光アンテナ搭載 LiDAR チップによる距離画像取得, 応用物理学会秋季講演会, no. 13a-N321-10, 2021.

[10] 児玉直也, 鉄矢諒, 鎌田幹也, 玉貫岳正 馬場俊彦, "Si フォトニック結晶導波路光偏向器の光無線通信応用", 応用物理学会春季講演会, no. 22p-E303-2, 2022.

[11] 玉貫岳正, 伊藤寛之, 鉄矢諒, 鎌田幹也, 馬場俊彦, "スローライト Si フォトニクス FMCW LiDAR チップのリアルタイム動作", 応用物理学会春季講演会, no. 25a-E303-3,

2022.

[12] 鉄矢諒, 児玉直也, 馬場俊彦, "熱光学制御によるフォトニック結晶光アンテナの送受信特性改善", 応用物理学会春季講演会, no. 25p-E303-4, 2022.

[13] 鎌田幹也, 阿部紘士, 伊藤寛之, 玉貫岳正, 鉄矢諒, 倉橋諒, 馬場俊彦, "Si フォトニクスフル集積 LiDAR チップにおける櫛状ノイズの考察", 応用物理学会春季講演会, no. 25p-E303-6, 2022.

[14] 權藤潤, 玉貫岳正, 鉄矢諒, 鎌田幹也, 伊藤寛之, 馬場俊彦, "ステップ状光ビーム走査を用いたスローライト FMCW LiDAR の実証", 応用物理学会春季講演会, no. 25p-E303-8, 2022.

[15] 鎌田幹也, 玉貫岳正, 鉄矢諒, 伊藤寛之, 阿部紘士, 倉橋諒, 馬場俊彦, "Si フォトニクスフル集積 FMCW LiDAR チップの環境光耐性", 応物秋季講演会, 2022（発表予定）.

[16] 窪田陸, 鎌田幹也, 鉄矢諒, 玉貫岳正, 馬場俊彦, "Si フォトニック結晶光偏向器のビームコリメート用プリズムレンズ(Ⅶ)---薄型・高 NA 設計と 2 枚組設計---", 応物秋季講演会, 2022（発表予定）.

[17] 山本航平, 鉄矢諒, 岡野誠, Cong Guangwei, 山本宗継, 山田浩治, 馬場俊彦, "熱光学制御 SLG 光ビームスキャナのドーピング濃度依存性", 応物秋季講演会, 2022（発表予定）.